Adhesion of fluctuating membranes

Adhäsion fluktuierender Membranen

Der

Naturwissenschaftlichen Fakultät

der

Friedrich-Alexander-Universität Erlangen-Nürnberg

FRIEDRICH-ALEXANDER
UNIVERSITÄT
ERLANGEN-NÜRNBERG

NATURWISSENSCHAFTLICHE
FAKULTÄT

---

zur

Erlangung des Doktorgrades Dr. rer. nat.

vorgelegt von

Timo Wolfgang Bihr

aus

Ellwangen/Jagst, Deutschland

Als Dissertation genehmigt von der Naturwissenschaftlichen Fakultät der Friedrich-Alexander-Unversität Erlangen-Nürnberg

Tag der mündlichen Prüfung:	9.07.2015
Vorsitzender des Promotionsorgans:	Prof. Dr. Jörn Wilms
Gutachter:	Prof. Dr. Ana-Sunčana Smith
	Prof. Dr. Eric Lutz

Contents

I Summary **9**

1 Summary **11**

2 Zusammenfassung **17**

II General introduction **23**

I.3 Introduction **25**

I.4 Physical models of membranes **29**
I.4.1 Molecular dynamics 30
I.4.2 Helfrich-Hamiltonian 31
I.4.2.1 The Monge Gauge 32

I.5 Biomimetic model systems and cell adhesion **43**
I.5.1 Reflection Interference Contrast Microscopy 45

I.6 Theoretical models of adhesion dynamics **47**
I.6.1 Ligand-receptor bonds and their dynamics 47
I.6.2 Equilibrium models of membrane adhesion 50
I.6.3 Dynamics of membrane adhesion 52
I.6.3.1 Nucleation 52
I.6.3.2 Microscopic dynamic models 54
I.6.3.3 Diffusion models 55

I.7 Diffusion limited growth 61

III Publications 65

P1 Two intertwined facets of adherent membranes: membrane roughness and correlations between ligand–receptors bonds 67

P2 Switching from Ultraweak to Strong Adhesion 87

P3 Nucleation of Ligand-Receptor Domains in Membrane Adhesion 97

P4 Multiscale approaches to protein-mediated interactions between membranes - Relating microscopic and macroscopic dynamics in radially growing adhesions 115

P5 From growth curves to association rates in specific membrane adhesion 139

P6 Facile colloidal coating of polystyrene nanospheres with tunable gold dendritic patches 153

IV Outlook 171

7 Outlook 173

V Bibliography 177

VI Miscellaneous 193

Curriculum vitae 195

Publication in peer-reviewed journals 198

Conferences 202

Articles in co-authorship 204

Statuary declaration 209

Danksagungen **211**

A Receptor jamming induces ring-like adhesions in model membranes **213**

Part I

Summary

1 Summary

In this thesis, we treat protein mediated adhesion between two lipid bilayer membranes. We describe the membranes with the help of the Canham-Helfrich [1, 2] theory which describes the membrane on a coarse-grained level with the help of only a few quantities like the bending rigidity. In the introduction, we discuss parts of this theory that are relevant for our work. This includes the derivation of a Langevin equation describing the time development of a membrane surrounded by a fluid and the influence of bonds (i. e. pinning centres) on the energetics and height fluctuations of the membrane. Furthermore, we discuss experimental aspects of cell adhesion and cell mimetic model systems. In the following chapter of the introduction, we treat ligand-receptor bonds and their dynamics. Additionally, several theoretical works on membrane adhesion are discussed. Finally, an example of the treatment of diffusion limited growth of adhesion domains is presented. Thereby, we illustrated the shortcomings of the conventional treatments in the literature. The last chapter of the introduction treats a seemingly completely different topic, namely the surface diffusion limited growth of metal domains on colloidal particles. Even though this phenomenon is not motivated by biology but rather by chemical engineering, there are parallels between both growth processes which lead to a collaboration with experimentalists. In the respective introductory chapter, we discuss the shape instabilities associated with diffusion limited (and analogous) growth processes and our work in this research field.

An overview of our publications and their thematic classification can be seen in figure 1.1. We distinguish between the mathematical treatment which could be either analytical approaches, numerical approaches or simulations and the length scale on which the problem is treated. Thereby, we have three possibilities. The nanoscopic length scale is the length scale of single molecules, i. e. the length

treatment \ length scale	nanoscopic (molecule)	microscopic (membrane)	mesoscopic (cell/colloid)
analytical	Publication 3, 4		Publication 5
numerical	Publication 3		
simulation	Publication 1, 2, 3	Publication 1, 2, 4	Publication 4, 6

Figure 1.1: Thematic classification of the publications in this thesis. We distinguish between the mathematical treatment (top to bottom) and the length scale (left to right) on which the respective problem was treated.

scale that is accessible with electron microscopes or super-resolved fluorescence microscopy for which the nobel prize in chemistry was awarded in 2014 [3]. On this length scale, we focus on the dynamics of single molecules like the binding dynamics between ligands and receptors. Under the microscopic length scale, we understand the typical length scale of the membrane which is defined by its undulations (see for example equation (4.7)). The undulations are in turn determined by the membrane properties. This length scale is accessible with conventional light microscopes. Here, the focus is on the behaviour of the membrane. Finally, we define the mesoscopic length scale as the length scale of a cell or a colloid where structures are almost visible by the bare eye. This is the largest length scale that is possible for the problems that we treat in this thesis. Examples for phenomena on those length scales are depletion zones around the growing domains emerging in diffusion limited growth or the morphology of metal domains grown in a surface diffusion limited growth process.

In Publication P1, we study the equilibrium fluctuations of a membrane that is adhered to an underlying scaffold. The interaction between the membrane and the scaffold has two contributions (like in the rest of the publications about membrane adhesion in this thesis). The first contribution is a non-specific harmonic interaction that accounts for various contributions like van-der-Waals interactions or gravity [4]. The other contribution is the specific interaction induced by ligand-receptor bonds. Here, we focus on the case where the binders are immobile and are abundant on the scaffold and as well in the membrane. We obtain our results with Langevin simulations that develop the membrane in time

numerically and find that the correlations between the bonds and the membrane roughness is always larger than in the case of a random bond configuration. Furthermore, these two quantities follow master curves that only depend on the instantaneous bond density. Hence, we show in this work that in principle the membrane roughness could be mapped to the local bond density in experiments.

In the following Publication P2, we use this insight to detect possible nucleation events in experiments with biomimetic model cells. These nucleation events mark the beginning of the transition between ultraweak adhesion, where the membrane resides in the minimum of the non-specific potential, to strong adhesion where the membrane is bound to the substrate by ligand-receptor bonds. In the experiments, the time evolution is observed with Dynamical Reflective Interference Contrast Microscopy (Dy-RICM). We interpret the so obtained data with Langevin-simulations similar to those of Publication P1. With the simulation data, we find that the membrane roughness is maximal if it resides at intermediate heights while it is undergoing the transition from ultraweak adhesion to strong adhesion. We observe the same signature in the experiments and are, hence, able identify such transitions, i. e. nucleation events. Furthermore, it is possible to detect such nucleation seeds while their size is still smaller than the optical resolution limit because such seeds also influence the membrane in their vicinity.

Publication P3 discusses a comprehensive theory of the dynamics of the nucleation of ligand-receptor domains between two membranes (or a membrane and a substrate). As a first step, we calculate the critical number of bonds that are sufficient for a stable bond domain in a capillary approximation. We find that in the experimental relevant parameter regime this number is very small. In order to describe the nucleation dynamics, we set up a master equation that develops the probability of having a certain number of bonds in an unstable domain in time and that is solved numerically. In this master equation, the transition probabilities from one state to another state are determined by effective reaction rates. These effective reaction rates are Dembo or Bell rates [5, 6] averaged over membrane height distribution. In order to justify this averaging procedure, we additionally simulate the nucleation dynamics with the Langevin scheme already used in Publication P1 and P2. The results between the two approaches agree very well proving that the averaging procedure to obtain the effective reaction rates is accurate and, thus, the effective reaction rates describe the reaction kinetics properly. Furthermore, we approximate the average nucleation time analytically. This approximation works very well for the experimental relevant parameters used in the other two approaches. We find that the nucleation dynamics is very sensitive to the critical number of bonds necessary for a stable domain. Just one additional bond can increase the average nucleation time by orders of magnitude. Moreover, there is an optimal density for stiff bonds where the average nucleation

time is minimal. This points to a potential regulatory mechanism in biological cells controlling the cell recognition process.

In the next Publication P4, we develop a new simulation scheme that can simulate membrane adhesion based on the effective reaction rates that were already mentioned in the last paragraph. We present a thorough discussion of the Langevin scheme and the new scheme with the effective rates. As a first step to derive the effective reaction rates, we calculate the average membrane profile and the membrane height fluctuations depending on the bond configuration. In this calculation, we find that for our Helfrich-Hamiltonian the membrane height distribution is Gaussian. This result is then used to obtain the averaged Dembo and Bell rates [5, 6], i. e. the effective reaction rates. Furthermore, we discuss the role of the bond configuration on the effective reaction rates. Then, the simulation scheme is presented and the possible performance gain compared to the Langevin scheme is discussed. As it turns out, the very low computational cost of the new simulation scheme enable to simulate systems on biological relevant length and time scales and to compare our simulation results directly to experimental data. As a proof of the accuracy of the effective reaction rates, we compare the results of the new simulation scheme with the results of the Langevin scheme that develops the membrane explicitly in time. The comparison reveals an excellent agreement between both schemes in the considered parameter regime. We conclude the publication with the discussion of the radial growth of adhesion domains. Here, we focus on the regime with a large binder density where the growth dynamics is reaction limited and the low density regime where the growth is limited by the diffusion of the binders to the domain.

In the last publication P5 about binder mediated membrane adhesion, we describe the growth dynamics of adhesion domains with the help of the diffusion equation. More specifically, we describe the growth with a boundary value problem similar to the Stefan problem [7]. In contrast to earlier works [8–11], we incorporate the reaction rate self-consistently into the boundary conditions. In this boundary value problem, we have for low mobile binder densities a short time regime that is reaction limited and an asymptotic regime that is diffusion limited. Furthermore, the growth is always reaction limited for large densities. These theoretical results enable to extract the reaction rate between ligands and receptors embedded in opposing membranes without interfering their dynamics. As an application, we extract the reaction rates of several binding pairs in different experimental environments and find values that are consistent with earlier measurements. Additionally, our values are consistent with theoretical expectations. For example, we determine a larger reaction rate if the membrane height fluctuations are enhanced (see also publication P4). Finally, we observe the transition between the low density and the large density regime confirming one of the main results of our theory.

The partial coating of colloidal particles with gold is treated in publication P6. In this article, we describe an experimental method to produce such partially coated colloids (patchy particles) and interpret the results theoretically. In the experiment, chloroauric acid and ascorbic acid are dissolved in a solution of cationic polystyrene (PS) colloids. After the addition of the two acids, an immediate color change of the solution is observed. This color change shows the influence of the metal patch on the interaction between light and the PS colloids. Electron micrographs of the colloids reveal that the morphology of the metal domains vary from almost radial domains to dendrite domains. We explain these variations with changes in the sticking probability of the diffusing gold precursor. Here the sticking probability is the probability to get bound (under the condition that the metal precursor is next to the gold domain) during the time that the metal precursor requires to diffuse its own diameter. We find that according to this hypothesis and accompanying simulations of diffusion limited aggregation increasing the reaction temperature lowers the sticking probability whereas increasing the concentration of ascorbic acid increases the sticking probability. We attribute this finding to the influence of the temperature and the ascorbic acid on the diffusion of the metal precursor on the colloid surface.

2 Zusammenfassung

In dieser Dissertation, behandeln wir die Ädhesion mittels Bindungsmolekülen zwischen Membranen, die aus jeweils einer Lipiddoppelschicht bestehen. Dabei beschreiben wir die Membran mit Hilfe der Canham-Helfrichtheorie [1, 2], die die Membran auf einer vergröberten Stufe mithilfe von nur wenigen Größen wie der Biegesteifigkeit beschreibt. In der Einleitung, diskutieren wir Teile dieser Theorie, die relevant für diese Arbeit hier sind. Dies beinhaltet die Herleitung einer Langevingleichung, die die Zeitentwicklung einer Membran, umgeben von einer Flüssigkeit und den Einfluss von Bindungen (also Haftstellen) auf die Energie und die Höhenfluktuationen der Membran, beschreibt. Des weiteren diskutieren wir experimentelle Aspekte der Zelladhäsion und zellmimetischer Modellsysteme. Im darauffolgenden Kapitel der Einleitung, behandeln wir Liganden-Rezeptorenbindungen und deren Dynamik. Zusätzlich, diskutieren wir einige theoretische Studien über Membranadhäsion. Zu guter Letzt, wird ein Beispiel diffusionsbegrenzten Wachstums sowie dessen Behandlung präsentiert. Dabei illustrieren wir die Unzulänglichkeiten der konventionellen Herangehensweise in der Literatur. Das letzte Kapitel der Einleitung behandelt ein scheinbar gänzlich anderes Thema, nämlich diffusionsbegrenztes Wachstum von Metalldomänen auf der Oberfläche kolloidaler Teilchen. Obwohl dieses Phänomen nicht von der Biologie sonder eher vom Chemieingenieurwesen motiviert ist, gibt es Parallelen zwischen beiden Wachstumsprozessen, die zu einer Zusammenarbeit mit Experimentatoren geführt hat. Im entsprechenden Einleitungskapitel, diskutieren wir die Forminstabilitäten, die mit diffusionsbegrenztem (und analogem) Wachstumsprozessen verbunden sind und unseren Beitrag zu diesem Forschungszweig.

Ein Überblick unserer Veröffentlichungen und deren thematische Einordnung ist in Abbildung 2.1 zu sehen. Wir unterscheiden zwischen der mathematischen Herangehensweise die entweder analytisch, numerisch oder über Simulationen sein kann und der Längenskala auf der das Problem betrachtet wird. Es gibt hier

Längenskala / Ansatz	nanoskopisch (Molekül)	mikroskopisch (Membran)	mesoskopisch (Zelle/Kolloid)
analytisch	Publikation 3, 4		Publication 5
numerisch	Publikation 3		
Simulation	Publikation 1, 2, 3	Publikation 1, 2, 4	Publikation 4, 6

Figure 2.1: Thematische Einordnung der Veröffentlichung dieser Dissertation. Wir unterscheiden zwischen der mathematischen Herangehensweise (von oben nach unten) und der Längenskala (von links nach rechts) auf der das jeweilige Problem behandelt wird.

drei Möglichkeiten. Zuallererst, die nanoskopische Längenskala auf der Ebene der einzelnen Moleküle, das heißt die Längenskala die mit Elektronenmikroskopen oder superaufgelösten Fluoreszenzmikroskopen, für die der Nobelpreis in Chemie im Jahr 2014 [3] vergeben wurde, aufgelöst werden kann. Auf dieser Längenskala, konzentrieren wir uns auf die Dynamik der einzelnen Moleküle wie der Bindungsdynamik zwischen Liganden und Rezeptoren. Unter der mikroskopischen Längenskala, verstehen wir die typische Längenskala der Membran, die durch ihre Verformungen (siehe zum Beispiel Gleichung (4.7)) bestimmt ist. Diese Membranverformungen sind wiederum durch die Membraneigenschaften bestimmt. Die Längenskala der Membranverformungen ist mit herkömmlichen Lichtmikroskopen zugänglich. Hier, liegt der Fokus auf dem Verhalten der Membran. Schließlich, definieren wir die mesoskopische Längenskala als die Längenskala einer Zelle oder eines Kolloids. Dies ist die größtmögliche Längenskala für die Problemstellungen, die wir in dieser Dissertation betrachten. Beispiele für Phänomene auf dieser Längenskala sind die Verarmungszonen, die um die wachsenden Domänen bei diffusionslimitierten Wachstum auftreten oder die Morphologie vom Metalldomänen, die durch einen diffusionslimitierten Prozess auf einer Oberfläche gewachsen sind.

In der Veröffentlichung P1 untersuchen wir die Gleichgewichtshöhenfluktuationen einer Membran, die an ein darunterliegendes Substrat adhäriert ist. Die Wechselwirkung zwischen der Membran und dem Substrat hat dabei zwei Beiträge (wie auch in den restlichen Veröffentlichungen dieser Arbeit). Der erste Beitrag ist ein nicht-spezifisches harmonisches Potential, das verschiedene Wechselwirkun-

gen wie van-der-Waals Kräfte oder die Schwerkraft zusammenfassen soll [4]. Der andere Beitrag ist die spezifische Wechselwirkung durch die Bindungen zwischen Liganden und Rezeptoren. Hier konzentrieren wir uns auf den Fall, in dem die Bindungsproteine nicht diffundieren und im Überfluss auf dem Substrat sowie in der Membran vorhanden sind. Wir erhalten unsere Resultate mithilfe von Langevinsimulationen, die die Membran in der Zeit entwickeln. Wir beobachten, dass die Korrelationen zwischen den Bindungen und die Rauhigkeit der Membran immer größer ist als im Fall einer zufälligen Bindungskonfiguration. Des weiteren gehorchen diese beiden Größen universellen Kurven, die nur von der momentanen Dichte abhängen. Folglich zeigen wir damit dass im Prinzip die Rauhigkeit der Membran mit der lokalen Bindungsdichte eindeutig im Zusammenhang steht.

In der folgenden Veröffentlichung P2 verwenden wir diese Erkenntnis um mögliche Nukleationsereignisse im Experiment mit biomimetischen Modellzellen zu detektieren. Diese Nukleationsereignisse kennzeichnen den Beginn des Übergangs zwischen der sehr schwachen Adhäsion, in der die Membran sich im Minimum des nicht-spezifischen Potentials aufhält, und der starken Adhäsion in die Membran durch Bindungen zwischen Liganden und Rezeptoren an das Substrat gebunden ist. Im Experiment wird die Zeitentwicklung der Membran mit Dy-RICM (Dynamical Reflective Interference Contrast Microscopy) gemessen. Wir interpretieren die so erhaltenen Daten mithilfe von Langevin-Simulationen, die ähnlich sind zu denen aus Veröffentlichung P1. In diesen Simulationsdaten beobachten wir, dass die Membranrauhigkeit am größten ist während die Membran im Übergang von der sehr schwachen zur starken Adhäsion ist und sich zwischen den beiden jeweiligen charakteristischen Höhen dieser Adhäsionszustände befindet. Im Experiment beobachten wir die gleiche Signatur und sind folglich in der Lage solche Übergänge, also Nukleationsereignisse, zu identifizieren. Darüber hinaus ist es möglich Nukleationskeime zu beobachten, während ihre Größe noch kleiner als die optische Auflösungsgrenze ist, da solche Keime auch die Membran in ihrer Umgebung beeinflussen.

Veröffentlichung P3 behandelt eine umfassende Theorie der Nukleationsdynamik von Adhäsionsdomänen, die aus Bindungen zwischen Liganden und Rezeptoren bestehen. Als ersten Schritt berechnen wir in Kapillarnäherung die kritische Anzahl von Bindungen die hinreichend für eine stabile Bonddomäne ist. Es stellt sich heraus, dass im experimentell relevanten Parameterbereich diese Anzahl sehr klein ist. Um die Nukleationsdynamik zu beschreiben, stellen wir eine Mastergleichung auf, die die Wahrscheinlichkeit, dass sich eine bestimmte Anzahl von Bindungen in einem nicht stabilen Domäne befindet, in der Zeit entwickelt und lösen diese numerisch. In dieser Mastergleichung sind die Übergangswahrscheinlichkeiten von einem Zustand in den nächsten gegeben durch effektive Reaktionsraten. Diese sind die Dembo- bzw. Bellraten [5, 6] gemittelt über die Membranhöhenverteilung. Um diese Mittlung zu rechtfertigen, simulieren wir

zusätzlich die Nukleationsdynamik mit der Langevinmethode, die schon in der Veröffentlichung P1 und P2 verwendet wurde. Die Ergebnisse zwischen beiden Ansätzen stimmen sehr gut überein. Dies beweist, dass die Mittlung, um die effektiven Raten zu erhalten sehr gut, ist und folglich die effektiven Raten die Reaktionskinetik zutreffend beschreiben. Des weiteren näheren wir die durchschnittliche Nukleationszeit analytisch. Diese Näherung funktioniert hervorragend für die experimentellen relevanten Parameter, die in den anderen zwei Ansätzen verwendet wurden. Wir sehen, dass die Nukleationsdynamik sehr empfindlich von der kritischen Anzahl der Bindungen in einer stabilen Domäne abhängt. Nur eine zusätzliche Bindung kann die durchschnittliche Nukleationszeit um einige Größenordnungen erhöhen. Darüberhinaus existiert bei steifen Bindungen eine optimale Dichte bei der die durchschnittliche Nukleationszeit minimal ist. Dies weist auf einen möglichen regulatorischen Mechanismus in biologischen Zellen hin, der die Zellerkennung steuert.

In der nächsten Publikation P4 entwickeln wir eine neue Simulationsmethode, mit der wir in der Lage sind, die Dynamik einer adhärierenden Membran zu simulieren. Diese Methode basiert auf den effektiven Reaktionsraten, die schon im letzten Absatz erwähnt wurden. Als ersten Schritt um die effektiven Reaktionsraten herzuleiten, berechnen wir das durchschnittliche Membranprofil und die Membranhöhenfluktuationen in Abhängigkeit der Bindungskonfiguration. In dieser Rechnung stellt sich heraus, dass für unseren Helfrich-Hamiltonian die Membranhöhenverteilung gaussförmig ist. Dieses Resultat wird dann verwendet, um die über die Membranhöhenverteilung gemittelten Dembo- und Bellraten, also die effektiven Reaktionsraten, zu erhalten. Daraufhin präsentieren wir das Simulationsschema und diskutieren die mögliche Ersparnis an Simulationszeit verglichen mit der Langevinsimulation. Wie sich herausstellt, ermöglichen die sehr niedrigen Simulationszeiten des neuen Simulationsschema, Systeme auf biologisch relevanten Längen- und Zeitskalen zu simulieren und die Simulationsergebnisse direkt mit experimentellen Daten zu vergleichen. Zum Beweis der Anwendbarkeit der effektiven Raten vergleichen wir die Ergebnisse des neuen Simulationsschemas mit den Ergebnissen der Langevinsimulation, die die Membran im Gegensatz zum neuen Schema explizit in der Zeit entwickelt. Der Vergleich zeigt eine hervorragende Übereinstimmung im untersuchten Parameterbereich zwischen beiden Schemata. Wir beschließen die Veröffentlichung mit der Diskussion des radialen Wachstums von Adhäsionsdomänen. Hier konzentrieren wir uns auf die Parameterbereiche mit großen Dichten von Bindungsproteinen, wo das Wachstum reaktionslimitiert ist und den Parameterbereich mit niedrigen Dichten, wo das Wachstum durch die Diffusion der Bindungsproteine zur Domäne limitiert ist.

In der letzten Veröffentlichung P5 über Membranadhäsion, die durch Bindungsproteine vermittelt wird, beschreiben wir die Wachstumsdynamik von Ad-

häsionsdomänen mit der Hilfe der Diffusionsgleichung. Genauer gesagt, beschreiben wir das Wachstum mit der Hilfe eines Randwertproblems ähnlich zum Stefanproblem [7]. Im Gegensatz zu früheren Arbeiten [8–11], fügen wir selbstkonsistent eine Reaktionsrate in die Randbedingungen ein. In diesem Randwertproblem gibt es für kleine Dichten der diffundierenden Bindungsproteine ein Kurzzeitregime, das reaktionslimitiert ist und ein asymptotisches Regime, das diffusionslimitiert ist. Des weiteren ist das Wachstum bei hohen Dichten immer reaktionslimitiert. Diese theoretischen Resultate ermöglichen es, die Reaktionsrate zwischen Liganden und Rezeptoren, die sich in gegenüberliegenden Membranen befinden, zu messen, ohne deren Dynamik zu stören. Als Anwendung extrahieren wir die Reaktionsraten verschiedener Bindungspaare in unterschiedlichen experimentellen Umgebungen und erhalten Werte, die mit früheren Messungen konsistent sind. Zusätzlich sind unsere Werte auch konsistent mit theoretischen Erwartungen. Zum Beispiel bestimmen wir eine größere Reaktionsrate, wenn die Membranhöhenfluktuationen erhöht sind (siehe hierzu auch Veröffentlichung P3). Schließlich beobachten wir den Übergang zwischen dem Regime mit kleinen Dichten und dem Regime mit großen Dichten, was eines unserer Hauptresultate unserer Theorie bestätigt.

Die teilweise Beschichtung von kolloidalen Teilchen mit Gold wird in Veröffentlichung P6 behandelt. In diesem Artikel beschreiben wir eine experimentelle Methode um teilweise beschichtete Kolloide (sogenannte “patchy particles”) herzustellen und interpretieren die Ergebnisse theoretisch. Im Experiment wird Tetrachlorogoldsäure und Ascorbinsäure in einer Lösung mit kationischen Polystyrolkolloiden (PS-Kolloiden) gelöst. Nach der Beigabe der beiden Säuren findet ein unmittelbarer Farbwechsel der Lösung statt. Dieser Farbwechsel zeigt den Einfluss der Metallschicht auf die Wechselwirkung zwischen Licht und den PS-Kolloiden. Aufnahmen eines Elektronenmikroskops der Kolloide zeigen, dass die Gestalt der Metalldomänen zwischen fast radialen und dendritischen Domänen variiert. Wir erklären diese Variationen mit Änderungen der Anhaftwahrscheinlichkeit des diffundierenden Vorläuferstoffs des Golds. Hier ist die Anhaftwahrscheinlichkeit die Wahrscheinlichkeit des Goldvorläuferstoffs gebunden zu werden (unter der Voraussetzung, dass der Goldvorläuferstoff sich direkt an der Golddomäne befindet) während der Zeit, die der Metallvorläufer braucht um seinen eigenen Umfang zu diffundieren. Wir beobachten, dass laut dieser Hypothese und zusätzlichen Simulationen diffusionsbegrenzter Aggregation eine zunehmende Reaktionstemperatur die Anhaftwahrscheinlichkeit senkt wohingegen eine zunehmende Konzentration von Ascorbinsäure die Anhaftwahrscheinlichkeit erhöht. Wir führen diesen Befund auf den Einfluss der Temperatur und der Ascorbinsäure auf die Diffusion des Goldvorläuferstoffs auf der Kolloidoberfläche zurück.

Part II

General introduction

I.3 Introduction

Cell adhesion plays a crucial role in many biological processes like the immune response, the signal transduction or maintaining the structure of multicellular organisms (see Sackmann and Smith [12] for a recent review from the physical point of view). The probably most fascinating example of such an adhesion process is the dynamics of the immunological synapse (see Dustin and Groves [13] for a recent review). This synapse forms between an antigen presenting cell (APC) and a T-Cell (or also other immune cells) and consists of proteins in the opposing membrane that interact by highly specific lock and key forces. The formation of this synapse is a highly complex process where unregulated and regulated processes play a role and has attracted much interest in the biological community [13].

However, due to the complexity of biological cells, the interpretation of experiments with truly biological cells are elusive and so much interest focuses on biomimetic model systems [14]. These model systems provide insights into many features of cell adhesion (see for example [15]). Furthermore, experiments with such systems are potentially more reproducible than experiments with biological cells. A sketch of a typical biomimetic model system can be seen in figure 3.1. Usually, biomimetic model systems mainly consist of a vesicle which is placed above a supported lipid bilayer. Ligand-receptor pairs mimic lock and key forces between the two membranes whereas a polymer cushion mimics the glycocalyx. Depending on the set-up, the binders can be immobilized, however at least one binding species should be mobile to enable stable adhesion. From below the supported membrane and with advanced experimental techniques [16] it is possible to observe the contact zone between the vesicle and its counterpart. Furthermore, additional data can be obtained like membrane height fluctuations (see also section I.5). This data provides reliable and meaningful information about the thermal equilibrium and the dynamics of intermembrane adhesion [17–19].

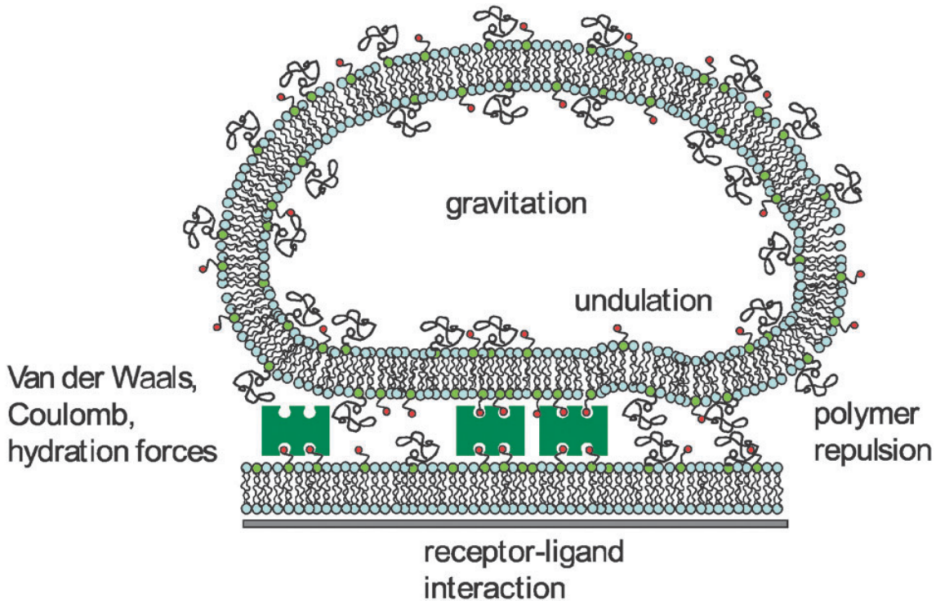

Figure 3.1: Biomimetic model system consisting of a vesicle with polymers for a repulsive interaction, a supported lipid bilayer and binders embedded in both membranes. The interaction between the membranes is determined by van-der-Waals forces, Coulomb forces and hydration forces. The vesicle's membrane can still fluctuate while the fluctuations of the membrane on the substrate are suppressed due to the solid surface below. Figure from [14].

Physical modelling of intermembrane adhesion is a challenge because many processes on many different length scales and time scales determine the dynamics. The process happening on the shortest length scale is the binding dynamics of the ligand-receptor bonds. This process happens on the length scale (in the order of nanometer) of the binding potential between ligand and receptor. This length scale is connected to the Bell-rates [6] that describe the reaction dynamics of ligand-receptor bonds. Additionally, there is an intrinsic reaction rate between both binder species which determines the speed of the binding dynamics. On a longer length scale, the membrane containing the binders determines the dynamics. The membrane dynamics can be treated with the Canham-Helfrich theory [1, 2] which describes the energetics of membranes in dependence of its geometrical shape. Due to the flexibility of biological membranes, the membrane shape fluctuates on a length scale of around 100 nm with amplitudes of several nanometers and on time scales of milliseconds [4]. These membrane shape fluctuations determine the number of encounters between ligands and receptors and hence contribute to the reaction dynamics. Finally, in the late stages of the adhesion process, the membrane (or the substrate) can get depleted of binders around the adhesion domain, especially for low binder densities and large reaction rates [8–11, 20]. Consequently, the binders have to diffuse to the adhesion patch and the diffusion limits the growth of the adhesion domain. This limit is particularly relevant for true cells because only very few adhesion molecules reside on the cell membrane.

The treatment of the above discussed processes forms the backbone of this thesis. In chapter I.4, we give a short, thematic introduction into the modelling of membrane especially on the Canham-Helfrich theory [1, 2]. Here, we focus on the Monge gauge [21], the parametrization of the membrane that we use throughout this thesis. Then, we discuss selected experiments with biomimetic model systems and the experimental techniques that are typically used (chapter I.5). Finally, we discuss in section I.6 different models of cell adhesion describing the thermodynamic equilibrium and the dynamics.

In part III of the thesis, we describe the adhesion process and connect the three different dynamics processes, discussed above, namely the binding dynamics, the membrane dynamics and the binder diffusion. Initially, we simulate the membrane with a Langevin simulation (publication P1 and P2, also figure 3.2 for a snapshot of the simulation). Here, we couple the reaction dynamics and the membrane dynamics, separately. With this simulation scheme, we explore the correlations between ligand-receptor bonds depending on their density. Later, we use this results to detect nucleation seeds of adhesion patches that are below the optical resolution of standard optical microscopes. Next, we derive effective reaction rates which combine the Bell dynamics with the membrane dynamics if the intrinsic reaction rate is much smaller than the time scale of the membrane

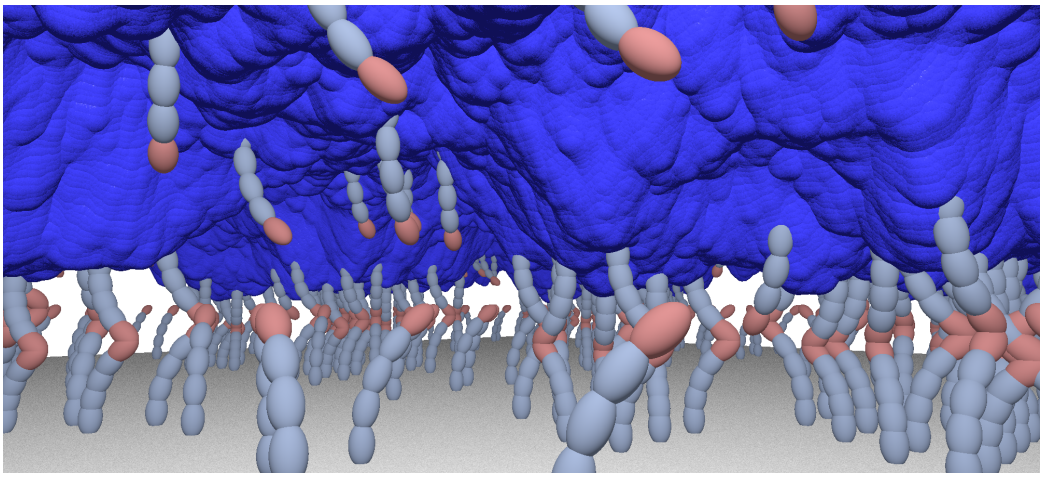

Figure 3.2: Snapshot of a simulation of intermembrane adhesion via cadherin bonds. The cadherins (embedded in the membrane) bind to other cadherins (on the substrate). As the membrane is flexible, the membrane deforms when two binders form a bond. Furthermore, there are membrane shape fluctuations due to stochastic forces caused by thermal fluctuations.

shape fluctuations (publication P3). On this basis, we develop a semi-analytical theory of the nucleation of adhesion domains. Furthermore, we present a Monte Carlo simulation scheme based on the concept of our effective reaction rates which is applicable on biological relevant length and time scales (see publication P4). Finally, we investigate the transition between reaction limited and diffusion limited growth behaviour (see publication P5). In this publication, we analyse experimental growth curves and extract the reaction rate for different binding pairs in different environments.

Additionally to our biologically motivated work, we also model the surface diffusion limited growth of metal domains on colloid particles. This was motivated by the experimental work of Klupp Taylor and co-workers [22–24]. We give an overview of diffusion limited growth and related phenomena in chapter I.7 and mainly discuss the instability of the shape of the growing domain. In publication P6, we discuss the different morphologies of the resulting domains in the experiment and explain this with changes of the tracer density, the diffusion constant and the reaction rate.

I.4

Physical models of membranes

Biological membranes separate the interior of a cell from its environment. More specifically, they form a confined space where biological processes take place, undisturbed by environmental influences. Furthermore, the biological membrane controls the exchange of material between inside and outside the cell and senses external signals. It is even speculated that the processes that led to the very first development of life happened within a closed membrane, i. e. a vesicle.

Biological membrane are organelles comprised of many different kinds of proteins and lipids. The latter are so-called amphiphiles that have a polar head group, which is hydrophilic, and a non-polar double-chained hydrocarbon tail, which is hydrophobic. If the lipids are embedded in a suitable solvent (usually water), they can form large connected entities like vesicles or lipid bilayers [25, 26]. The hydrophobic hydrocarbon tails point to the middle of the bilayer, whereas the hydrophilic polar heads are exposed to the surrounding water molecules (see for example [27]). Such bilayers are not static structures. Instead, the lipids as well as the proteins diffuse freely within the membrane and hence the membrane can be considered a two-dimensional fluid [28]. Additionally, the surrounding fluid acts on the membrane by thermally fluctuating, hydrodynamic forces (see Seifert [29] and references therein).

In this chapter, we present an overview of the two main approaches to describe the dynamics of membranes and discuss their respective potentials and limitations. Besides that, we will introduce the relevant length and time scales. In molecular dynamics (MD) simulations (see Lyman and Patel [30] for a recent review), the movement of every atom or of different groups of the lipids is simulated explicitly. An alternative approach to molecular dynamics are continuum methods. They rely on the fact that the membrane thickness is several orders of

magnitude smaller than its lateral dimension and hence can be described as an infinite thin sheet (see [31] for a review). Within this approach, the energetics are described by the so-called Helfrich-Hamiltonian, which Canham [1] and Helfrich [2] originally introduced.

As of now, about 10^5 lipids can be simulated in MD simulations, which corresponds to a patch of the size of around $150\,\mathrm{nm} \times 150\,\mathrm{nm}$ on a timescale of around one millisecond. This is still orders of magnitude below the length and time scales of cell-sized objects. Brown estimated [32] on the basis of Moore's law that it will take around 50 years until it will be possible to simulate membranes atomistically on such scales. Furthermore, molecular dynamics simulations cannot give analytical insights in contrast to the Helfrich theory. For this reason, the Helfrich-Hamiltonian is favored if molecular details are not important. This is for example particularly the case for a low concentration of proteins or transport phenomena within the membrane.

I.4.1 Molecular dynamics

As powerful computers have been become readily available over the last few decades, many computational models and software packages for the simulation of membranes have been developed (see for example [30, 33] for recent reviews). In principle, one distinguishes between atomistic simulations, where every single atom is simulated explicitly with the Newtonian equations of motion, and coarse grained simulations, where several atoms are put into one "super atom". Likewise, the surrounding fluid can be simulated explicitly or integrated implicitly into the simulation scheme. The latter schemes are called solvent free simulations. Coarse-grained simulations are of course less computationally expensive and hence more suitable for mesoscopic and macroscopic effects, whereas atomistic simulations are necessary if one is interested in molecular details.

The first atomistic MD simulations of lipid bilayer membranes were done in the early eighties of the last century [34, 35]. Even though the simulated membranes were very small (in the order of 100 lipids and below), they were sufficient to reproduce experimentally obtained order parameters very well [35]. Coarse-grained models of membranes were developed later. Examples of software packages that are able to simulate membranes on coarse-grained level are the Martini force field [36, 37] and the Espresso package [38]. Such packages have been heavily used and the interested reader is referred to the review of Lyman [30] and the references therein.

An interesting example of coarse-grained models is the work of Reynwar et al. [39] about the aggregation and vesiculation of membrane proteins. They showed that curved membrane proteins or capsids can aggregate on the membrane even

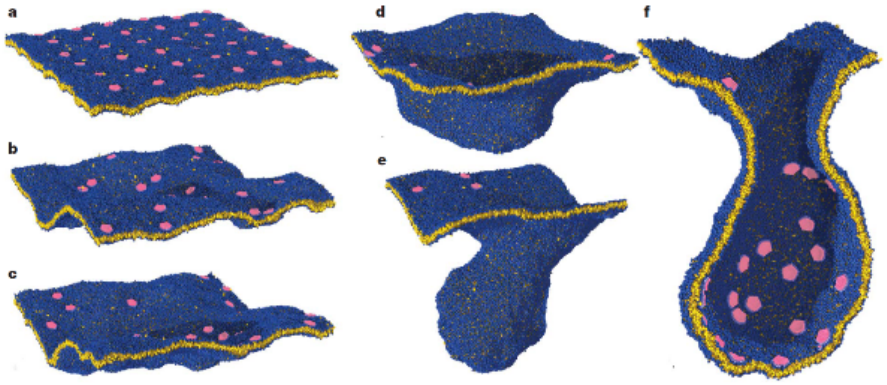

Figure 4.1: Different stages of vesiculation from MD simulations. First, the capsids cluster. This causes a local deformation of the membrane. Eventually, a vesicle develops out of this deformation. The times of the simulation snapshots are a) 0, b) 20,000 c) 40,000, d) 50,000, e) 60,000 and f) 70,000 timesteps. The total simulation time was about 10^{-3} s. From Reynwar et al. [39].

though approximate results of the Helfrich theory (see section I.4.2) suggest that proteins with isotropic curvatures repel each other [40–42]. Furthermore, this aggregation bends the membrane locally thereby initiating the formation of a vesicle (see also figure 4.1).

I.4.2 Helfrich-Hamiltonian

In contrast to MD-simulations, the Helfrich-Hamiltonian [1, 2] requires only very few parameters instead of the whole number of different interaction parameters used in molecular dynamics approaches. The Helfrich-Hamiltonian in its most general form is

$$\mathcal{H}_B[h(\mathbf{x})] = \int \mathrm{d}A \left[\frac{\kappa}{2}(2H - c_0)^2 + \kappa_c K\right], \tag{4.1}$$

where κ is the bending rigidity, H the mean curvature, c_0 the intrinsic curvature of the sheet, κ_c the saddle play modulus and K the Gaussian curvature. The surface integral over the Gaussian curvature, total curvature, is according to the Gauss-Bonnet theorem proportional to the Euler characteristic [43]. In a nutshell, the Euler characteristic counts the number of holes, cavities and edges of the surface. In addition to the bending terms of equation (4.1), other energetic contributions may have to be taken into account such as external potentials,

external forces or surface tension.

The Gaussian curvature is constant for an infinitely large sheet. This follows from the Gauss-Bonnet theorem (see for example [43]) and the fact that the membrane does not have any holes and does not separate into disconnected membrane patches. Consequently, the Gaussian curvature is not considered in this thesis.

In contrast to molecular dynamics, this continuum approach allows studies on mesoscopic length scales such as studies on equilibrium shape of cell-sized vesicles (see [44] for a recent review). For example, Seifert et al. determined a phase diagram of axisymmetric shapes depending on the area difference of the layers of the membrane and the reduced volume [45]. Later, nonaxisymmetric shapes were also treated numerically by Jarić et al. [46] and by Ziherl and Svetina [47]. They found that between the regimes with axisymmetric oblate shapes (discocytes) and axisymmetric prolate shapes (cigars) rackets and starfish-like shapes minimize the energy.

Another example where the Helfrich theory is more suitable than MD is the wrapping of nanoparticles into membranes [48–51]. Within the Helfrich formalism, it is possible to model the wrapping with only a few energetic contributions and obtain an analytical understanding of the process. Essentially, there is an energetic interplay between the bending energy, the surface tension and the adhesion energy. In this context, Raatz et al. [51, 52] showed that the range of the interaction potential between nanoparticle and membrane plays a very important role. Furthermore, the influence of the geometry (i.e. spherical particles or ellipsoidal particles) on the wrapping was studied [49, 50]. It turns out that, one major difference between spherical and ellipsoidal particles is the existence of partially wrapped particles for ellipsoidal particles even for tensionless membranes whereas spherical particles are either completely wrapped or not at all [50].

I.4.2.1 The Monge Gauge

As in our considerations the membrane is above a solid substrate, the most convenient parametrization of the membrane surface is the Monge gauge. In this parametrization, the height of the membrane surface is just a function of the Cartesian coordinates. In order to write the membrane surface as a unique function, this requires that the membrane does not have overhangs (see also Fig. 4.2).

The Monge gauge has been used for the numerical simulation of membranes [32, 53, 54]. This can include equilibrium dynamics [55, 56], the dynamics [53, 57–59] of membrane adhesion, diffusion of large proteins within the membrane [60–64] or the membrane fluctuations of a pinned membrane [65]. In these studies, either Monte Carlo methods or a Langevin equations were used. Thereby,

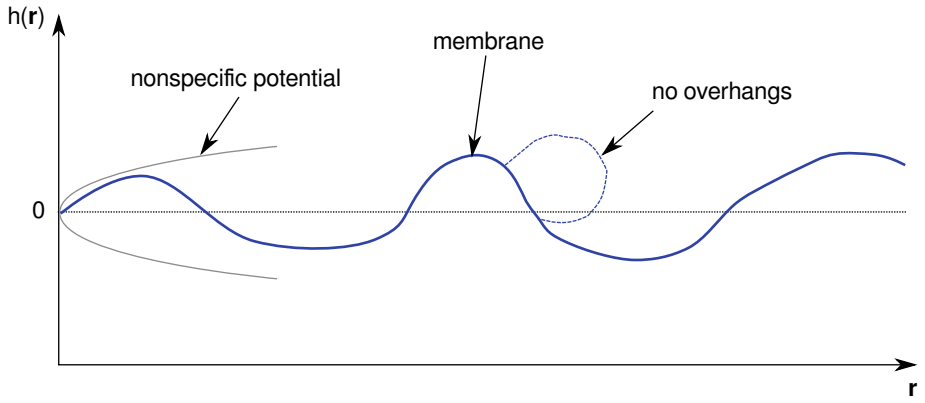

Figure 4.2: Sketch of a membrane in Monge gauge. The membrane fluctuates within a nonspecific harmonic potential. In Monge gauge, the membrane must not have overhangs because, otherwise, the membrane profile could not be written as a unique function of Cartesian coordinates.

Langevin equations have the advantage that the membrane dynamics can be extracted readily.

The mean curvature of the membrane in Monge gauge is [21]

$$H = \nabla \cdot \left(\frac{\nabla h(\mathbf{r})}{\sqrt{1 + (\nabla h(\mathbf{r}))^2}} \right), \tag{4.2}$$

where $h(\mathbf{r})$ is the membrane profile. Due to bending, the area of the membrane is increased by an excess area A_{excess} such that we require an additional term in the Helfrich Hamiltonian. The associated energy penalty is usually assumed to be proportional to the area increase and the surface tension Σ. In the Monge gauge, this energy penalty can be written as [21]

$$\mathcal{H}_S[h(\mathbf{r})] = \Sigma A_{\text{excess}} = \int \mathrm{d}^2\mathbf{r}\, \Sigma \sqrt{1 + (\nabla h(\mathbf{r}))^2} - \Sigma A, \tag{4.3}$$

where A is the area of the flat membrane. In order to simplify the calculations, one usually applies a small-gradient approximation to calculate the curvature and the excess area, i. e. $|\nabla h(\mathbf{r})| \ll 1$. In this approximation, we have

$$H \approx (\Delta h(\mathbf{r}))^2 \tag{4.4}$$

and

$$\mathcal{H}_S[h(\mathbf{r})] \approx \int \mathrm{d}^2\mathbf{r}\,\frac{1}{2}\Sigma\,(\nabla h(\mathbf{r}))^2\,, \tag{4.5}$$

where Δ is the Laplace operator.

For our work on membrane adhesion, we assume that the membrane fluctuates above a solid substrate around the minimum of a nonspecific potential (see figure 4.2). This potential is induced by several contributions like Helfrich repulsion, van-der-Waals interactions or gravity [4]. For simplicity, we approximate the nonspecific potential harmonically. The curvature of this potential is γ.

Summarizing the results from above, our Helfrich Hamiltonian is in the small-gradient approximation given by [21, 32]

$$\mathcal{H}[h(\mathbf{r})] \approx \int_A \mathrm{d}^2\mathbf{r}\left[\kappa(\Delta h(\mathbf{r}))^2 + \frac{1}{2}\Sigma\,(\nabla h(\mathbf{r}))^2 + \frac{\gamma}{2}h(\mathbf{r})^2\right]. \tag{4.6}$$

This Hamiltonian serves as the basis of our considerations[1] in this thesis.

Behaviour of membranes without bonds

As membranes can exist in solvents such as water, they are subject to thermal forces leading to membrane shape fluctuations [66]. If the surface tension is not zero, the amplitude of the membrane height fluctuations in Monge gauge (i.e. the fluctuations around the equilibrium height of the membrane above the substrate) is given by [67]

$$\sigma \equiv \langle \Delta h^2 \rangle = \frac{k_\mathrm{B}T}{A}\sum_{\mathbf{q}}\frac{1}{\kappa q^4 + \Sigma q^2 + \gamma} \approx \frac{\arctan\left(\sqrt{4\kappa\gamma - \Sigma^2}/\Sigma\right)}{2\pi\sqrt{4\kappa\gamma - \Sigma^2}}, \tag{4.7}$$

where $\mathbf{q}$ are the Fourier modes. The amplitude in the limit of vanishing surface tension is

$$\lim_{\Sigma\to 0}\sigma = \frac{k_\mathrm{B}T}{8\sqrt{\kappa\gamma}}. \tag{4.8}$$

As can be seen from equation (4.7), the surface tension and the interaction potential suppress modes with long wavelengths whereas the bending suppresses modes with short wavelengths. Typical values of the fluctuation amplitude for giant unilamellar vesicles (GUVs) lie in the range between 10 and 100 nm^2 [68].

Due to bending rigidity and surface tension, the height fluctuations are not independent from lipid to lipid but instead the thermal forces lead to undulations of the membrane. In the limit of vanishing surface tension, the typical radius of

[1] Surface tension is usually neglected in this thesis

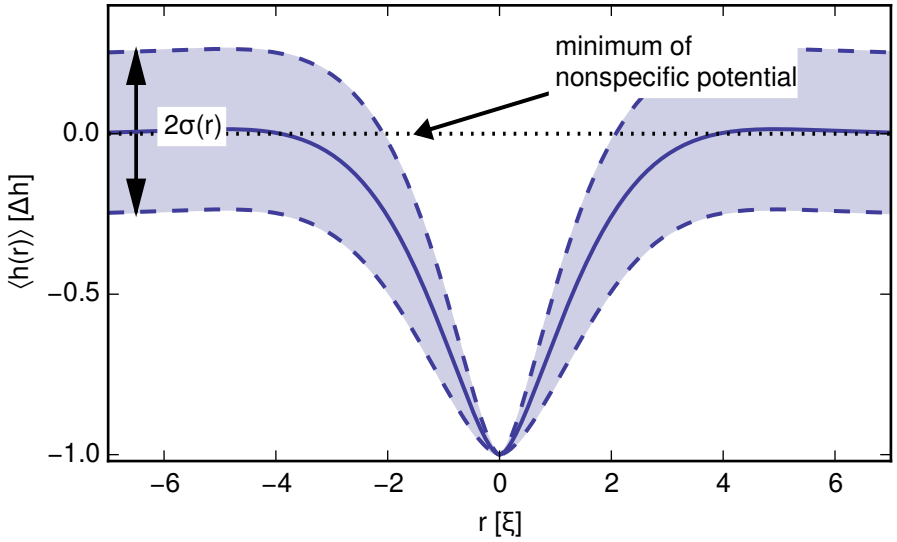

Figure 4.3: Profile (full blue line) and height fluctuations (shaded area) of a tensionless membrane bound at the center. The bond is assumed to be stiff. The membrane relaxes back into its minimum on a length scale of $\xi = (\kappa/\gamma)^{1/4}$. Likewise, the height fluctuations converge to their free value on this length scale.

such an undulation is determined by the height correlation function [69]

$$g(R) = -\frac{k_B T}{2\pi\sqrt{\kappa\gamma}}\,\mathrm{kei}\left(\frac{R}{\xi}\right) \tag{4.9}$$

where $\mathrm{kei}(x)$ is the so-called Kelvin function [70], R is the distance between the two considered points in the membrane and ξ is the lateral correlation length given by

$$\xi \equiv \sqrt[4]{\frac{\kappa}{\gamma}}. \tag{4.10}$$

On this length scale, the Kelvin function converges exponentially to zero. In experiments, the lateral correlation length is usually on the order of about 100 nm for tensionless membranes [4]. If the membrane is not tensionless, theoretical results [71] indicate that the lateral correlation length increases only slightly.

Behaviour of membranes with bonds

We consider membranes that are bound to an underlying scaffold via ligand-receptor bonds (see also figure 3.2). These bonds can be either flexible, i. e. fluctuate in length or stiff, i. e. do not fluctuate in length. We model such bonds as springs with a spring constant λ and the distance Δh between the minimum of the nonspecific harmonic potential (set to zero in equation 4.6) and the rest length of the bond l_0. In the case of stiff bonds, the spring constant λ is infinite, of course. The Helfrich-Hamiltonian for such a model system is

$$\mathcal{H}_b[h(\mathbf{r})] \approx \mathcal{H}[h(\mathbf{r})] + \int \mathrm{d}^2\mathbf{r} \sum_{\mathbf{i}=0}^{N_b} \delta(\mathbf{r}-\mathbf{r_i}) \frac{\lambda}{2} \left(h(\mathbf{r}) - \Delta h\right)^2, \tag{4.11}$$

where N_b is the number of the bonds, $\mathbf{r_i}$ is the position of bond $\mathbf{i}$ and Δh is the height difference $h_0 - l_0$ between receptor and ligand. In section P3 (see also Schmidt et al. [68]), we derive from this expression a very general formula for the average membrane profile and the membrane fluctuations. More specifically, the average membrane profile and the membrane fluctuations can be calculated for any possible bond configuration without further approximations. Furthermore, one can calculate the bending energy for an arbitrary bond configuration from equation (4.11) (see Schmidt et al.[71] or Speck et al. [72]).

The average membrane profile around a single bond (see also figure 4.3), derived from those expressions (see equation (13) of the Supplementary Material of publication P3), is

$$\langle h(R) \rangle = -\frac{4}{\pi} \Delta h \frac{\lambda}{8\sqrt{\kappa\gamma} + \lambda} \operatorname{kei}\left(\frac{R}{\xi}\right). \tag{4.12}$$

Here, R is the distance from the bond. In the limit of stiff bonds, this reduces to the well known formula [73]

$$\lim_{\lambda\to\infty} \langle h(R) \rangle = -\frac{4}{\pi} \Delta h \operatorname{kei}\left(\frac{R}{\xi}\right). \tag{4.13}$$

Additionally, binding also reduces the membrane fluctuations. Here, the amplitude is given by

$$\langle h^2(R) \rangle \equiv \sigma(R) = \frac{1}{8\sqrt{\kappa\gamma}} - \frac{\lambda}{8\sqrt{\kappa\gamma} + \lambda} \frac{2 \operatorname{kei}^2\left(\frac{R}{\xi}\right)}{\pi^2\sqrt{\kappa\gamma}}. \tag{4.14}$$

Intuitively, the bond reduces the fluctuations of the free membrane (first term) by the second term which decays on the scale of the lateral correlation length ξ.

Furthermore, the membrane fluctuations at the binding site (i. e. the limit $R \to 0$ in the above equation)

$$\lim_{R\to 0} \sigma(R) = \frac{1}{8\sqrt{\kappa\gamma} + \lambda} \tag{4.15}$$

provide an interesting interpretation. The membrane just adds an additional spring stiffness of $8\sqrt{\kappa\gamma}$ to the bond. In other words, the membrane and the spring can be considered two connected springs. Not surprisingly, the average membrane profile and the membrane fluctuations are also described by a Kelvin function [74], as in the case without bonds, and also decay on the scale of the lateral correlation length ξ.

If the bond pulls the membrane out of its equilibrium position, the energy of the membrane and the bond (or the backbone of the bond) is increased due to the deformations of the membrane and the bond and the energy to overcome the nonspecific potential. The associated energy penalty (not considering entropic contributions and binding enthalpy) of these three contributions [71] is

$$E_1 = 4k_B T\sqrt{\kappa\gamma}\frac{\lambda}{8\sqrt{\kappa\gamma} + \lambda}(\Delta h)^2. \tag{4.16}$$

In the case of a stiff bond, the membrane deformation energy[2] reduces to

$$E_1^{\text{stiff}} \equiv \lim_{\lambda\to\infty} E_1 = 4k_B T\sqrt{\kappa\gamma}(\Delta h)^2, \tag{4.17}$$

which was originally derived by Bruinsma et al. [73].

Neighboring bonds reduce this energy if they are close enough to each other (approximately within the lateral correlation length). More specifically, two neighboring bonds reduce the area where the membrane is bent. Furthermore, the area where the membrane is moved out of its equilibrium position is reduced. This membrane-mediated interaction can be described by a coupling matrix [71, 72, 75, 76]

$$M_{ij} = \frac{\delta_{ij}}{\lambda} - \frac{\mathrm{kei}\left(\frac{|\mathbf{r_i}-\mathbf{r_j}|}{\xi}\right)}{2\pi\sqrt{\kappa\gamma}}, \tag{4.18}$$

where the indices i and j label the bonds. With this matrix, the membrane

[2] For convenience, we call this energy penalty membrane deformation energy, even though all three energy contributions are considered in equation (4.16).

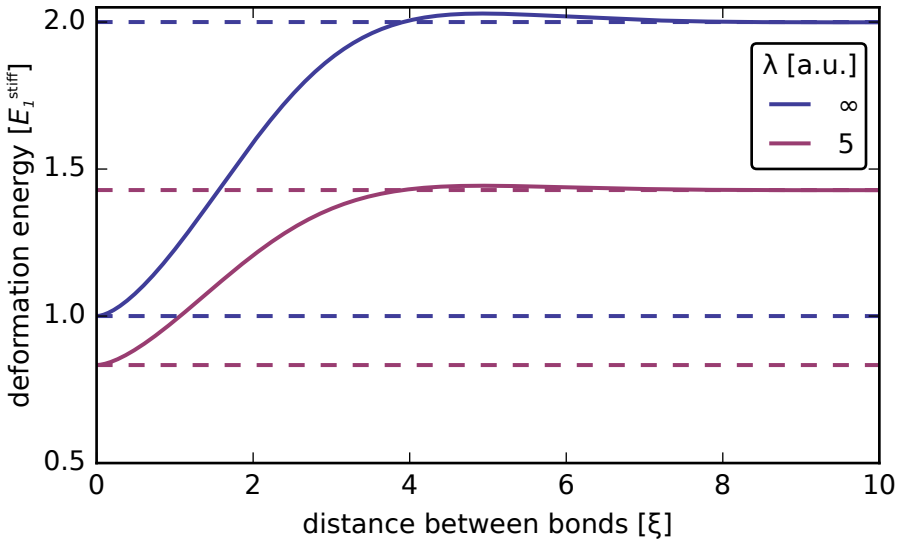

Figure 4.4: Membrane deformation energy of a bond configuration with two bonds as a function of their distance in units of the membrane deformation energy for a single stiff bond. We show a curve for stiff bonds and one curve for soft bonds. The dashed lines show the limit of infinitely separated bonds (i.e. two times the deformation energy of a single bond) and two bonds at the same position. If two stiff bonds have the same position, they act effectively as a single bond. Soft bonds have a higher energy than a single bond because, now, they can be considered a single bond with double spring stiffness λ.

deformation energy can be written as

$$E_D = \frac{1}{2} k_B T \sum_{ij} (\Delta h)_i M_{ij}^{-1} (\Delta h)_j, \tag{4.19}$$

where $(\Delta h)_i$ is a vector containing the height differences Δh and the coupling matrix M_{ij} has to be inverted. Equation (4.19) describes the interplay between the energy penalty of a single bond and the interaction energy that decays on the scale of the lateral correlation length ξ (see last term of equation 4.18).

As an example, we show in figure 4.4 the membrane deformation energy of a configuration with two bonds. We distinguish between stiff and soft bonds. In the limit of infinite separation, the bonds do not feel an interaction and hence the membrane deformation energy is two times the membrane deformation energy of a single bond. If two stiff bonds share the same position, they can be considered

a single bond with the respective membrane deformation energy. However, this is not true if the bonds are soft. In this case, the two bonds act like a single bond with twice the spring stiffness.

If the effective cooperativity parameter

$$\chi \equiv \frac{\lambda}{8\sqrt{\kappa\gamma}} = \frac{1/(8\sqrt{\kappa\gamma})}{1/\lambda} \tag{4.20}$$

is small, the coupling matrix M_{ij} (see equation (4.18)) can be inverted approximately. Intuitively, the effective cooperativity parameter is the ratio between the membrane height fluctuations and the fluctuations of the bond (see last equal sign in equation (4.20)). Hence, this approximation is valid if the fluctuations of the "free" bond would be much larger than the membrane height fluctuations. In the discussed approximation, one obtains a distance dependent interaction energy between two neighboring bonds (see also [77]) given by

$$J_{ij} \approx -\frac{\lambda^2 \,\mathrm{kei}\left(\frac{|r_i - r_j|}{\xi}\right)}{2\pi\sqrt{\kappa\gamma}} \,(\Delta h)^2 \,. \tag{4.21}$$

With this result, Ising-like models of cell adhesion were developed [72, 75, 76] (see also discussion in the next chapter).

Langevin equation and membrane hydrodynamics

The Helfrich-Hamiltonian alone is only able to describe the statics and the thermal equilibrium of the membrane. However, Langevin equations that are derived from the Helfrich-Hamiltonian can describe its dynamics. Here, we discuss very shortly the Langevin formalism. Our discussion is based on the review article by Brown [32].

In the Monge gauge, the time development of the membrane height $h(\mathbf{r}, t)$ is given by

$$\frac{\partial h(\mathbf{r}, t)}{\partial t} = \int_{-\infty}^{\infty} \mathrm{d}\mathbf{r}' \, \Lambda(\mathbf{r} - \mathbf{r}') \left[F(\mathbf{r}', t) + \xi(\mathbf{r}', t)\right] , \tag{4.22}$$

where $F(\mathbf{r}', t) = -\delta\mathcal{H}[h(\mathbf{r}, t)]/\delta h(\mathbf{r}, t)$ is the force acting on the membrane due to the respective Helfrich Hamiltonian (see for example equation (4.6)), $\Lambda(\mathbf{r} - \mathbf{r}')$ is the hydrodynamic kernel which describes the influence of the surrounding fluid (see discussion below) and $\xi(\mathbf{r}', t)$ is a stochastic force acting on the membrane.

This stochastic force fulfills the fluctuation-dissipation theorem [78, 79]

$$\begin{aligned} \langle \xi(\mathbf{r},t) \rangle &= 0 \\ \langle \xi(\mathbf{r},t)\xi(\mathbf{r}',t') \rangle &= 2k_{\mathrm{B}}T\Lambda^{-1}\delta(\mathbf{r}-\mathbf{r}')\delta(t-t'). \end{aligned} \tag{4.23}$$

As our Hamiltonian (equation (4.6)) is quadratic, the Fourier modes $h(\mathbf{k},t)$ decouple. The Langevin equations for the single modes is

$$\frac{\partial h(\mathbf{k},t)}{\partial t} = \omega_k h(\mathbf{k},t) + \Lambda_k \xi_k, \tag{4.24}$$

where ω_k is the wave-vector dependent relaxation frequency

$$\omega_k = \Lambda_k \left(\kappa k^4 + \Sigma k^2 + \gamma \right). \tag{4.25}$$

These decoupled equations are simply Ornstein-Uhlenbeck processes [80, 81] which describe an overdamped particle in a harmonic potential under the influence of a stochastic force.

The hydrodynamic kernel is derived under the well justified assumptions that the out-of-plane movements of the membrane are small[3] and that we are in the regime of low Reynolds numbers, where we can use the Stokes equation [78]. Under the additional assumption that the membrane is sufficiently far away from a wall, the hydrodynamic kernel in real space is given by

$$\Lambda(\mathbf{r}) = \frac{1}{8\pi\eta r} \tag{4.26}$$

or in Fourier space

$$\Lambda_k = \frac{1}{4\eta k}, \tag{4.27}$$

where η is the viscosity of the surrounding solvent. If, otherwise, the membrane is close to a wall the hydrodynamics and hence the hydrodynamic kernel change. In Seifert [82], the full expression for the hydrodynamic kernel of a membrane is derived and it is shown that our approximation is only valid for

$$k \gg \frac{1}{\bar{h}}, \tag{4.28}$$

where $\bar{h}$ is the average height of the membrane. In our case and the parameter that we use, this means that only the four smallest k-modes are affected appreciably by our approximation.

[3] This assumption has already been used for our Hamiltonian (see equation 4.2 and below).

The Langevin equation (4.22) and variations thereof serve as the starting point of many studies about membrane dynamics. These include the analysis of bound membranes [65, 68] or the diffusion of proteins within membranes [60–63].

Based on earlier work [17], we use the Langevin equation to set up a simulation scheme to study the equilibrium dynamics of an adhered membrane in publication P1. In the next publication, P2, we combine our theoretical results with experiments and describe a method to detect nucleation seeds or small adhesion using the average membrane height and the membrane roughness. In our work of nucleation dynamics (see publication P3), we compare results from Langevin simulations with results from an analytical model. The agreement between both approaches shows that membrane height fluctuations can be averaged out.

I.5

Biomimetic model systems and cell adhesion

Adhesion between different cells or the extracellular matrix (ECM) is essential for the existence of multicellular organisms and is usually mediated by so-called cell adhesion molecules (CAM) (see Sackmann and Smith [12] for a review from the physical point of view). Such molecules like cadherins can connect different cell membranes. Alternatively, integrins connect cell membrane to the ECM. Thereby, CAMs form highly exclusive bonds with their respective partners.

The dynamics of protein-mediated adhesion is very complex due to the large number of different proteins that are embedded in the membrane. For this reason, biomimetic model systems were developed in order to give insight into the physical mechanisms playing a role in cell adhesion (see for example [14, 83–85]). These model systems can have different levels of simplification.

A particularly useful model system, yet very close to the in-vivo situation, relies on a so-called supported lipid bilayer (SLB) [84]. An SLB can contain different molecules serving different purposes like binding proteins for the intermembrane adhesion or repellers. Grakoui et al. [86] used this method to observe the dynamics of the immune synapse for one of the first times. A T-Cell was placed above an SLB which contained fluorescently labelled MHC-peptides (major histocompatibility complex-peptides) and ICAM-1s (intercellular adhesion molecule 1) that could diffuse freely in the bilayer. Hence, the SLB replaced the antigen presenting cell that the T-Cell is supposed to engage. They observed that initially a bullseye pattern formed where the MHC-peptides form the outer ring and the ICAM-1 molecules formed the interior disk (see figure 5.1). However, the pattern was inverted in the later stages, i. e. MHC-peptides are transported inwards on a time scale of about 10 minutes.

Other interesting systems involve artificial substrates with RGD ligands (bind-

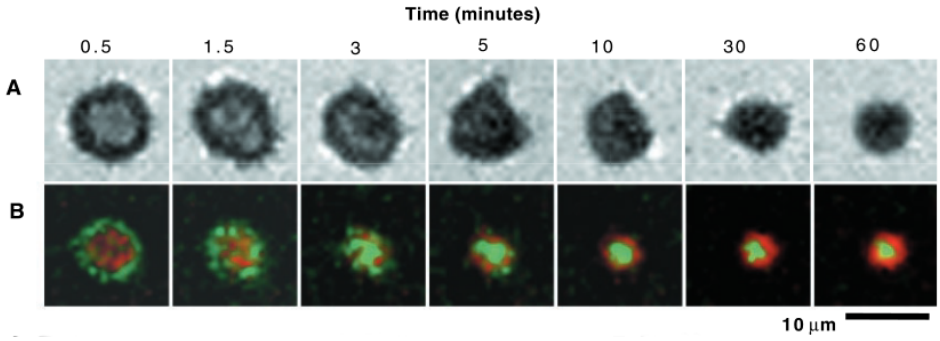

Figure 5.1: Formation of a T-Cell synapse (from [86]). **A** Images of the contact point between T-Cell and SLB. Contacts appear as dark gray on a light background. **B** Images of MHC-peptide (green) and ICAM-1 (red) accumulation. The ring pattern inverts on a time scale of 10 minutes.

ing partners of integrin) [87]. Here, the RGD ligands are attached to gold dots that can be organized in arbitrary patterns. Above the substrate, a cell is placed. As an application, they placed several clusters of gold dots on the substrate and varied the distance between the gold dots [88, 89]. They found that above a critical distance, mature and stable integrin adhesions or focal adhesions do not appear. Furthermore, they studied the influence of the order (or disorder) of binding partner on the substrate on cell adhesion [90]. According to their results, disorder does not affect the adhesion process for the investigated cells if the density is sufficiently large. However, below a critical density they could not observe adhesion if the pattern was disordered. Recently, they used their nanopatterned arrays to investigate T-Cell activation [91]. In their study, the T-Cell response was initiated at a distance between the antigens above 90 to 140 nm. Furthermore, they found by leaving areas on the substrate free of antigens that the total number of antigens presented to the T-Cell is more important than the distance between the antigens.

Additional simplification involves replacing the model cells by giant unilamellar vesicles (GUVs). Embedded in the vesicle membrane, there are cell adhesion molecules (or their respective binding partners) and repeller molecules in order to prevent a direct contact between both membranes [14]. As before, the vesicle is usually placed above a supported lipid bilayer.

The simplicity of these model systems has advantages, from the experimental and as well from the theoretical side. From the theoretical side, physical models with only a few parameters can be developed because of the uncomplicated structure of the vesicle (and the SLB) with only a few different species of molecules. This is a major simplification in contrast to biological membranes with at least dozens of different and interacting proteins.

From the experimental point of view, Reflective Interference Contrast Microscopy (RICM) [16, 92] delivers data from the contact zone between the vesicle and the SLB that can be relatively easily analysed as the membrane and the interior near the membrane has a very simple structure. More specifically, one can extract the height dynamics from which one obtains the average membrane height, the membrane height fluctuations and its time correlation function [4, 93]. From this data, it is possible to obtain information about the potential between membrane and substrate [93] or the organization of bond assemblies [18]. Furthermore, the dynamics of the adhesion zone can be easily investigated [8, 17, 94].

I.5.1 Reflection Interference Contrast Microscopy

While there are a lot of techniques to observe proteins in a lipid bilayer, like Fluorescence Recovery after Photobleaching (FRAP) or Fluorescence Correlation Spectroscopy (FCS) (see [95, 96] for reviews of these two methods), there are only a few techniques to measure the membrane height like Interferometric Fluctuation Detection [97] or Reflective Interference Contrast Microscopy (RICM) (see [16] for a recent review).

RICM uses the interference of reflecting light beams reflected from two interfaces on top of each other (see figure 5.2). In the experimental setup, a monochromatic light beam I_0 gets reflected at the interface between glass and water (new beam I_1) and at the interface of water and lipid bilayer (new beam I_2). The two reflected beams interfere and the intensity of the outgoing beam for quasi-normal incidence is given by [16, 98]

$$I = I_1 + I_2 + 2\sqrt{I_1 I_2}\cos\left(2kh(x,y) + \pi\right) \tag{5.1}$$

where k is $2\pi n_1/\lambda$ with λ as the wave length of the incoming beam and n_1 as refraction index (see figure 5.2). The intensities of the outgoing beams I_1 and I_2 depend on the Fresnel reflection coefficient and the intensity of the incoming beam. The above equation only depends on the height of membrane $h(x,y)$ and so one can infer the height from the intensity of the reflected beam.

The main problem of RICM is that the phase of the reflected beams is not known, i. e. the height is only known to a factor modulo $\lambda/2n$ (where λ is the wavelength of the incoming beam and n the refractive index of the medium). This means that in the case of green light one has to make sure that the membrane height is below 100 nm in order to get an unambiguous result [16]. Dual-wave RICM overcomes this problem [99]. Here, the interferograms of two wavelengths are used to determine the height. Of course, the ambiguity of the height does

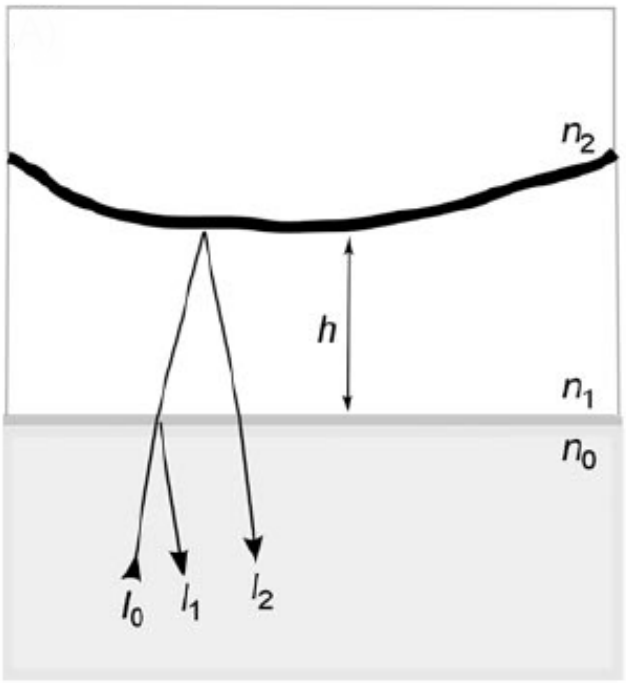

Figure 5.2: Sketch of an RICM setup. An incoming monochromatic light beam I_0 is partially reflected at the substrate I_1 and at the membrane I_2. The two outgoing beams interfere depending on the height of the membrane. The n_i are the respective refraction indices. Adopted from Limozin et al. [16].

not disappear completely. However, in the case of a green and a blue light source, the range of unambiguous height determination is lifted to 800 nm [16]. Furthermore, the accuracy of the height determination is slightly better than in single wave RICM (2 to 3 nanometer compared to 4 nanometer for colloidal beads) [99] .

If one considers a fluctuating membrane, one is not only interested in the height profile but also in the membrane height fluctuations. The membrane height fluctuations are obtained with the help of Dy-RICM (Dynamical RICM) with and without in combination with Dual-wave RICM [92, 93]. For that purpose, the height profile has to be determined many times, from which one reconstructs a pixel by pixel map of the fluctuation amplitude. This map delivers information about the confinement of the membrane coming for example from the interaction between the membranes (van-der-Waals forces etc.) or ligand-receptor bonds connecting the membrane and the SLB [18, 100].

I.6 Theoretical models of adhesion dynamics

I.6.1 Ligand-receptor bonds and their dynamics

Since 1978, when Bell [6] postulated the later called Bell rates for the dissociation of ligand-receptor bonds, the formation and dissociation of ligand-receptor bonds has become a very active research field on the theoretical, computational and experimental side (see for example [101, 102] for reviews). Bell suggested that the dissociation rate of a bond with binders in opposing membranes depends exponentially on the force applied on the bond

$$k_{\text{off}} \equiv k_0 \exp\left(\frac{F x_b}{k_{\text{B}} T}\right). \tag{6.1}$$

Here, k_0 is the dissociation rate without an applied force, F is the force applied on the bond, x_b is the distance between the minimum of the interaction potential and the transition state barrier and $k_{\text{B}}T$ the unit of thermal energy. Later, theoretical considerations (see for example [101, 103, 104]) confirmed Bell's hypothesis. Based on the Kramer's theory [105], which describes the overdamped kinetics of bonds in a condensed liquid, Evans argues that an applied force lowers the transition state barrier (see also figure 6.1). Consequently, the rate for dissociation increases. Furthermore, if one assume a sharp transition between bound and unbound state, the location or the energy barrier is insensitive to the applied force and one obtains the Bell rates.

In experiments, the reaction kinetics of ligand-receptor bonds can be studied with the help of atomic force microscopy (AFM) or biomembrane force probes (BFP). Using this methods, the lifetime of the biotin-avidin bond was measured [106–108]. It turned out that its lifetime depends on the loading rate and lies between 10^{-3} and 10^{2} seconds [108]. This is in accordance with theoretical results

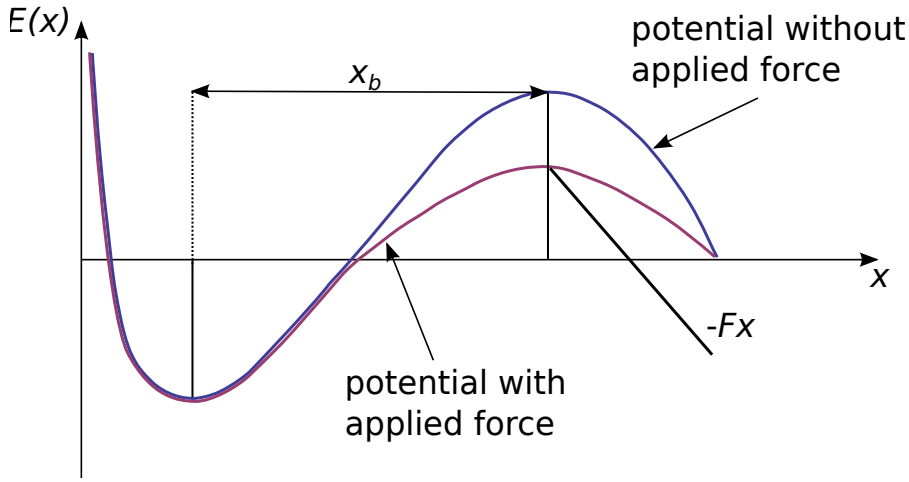

Figure 6.1: Conceptual landscape of a ligand-receptor bond without an applied force (blue) and with an applied force. The force leads to a lowering of the activation barrier which increases the rate for escaping over the barrier, i. e. for unbinding (see main text for details).

about the strength of adhesion molecules [103] and simulation studies [109]. Other bonds that have been investigated were carbohydrate–selectin bonds [104] or cadherin bonds [110].

The survival time of adhesion domains under force does not only depend on the survival time of a single bond but also on the rebinding probability of a bond. This problem was studied theoretically [111–120] and experimentally by colloidal probe microscopy [121, 122] and by biomembrane force probes [123] (see figure 6.2). In these experiments, domains consisting of, for example, carbohydrate-carbohydrate bonds [122] or biotin-avidin bonds [123] were studied. Microscopic parameters were extracted that were consistent with single bond experiments. Additionally, in contrast to single bond experiments, the rebinding probability was also determined.

Even though it is intuitive that bonds break faster if a force is applied, there are bonds, so-called catch bonds, that are stabilized by an applied force (see [124] for a review). Such bonds were originally suggested by Dembo et al. [5]. The microscopic mechanism behind this strengthening is elusive. However, recent molecular dynamics simulations of the cadherin protein propose that pulling forces allow for the formation of hydrogen bonds within the complex, thereby stabilizing the bond [125].

Another interesting feature of ligand-receptor binding is the different dissociation constant K_d in different dimensions. In a three dimensional environment,

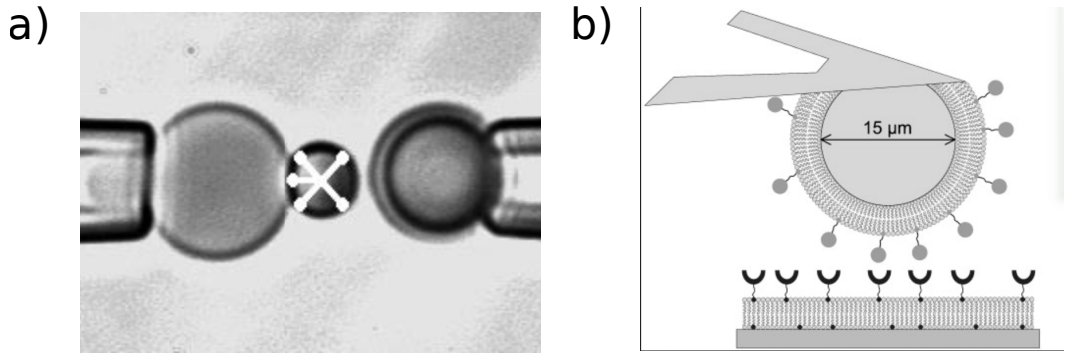

Figure 6.2: Experimental techniques force spectroscopy of single or multiple bonds. a) Biomembrane force probe (BFP): The BFP on the left is stationary. On the right, is the microbead test surface. The force on the test surface is controlled by the suction in the pipette. Figure from [108]. b) Colloidal force microscopy: A mircobead attached to a cantilever of an AFM and coated with a lipid bilayer membrane is placed above a supported lipid bilayer. Both bilayer are prepared with binding proteins that can form bonds. Figure from [121].

a binding pair has a dissociation constant $K_d^{(3D)}$ that is defined as the ratio of the association and dissociation rate of the bond and has a dimension of a three dimensional concentration (for example moles per liter). However, the two dimensional dissociation constant $K_d^{(2D)}$ (i.e. when the binders are confined to a plane like in the case of a biological membrane) has a dimension of the respective two dimensional quantity [126]. It has been suggested [127], to transform these two dissociation constant by

$$K_d^{(3D)} = hK_d^{(2D)}, \tag{6.2}$$

where h is the so-called confinement length. More specifically, the two binders are confined in a volume with a width h below (or above) the plane in which they diffuse laterally. This confinement length has been measured for several binding pairs, whereas different experimental techniques delivered discrepant values (see Wu et al. [126] and references therein).

Wu et al. [126, 128] attributed the confinement length to the suppression of rotational motion of a binder embedded in a membrane and considered the cadherin-cadherin binding pair exemplarily. Schmidt et al. [71] argued that besides these contributions the suppression of the membrane fluctuations and the confinement of one of the binders in the binding pocket of the other binder also lead to a change of the dissociation constant. Additionally, the bending of

the membrane and stretching of the bond influences the energetics of the ligand-receptor bond [17, 71]. Hu et al. [129] picked up these ideas and ran explicit MD simulations of the binding process of binders in opposing membranes. Their results confirmed that the change of the dissociation constant is due to the suppression of membrane fluctuations, rotational and translational degrees of freedom of the binders. Hence, the 2D-dissociation constant depends indirectly on membrane parameters like the bending rigidity or the surface tension that determine the membrane fluctuations. Furthermore, they also observed in their molecular dynamics simulations that both the association and the dissociation rates, which set the dissociation constant, change if the binders are embedded in different membranes (see also [20]).

In publication P5, we present a method to measure the association rate of ligand receptor bonds in a two dimensional environment. In contrast to the presented methods where some kind of force probes are used, our method does not rely on such set-ups. Instead, the reaction rate is self-consistently estimated from the growth behaviour of the adhesion patches. This method has the great advantage that the reaction rates are not influenced by the probe but only depend on the experimental environment of the binders. We applied this method on several different binding pairs embedded in different membranes and find in accordance with our earlier work [71, 74] and Hu et al. [129] that the association rate depends on the membrane roughness and fluctuation amplitude, respectively (see publication P5). Moreover, we find that the number of encounters between membrane and substrate can be reduced by repelling molecules embedded in the membrane. This also leads to a reduction of the association rate between both binders due to the reduced number of encounters between both membranes.

In publication P4, we develop a theory about effective reaction rates based on the Bell rates [6]. This theory describes the reaction kinetics of ligand-receptor bonds where at least one binder species is embedded in a fluctuating membrane. Based on these effective reaction rates, we develop a simulation scheme which can reproduce the results of the Langevin simulation discussed in section I.4.2. In contrast to this simulation scheme, we are able to simulate on biological relevant length and time scales. Furthermore, we use these effective reaction rates in our theory describing the nucleation dynamics of adhesion domains (see section I.6.3 and publication P3).

I.6.2 Equilibrium models of membrane adhesion

The first to address the equilibrium of membrane adhesion were Bell, Dembo and coworkers [127, 130, 131]. They investigated the balance between the binding enthalpy and the entropy cost of the mobile binders when they form a bond

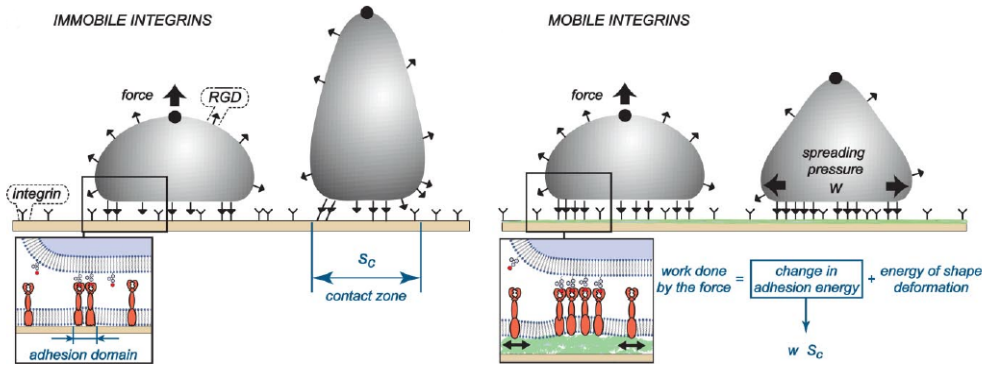

Figure 6.3: Schematic representation of a vesicle with and without a lifting force. Cell adhesion molecules (in this case integrin and RGD) can form bonds between the cell mimetic vesicle and the substrate. In the left sketch the integrins are immobile whereas on the right side the integrins are mobile. This leads to an increased spreading pressure and hence to a larger contact zone. Figure from [94].

thereby getting immobile. Furthermore, they considered repulsive energy contributions due to the glycocalyx and the binding enthalpy of the ligand-receptor bonds in several scenarios.

Bruinsma and coworkers [73] investigated the influence of membrane properties on the self-assembly of ligand-receptor bonds connecting the two opposing membranes using the Helfrich formalism. They distinguished two different regimes, the van-der-Waals regime where the interaction between the membranes is dominant and the Helfrich regime where entropic interactions due to collisions between the two membranes are most important. In the van-der-Waals regime, Bruinsma and coworkers found an attractive interaction between the bonds that decays exponentially (see also section I.4.2) on the length scale of the lateral correlation length which can, under certain conditions, lead to a clustering of the bonds. In the Helfrich regime, they found an entropic repulsion between the two membranes due to collisions caused by thermal height fluctuations. This entropic repulsion can be described by an effective potential [132] that depends on the mean separation of the two membrane sheets. Here, the bonds can also cluster to a domain.

Lipowsky [133] considered the adhesion from another point of view and investigated the influence of the membrane rigidity and the surface tension on the adhesion state. He found that the concentration of stickers has to exceed a threshold value for stable adhesion. This threshold also depends on the surface tension of the membrane. Later, Weikl, Lipowski et al. developed a Monte Carlo

simulation scheme based on this work [55] and identified several mechanisms for adhesion induced phase separation.

Smith and Seifert [134, 135] extended the work of Bell, Dembo and coworkers [127, 130, 131] and included other contributions like the influence of competing binders or steric repulsion. Besides this local contributions, they also considered the bending energy of the (whole) vesicle [136] or external detachment forces [137, 138]. This theory was then used to interpret experiments of the equilibrium adhesion domains [139, 140] and adhesion domains under force [94] (see also figure 6.3). In the latter experiments, they showed that the adhesion strengthens under a lifting force, even in vesicles without cytoskeleton. This effect also depends on the mobility of the binders.

I.6.3 Dynamics of membrane adhesion

I.6.3.1 Nucleation

In the initial stage of the adhesion process, stable nucleation seeds have to be formed. The formation of this seed depends on the interplay between the gain of energy through ligand-receptor bonds and the energy increase due to pulling the membrane closer to the substrate and due to bending the membrane at the rim of the seed (see figure 6.4). In the spirit of the capillary approximation [141], we can separate all contributions in a part that is proportional to the area of the seed and another part that is proportional to its circumference. The part proportional to the area depends on the binding enthalpy and the energy required for pulling the membrane out of its equilibrium position. The part proportional to the circumference depends on the energy needed to bend the membrane at the rim and, again, the energy for moving the membrane at the rim of the adhesion domain out of the equilibrium position.

The most important energy scale in the context of nucleation is the membrane deformation energy of an isolated bond [73] (see also section I.4.2)

$$E_1 = 4k_BT\sqrt{\kappa\gamma}(\Delta h)^2. \tag{6.3}$$

If this energy is smaller than the binding enthalpy of the ligand-receptor bond only one bond is sufficient to form a stable seed. In this case, nucleation is very fast compared to binding pairs where the binding enthalpy is smaller than the membrane deformation energy in equation (6.3) and consequently more than one bond is required to form a stable seed. Furthermore, the energy loss due to pulling the membrane down has to be smaller than the energy gain due to the

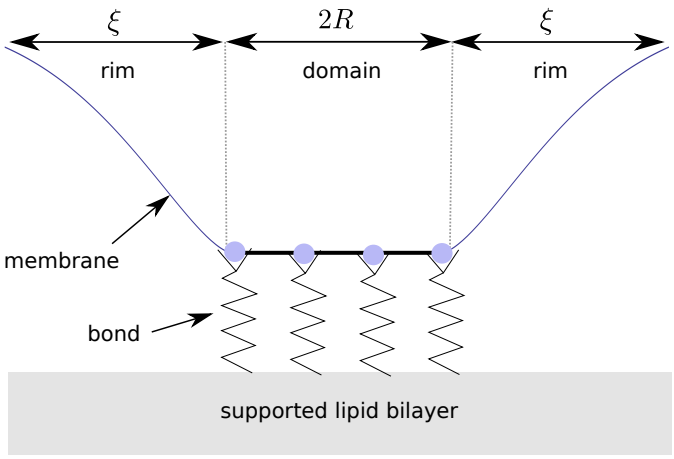

Figure 6.4: Sketch of a small domain. The length of the rim and the area of the adhesion domain determines the energy of the domain. The rim causes an energy loss because the membrane is partially pulled down and bent at the edge. Within the domain, we have an energy gain due to the ligand-receptor bonds and an energy loss because the bonds pull the membrane down.

ligand-receptor bonds, i. e.

$$\gamma \Delta h^2 < \rho_b \epsilon_b. \tag{6.4}$$

In publication P3, we present a scaling argument to obtain the critical number of bonds from the above equations. It will turn out that within our approximation the critical number of bonds for experimental relevant parameters is very small, i. e. between two and four bonds. Experimental results of the nucleation stage are rare due to difficulties to detect adhesion domains below the diffraction limit [18]. However, the available experimental results [8, 14] suggest that the seed is indeed very small, i. e. around 100 nm and confirm our and other results derived from a Helfrich-Hamiltonian [56, 74, 142].

The dynamics of nucleation is of course determined by the dynamics of the formation of the first bonds. The formation of the first bonds is limited by the number of encounters between both binders. Whereas in usual three dimensional environments, where the movement of the binders is not restricted within their respective membranes, the number of encounters mainly depends on the density of both binding partners, in our setup the height fluctuations, which bring the ligand and the receptor into reaction distance, play a major role [74, 129, 143, 144] in bringing the binders into reaction distance.

Based on this reasoning, we derive in publication P3 effective reaction rates where the membrane height fluctuations are averaged out. These effective rates are then used in a master equation from which we can determine the average nucleation time analytically. The master equation delivers the same results as the full Langevin formalism discussed in section I.4.2. Thereby, we estimate the critical nucleation number by the capillary approximation that was discussed above. This is the first model of its kinds for the nucleation dynamics in this field. Partially, it is experimentally confirmed by Fenz et al. [59] who determined that the nucleation seed has to be very small.

I.6.3.2 Microscopic dynamic models

Due to the large range of different interaction mechanisms between ligand-receptor bonds, many different theoretical models have been developed to describe intermembrane adhesion on a microscopic level [72, 75, 76, 143–147]. This interaction can be induced by bending of the membrane around isolated bonds, entropic interactions due to collisions with an underlying wall or due to the suppression of membrane fluctuations by bonds.

Speck et al. [72] developed a model which accounts for the interaction between flexible bonds. In the limit of large length fluctuations of the binding proteins and large distances between the bonds this model can be mapped to the Ising model. Thereby, the interaction between the different bonds is given by equation (4.21). This formula is valid as long as the bonds are very soft. In this regime, kinetic Monte Carlo simulations confirmed that the model accurately describes the adhesion dynamics by reproducing results from higher level Langevin simulations. Later, entropic interactions between the bonds were considered in the model [75]. This interaction was not sufficient for stable adhesion domains. However, adhesion domains were possible if additional interactions were introduced.

Farago and co-workers [145–147] considered also entropic interactions between the bonds. This time, the entropic interaction is due to the Helfrich-repulsion [132], a repulsion due to collisions between the fluctuating membrane and a wall. The authors observed a first-order transition between a gas-like phase and a condensed phase (only when there was an additional interaction between the bonds).

Raudino and Pannuzzo [143] developed a semi-quantitative theory of the spreading rate of an adhesion domain. They focused on the case when the binding kinetics is limited by the encounters between both membranes (or the binders embedded in these membranes) and found an upper limit for the spreading rate. Additionally, they treated the nucleation dynamics in a similar manner [144]. While on first sight this spreading rate seems to be our effective reaction rates

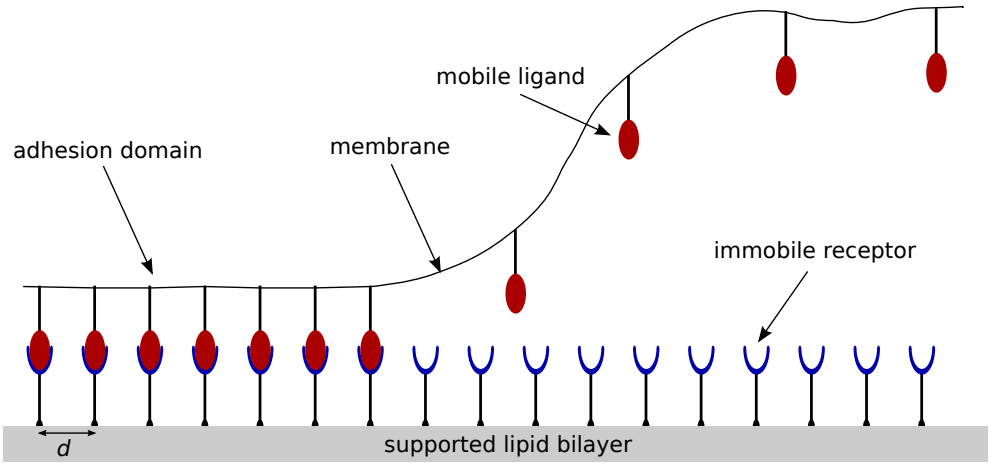

Figure 6.5: Sketch of the rim of the adhesion domain. The red ligands diffuse to the rim where they form bonds with the immobile receptors increasing the size of the adhesion domain. The distance between the bonds d is $\sqrt{1/\rho_b}$.

[74, 148], this is on closer inspection not the case. In their model, Raudino and Pannuzzo [143] assume that the membrane binds immediately if it touches the substrate (or a binder in the opposing membrane). However, we assume that the membrane has to get into reaction distance several times before it can bind. Furthermore, we develop a Monte Carlo scheme based on our rates [148].

I.6.3.3 Diffusion models

Very often diffusion of the mobile binders to the adhesion domain is the slowest process of the adhesion dynamics and hence other processes do not have to be considered in order to describe the dynamics. This means that the spreading of the adhesion domain is limited by the diffusion of one of the binders [8, 149] (i. e. diffusion limited). More specifically, the binders in the upper membrane or the binders in the lower membrane[1] have to diffuse to the rim of the adhesion domain where they form bonds thereby increasing the area of the adhesion domain (see also figure 6.5). In this regime, the radius of the adhesion domain grows with $\sqrt{t}$ [8, 10, 11, 60] whereas in the reaction limited regime the radius grows linearly in time [8, 10]. The transition between the reaction limited and the diffusion limited behavior depends mainly on the ratio between the bond density and the density of the diffusing binder species [10] and was also observed in experiments

[1] We only consider the case where one binder (called ligand) is mobile. The other one is considered to be immobile. If both binders would be mobile the problem is much more complex and, accordingly, much more difficult to model analytically.

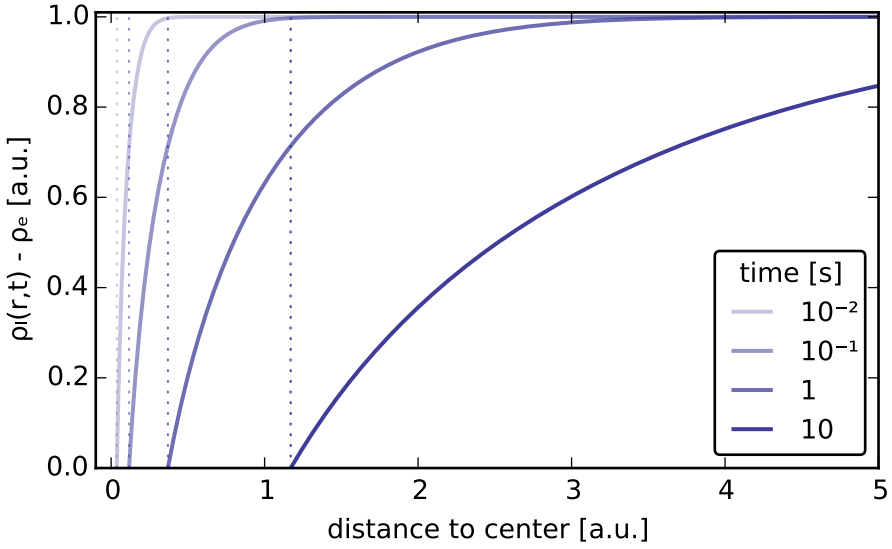

Figure 6.6: Density profiles for different stages of the growth phase. The density was set such that $\left(\rho_l^0 - \rho_e\right)/\rho_b = 0.1$. Each curve begins at the rim of the domain (see dotted lines). The width of the profiles gets larger with increasing time, i. e. a depletion zone develops. Its width scales with $\sqrt{Dt}$.

[8].

Boundary value problems for diffusion limited growth processes consist of the diffusion equation and boundary conditions describing the growth of the domain and setting the densities (or fluxes) at the boundaries. As an example, we present a radially symmetric, two dimensional boundary value problem (see also [10])

$$\frac{\partial \rho_l(r,t)}{\partial t} = D\left(\frac{\partial^2 \rho_l(r,t)}{\partial r^2} + \frac{1}{r}\frac{\partial \rho_l(r,t)}{\partial r}\right), \tag{6.5}$$

where r is the distance to the center of the domain, D the diffusion constant of the diffusing species and $\rho_l(r,t)$ the density of the diffusing species. The growth of the adhesion domain is given by the diffusive flux onto it

$$\frac{\partial R(t)}{\partial t} = \frac{1}{\rho_b} D \frac{\partial \rho_l(r,t)}{\partial r}\bigg|_{r=R(t)}, \tag{6.6}$$

where $R(t)$ is the radius of the domain and ρ_b the bond density within the adhesion domain. Here we assume that the bond density is constant during the

whole growth process. The density at the edge is fixed

$$\rho_l(R(t), t) = \rho_e. \tag{6.7}$$

Furthermore, we assume that the density of mobile binders is constant at the beginning of the growth phase and the size of the initial seed is negligible, i.e.

$$\rho_l(r, 0) = \rho_l^0 \quad \text{and} \quad R(0) = 0. \tag{6.8}$$

This boundary value problem is a variant of the Stefan problem [7, 150], which was originally formulated to describe the growth of ice shelfs.

As in the literature of membrane adhesion, the derivation of the solution of the boundary value problem (equations (6.5) to (6.8)) is not shown and, especially, it is not stated that the solution is only an approximation, we sketch the calculation leading to the quasistationary solution used throughout the literature about membrane adhesion (see for example [10, 11]). Our derivation is based on the calculation in the article of Frank [151]. In order to find a quasistationary solution, we set

$$s \equiv \frac{r}{\sqrt{Dt}}. \tag{6.9}$$

This transformation converts the diffusion equation (6.5) into an ordinary differential equation

$$\frac{\partial^2 \rho_l(s)}{\partial s^2} = -\left(\frac{1}{s} + \frac{s}{2}\right) \frac{\partial \rho_l(s)}{\partial s}. \tag{6.10}$$

The resulting differential equation can be solved by integration and, eventually, we obtain

$$\rho_l(r, t) = \rho_l^0 - \frac{\rho_l^0 - \rho_e}{\mathrm{Ei}\left(\frac{R^2(t)}{4Dt}\right)} \mathrm{Ei}\left(\frac{r^2}{4Dt}\right), \tag{6.11}$$

where $\mathrm{Ei}(x)$ is the so-called exponential integral function [70], defined as

$$\mathrm{Ei}\,(z) = \int_{-\infty}^{z} \mathrm{d}t\, \frac{\exp(t)}{t}. \tag{6.12}$$

Exemplary plots of $\rho_l(r, t)$ can be seen in figure 6.6. The width of the depletion zone (zone with a reduced density of binders) grows with $\sqrt{Dt}$. In other words, equation (6.11) does not have a stationary solution in contrast to the three dimensional case [152].

The solution of our boundary value problem (equation (6.11)) still depends on the radius of the domain, the quantity that we are actually interested in. We

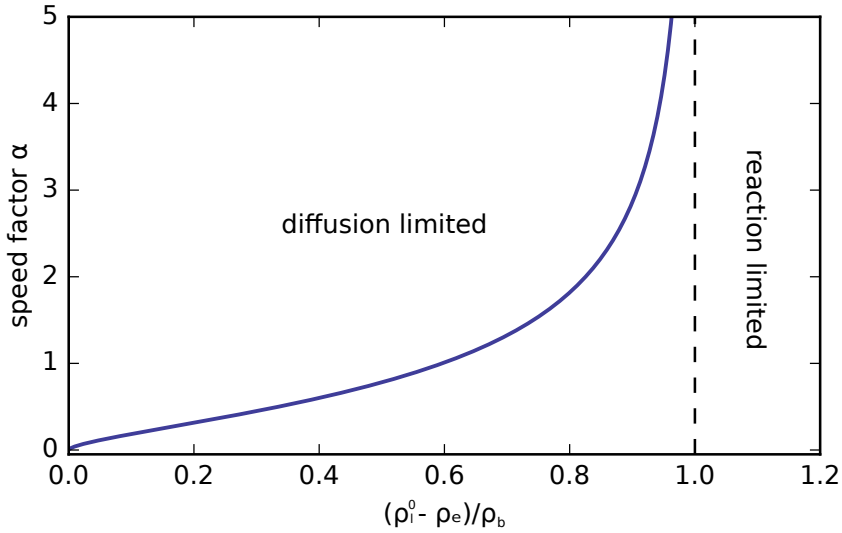

Figure 6.7: Graphical solution of equation (6.14). If $(\rho_l^0 - \rho_e)/\rho_b$ is smaller than one, there is a solution of this equation. Hence, in this regime, the growth is diffusion limited. However, in the opposite case, there is not a solution. Here the growth is reaction limited.

assume that the radius is proportional to $\sqrt{Dt}$ [10], i. e.

$$R(t) = 2\alpha\sqrt{Dt}, \tag{6.13}$$

where α is a dimensionless prefactor, the so-called speed factor, that will be determined later. By definition, we consider such a growth law diffusion limited. We substitute the above expression together with the solution (equation (6.11)) into the relation for the domain growth (equation (6.6)) and, thereby, obtain an implicit equation from which we determine the speed factor α

$$\frac{\rho_l^0 - \rho_e}{\rho_b} = \alpha^2 \,\mathrm{Ei}\left(\alpha^2\right) \exp\left(\alpha^2\right). \tag{6.14}$$

This expression cannot be inverted in closed form such that we obtain a formula for the speed factor α. However, we plot this relation in figure 6.7. The graph shows that there is only a solution if $(\rho_l^0 - \rho_e)/\rho_b$ is smaller than one. In this case, the growth is diffusion limited with the speed factor α from the plot in figure 6.7 or equation (6.14), respectively. Furthermore, a solution for the speed factor does not exist if the ligand density is too large. In this case, the behaviour

is reaction limited, i. e. limited by the reaction kinetics between ligands and receptors. In this regime, the radius is proportional to time.

This can be understood intuitively. Let us assume that a new bond is formed in a, for the sake of simplicity, one dimensional adhesion domain. This increases the radius by $1/\rho_b$ (with ρ_b as the bond density within the domain). If the ligand density ρ_l^0 is larger than the bond density, the rim jumps so far into the ligand reservoir such that the ligand density looks the same as before for the advancing front. Hence, a depletion zone does not form and, therefore, the ligands do not have to diffuse a (mesoscopic) distance to get to the rim. Consequently, the growth is only limited by the reactions between the two binders.

The result that the growth of the domain is proportional to the square root of time raises a question: How can be the speed of radius be infinite at the beginning?[2] In publication P5, we answer this question and generalize the formalism discussed in this subsection. In the above formalism, we assume implicitly that the reaction rates are infinite. However, with the introduction of a different boundary condition (so-called radiation boundary condition in the theory of heat conduction), it is possible to introduce finite reaction rates. The growth behavior is asymptotically purely diffusion limited and has the same behavior as in the usual formalism presented above. In the short time regime, the behavior is determined by the reaction kinetics. Applying this theory, we are able to extract association rates of ligand-receptor bonds from growth curves of adhesion domains and investigate the role of the membrane properties (and of the whole environment) on the reaction kinetics (see section I.6.1 for details).

Very often diffusion limited growth is associated with shape perturbations [153–155]. Here, the diffusive flux driving the growth of the domain is larger at exposed spots of the domain. This leads to a faster growth, there and hence to shape perturbations. Surface tension [153, 156], diffusive fluxes within the domain [156, 157] and other effects stabilize the radial shape. Shenoy et al. considered the interplay between the surface tension and the diffusive flux and found a typical domain radius below which the shape is stable and radial but unstable above [10]. Experimental results [8] seem to confirm their theoretical results.

Furthermore, endocytosis (the wrapping of virus in a cell membrane, see also section I.4.1) can also be mediated by ligand-receptor bonds. Gao et al. [11] studied the influence of the membrane properties and the diffusion on the wrapping dynamics. He found that a minimum radius exists below which a virus does not wrap. This minimum radius depends on the bending rigidity, the binding enthalpy of the ligand receptor bond and the densities of ligands and receptors. At a certain optimal radius of the virus, the wrapping time is minimal because

[2] The derivative of the radius $R(t)$ diverges at $t = 0$ and so does the growth speed.

of a competition between the thermodynamic driving force and the diffusion.

Summarizing, diffusion limited models can be used if the binder density of the mobile species is small compared to the bond density of the resulting adhesion domain. Additionally, the reaction rate has to be large such that it does not limit the dynamics to a larger extent than the diffusion. This condition is especially fulfilled in the asymptotic time regime (see publication P5). The main disadvantage of a purely diffusion limited growth, if one is interested in the reaction kinetics, is that it only depends on the binder densities and the diffusion constant and hence reaction rates cannot be determined from diffusion limited growth curves. However, if the reaction kinetics initially limits the dynamics, the association rates between the two binders in their respective environment are accessible.

I.7 Diffusion limited growth

Diffusion limited growth is ubiquitous in nature. As explained in section I.6.3, the growth in such a regime is limited by the diffusion of mobile tracers to the growing domain. Examples range from the growth of fossils (like stromatolites) [158] over the growth of microbacterial colonies [159] to electrochemical deposition (see also figure 7.1a) to c)). In contrast to section I.6.3, diffusion limited growth is typically associated with shape perturbations or even fractal structures that look very appealing.

The first discussing the connection between diffusion limited growth and shape perturbation of the growing domain were Mullins and Sekerka [153, 160]. They studied the role of the surface tension of the growing domain and how it suppresses shape perturbations induced by diffusive flux. Almost two decades later, Witten and Sander [154, 155] published their celebrated model of diffusion limited aggregation (DLA). There, they showed that in the zero-density limit and the limit of infinitely large reaction rates fractal structure develop with a fractal dimension of around 1.7 in the two dimensional case. Later this model was refined to finite densities [161–164] and finite reaction rates [165, 166]. Furthermore, Nagatani [167] showed with the help of renormalization techniques that, even though there are two fixed points for a reaction limited and a diffusion limited growth mode, only the diffusion limited growth mode has a stable fixed point. Recently, Cuerno and coworkers [156, 157] resumed the work of Mullins and Sekerka and considered different contributions additionally to the surface tension that suppress shape perturbations like finite reaction rates or diffusion within the domain.

Mathematically, the shape instability can be explained by the coupling between the growth speed of the domain and the concentration gradient [153, 160]. Thereby, the concentration is (at least in steady state) determined by the Laplace

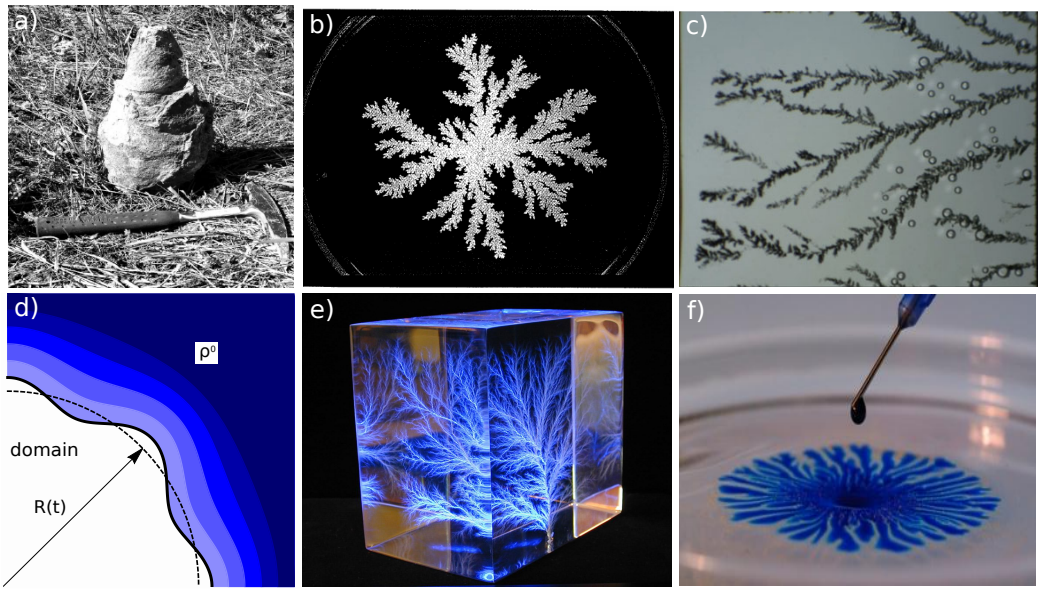

Figure 7.1: Figures to diffusion limited growth and related phenomena. a) Stromatolite (from [158]), b) Microbacterial colony (from [168]), c) electrochemical deposition (from [169]), d) sketch of diffusion limited growth (see main text for details), e) dielectric breakdown (from [170]), f) Saffman-Taylor instability (from [171]).

equation. More specifically, the governing equations (in the steady state) read

$$\Delta\rho(\mathbf{r}) = 0 \tag{7.1}$$

and

$$v = \nabla\rho(\mathbf{r}), \tag{7.2}$$

where $\rho(\mathbf{r})$ is the density of the diffusing species and v the growth speed of the domain.

We can understand this instability intuitively (see figure 7.1d), see also Shenoy and Freund [10]). Spots at the interface that are more exposed to the tracer reservoir (i. e. spots where the radius is larger) see a larger gradient of the tracer density. As the diffusive flux is proportional to the density gradient (see equation 7.2), the diffusive flux towards these spots and, hence, the growth there is enhanced. On the other hand, spots less exposed to the reservoir see a smaller gradient and feel a smaller diffusive flux. In a nutshell, the growth of a domain at more exposed parts is enhanced compared to less exposed parts. Accordingly, this creates a positive feedback, shape perturbations are enhanced and hence a radial domain is unstable with respect to its shape.

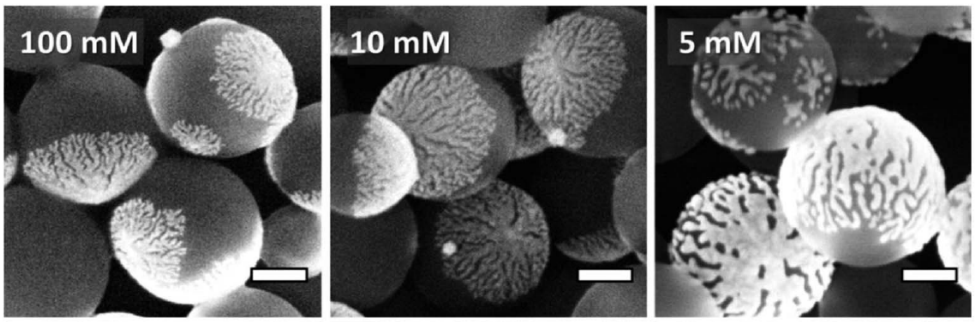

Figure 7.2: SEM figures of different patchy particles grown in a solution with different concentrations of ascorbic acid (see publication P6 for details). Here, the domains consist of gold. The scale bar corresponds to 200 nm. From [24].

Due to the universal form of the constituting equations (7.1) and (7.2), the phenomenon of such shape instabilities is not restricted to diffusion limited growth but also to other growth phenomena like the dielectric breakdown [172] (see also figure 7.1e)). The most prominent example is probably the Saffman-Taylor instability [173] or viscous fingering (see figure 7.1f)). Here, we talk about the displacement of a fluid with a high viscosity by another with a lower viscosity in a quasi two dimensional setup (Hele-Shaw cells) or in porous media. Thereby, the displacement speed is coupled to the gradient of the pressure which in turn is determined by the Laplace equation. This is a highly relevant problem in the field of oil recovery in porous rock when water is pumped in the oil reservoir in order to displace the oil [173]. If the pressure is too large, water and oil mix due to viscous fingering which is not desired.

The experimental motivation for our work is the method of the synthesis of colloidal patchy particles developed by Klupp Taylor and coworkers [22–24]. With this method, it is possible to produce colloidal particles that are partially covered by metal domains (see figure 7.2). Thereby, the domains can be either radial or have dendrite structures. The partially dendrite structure of the metal domains suggests that their growth is driven by surface diffusion limited growth, i. e. the growth is limited by the diffusion of the metal precursor on the colloidal surface.

In contrast to the growth scenario in chapter P5, the growth scenario that we discuss here shows clear shape perturbations and partially fractal growth. This can be explained with the different physical properties of the domains and the fact that the growth in publication P5 is initially reaction limited. The final morphology depends very strongly on experimental parameters like temperature, pH-value or the ammonia concentration [22–24]. We do not assume that those parameters influence equilibrium parameters like the surface tension that suppresses shape perturbations in the Mullins-Sekerka scenario [153, 160]. Instead, we make the

hypothesis that the changes of the experimental parameters influence three theoretically accessible parameters, namely the initial tracer concentration on the colloidal surface, the sticking probability and the detachment probability. Furthermore, we consider systems with a finite size and periodic boundaries like the colloidal particles in the experiment. The sticking probability s and the detachment probability p are defined as the probabilities for a tracer to bind to the domain (if it is next to it) or to unbind from it

$$\begin{aligned} s &= 1 - \exp\left(-k_{\mathrm{on}}\delta t\right) = 1 - \exp\left(-\frac{k_{\mathrm{on}}a^2}{4D}\right) \\ p &= 1 - \exp\left(-k_{\mathrm{off}}\delta t\right) = 1 - \exp\left(-\frac{k_{\mathrm{off}}a^2}{4D}\right), \end{aligned} \tag{7.3}$$

where $\delta t = a^2/4D$ is the time for a metal precursor to move its typical diameter a and D is the diffusion constant of the tracer on the colloidal surface. The sticking probability determines the number of domain sites that a tracer visits before it binds to the domain. As we point out in publication P6, this leads to a roughening of the resulting structures. We approximate the sticking probability s and the detachment probability p for small s and p by

$$\begin{aligned} s &\approx k_{\mathrm{on}}a^2/4D \\ p &\approx k_{\mathrm{off}}a^2/4D. \end{aligned} \tag{7.4}$$

Thereby, the ratio between the detachment probability and the sticking probability defines via local detailed balance

$$\epsilon_b = k_B T \ln\left(\frac{s}{p}\right) \tag{7.5}$$

the attachment energy ϵ_b for adding a tracer particle to the domain.

In publication P6, the growth of gold patches on polystyrene spheres is discussed from the experimental and as well from the theoretical point of view. Therein, we obtain mostly dendrite structures that, however, still differ in their morphology depending on the experimental parameters like temperature or the concentration of ascorbic acid. We perform simulations of diffusion limited aggregation considering the sticking probability, the detachment probability and the initial tracer density at the same time. Building on our simulation results, we are then able to identify the influence of the experimental parameters on those three theoretically accessible parameters. We find, for example, that the concentration of ascorbic acid hinders the diffusion of the metal precursor on the surface of the colloid.

Part III

Publications

P1

Two intertwined facets of adherent membranes: membrane roughness and correlations between ligand–receptors bonds

Two intertwined facets of adherent membranes: membrane roughness and correlations between ligand–receptors bonds

Ellen Reister[1], Timo Bihr[1], Udo Seifert[1] and Ana-Sunčana Smith[1,2]

[1] II. Institut für Theoretische Physik, Universität Stuttgart, Pfaffenwaldring 57, 70550 Stuttgart, Germany
[2] Institut für Theoretische Physik and the Excellence Cluster: Engineering of Advanced Materials, Universität Erlangen-Nürnberg, Staudtstrasse 7, 91058 Erlangen, Germany

New Journal of Physics **13** (2011) 025003

DOI: 10.1088/1367-2630/13/2/025003
http://iopscience.iop.org/1367-2630/13/2/025003

Abstract We study equilibrium fluctuations of adherent membranes by means of Langevin simulations in the case when the interaction of the membrane with the substrate is twofold: a non-specific homogeneous harmonic potential is placed at large distances, whereas discrete ligand–receptor interactions occur at short distances from the flat substrate. We analyze the correlations between neighboring ligand–receptor bonds in a regime of relatively strong membrane fluctuations. By comparison with the random distribution of bonds, we find that the correlations between the bonds are always positive, suggesting spontaneous formation of domains. The equilibrium roughness of the membrane is then determined by fluctuations in the number density of bonds within the domains. Furthermore, we show that the excess number of bonds arising due to correlations and the instantaneous roughness of the membrane both follow master curves that depend only on the instantaneous bond density and not on the intrinsic binding strength of the ligand–receptor pair. The master curves show identical trends, further corroborating the link between membrane roughness and bond correlations.

New Journal of Physics
The open-access journal for physics

Two intertwined facets of adherent membranes: membrane roughness and correlations between ligand–receptors bonds

Ellen Reister[1], **Timo Bihr**[1], **Udo Seifert**[1] and **Ana-Sunčana Smith**[1,2,3]

[1] II. Institut für Theoretische Physik, Universität Stuttgart, Pfaffenwaldring 57, 70550 Stuttgart, Germany
[2] Institut für Theoretische Physik and the Excellence Cluster: Engineering of Advanced Materials, Universität Erlangen-Nürnberg, Staudtstrasse 7, 91058 Erlangen, Germany
E-mail: smith@physik.uni-erlangen.de

New Journal of Physics **13** (2011) 025003 (15pp)
Received 13 August 2010
Published 3 February 2011
Online at http://www.njp.org/
doi:10.1088/1367-2630/13/2/025003

Abstract. We study equilibrium fluctuations of adherent membranes by means of Langevin simulations in the case when the interaction of the membrane with the substrate is twofold: a non-specific homogeneous harmonic potential is placed at large distances, whereas discrete ligand–receptor interactions occur at short distances from the flat substrate. We analyze the correlations between neighboring ligand–receptor bonds in a regime of relatively strong membrane fluctuations. By comparison with the random distribution of bonds, we find that the correlations between the bonds are always positive, suggesting spontaneous formation of domains. The equilibrium roughness of the membrane is then determined by fluctuations in the number density of bonds within the domains. Furthermore, we show that the excess number of bonds arising due to correlations and the instantaneous roughness of the membrane both follow master curves that depend only on the instantaneous bond density and not on the intrinsic binding strength of the ligand–receptor pair. The master curves show identical trends, further corroborating the link between membrane roughness and bond correlations.

[3] Author to whom any correspondence should be addressed.

Contents

1. Introduction 2
2. Model 3
3. Correlations between bonds 7
4. Instantaneous membrane roughness and the coordination of bonds 8
5. Equilibrium membrane roughness and fluctuations in bond density 10
6. Conclusions 12
Acknowledgments 13
Appendix: Simulation scheme 13
References 14

1. Introduction

The adhesion between fluid membranes and flat substrates mediated by specific ligand–receptor bonds has been extensively studied in recent decades (for a recent review see [1]). One driving force underlying such an extensive scientific activity is the relevance of this system to the adhesion of living cells [2]. A typical *experimental* realization of an adhesion assay involves a protein-carrying giant unilamellar vesicle that binds to a functionalized substrate [3]–[5]. The first step of adhesion is associated with the sedimentation of the vesicle into a non-specific potential minimum at relatively large distances from the substrate [6, 7]. The fluctuations of the membrane allow then for the formation of first ligand–receptor bonds [8] upon which tight contacts close to the substrate are established and specific adhesion takes place. Such behavior is well described as adhesion in a potential acting between the membrane and the substrate that contains two wells: a non-specific one further away from the substrate and a specific one in its vicinity [8, 10, 11].

If bare glass substrates were involved in the adhesion assay, the non-specific interactions driving the first step of adhesion would be dominated by the relatively strong van der Waals attraction of the glass. Similarly, substrates with strong Coulomb attraction could be envisaged. In these cases, the Helfrich steric repulsion imposed by fluctuations of the membrane would be overcome and the vesicle membrane would strongly adhere on the substrate. The non-specific minimum would be positioned very close to the substrate and its depth considerable. For the control of the generic non-specific substrate–vesicle interactions, a variety of experimental techniques have been developed [9], often involving soft polymers incorporated either into the vesicle membrane and/or deposited on the substrate. As a result, the non-specific minimum is pushed to far distances from the substrate and is characterized by a considerably smaller strength and curvature than the specific minimum associated with the formation of ligand–receptor bonds. Consequently, the two minima are well separated, which is a prerequisite for a successful specific adhesion assay as it allows for proper differentiation between non-specific and specific adhesion [1].

From a *theoretical* point of view, adhesion is often studied in the presence of membrane fluctuations but without the non-specific potential, which ignores subtle effects induced by the presence of a secondary minimum in the free energy. Even so, for the case of an effective membrane–substrate potential with a single minimum, valuable information on cooperativity

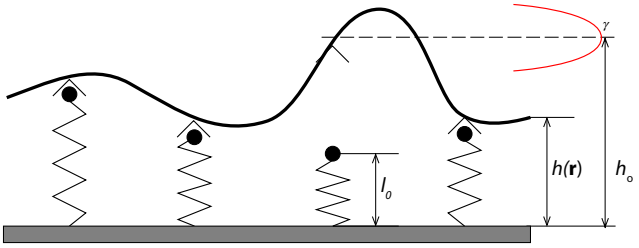

Figure 1. A membrane made to adhere on a substrate by receptor–ligand bonds. The rest length of the tether l_0 representing a bond is marked. The local instantaneous height $h(r)$, which deviates from the minimum of the non-specific potential placed at h_0, is shown. The potential of strength γ is depicted with the red curve.

of bonds [12, 13], membrane roughness [14, 15] and the development of domains has been obtained [16, 17]. The analysis of a Hamiltonian containing a non-specific interaction potential [18]–[20] shows that a large section of the phase space is actually associated with a single well effective free energy. However, deeper understanding of the relevant mechanisms driving the adhesion in the regime relevant to experimental realizations of the system must involve a secondary minimum. Then a study where microscopic degrees of freedom are monitored directly, and their impact on the macroscopic behavior of the system analyzed in detail, should be performed. To address that issue, we concentrate on the part of the phase space where the free energy has features of a double-well potential. We study the equilibrium of the bonded-membrane system that is propagated in time by Langevin dynamics simulations in which the membrane can experience significant fluctuations. Our goal is to understand the interplay between specific and non-specific interactions and show that by means of finite elasticity, membrane roughness couples to correlations between bonds formed on the neighboring sites.

2. Model

The system (figure 1) consists of a fluctuating membrane that interacts with a substrate by a weak homogeneous harmonic potential whose strength and distance from the substrate are derived from the position and curvature of the non-specific minimum found in experiments [6, 8]. Further, specific ligand–receptor interactions are imposed on a regular square lattice and are modeled as harmonic tethers. Ligands embedded in the fluctuating membrane are arranged on a regular lattice and move with the membrane only in the direction perpendicular to the surface. Receptors are immobilized at the same positions $\mathbf{r}_i$ on the flat substrate. Each bond has a statistical probability to be open or closed, depending on the local temporal position of the membrane (see the appendix for details). The appropriate energy functional for a system including both, the membrane and the bonds, is

$$\mathcal{H}[h(\mathbf{r})] = \int_A \mathrm{d}^2\mathbf{r}\,\left\{\frac{\kappa}{2}\left(\nabla^2 h(\mathbf{r})\right)^2 + \frac{\gamma}{2}\left(h(\mathbf{r}) - h_0\right)^2\right\} - \sum_{j=1}^{N_t} b_j\left(\epsilon_b - \frac{K}{2}\left(h(\mathbf{r}_j) - l_0\right)^2\right). \tag{1}$$

The first term expresses the bending energy of a membrane with projected area A and bending rigidity κ. The membrane height profile $h(\mathbf{r})$ is given in the Monge gauge as a function of its projected position $\mathbf{r}$ on the substrate plane. The non-specific membrane–substrate interaction, given by the second term, is modeled by a harmonic potential with strength γ placed at a distance h_0 from the wall ($l_0 < h_0$). The last term describes the total interaction between ligands and receptors positioned opposite to one another at $\mathbf{r}_j$, j indexing each of N_t binding sites. Since the formation of a bond is taken to be a statistical event, only formed bonds with $b_j = 1$ contribute to the free energy. Otherwise, if the bond is open, $b_j = 0$. Since both the binding and the unbinding rates (k_{on} and k_{off}, respectively) are associated with distributions, the energy that each bond contributes to the free energy is not a unique value, but is a distribution too. Consequently, the binding affinity on the level of a bond [8] is defined as the average of its respective distribution

$$\beta E_{\mathrm{a}} = \left\langle \ln\left[\frac{k_{\mathrm{off}}}{k_{\mathrm{on}}}\right]\right\rangle = \beta\left\langle \epsilon_{\mathrm{b}} - \frac{K}{2}(h(\mathbf{r}_j) - l_0)^2\right\rangle \tag{2}$$

and is intimately related to the detailed balance condition (equation (A.1)) that governs the formation of bonds.

For a system described by equation (1), the free energy of a binding site $f(h)$ can be calculated explicitly for the case of an infinitely stiff membrane ($\kappa \to \infty$) from the partition function [18, 20]

$$\beta f(h) = -\frac{1}{N_t}\ln \mathcal{Z} = \frac{\beta\gamma}{2}\frac{1}{\rho}(h - h_0)^2 - \ln\left(1 + \exp\left[-\beta\left(\frac{K}{2}(h - l_0)^2 - \epsilon_{\mathrm{b}}\right)\right]\right), \tag{3}$$

where $\rho \equiv N_t/A$ is the density of binding sites, and $\beta \equiv k_{\mathrm{B}}T$, k_{B} being the Boltzmann constant and T the temperature.

As shown in figure 2, this free energy can have two minima. If an infinitely large and stiff membrane is placed in such a potential, it will reside in the minimum with the lower energy. As the relative strength of the minima changes in response to the variation of some parameter (e.g. intrinsic binding strength or the spring constant), the membrane jumps between two minima and exhibits a first-order transition. At finite temperatures and in a system of finite size, the stiff membrane as a whole spends a fraction of time in one minimum and the remainder of time in the other minimum. The occupancy of the two minima is given by the respective Boltzmann factors, the latter themselves depending on the membrane size.

For the simulations of a membrane that experiences both a finite bending stiffness and thermal fluctuations ($\beta\kappa = 10$), the parameters are chosen in such a way that the underlying free energy possesses the two minima (figure 2). Specifically, the system is parameterized by a square 64×64 lattice with a lattice constant $a \simeq 10\,\mathrm{nm}$. The system has $N_t = 64$ binding sites arranged on a square 8×8 lattice such that the distance between neighboring binding sites is $8a$. The time scale of the system is given by the viscosity of the water surrounding the membrane, which, at a temperature of $T = 300\,\mathrm{K}$, is $\eta = 10^{-9}\,\mathrm{Js\,cm^{-3}}$ or $2.4 \times 10^{-7} k_{\mathrm{B}}T\mathrm{s}a^{-3}$ in simulation units. The reaction rate of the unstressed tether is set to $k_0 = 2000\,\mathrm{s^{-1}}$ and the discrete time step in the simulation is chosen as $\Delta t = 10^{-9}\,\mathrm{s}$, which is well under the smallest membrane time scale $\tau = 4\eta/(\beta\kappa k_{\mathrm{max}}^3) \simeq 1.1 \times 10^{-9}\,\mathrm{s}$. This reaction rate is somewhat faster than the typical biological rates. However, the choice of k_0 has no effect on the equilibrium averages of the system. For dynamic fluctuations around the equilibrium, due to the clear separation of bond and membrane time scales, k_0 simply sets the time unit, a conclusion that has been tested by varying k_0 over several orders of magnitude (data not shown). The strength

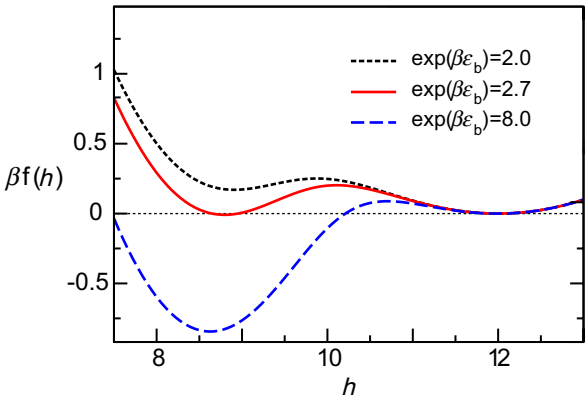

Figure 2. The effective free energy $\beta f(h)$ is shown for several values of ϵ_b and for $a^2\beta K = 1.25$ for the case of an infinitely stiff membrane. The non-specific potential is placed at $h_0 = 12a$, while the rest length of the tethers is $l_0 = 8a$. Two minima are observed for $\ln(1.39) < \beta\epsilon_b < 5.4$. The so-called non-specific minimum at $h \simeq 12a$ is the signature of the bare non-specific membrane–substrate potential. A second minimum with a higher density of ligand–receptor bonds resides at lower heights $h \simeq 8a$ and is, because it originates from the ligand–receptor interaction potential, named the specific minimum. At the critical $e^{\epsilon_b} \simeq 2.7$, the two minima have the same free energy, and a first-order phase transition takes place for an infinitely stiff and infinitely large membrane.

γ of the bare non-specific potential is $\gamma = 3.125 \times 10^{-3} k_B T a^{-4}$, which equals $1.25 \times 10^9\,\mathrm{Jm}^{-4}$, and the potential minimum is placed at $h_0 = 12a$. The rest length of the springs is $l_0 = 8a$. The typical intrinsic binding energy ϵ_b of a ligand–receptor pair is a few $k_B T$, while the spring stiffness is set to $K = 1.25\, k_B T\, a^{-2}$ (equivalent to $K \simeq 5 \times 10^{-5}\,\mathrm{Nm}^{-1}$). For each set of parameters, the equilibrium dynamics simulations were performed following the protocol described in the appendix.

Fluctuations of the membrane and the membrane elasticity change the potentials shown in figure 2, and the membrane can reside in both minima simultaneously. The phase diagram for the simulated system can be constructed by evaluating the overall mean height $\bar{h}$ or the mean bond number density $\bar{\phi}$ as a function of the intrinsic binding strength. Here $\bar{h}$ and $\bar{\phi}$ are defined as

$$\bar{h} = \frac{\sum_i \langle h_i(\mathbf{r})\rangle}{\sum_i 1} \quad \text{and} \quad \bar{\phi} = \frac{\sum_i \phi_i}{\sum_i 1} = \frac{\sum_i \langle b_{j,i}\rangle}{\sum_i 1}, \tag{4}$$

with the sums accounting for the average over all instances of discredited time t_i, and $\sum_i 1$ equals the total number of frames available to the analysis. The brackets indicate averaging over spacial coordinates of the membrane profile $h_i(\mathbf{r})$ or bond realizations $b_{j,i}$ at each bond site $\mathbf{r_j}$, the latter giving rise to the instantaneous number density of formed bonds ϕ_i. A bar indicates a property that has been averaged over both the temporal and spatial coordinates. This notation for averaging will be used as a convention throughout this paper.

As can be seen from the simulation data shown in figure 3, the transition occurs between $\beta\epsilon_b = 3.45$ and $\beta\epsilon_b = 3.50$. At binding strengths lower than $\beta\epsilon_b = 3.45$ (lower branch),

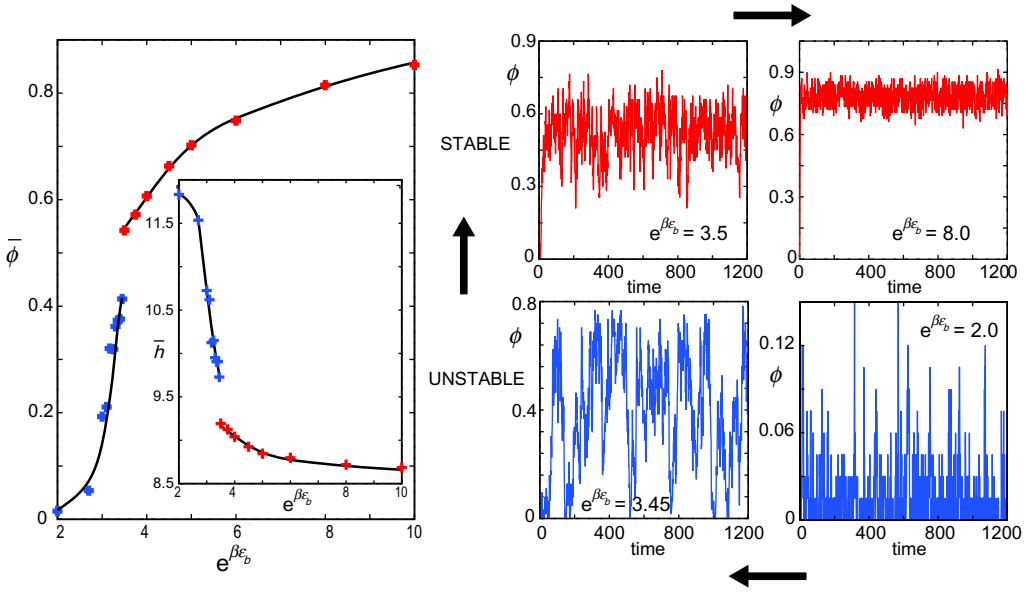

Figure 3. Left: the average number density of bonds $\bar{\phi}$ and the mean membrane-substrate distance $\bar{h}$ (inset), as a function of the binding energy $e^{\beta\epsilon_b}$. Right: the time evolution of the number of bonds N_b within the membrane patch in equilibrium. The arrows point to the direction of the growing intrinsic binding strength. At very low $e^{\beta\epsilon_b}$, only few bonds appear but all dissociate very quickly. As $e^{\beta\epsilon_b}$ increases toward the transition value, the domain becomes more stable, although occasionally the number of bonds both drops to zero or considerably overshoots the mean value. For $e^{\beta\epsilon_b}$ above the critical value, the number of bonds is always larger than zero. As the intrinsic binding strength further increases, the fluctuations in the number of bonds decrease.

configurations with no bonds occur in equilibrium (specific adhesion is unstable), whereas at binding strengths larger than $\beta\epsilon_b = 3.5$, a finite number of bonds are always present in the system, and the specific adhesion is stable (upper branch). This behavior is reminiscent of the first-order transition discussed above.

From the simulated time evolution of the membrane profile it is possible to extract the membrane height distribution function (data not shown). An effective free energy can then be defined as the logarithm of that height distribution. As such, the effective potential has also two minima, although in a somewhat reduced range of intrinsic binding strengths $\beta\epsilon_b$. Interestingly, the critical binding strength at which the transition occurs is larger than both the binding strength ($\beta\epsilon_b \simeq 3.1$) at which the effective potential obtained from simulations has two degenerate minima and the binding strength ($\beta\epsilon_b \simeq 2.7$) at which the effective potential for a stiff infinite membrane has two degenerate minima (figure 2).

Typically, a soft fluctuating membrane patch has, on average, a smaller number of bonds than the stiff membrane segment of the same size, which can be calculated by the use of the partition function $\mathcal{Z}$. The only exception is very low intrinsic binding strengths at which a stiff membrane makes no bonds. In this regime, a fluctuating membrane establishes some unstable bonds contributing to the non-zero average bond density, due to random excursions to the close proximity of the substrate. Furthermore, the observation is that even in such cases, specific

adhesion often appears not as individual bonds but as few bonds together. This indicates that in adhesion of fluctuating soft membranes, correlations between bonds may arise due to the deformability of the bilayer.

3. Correlations between bonds

Correlations between neighboring bonds emerge from membrane deformations taking place in the vicinity of a bond in a region whose size is typified by the lateral correlation length. If there is another binding site within this region, the probability for forming a bond at this second site increases with respect to the part of the membrane fluctuating in the non-specific minimum [8], simply because the ligands and receptors are brought closer together. Since the membrane above the neighboring site is on average, due to deformations, closer to the substrate, the formation of bonds is locally promoted, or said in another way, correlations between bonds are induced. There are no correlations between bonds in an infinitely soft or infinitely rigid membrane, for which the lateral correlation length is either zero or infinite because the local environment where the membrane is deformed does not exist. On the other hand, the fluctuations of the membrane effectively decrease the strength of the bare non-specific potential and increase the distance between the membrane that is not specifically bound and the substrate [21], which in turn affects the deformation of the membrane between the bonds. Correlations hence arise from the balance between the deformation and fluctuations of the membrane with finite bending elasticity on the one hand, and the non-specific potential that attracts the unbound membrane and induces deformations of the bonds on the other hand.

We focus on correlations between the bonds at nearest neighboring sites by calculating the relative mean coordination number. This is achieved by determining first the mean coordination number $\bar{c}$ from calculating the number of bonds with 0–4 bonded neighbors in 10^3 equilibrium realizations of the system. The average number of bonded neighbors is then determined by calculating the mean over all bonds and frames. However, bonds placed on fully random positions at the density ϕ^{r} will also have a finite coordination number c^{r} with $c^{\mathrm{r}} = 4\phi^{\mathrm{r}}$, for a large lattice ignoring finite size effects. For ϕ^{r} fixed at the value corresponding to the equilibrium bond density in a given simulation ($\phi^{\mathrm{r}} = \bar{\phi}$), positive correlations occur when the relative coordination number of a bond $(\bar{c} - c^{\mathrm{r}})/c^{\mathrm{r}}$ is larger than zero. Here $(\bar{c} - c^{\mathrm{r}})$ is the mean excess coordination number, which is the average surplus of bonded neighbors relative to the random (uncorrelated) distribution.

Inspection of the left panel in figure 4 shows clearly that positive correlations typify the parameter space investigated herein. At low densities, in the unstable branch, the correlations between the bonds are strong. The equilibrium life time of a bond is extended in comparison to the life time of isolated bonds signifying coupling effects. At high densities of bonds, the correlations saturate to zero. Ultimately, when all sites are occupied by bonds ($\bar{\phi} = 1, \beta\epsilon_{\mathrm{b}} \to \infty$) the system does not differ from a random distribution, and all correlations are lost.

The probability for the appearance of a certain coordination number n for various parameter sets is shown for both the simulation data and random distributions (top right panels in figure 4). For the random distribution and a large lattice, the expectation value for the probability that a bond will have a coordination number $n = 0, \ldots, 4$ is simply given by the binomial distribution

$$p^{\mathrm{r}}(n) = 4!/[n!(4-n)!](\phi^{\mathrm{r}})^n(1-\phi^{\mathrm{r}})^{4-n}. \tag{5}$$

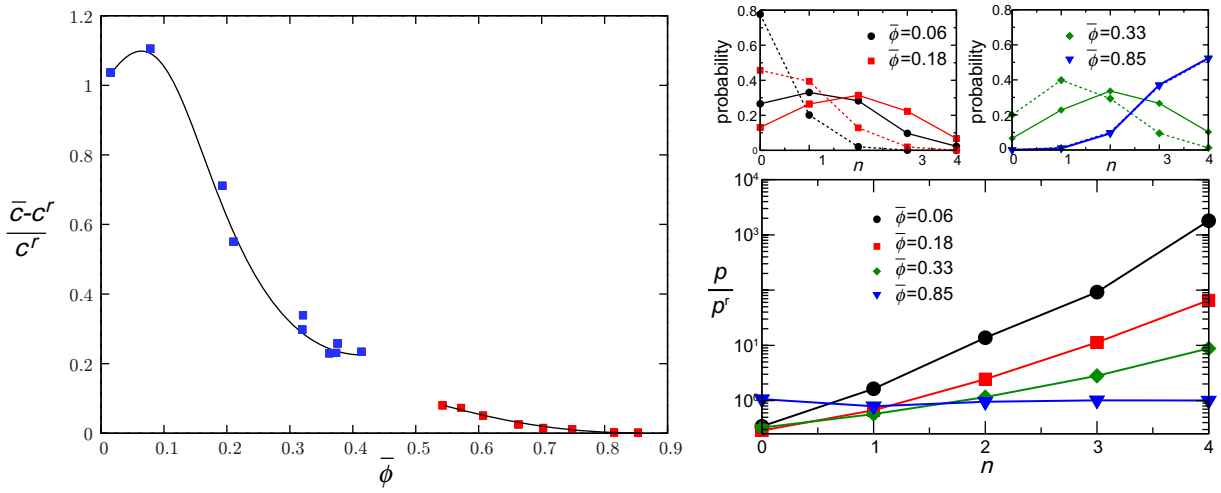

Figure 4. Left: relative coordination number $(\bar{c} - c^{\mathrm{r}})/c^{\mathrm{r}}$ as a function of the mean bond density $\bar{\phi}$. Simulation data are shown with symbols, whereas the line is only a guide to the eye. Top right: the probability for appearance of a certain coordination number $n = 0, \ldots, 4$ for various parameter sets are shown both for the simulation data ($p(n)$, full lines) and random distributions ($p^{\mathrm{r}}(n)$, dashed lines). Bottom right: the ratio of probabilities $p(n)/p^{\mathrm{r}}(n)$.

In the simulations of soft fluctuating membranes, it is most likely that a bond will have one neighbor bound, at low binding affinities or bond densities ($\bar{\phi} = 0.06$) . However, the probability that the bond will have more than one neighbor is considerably larger than in the system with randomly distributed bonds, and the likelihood of appearance of a bond with four neighbors is more than 1000 times larger (bottom right panel in figure 4). As the binding affinity and the density of bonds increase, the most likely number of bound neighbors increases gradually. However, the difference in the distribution of neighbors between the simulated and the random system gradually decreases, consistent with the decrease of correlations between the bonds at larger binding affinities and mean bond densities.

4. Instantaneous membrane roughness and the coordination of bonds

For a deformable membrane adhering in a potential with two wells, the non-specific potential will attract the membrane between the bonds inducing deformations in the vicinity of the bonds. Furthermore, membrane fluctuations produce random forces acting on each bond. These forces are of larger amplitudes if the bonds are further apart [8], which affects the overall stability of the bonds. Obviously, if the bonds are confined into a domain, the membrane fluctuations are minimized within the domain, which may in turn stabilize the agglomerate. It is thus pertinent to study the roughness of the membrane in order to understand the correlations between the bonds. We first calculate the instantaneous membrane roughness as a function of the instantaneous density of bonds given by

$$\left(\xi^{\perp}(\phi)\right)^2 \equiv \frac{\sum_i (\xi_i^{\perp})^2 \delta(\phi_i - \phi)}{\sum_i \delta(\phi_i - \phi)}, \tag{6}$$

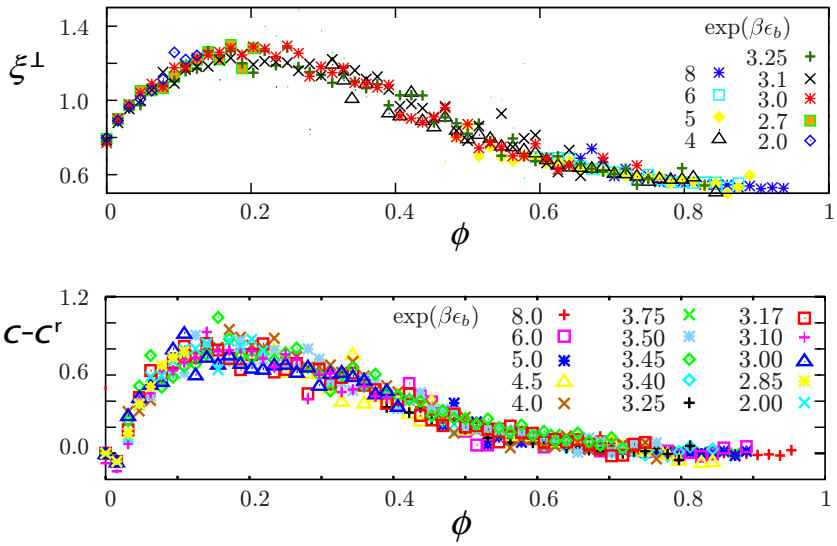

Figure 5. Top: the membrane roughness $\xi^{\perp}(\phi)$ as a function of the bond density for several binding affinities. The limiting values of roughness, $\xi^{\perp}(0) = (64\gamma\kappa)^{1/4} = 0.84$ and $\xi^{\perp}(1) = (64\,K\rho\kappa)^{1/4} = 0.52$, are accurately reproduced. Bottom: the excess coordination number $c(\phi) - c^{\mathrm{r}}(\phi)$ as a function of the bond density. Comparison of both panels reveals that both $\xi^{\perp}(\phi)$ and $c(\phi) - c^{\mathrm{r}}(\phi)$ follow master curves that mutually show the same trends.

with the instantaneous roughness $\xi_i^{\perp}$ calculated according to

$$(\xi_i^{\perp})^2 \equiv \langle h_i(\mathbf{r})^2 \rangle - \langle h_i(\mathbf{r}) \rangle^2. \tag{7}$$

Likewise, in order to understand how the domain formation is related to the instantaneous density of bonds and the roughness of the membrane, the excess coordination number for a certain density is determined as

$$c(\phi) - c^{\mathrm{r}}(\phi) \equiv \frac{\sum_i (c_i(\phi) - c^{\mathrm{r}}(\phi))\delta(\phi_{\mathrm{i}} - \phi)}{\sum_i \delta(\phi_i - \phi)}. \tag{8}$$

The delta function in the above definitions takes care that the time average is made only over those i's (i.e. frames) for which at t_i the number density of bonds is equal to the selected ϕ.

In figure 5,[4] the roughness $\xi^{\perp}(\phi)$ and the excess coordination $c(\phi) - c^{\mathrm{r}}(\phi)$ are shown for several intrinsic binding strengths ϵ_{b} in the top and the bottom panel, respectively. The most striking feature in these graphs is that all data follow master curves, and the dependence on the intrinsic binding strength falls within the spread of data points belonging to a curve associated with a particular ϵ_{b}. Furthermore, the master curves show very similar trends. Specifically, the roughness of the membrane increases until $\phi \simeq 0.2$, upon which a decrease in roughness as a function of the bond density takes place. This clearly suggests that correlations between bonds and the instantaneous roughness are interrelated through the instantaneous number of bonds.

[4] For small and large binding affinities, realizations with a very large or very small number of bonds, respectively, may be rarely found. In these cases, there were not suffincient data for averaging over the number of such realizations and hence these parts of the curves have not been shown.

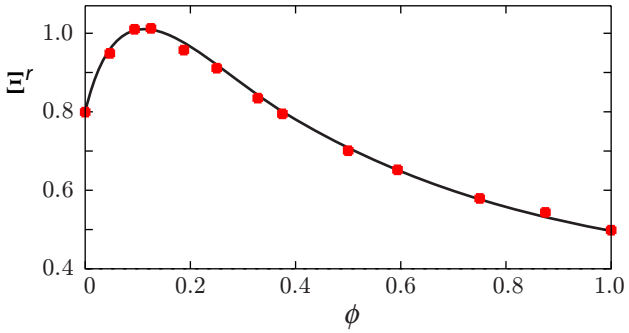

Figure 6. Random roughness Ξ^{r} as a function of the density of randomly distributed bonds ϕ.

Such an analogy of behavior in the excess coordination of bonds and the roughness $\xi^{\perp}$ shows that there is a certain connection between these two properties of the system. It is consistent with the observation that at low binding strengths the probability that a bond has a large number of neighbors is significantly bigger than in the random system, as shown in figure 4. This suggests that even at low affinity the bonds correlate to form unstable, short-lived domains. Furthermore, the deformations of the tethers are also insensitive to the intrinsic binding strength (data not shown). Consequently, if one fixes the density of bonds, the morphology of the bound membrane is dependent on ϵ_{b} to a very little extent. The binding strength acts only to set the statistical probability for the appearance of certain bond densities.

5. Equilibrium membrane roughness and fluctuations in bond density

The equilibrium membrane roughness $\bar{\Xi}^{\perp}(\bar{\phi})$, which should be distinguished from the instantaneous roughness $\xi^{\perp}(\phi)$ discussed above, arises from the long-time behavior of the system, as a property averaged over both time and spatial coordinates of the membrane profile. To explore how this roughness $\bar{\Xi}^{\perp}$ depends on the system parameters, we choose an experimentally accessible definition

$$\left(\bar{\Xi}^{\perp}(\bar{\phi})\right)^2 \equiv \frac{\sum_i \langle h_i(\mathbf{r})^2\rangle - \bar{h}^2}{\sum_i 1}. \tag{9}$$

Here $\bar{h}$ is the overall mean height of the membrane (figure 3) and $\bar{\Xi}^{\perp}$ is evaluated directly from the simulations.

In order to compare the equilibrium mean roughness with the random roughness $\Xi^{\mathrm{r}}(\phi)$ (figure 6), the latter first had to be evaluated. Therefore, for each bond density ϕ, 1000 membrane configurations with randomly distributed bonds have been generated. We calculate the mean roughness from this set of 1000 realizations according to equation (9), except that now index i enumerates different random configurations.

We investigate the ratio $\bar{\Xi}_{\perp}/\Xi^{\mathrm{r}}$. Inspection of the top panel in figure 7 shows that this ratio is always larger than unity, signifying that, like the correlations, the equilibrium roughness of the membrane is always larger than in the system with randomly distributed bonds. From the point of view of the argument that the bonds have a tendency to form domains, such increased roughness is intuitively an unexpected result. Within domains, the membrane fluctuations (hence

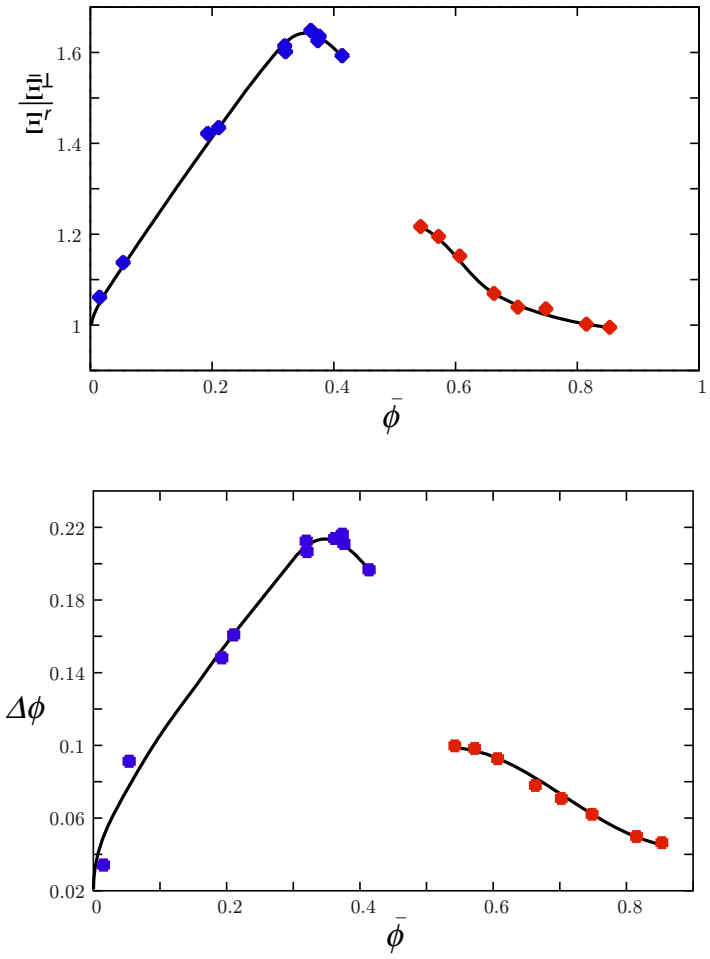

Figure 7. The mean equilibrium roughness of the membrane relative to the roughness of the membrane with a random bond distribution $\bar{\Xi}^{\perp}/\Xi^{\mathrm{r}}$ (top) and the deviation from the mean density of bonds $\Delta\phi$ (bottom) as a function of the mean bond density $\bar{\phi}$.

roughness) are supposedly suppressed, which in turn could lead to a decreased roughness with respect to the random distribution of bonds.

The understanding of the obtained results, however, emerges from re-inspecting figure 3. Generally, for a fixed binding strength, the instantaneous bond density ϕ_{i} adopts values in a certain range around the mean bond density $\bar{\phi}$, where $\bar{\phi}(\epsilon_{\mathrm{b}})$ was shown previously (left panel in figure 3). As the mean density of bonds changes (due to the variation of ϵ_{b}), the attained range of ϕ_{i}, e.g. the intensity of deviations $\Delta\phi$ from the mean equilibrium density of bonds, defined as

$$\left(\Delta\phi(\bar{\phi})\right)^2 \equiv \frac{\sum_i(\phi_i-\bar{\phi})^2}{\sum_i 1}, \tag{10}$$

differs significantly (right panels in figure 3). However, every ϕ_i contributes to $\bar{\Xi}^{\perp}$ through a membrane profile of a characteristic roughness $\xi^{\perp}$ (figure 5). Consequently, large deviations from the mean equilibrium density of bonds lead to large variations in the instantaneous

roughness $\xi^{\perp}$, which in turn affect the average equilibrium roughness $\bar{\Xi}^{\perp}$. It is thus evident that the intensity of fluctuations in the equilibrium density has an impact on the overall equilibrium roughness $\bar{\Xi}^{\perp}$. Indeed, a remarkable resemblance in behavior of $\bar{\Xi}^{\perp}/\Xi^{r}$ and $\Delta\phi$ can be seen by comparison of the two panels in figure 7.

A more detailed analysis of $\xi^{\perp}$ in figure 5 confirms the above reasoning. At small mean bond density or binding strength ϵ_b (the unstable branch in figure 3), the $\xi^{\perp}(\phi)$ curves do not extend far from $\phi = 0$, which allows only for small deviations $\Delta\phi$. Nevertheless, the fluctuations are large relatively to $\bar{\phi}$ ($\Delta\phi/\bar{\phi}$ is considerable) and $\bar{\phi}$ badly represents the instantaneous ϕ_i (see lower panels on the right in figure 3). As ϵ_{b} increases to intermediate values, ϕ_{i} assumes almost all values between zero and unity. It is in this regime that $\bar{\Xi}^{\perp}$ as well as $\Delta\phi$ are maximal. For ϵ_{b} at which the unstable branch approaches the transition point, the conformations with a large number of bonds somewhat occur more frequently, leading to a slight decrease in both $\Delta\phi$ and $\bar{\Xi}^{\perp}/\Xi^{\mathrm{r}}$.

In the stable branch, $\bar{\phi}$ well characterizes the system at any instance of time (see right upper panels in figure 3). The fluctuations in the density of bonds are less intense than in the unstable branch, as ϕ never reaches zero. As the bonds forming the adhesion domains are strengthened by the increasing binding strength of the ligand–receptor pair, $\Delta\phi$ decreases even more. The equilibrium mean roughness reflects this behavior very well. Ultimately, when the mean density $\bar{\phi}$ reaches unity, the distribution of bonds does not differ from a random one and $\bar{\Xi}^{\perp}/\Xi^{\mathrm{r}} = 1$. Similarly, when there is on average one or fewer bonds formed ($\bar{\phi} \to 0$), a random configuration cannot be distinguished from any other configuration and $\bar{\Xi}^{\perp}/\Xi^{\mathrm{r}}$ reaches unity as well. In this regime, the deviations from the mean density of bonds reduce to zero.

6. Conclusions

The work presented herein shows that the role of fluctuations in membrane adhesion is twofold. On the one hand, the fluctuations decrease the overall adhesiveness of membranes and a larger effective binding affinity must be involved to obtain the same member of bonds as in non-fluctuating membranes. On the other hand, membrane roughness is intimately associated with positive correlations between the bonds simply because the latter drive the formation of domains. If the effective binding affinity (the mean contribution of a bond to the free energy) is such that the formation of a bond decreases the total energy, domains are stable. In this regime, the equilibrium roughness is small, and the correlations between the bonds, although positive, decay toward zero with increasing the mean density of bonds. However, the correlations between the bonds are very important in the regime of unstable specific adhesion where the number of formed bonds within the domain fluctuates significantly and the entire domain occasionally unbinds. In this case, equilibrium roughness of the membrane is significantly larger than the roughness of a membrane with no bonds or with randomly distributed bonds.

Since the instantaneous roughness reflects the instantaneous size of the domains, it should be, moreover, possible to use fluctuations as an imaging tool. This would be particularly useful in optical techniques where the lateral resolution of the order of 100 nm is still too large to observe individual bonds. However, local fluctuations of the membrane can be measured accurately. Corroborated by our predictions, membrane roughness in equilibrium could be, in principle, mapped onto the density of bonds within the domain.

It was recently shown experimentally that mobility of ligands and receptors furthermore affects the distribution of bonds within domains [27–29], where an increase of fluctuations

have been observed in the process of the formation of the nucleation center [29]. Mobility certainly provides an additional entropic contribution to the free energy of the system. The current results are relevant to the situation in which one of the binding partners is immobilized (typically the receptors on the substrate), and the other binding partner is abundant in the opposing membrane (as in [4])—e.g. a high-density regime. Furthermore, the results discussed herein should be relevant for systems in which the diffusion time scale is much larger than the reaction time scale—a very-low-density regime that also has biological implications. However, the true impact of the diffusion remains to be elucidated quantitatively, in simulations and by other theoretical methods, particularly from the point of view of the relation between membrane roughness and correlations between bonds, revealed here as an essential feature of specifically adhering membranes.

Acknowledgments

We thank E Sackmann, K Mecke, T Speck and D Smith for helpful discussions and K Sengupta and S Fenz for critically reading the manuscript. US and A-SS acknowledge support from the Deutsche Forschungsgemeinschaft under grant no. DFG-SE 1119/2-1.

Appendix: Simulation scheme

The formation of each bond is associated with a binding k_{on} and an unbinding k_{off} rate whose ratio is given by the ratio of Boltzmann weights for bound and unbound states in equilibrium equation (1). This is equivalent to the locally fulfilled detailed balance condition

$$\frac{k_{\mathrm{off}}}{k_{\mathrm{on}}} = \exp\left[\beta\left(\frac{K}{2}(h(\mathbf{r}_j) - l_0)^2 - \epsilon_b\right)\right]. \tag{A.1}$$

Accordingly, the formation of the bond is associated with the intrinsic enthalpic gain ϵ_{b}, the so-called intrinsic binding strength, whereas the deformation of the tether from its rest length l_0 is determined by the spring constant K. Modeling of reaction rates takes into account the force that is exerted on the bond through the extension of the spring [18, 25, 26], leading to their height dependence

$$k_{\mathrm{off}} = k_0 \exp\left[\beta K \alpha \left(h(\mathbf{r}_j, t) - l_0\right)\right], \tag{A.2}$$

where k_0 is the reaction rate if the tether is not stressed, and α is of the order of the range of the binding potential. Using equation (A.1) the expression for the binding rate k_{on} emerges as

$$k_{\mathrm{on}} = k_0 \mathrm{e}^{\beta\epsilon_b} \exp\left[\beta K (h(\mathbf{r}_j, t) - l_0)\left(\alpha - \frac{h(\mathbf{r}_j, t) - l_0}{2}\right)\right]. \tag{A.3}$$

Since both rates are time-dependent exponential functions of the local membrane height, the farther away the membrane is from the substrate the more likely it is that a bond ruptures and the less likely that a bond forms. When ligand–receptor recognition takes place in solution, k_{on} and k_{off} are constants, and the binding affinity is defined as $E_{\mathrm{a}} = \ln[k_{\mathrm{off}}/k_{\mathrm{on}}]$. In the case of adherent membranes, both the binding and the unbinding rates become associated with distributions and the binding affinity of a bond is given by equation (2).

The equation of motion for the membrane shape configuration associated with the energy given in equation (1) is given by [22]

$$\frac{\partial h(\mathbf{k},t)}{\partial t} = \xi(\mathbf{k}) - \Lambda(\mathbf{k}) \left\{ \left[\kappa k^4 + \gamma\right](h(\mathbf{k},t) - \delta_{\mathbf{k},0} A\, h_0) + \sum_{j=1}^{N_t} b_j K(h(\mathbf{r}_j,t) - l_0) \mathrm{e}^{-\mathrm{i}\mathbf{k}\cdot\mathbf{r}_j} \right\}. \tag{A.4}$$

Here, the Fourier transform is performed according to

$$h(\mathbf{k}) = \int_A \mathrm{d}^2\mathbf{r}\, \mathrm{e}^{-\mathrm{i}\mathbf{k}\cdot\mathbf{r}} h(\mathbf{r}); \quad h(\mathbf{r}) = \frac{1}{A}\sum_{\mathbf{k}} \mathrm{e}^{\mathrm{i}\mathbf{k}\cdot\mathbf{r}} h(\mathbf{k}). \tag{A.5}$$

In equation (A.4) $\xi(\mathbf{k})$, the stochastic force providing thermal fluctuations of the membrane, and $\Lambda(\mathbf{k})$, the Onsager coefficient, are related via the fluctuation–dissipation theorem

$$\langle \xi(\mathbf{k})\xi(\mathbf{k}')\rangle = 2k_\mathrm{B}T\,\Lambda(\mathbf{k})\delta(\mathbf{k}+\mathbf{k}'). \tag{A.6}$$

It was shown previously [23] that the Onsager coefficient depends on the mean distance between the membrane and the substrate. However, for the parameters used herein, this distance is sufficiently large and only the four smallest **k**-modes are affected appreciably, a result emerging from the comparison of simulations with the full treatment of hydrodynamic interactions with the current setup. For simplicity, only the hydrodynamic interactions between the solvent (of viscosity η) and the membrane are taken into account: $\Lambda(\mathbf{k}) = 1/(4\eta k)$, where $k \equiv |\mathbf{k}|$ and $k > 0$, whereas the interaction with the wall has been neglected. On the same level of approximation, for the $k = 0$ mode, which describes the mobility of the center of mass of the membrane, the Onsager coefficient is set to $\Lambda(\mathbf{k}=0) = 3\sqrt{A}/(8\pi\eta)$ [24]. In any case, averaged properties of the system do not depend on the treatment of hydrodynamic interactions.

The membrane shape is evolved by discretely integrating the Langevin equation (A.4) in time with a constant time step Δt on a square lattice [8, 22]. Following each membrane step, the configuration of all receptor–ligand pairs is updated where an existing bond is broken with the probability $k_\mathrm{off}\Delta t$, while a bond is formed with the probability $k_\mathrm{on}\Delta t$. As can be seen from equations (A.2) and (A.3), the typical time scale for these events is set by the reaction rate k_0. The initial configuration for each run is a membrane with no bonds placed at $h = 12a$ and at least the first 10 ms were used for the equilibration and a production run was carried out for another 50 ms. The data are written out every 0.05 ms, which in total provides 1000 configurations for analysis.

References

[1] Smith A-S and Sackmann E 2009 *ChemPhysChem* **69** 1969
[2] Dustin M L 2007 *Curr. Opin. Cell Biol.* **19** 529
[3] Sackmann E 1996 *Science* **271** 43
[4] Lorz B G, Smith A-S, Gege C and Sackmann E 2007 *Langmuir* **23** 12293
[5] Cuvelier D and Nassoy P 2004 *Phys. Rev. Lett.* **93** 228101
[6] Rädler J O, Feder T J, Stray H H and Sackmann E 1995 *Phys. Rev.* E **51** 4526
[7] Limozin L and Sengupta K 2010 *Phys. Rev. Lett.* **088101** 104
[8] Reister-Gottfried E, Sengupta K, Lorz B, Sackmann E, Seifert U and Smith A-S 2008 *Phys. Rev. Lett.* **101** 208103
[9] Tanaka M and Sackmann E 2005 *Nature* **7059** 656

[10] Bruinsma R and Sackmann E 2001 *C. R. Acad. Sci.* IV **2** 803
[11] Bruinsma R, Behrisch A and Sackmann E 2000 *Phys. Rev.* E **61** 4253
[12] Lipowsky R 1996 *Phys. Rev. Lett.* **77** 1652
[13] Weikl T R and Lipowsky R 2001 *Phys. Rev.* E **64** 011903
[14] Zuckerman D and Bruinsma R 1995 *Phys. Rev. Lett.* **74** 3900
[15] Krobath H, Schütz G J, Lipowsky R and Weikl T R 2007 *Europhys. Lett.* **78** 38003
[16] Weikl T R, Netz R R and Lipowsky R 2000 *Phys. Rev.* E **62** R45
[17] Brochard-Wyart F and de Gennes P G 2002 *Proc. Natl Acad. Sci. USA* **99** 7854
[18] Weikl T R, Andelman D, Komura S and Lipowsky R 2002 *Eur. Phys. J.* E **8** 59
[19] Bruinsma R, Goulian M and Pincus P 1994 *Biophys. J.* **67** 746
[20] Speck T, Reister E and Seifert U 2010 *Phys. Rev.* E **82** 021923
[21] Lipowsky L and Leibler L 1986 *Phys. Rev. Lett.* **56** 2541
[22] Reister-Gottfried E, Leitenberger S M and Seifert U 2007 *Phys. Rev.* E **75** 011908
[23] Seifert U 1994 *Phys. Rev.* E **49** 3124
[24] Lin L C-L and Brown F L H 2004 *Biophys. J.* **86** 764
[25] Bell G I 1978 *Science* **200** 618
[26] Hänggi P, Talkner P and Borkovec M 1990 *Rev. Mod. Phys.* **62** 251
[27] Smith A-S, Fenz S and Sengupta K 2010 *Euro. Phys. Lett.* **89** 28003
[28] Fenz S, Merkel R and Sengupta K 2009 *Langmuir* **25** 1074
[29] Smith A-S, Sengupta K, Goennenwein S, Seifert U and Sackmann E 2008 *Proc. Natl Acad. Sci. USA* **105** 6906

P2

Switching from Ultraweak to Strong Adhesion

Switching from Ultraweak to Strong Adhesion

Susanne F. Fenz[1,2], Timo Bihr[3], Rudolf Merkel[2], Udo Seifert[3], Kheya Sengupta[4] and Ana-Sunčana Smith[5]

[1] Institute of Complex Systems 7: Biomechanics Forschungszentrum Jülich GmbH, 52425 Jülich, Germany
[2] Leiden Institute of Physics, Leiden University, 2333 CA Leiden, The Netherlands
[3] II. Institute of Theoretical Physics, University of Stuttgart, 70550 Stuttgart, Germany
[4] CNRS UPR 3118, Centre Interdisciplinaire de Nanosciences de Marseille Aix-Marseille Université Campus de Luminy, 13288 Marseille cedex 9, France
[5] Institute of Theoretical Physics and Excellence Cluster: Engineering of Advanced Materials and University Erlangen-Nürnberg, Germany

Advanced Materials **23** (2011) 2622–2626

DOI: 10.1002/adma.201004097
http://onlinelibrary.wiley.com/doi/10.1002/adma.201004097/abstract

Abstract Intrinsically strong avidin-neutravidin bonds can exhibit ultraweak adhesion mediated by transiently bound domains and can undergo a transition to a stable strong adhesion by locally increasing bond density.

ADVANCED MATERIALS
www.advmat.de

Materials Views
www.MaterialsViews.com

Switching from Ultraweak to Strong Adhesion

*Susanne F. Fenz, Timo Bihr, Rudolf Merkel, Udo Seifert, Kheya Sengupta, and Ana-Sunčana Smith**

Nature switches from weak to strong adhesion at the cellular level to spectacular effect – for example, for incredibly sensitive recognition and decisive action during immune response.[1] If realized in an artificial system, such a switching could one day be harnessed as a powerful tool to manipulate weakly interacting objects. The first step towards realizing such a system involves understanding how to create and detect ultraweak adhesion and how to then switch-on a strong interaction. So far, in the context of model membranes, weak adhesion has been achieved only with a ligand-receptor of intrinsically low binding affinity.[2] Whatever, the intrinsic strength of the bonds, so far they were usually found to be arranged in compact stable domains.[3] Here, we present experiments and simulations that indicate how to create and detect ultraweak adhesion in the context of fluid two dimensional membranes interacting via specific ligand/receptor bonds. Thus, specific adhesion is mediated by transient domains consisting of sparsely distributed bonds. Amazingly, we demonstrate that the avidin/biotin pair – famous for forming the strongest receptor/ligand bond known in nature, mediates ultraweak adhesion under suitable circumstances. This choice of binders allows us to switch on strong binding once sensitive detection is achieved – without resorting to a second binding pair – something not possible with intrinsically weak binders. However, this goal necessitates an appropriate design strategy elaborated below.

The in vitro system consists of two membranes: a solid supported lipid bilayer (SLB) and the freely fluctuating membrane of a giant unillamelar vesicle (GUV). A GUV is a two dimensional membrane enclosing a fluid and immersed in a fluid. Various kinds of synthetic vesicles have been fabricated, the best known being liposomes made from artificial lipids.[4] These, along with more recently discovered polymersomes made from di-block co-polymers[5] and dendrimersomes made from janus dendrimers,[6] are finding their way into various applications, in particular as carriers in drug delivery. We choose to work with liposomes that are the softest and closest to natural cell membranes[3] but the general concepts apply to any unilamellar vesicle.

When two membranes are at finite distances, omnipresent physical forces combine to produce a homogeneous nonspecific interaction potential.[7] The forces arise from gravity, Coulomb and van der Waals interactions as well as the steric repulsion produced by vesicle membrane fluctuations.[8] In our system fluctuations are very important since the vesicle membrane is soft (bending modulus = 20 k_BT,[9] k_B being the Boltzmann constant and T the temperature) and non-tense. In order to keep the non-specific potential very weak, standard methods to screen the van der Waals attraction of the glass were used.[10] In addition, lipid-anchored PEG was added to the vesicle to further hinder direct contact of the two membranes. Under such circumstances the GUV near the SLB deforms to make a contact zone in which the two membranes are essentially parallel and interact very weakly. In our case, non-specific interactions lead to a contact zone in which the mean intermembrane distance is 95 nm and the GUV membrane roughness, defined as a standard deviation from the mean height is about 8 nm.

To effectuate specific adhesion, the ligand biotin was incorporated into the membrane of both the GUV and the SLB. Since biotin does not recognize itself, the receptor neutravidin is allowed to bind specifically to the SLB. This interaction is a basically irreversible (biotin-neutravidin binding is one of the strongest and most stable in nature – intrinsic binding strength $\nu_0 = 35\ k_BT$). Upon deposition to SLB, neutravidin still has two binding sites that are exposed to the biotin on the GUV. Such a setup was previously used to establish strong vesicle adhesion by formation of domains with densely packed bonds.[9–12] However, it has been suggested recently that the mean density of binders confined to fluctuating surfaces considerably affects the binding affinity of the pair[13] leading to effectively smaller affinities at low binder densities. Furthermore, sparse arrangements of bonds have been reported in adhesion assays in which both binders were mobile prior to the establishment of the bond.[14,15] Precisely by tailoring very dilute domains, we target ultraweak specific adhesion.

In constructing a system with ultraweak specific adhesion, the true challenge lies in the imaging of dilute domains which are also expected to be very dynamic. New super-resolution

Prof. Dr. A.-S. Smith
Institute of Theoretical Physics and Excellence Cluster: Engineering of Advanced, Materials
University Erlangen-Nürnberg, Germany
E-mail: smith@physik.uni-erlangen.de
Dr. S. F. Fenz,[†] Prof. Dr. R. Merkel
Institute of Complex Systems 7: Biomechanics
Forschungszentrum Jülich GmbH, 52425 Jülich, Germany
T. Bihr,[†] Prof. Dr. U. Seifert
II. Institute of Theoretical Physics
University of Stuttgart
70550 Stuttgart, Germany
Dr. K. Sengupta
CNRS UPR 3118, Centre Interdisciplinaire de Nanosciences de Marseille
Aix-Marseille Université Campus de Luminy
13288 Marseille cedex 9, France
Dr. S. F. Fenz[†]
Current address: Leiden Institute of Physics, Leiden University
2333 CA Leiden, The Netherlands
[†] S.F.F. and T.B. have contributed equally to this work.

DOI: 10.1002/adma.201004097

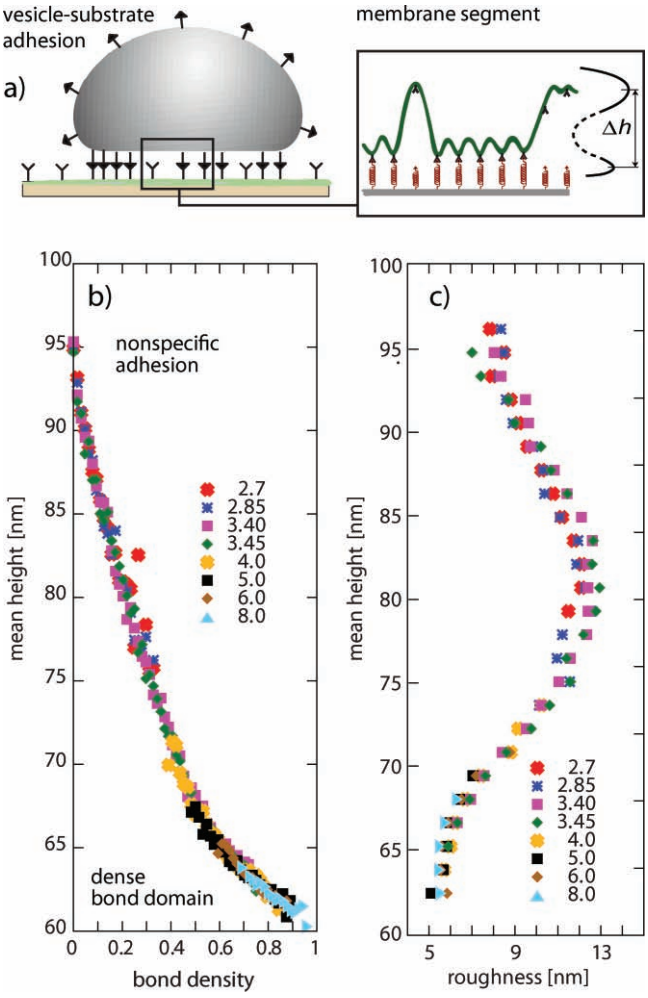

Figure 1. a) GUV adhering to SLB by formation of numerous ligand-receptor bonds. b,c) Master curves for the bond density and membrane roughness as a function of the mean height of the membrane patch simulated in equilibrium. A variety of symbols are for different ligand-receptor binding strengths $\exp(\nu_0/k_BT)$. For each ν_0 only a section of the master curves is available in equilibrium.

microscopes are capable of detecting very small clusters of fluorescently labelled proteins but lack the time resolution to detect transient domains.[16] On the other hand, dynamic FRET imaging[17] which may have the required time resolution, is currently not achievable on the single bond level. We therefore use fluctuation contrast microscopy or Dy-RICM that can detect subtle differences in fluctuations in order to give information on bonds.[15]

When specific binding takes place, the interaction potential develops a deep "specific" minimum at an intermembrane distance of about 8 nm corresponding to the size of the neutravidin-biotin complex. At the location of the bond the membrane is pulled close to the substrate into the specific minimum (**Figure 1**a). If a compact array of bonds forms, it freezes all membrane fluctuations. However, the fluctuation behavior of a membrane pinned by a dilute array of bonds is not a priori known. In fact, at low density of bonds, the membrane between the bonds is pushed away from the substrate towards the minimum of the nonspecific potential. The extent of this deformation depends on the density of bonds and affects their stability. Furthermore, fluctuations in very sparse domains are expected to produce considerable entropic pulling forces which only strong bonds can sustain. In addition, overall membrane roughness seems to be related to the density of bonds.[18] On a level of a single bond these effects are captured by an effective, density-dependent binding affinity that is typically smaller than the intrinsic binding strength of the pair ν_0.[13]

To find the relation between the membrane roughness and the number of formed bonds, we constructed the analog of the experimental situation in silico and performed a set of Langevin simulations[13–19] of an adhered membrane segment of a size 0.6 μm × 0.6 μm, where we varied ν_0 (e.g., the stability of bonds). It was shown previously by similar simulations that such modeling can reproduce the measured topography of an adherent membrane[20] as well as the dynamics of adhesion.[13] We simulate the vesicle membrane as a fluctuating surface of appropriate bending stiffness placed in a nonspecific harmonic potential at a given distance from the supported membrane, all three parameters being chosen in accordance with experimental values. The bonds are allowed to form at predefined positions and serve to pin the membrane to the substrate (Figure 1a). Each bond is given a binding and an unbinding rate that depend on the instantaneous intermembrane distance at the position of the bond. In order to obtain the equilibrium within a time accessible to simulations, the relative distance between the non-specific and the specific minimum (Δh) was decreased from the experimental value of 100 nm to 40 nm. This, together with the choice to predefine the positions of the bonds, has a side-effect that intrinsic binding strengths had to be scaled to lower values comparing to those in vitro in order to observe unbinding events.

Since each bond has a finite life time, we find that the number of formed bonds fluctuates in time around a characteristic mean value following a Gaussian distribution.[21] In case that the effective binding affinity is large, the fluctuations in the number of bonds are small, hence the lifetime of a bond, is large.[19] The bonds are packed close together and form domains which never unbind completely. The mean height and roughness are low while the density of bonds is high (e.g., data for $\exp(\nu_0/k_BT) > 4$ in Figure 1b,c). If the effective binding affinity is so low that the binding events are very rare, fluctuations in the number of bonds are again very low (data not shown). In this case bonds have very short lifetimes and the membrane is at large mean heights, while the roughness of the membrane is determined by the stiffness of the membrane and the nonspecific potential (e.g., $\exp(\nu_0/k_BT) < 2.85$).

For intermediate effective affinities, the fluctuations in the number of bonds are surprisingly the largest. In this regime domains of bonds are formed, then dissolved and reformed spontaneously, signifying that the specific adhesion takes place but is unstable – ultraweak. As the number of bonds changes, the instantaneous membrane topography changes too. This can be seen in Figure 1b where the number of bonds increases uniformly while the mean height of the membrane decreases. A stunning observation is that data for all intrinsic binding strengths follow the same master curve. This indicates that the space-averaged intermembrane distance of specifically bound

ADVANCED MATERIALS
www.advmat.de

Materials Views
www.MaterialsViews.com

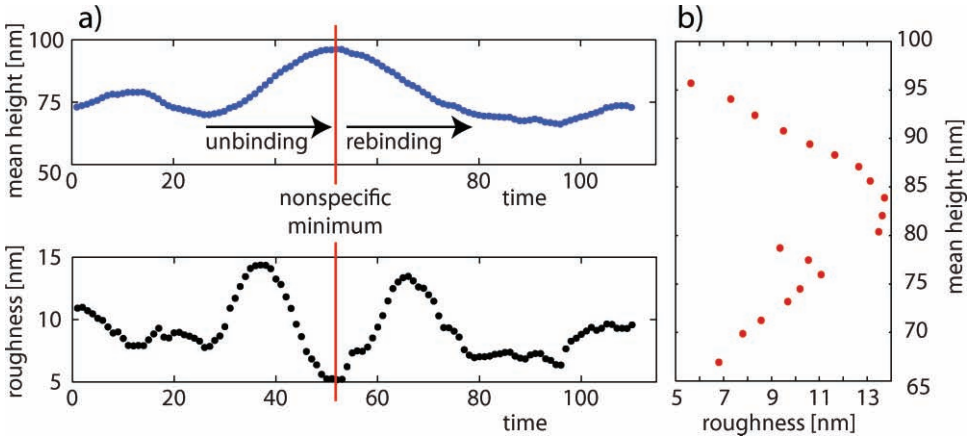

Figure 2. Transient domain from experiments. a) Time evolution of the mean height and roughness within the domain of size 0.4 μm × 0.6 μm. Time is given by the window index. b) Reconstructed master curve for the roughness. Error in the height arises from shot-noise and is about 4 nm for all heights. Error in the roughness, arising from shot-noise as well as binning, peaks to about 5 nm between 75 and 80 nm height. For details see the Methods.

membranes can be unambiguously related to the number of bonds that pin them together.

The membrane roughness (Figure 1c), which is defined as the average root mean square deviation from the average local height of the membrane within the patch is another relevant parameter which describes its topography. A striking realization is that roughness, like the bond density, follows a master curve as a function of the mean height, which means that roughness too can be related to the number of bonds. However, roughness has a non-monotonic dependence on the height of the membrane, a feature that arises from the specificity of adhesion.[19] Consequently, the relation between the bond density and the mean height, as well as that between the membrane mean height and its roughness can be exploited experimentally. This is particularly important because now there is no need for direct visualization of bonds: the ultraweak adhesion can be detected by monitoring the membrane mean height and roughness (**Figure 2**).

We now turn once more to the experiments. In a typical intermembrane contact zone (area about 100 μm^2), at any given time, there are usually several transient domains (sized 0.5–5 μm^2). The intermembrane distance in these domains vary indicating that the bond density in the domain varies. A typical development of a transient domain is shown in Figure 2a. As expected, the mean height of the domain changes considerably during its life-time. Simultaneously, the roughness of the membrane shows the expected non-monotonic behavior. In particular, as the domain in Figure 2 starts to unbind at t = 28 (time in window index- see Methods), the distance from the SLB starts to increase until the minimum of the nonspecific potential, positioned at 95 nm, is reached at t = 57. We expect that at this stage most bonds are lost. During the unbinding, the roughness of the membrane starts to rise until the height of 85 nm was attained, but then as indicated in the simulations, the roughness begins to decrease while the domain continues to unbind and the membrane height increases beyond 85 nm. Immediately after the membrane reaches the maximum height, the bonds start to reform. Consequently the membrane height decreases from 95 nm back to 75 nm. As the height of 85 nm is crossed the roughness shows again its maximum value. From the data presented in Figure 2a, we constructed the master curve that relates the roughness to the mean height of the domain (Figure 2b) that qualitatively very well resembles the simulation curve shown in Figure 1c.

While the binding and unbinding of small transient domains occurs over the entire contact zone, sometimes the bond density in a small patch (1–2 μm^2) may reach very large values which then considerably reduces the intermembrane distance (**Figure 3**). Such a patch may act as a nucleation center from which a larger domain of densely packed bonds may eventually grow, and the switch to strong adhesion may take place. The domain shown in Figure 3, at an arbitrarily chosen zero time, was located in the unspecific minimum and fluctuated strongly (right column). Eventually, the whole patch was transferred to the specific minimum at 8 nm and fluctuations were frozen (left column), thus forming a stable domain. At an intermediate stage however, it is seen that the height of the membrane decreases, indicating that it is pulled closer to the substrate due to bond formation but this is accompanied by a dramatic increase in the fluctuations (middle rows). In some cases the incipient nucleation center fails and the final state is then again where the membrane patch resides in the unspecific minimum. Fundamentally the same dependence of the roughness on the mean height of the patch has been now obtained as in the case of unstable domains, the only difference being the much larger range of accessed heights.

To summarize, we have combined simulations and experimental results to show that intrinsically strong bonds can exhibit ultraweak adhesion mediated by transiently bound domains and can undergo a transition to a stable strong adhesion by locally increasing bond density. Our simulations unambiguously relate the mean height and the roughness to the number of formed bonds within a domain. The signature of ultraweak adhesion is in the form of a maximum roughness at intermediate heights between the unbound and the strongly bound state of the membrane. We have identified the same signature in experiments and successfully related the change in roughness to the formation of bond domains. This procedure thus also provides the means to

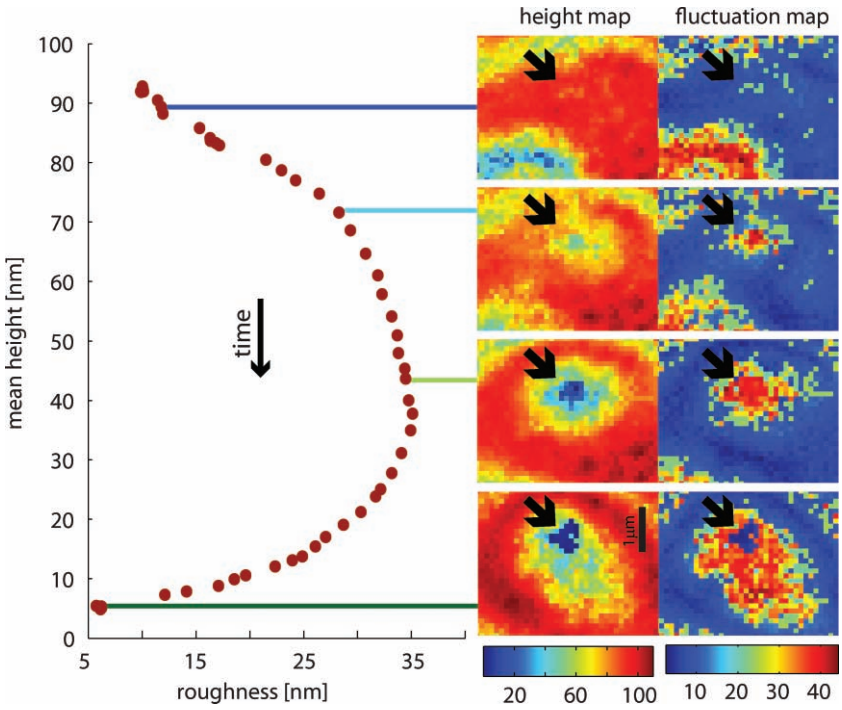

Figure 3. Nucleation center. Roughness as a function of the mean height. Different points in the curve are connected to associated height and fluctuation maps. The black arrows point to the nucleation cluster. The error bars are 4 nm. For details see *Methods*.

visualize nascent domains that are otherwise not detectable with the standard RICM technique. While our experiments were carried out in a model system, recent observation of cell-membrane fluctuations just prior to adhesion[22] may be an indication that the same signature can be found in cell adhesion.

The main difference between the simulations and experiments presented here arise from the fact that the former model interaction between two finite membranes, whereas in the latter, the interaction is between a finite vesicular membrane and an essentially infinite supported membrane that serves as source of binders penetrating into the contact zone. As a result, a patch of the membrane bound in an ultraweak but transient fashion can switch to strong and stable by locally increasing the bond density. This feature could be captured in the simulations simply by creating an open boundary at the edge of the simulation box.[24] The current comparison, however, is valid because of the clear separation of the reaction time scale and the diffusion time scale in vitro. Alternatively, at the level of experiments, the supported membrane could be made finite by construction of micrometer-sized membrane corrals. A much more stimulating possibility, however, is to experimentally control the ultraweak to strong switching, for example by increasing the mobility of the binders[9] or by controlling the membrane tension externally. Such a switch could be an exciting way to harness the discriminating power of a dual strong/weak adhesive system.

Experimental Section

Experimental details: SLBs were prepared with a film balance (Nima, Coventry, UK) applying the Langmuir-Blodgett (proximal layer, pure SOPC) and Langmuir-Schäfer (distal layer, SOPC with 2 mol% DOPE-PEG 2000 and 1 mol% DOPE-cap-Biotin) techniques. All lipids are from Avanti, Alabaster, AL. After preparation SLBs were passivated with bovine serum albumin (BSA, 98% purity, Sigma, Saint Louis, MO), incubated with neutravidin (Invitrogen, Eugene, OR) in large excess, and again passivated by incubation a BSA solution. After each binding step, excess protein was removed by exchanging the buffer against protein free PBS in a series of typically ten washing steps. GUVs consisting of SOPC with 2 mol% DOPE-PEG2000 and 1 mol% DOPE-cap-Biotin were produced via electro-swelling as described before.[23]

Experimental data analysis: Movies of GUVs imaged with reflection interference contrast microscopy (RICM[24]) were recorded at 10 Hz. For each frame a pixel-by-pixel height map was reconstructed applying the multi-interface RICM height reconstruction method.[25] The fluctuation amplitude in each pixel was calculated as the standard deviation of the mean height of the pixel averaged over 20 consecutive frames (frame 1-20, frame 2-21, etc) following the procedure described in ref. [15]. The window index denotes the number of the first frame included in the time window. The mean height and the roughness of the entire domain emerge from averaging over the mean height and the fluctuation amplitude of individual pixels, respectively. Error bars arise from the shot noise level in the corresponding pixels.[15] For the construction of the master curves, the mean height of the domain was binned every 1.5 nm, and the average roughness of the bin was calculated, giving rise to an additional contribution to the error bars. Furthermore, a small error in the height reconstruction may arise from scattering by pinning centers which we expect to be negligible due to the sparse distribution of scattering centers.

Simulation details: Langevin dynamics simulations of a membrane patch with bending rigidity = 10 k_BT, T = 300 K were performed as described in refs. [13–19]. The patch contains 64 binders placed on a 640 × 640 nm square lattice. Each ligand-receptor bond is assigned binding and un- binding rates that explicitly depend on the intrinsic binding strength (ν_0 = 1–10 k_BT), and the time dependent membrane-substrate distance.[26] A parabolic membrane-substrate potential (strength 13 J/cm^4) with a minimum at h_0 = 95 nm is imposed. The adhesion-induced movement of the membrane's center of mass was carried out as disclosed in ref. [27]. The bonds are modeled as dynamic harmonic springs of rest length l_0 = 55 nm, and stiffness k = 5 × 10^{-5} N/m). To scale the total adhesion time, 2000 binding events per second at l_0 are allowed.

Simulation data analysis: Average height and roughness was calculated for each of 1000 frames upon averaging over the topography at the given instance of time. For the construction of master curves, the mean density was binned every 1/64, and the average roughness and the height of the bin was calculated. If the bin had very low statistic in terms of hits, it was not taken into account (for further details on the simulation algorithm and the determination of observables, see ref. [19]).

Acknowledgements

We thank Ellen Reister for stimulating interactions. TB, US and A-S.S acknowledge funding by the Deutsche Forschungsgemeinschaft Grant SE 1119/2-1.

Received: November 5, 2010
Published online: April 15, 2011

[1] M. L. Dustin, *Curr. Opin. Cell Biol.* **2007**, *19*, 529.
[2] a) B. G. Lorz, A.-S. Smith, C. Gege, E. Sackmann, *Langmuir* **2007**, *23*, 12293; b) Z.-H. Huang, G. Massiera, L. Limozin, P. Boullanger, M.-P. Valignat, A. Viallat, *Soft Matter* **2010**, *6*, 1948.
[3] A.-S. Smith, E. Sackmann, *Chemphyschem* **2009**, *10*, 66.
[4] E. Sackmann, *Science* **1996**, *271*, 43.
[5] B. M. Discher, Y. Y. Won, D. S. Ege, J. C. Lee, F. S. Bates, D. E. Discher, D. A. Hammer *Science* **1999**, *284*, 1143.
[6] V. Percec, D. A. Wilson, P. Leowanawat, C. J. Wilson, A. D. Hughes, M. S. Kaucher, D. A. Hammer, D. H. Levine, A. J. Kim, F. S. Bates, K. P. Davis, T. P. Lodge, M. L. Klein, R. H. DeVane, E. Aqad, B. M. Rosen, A. O. Argintaru, M. J. Sienkowska, K. Rissanen, S. Nummelin, J. Ropponen, *Science* **2010**, *328*, 1009.
[7] K. Sengupta, L. Limozin, *Phys. Rev. Lett* **2010**, *104*, 088101.
[8] W. Z. Helfrich, *Z. Naturforsch.* **1978**, *30a*, 305.
[9] S. F. Fenz, A.-S. Smith, R. Merkel, K. Sengupta, *Soft Matter* **2011**, DOI:10.1039/C0SM00550A.
[10] M. Tanaka, E. Sackmann, *Nature* **2005**, *7059*, 656.
[11] D. Cuvelier, P. Nassoy, *Phys. Rev. Lett.* **2004**, *93*, 228101.
[12] P.-H. Puech, V. Askovic, P.-G. de Gennes, F. Brochard-Wyart, *Biophys. Rev. Lett.* **2006**, *1*, 85.
[13] E. Reister-Gottfried, K. Sengupta, B. Lorz, E. Sackmann, U. Seifert, A.-S. Smith, *Phys. Rev. Lett* **2008**, *101*, 208103.
[14] A.-S. Smith, K. Sengupta, S. Goennenwein, U. Seifert, E. Sackmann, *Proc. Natl. Acad. Sci. USA* **2008**, *105*, 6906.
[15] A.-S. Smith, S. Fenz, K. Sengupta, *Europhys. Lett.* **2010**, *89*, 28003.
[16] S. W. Hell, *Nat. Methods* **2008**, *6*, 24.
[17] Y. Suna, S. I. Shopovab, C.-S. Wub, S. Arnoldc, X. Fana, *Proc. Natl. Acad. Sci. USA* **2010**, *107*, 16039.
[18] H. Krobath, G. J. Schütz, R. Lipowsky, T. R. Weikl, *Europhys. Lett.* **2007**, *78*, 38003.
[19] E. Reister, T. Bihr, U. Seifert, A.-S. Smith, *New J. Phys. 2011, 13, 025003.*
[20] L. C.-L. Lin, J. T. Groves, F. L. H. Brown, *Biophys. J.* **2006**, *91*, 3600.
[21] T. R. Weikl, D. Andelman, S. Komura, R. Lipowsky, *Eur. Phys. J. E* **2002**, *8*, 59.
[22] A. Pierres, A. M. Benoliel, D. Touchard, P. Bongrand, *Biophys. J.* **2008**, *94*, 4114.
[23] S. Fenz, R. Merkel, K. Sengupta, *Langmuir* **2009**, *25*, 1074.
[24] L. Limozin, K. Sengupta, *Chemphyschem* **2009**, *10*, 2752.
[25] C. Monzel, S. F. Fenz, R. Merkel, K. Sengupta, *ChemPhysChem* **2009**, *10*, 2828.
[26] G. I. Bell, M. Dembo, P. Bongrand, *Biophys. J.* **1984**, *45*, 1051.
[27] L. C.-L. Lin, F. L. H. Brown, *Biophys. J.* **2004**, *86*, 764.

P3

Nucleation of Ligand-Receptor Domains in Membrane Adhesion

Nucleation of Ligand-Receptor Domains in Membrane Adhesion

Timo Bihr[1], Udo Seifert[1] and Ana-Sunčana Smith[2]

[1] II. Institut für Theoretische Physik, Universität Stuttgart, Pfaffenwaldring 57, 70550 Stuttgart, Germany
[2] Institut für Theoretische Physik and the Excellence Cluster: Engineering of Advanced Materials, Universität Erlangen-Nürnberg, Nägelsbachstrasse 49b, 91052 Erlangen, Germany

Physical Review Letters **109** (2012) 258101

DOI: 10.1103/PhysRevLett.109.258101
http://journals.aps.org/prl/abstract/10.1103/PhysRevLett.109.258101

Abstract We present a comprehensive model for the nucleation of domains in membrane adhesion. We determine the critical number of bonds in a nucleus and calculate the probability distribution of nucleation time from a discrete master equation. The latter is characterized by only four effective rates, which account for cooperative effects between bonds. We validate our model by finding excellent agreement with extensive Langevin simulations. In the range of parameters typical for cell adhesion, we find the critical number of bonds to be small. Furthermore, we find a characteristic separation between the bonds at which nucleation is particularly fast, pointing to potential regulatory mechanisms that could be used to control the cell recognition processes.

Nucleation of Ligand-Receptor Domains in Membrane Adhesion

Timo Bihr,[1] Udo Seifert,[1] and Ana-Sunčana Smith[2]

[1]*II. Institut für Theoretische Physik, Universität Stuttgart, Pfaffenwaldring 57, 70550 Stuttgart, Germany*

[2]*Institut für Theoretische Physik and the Excellence Cluster: Engineering of Advanced Materials, Universität Erlangen-Nürnberg, Nägelsbachstrasse 49b, 91052 Erlangen, Germany*

(Received 11 May 2012; published 19 December 2012)

We present a comprehensive model for the nucleation of domains in membrane adhesion. We determine the critical number of bonds in a nucleus and calculate the probability distribution of nucleation time from a discrete master equation. The latter is characterized by only four effective rates, which account for cooperative effects between bonds. We validate our model by finding excellent agreement with extensive Langevin simulations. In the range of parameters typical for cell adhesion, we find the critical number of bonds to be small. Furthermore, we find a characteristic separation between the bonds at which nucleation is particularly fast, pointing to potential regulatory mechanisms that could be used to control the cell recognition processes.

DOI: 10.1103/PhysRevLett.109.258101 PACS numbers: 87.16.D−, 87.15.kp, 87.16.A−

Cell adhesion is mediated by domains consisting of ligand-receptor bonds connecting either two cells or a cell with the extracellular environment. As key elements in the machinery of the cell recognition and mechanosensing [1], domains are implicated in up and down regulation of a number of processes [2] including determining the morphology [3] and protein expression [4] of stem cells, immunological response [5], cell differentiation [6], or the control of homeostatic pressure in tissues [7,8].

Adhesion domains are commonly studied on relatively long time and length scales, whereby the overall adhesion is sensitive to the density of immobilized binders and to the stiffness of the substrate [9,10]. This sensitivity was also reflected in the structure of the actin cortex [11] and the ability of cells to generate forces [12]. These forces were found to act on adhesion domains, rendering them unstable in all but a narrow range of sizes [10,13].

Much of the current understanding of the formation of domains arises from studies of vesicles specifically binding to a substrate (for reviews, see Refs. [14,15]). Thereby, domains form spontaneously, with densely packed ligand-receptor bonds [16,17]. However, the stability of bonds at the edge of the domain, as well as the number and the morphology of domains, were found to vary most with the density of binders on the substrate [18,19], reminiscent of observations in the cellular context. These results could be explained by extensive simulations [19–21] and by theoretical modeling of both the adhesion equilibrium [21,22] and the dynamics of growth, typically long after the stable seed of the domain was formed [16,17,23–27].

On the other hand, very little is known about the nucleation stage of domain formation. The related debate has focused upon establishing the size of a stable nucleus, where the seed of a domain was typically predicted to contain a large number of bonds [25,28,29]. However, the resolution of optical microscopes has recently become such that early stages of the domain formation could be studied [13,30]. Consequently, it was suggested that membrane fluctuations play an important role, and that already a few bonds may be sufficient to form a stable seed [31].

The difficulty in modeling the nucleation [32] arises from the coupling of the deformations of the fluctuating membrane and bond association and dissociation rates [19,33]. This coupling induces density dependent correlations [21,34], promotes the formation of bonds, and enhances the stability of already formed bonds [35]. Here, we elucidate the importance of these correlations for the nucleation and arrive at a theoretical prediction for the number of bonds in a stable seed, as well as the characteristic nucleation time. We demonstrate the validity of our approach by achieving a favorable comparison with relevant simulations and available experimental data [18,31]. The related technical formalism is presented in the Supplemental Material [36].

The model.—The membrane is assumed to contain freely diffusing ligands with a concentration of ρ_l. The ligands occasionally form bonds with receptors. The latter are immobilized on the substrate in the concentration ρ_r and modeled as thermalized harmonic springs of stiffness λ and rest length l_0. A bond is created when the distance between the ligand and the receptor is in the range α of a steplike interaction potential, the depth of which is given by the binding affinity of the pair ϵ_b. By considering the entropy cost associated with the change in receptor fluctuations upon bond formation, an effective affinity $\bar{\epsilon}_b = \epsilon_b + k_B T \ln[\lambda\alpha^2/(2\pi)]/2$ is deduced.

The Hamiltonian of the system (Fig. 1) explicitly accounts for the deformation of the fluctuating membrane [34,37] and the bonds [19]. They are both parametrized by the space and time dependent height $h(\mathbf{r}, t)$ of the membrane above the substrate. Hence,

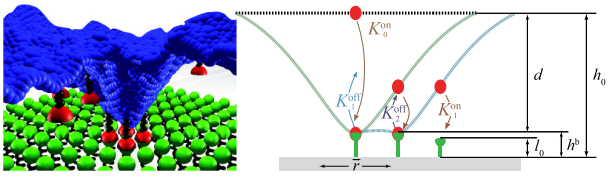

FIG. 1 (color online). Left: Snapshot of a nucleation site from a simulation. Right: Explicitly calculated membrane profiles for a seed with zero (black), one (green), and five (blue) bonds, the shapes of the latter two being nearly identical. Effective rates for the association (K_n^{on}) and the dissociation (K_n^{off}) of bonds in a growing seed are displayed.

$$\mathcal{H}[h(\mathbf{r},t)] = \int_A d^2\mathbf{r}\left\{\frac{\kappa}{2}[\nabla^2 h(\mathbf{r},t)]^2 + \frac{\gamma}{2}[h(\mathbf{r},t) - h_0]^2 + \sum_{i=1}^{N_t(t)} \delta(\mathbf{r}-\mathbf{r_i})\left[\frac{\lambda}{2}(h(\mathbf{r},t) - l_0)^2 - \epsilon_b\right]\right\}. \quad (1)$$

The Helfrich energy (first term) term describes the bending of the membrane in a harmonic potential (second term) of a strength γ with a minimum at h_0 [38]. The latter accounts for the glycocalyx and other implicit potentials (van der Waals, Coulomb, hydration...), whose role is to prevent unspecific contacts and keep the unbound membrane at a relatively large separation from the substrate [39]. The last term sums over the enthalpy of a total of $N_t(t)$ bonds formed at the set of positions $\{\mathbf{r_i}\}$. The entropy change associated with ligand diffusion during nucleation can be neglected.

The critical size of the stable nucleation seed.—In our variant of the capillarity approximation (see Supplemental Material [36]), we calculate the critical number of bonds N_c in the seed by balancing the increase in the free energy due to the membrane deformation and the decrease in binding enthalpy

$$N_c = 1 + \frac{4d^4\rho_r\gamma\sqrt{\gamma\kappa}}{\pi(\gamma d^2 - 2\bar{\epsilon}_b\rho_r)^2}. \quad (2)$$

Thereby, d is the change in height experienced by the membrane (see Fig. 1). Furthermore, we assume that all receptors within the seed are bonded [25,26] and recognize that the membrane profile (Fig. 1) associated with the formation of one bond [34,37] characterizes the shape of the moving edge in a small seed (deformation energy is proportional to the seed circumference).

Notably, N_c diverges when $\gamma d^2 = 2\bar{\epsilon}_b\rho_r$, beyond which specific adhesion is unstable. Because the receptors are immobile and ligands mobile, N_c explicitly depends on ρ_r but not on ρ_l. In the context of cell adhesion, in which active regulation can modify the local binder density, the membrane stiffness, or the glycocalyx, this result points to possible regulatory mechanisms. Under the conditions used in experiments on vesicles [18,31], Eq. (2) correctly predicts stable seeds of 2–4 bonds, depending on the affinity of the ligand-receptor pair in question (Fig. 2).

Nucleation dynamics.—The dynamics of nucleation is often addressed through the concept of the mean first passage time [40]. Thereby, one calculates the time τ for the system to evolve from the state A (no bonds), to the state B (N_c bonds). Depending on the path (the sequence of binding and unbinding events prior to the establishment of the N_cth bond), a distribution $\mathcal{P}(\tau)$ of first passage times emerges, the first moment of which is the mean first passage time or, in our case, the characteristic nucleation time $\bar{\tau}$. The corresponding master equation couples the time variation of all probabilities P_n for finding seeds with $n \leq N_c - 1$ bonds (see Supplemental Material [36]). These probabilities are primarily dependent on rates at which the bonds form and break.

The confinement of the receptors and ligands to opposing surfaces makes the association and dissociation rates, $k^{on}(h)$ and $k^{off}(h)$, dependent on the local instantaneous distance h between the two membrane [41]. By postulating local thermodynamic equilibrium for each receptor, these so-called Dembo's rates satisfy the detailed balance condition

$$\frac{k^{off}(h)}{k^{on}(h)} = \exp\left[\left(\frac{\lambda}{2}(h - l_0)^2 - \bar{\epsilon}_b\right)\right], \quad (3)$$

where we set $\beta \equiv (k_BT)^{-1} \equiv 1$. In the spirit of previous works [19,42,43], we relate k^{on} to the probability of finding a ligand and a receptor within the range of the interaction potential α, averaged over all receptor conformations

$$k^{on}(h) = k_0\sqrt{\frac{\lambda\alpha^2}{2\pi}}\exp\left[-\frac{\lambda}{2}\{(h - l_0) - \alpha\}^2\right]. \quad (4)$$

Thereby, k_0 is the intrinsic reaction rate (the inverse of the attempt frequency). The local unbinding rate k^{off} follows from the detailed balance equation (3) and is explicitly dependent on the effective binding affinity $\bar{\epsilon}_b$.

The time scale k_0^{-1} typical for binding and unbinding of a bond sets the time scale at which a membrane shape-profile associated with a particular configuration of n bond

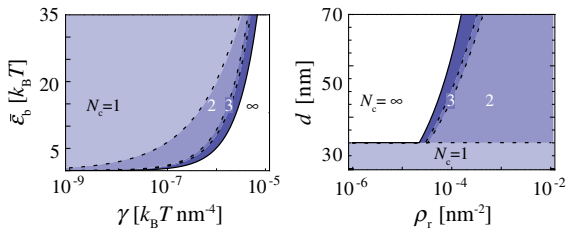

FIG. 2 (color online). Phase diagrams showing regions of unstable adhesion ($N_c = \infty$) and regions with a particular number of bonds forming a stable seed ($N_c = 1, 2, 3, \ldots$) for $\kappa = 10k_BT$ (k_B being the Boltzmann constant and T temperature), $\gamma = 3.125 \times 10^{-7} k_BT$ nm^{-4}, $h_0 = 80$ nm, and $l_0 = 40$ nm, $\epsilon_b = 6.97k_BT$, $\rho_l = 1.5625 \times 10^{-4}$ nm^{-2}, and $\lambda = \infty$. These parameters are used throughout unless otherwise indicated.

is stable. However, membrane fluctuations occur on time scales much shorter than k_0^{-1}. Consequently, the membrane samples the entire height probability distribution p_n, before an existing bond dissociates and a new one associates. The ligands also sample all available heights while attempting to form or break a bond. Simultaneously, rapid changes of $k^{\mathrm{on}}(h)$ and $k^{\mathrm{off}}(h)$ with fluctuations of the membrane take place. Such time-scale separation allows us to perform the key step in the development of our model, namely to define a set of effective rates K_n^{off} and K_n^{on} to break the nth or form the $(n+1)$th bond. These emerge by averaging the local rates $k^{\mathrm{on}}(h)$ and $k^{\mathrm{off}}(h)$ by means of the characteristic distribution p_n

$$K_n^{\mathrm{off}} \equiv \int dh^b\, p_n(h^b) k^{\mathrm{off}}(h^b)$$
$$K_n^{\mathrm{on}} \equiv \rho_l \int dh^r\, p_n(h^r) k^{\mathrm{on}}(h^r). \tag{5}$$

Thereby, h^b and h^r signify the height of the membrane at the position of a bond at the edge of a seed, and above the neighboring free receptor, respectively. The set $\{p_n\}$ can be calculated analytically and thus, one obtains effective rates that depend on the median $\bar{h}_n^{b,r}$ and the variance $\sigma_n^{b,r}$ of the relevant height distribution (see Supplemental Material [36] for details).

To form a seed with N_c bonds, one would need $2N_c$ effective rates. However, within the approximation of a moving front with a constant shape (Fig. 1), only four rates are required $\{K_0^{\mathrm{on}}, K_1^{\mathrm{on}}, K_1^{\mathrm{off}}, K_2^{\mathrm{off}}\}$. Here, the rate of association of the first bond K_0^{on} may be substantial even though the ligand is on average, out of reach of the receptor $[k^{\mathrm{on}}(h_0) \to 0]$. Namely, fluctuations bring the binding partners within the interaction range α where they may associate with the instantaneous rate $k^{\mathrm{on}}(h)$. Averaging over these events yields K_0^{on}.

The establishment of the first bond deforms the membrane to the height $h_1^b = h_0 - (8h_0\sqrt{\gamma\kappa} + \lambda l_0)/(8\sqrt{\gamma\kappa} + \lambda)$, and creates the characteristic shape of the moving front. This first bond unbinds with the rate K_1^{off} or, alternatively, the nucleation proceeds with the formation of the second bond at the rate of K_1^{on}. Because the membrane within the moving front is on average closer to the receptor than the free membrane (Figs. 1 and 3, inset), K_1^{on} is typically larger than K_0^{on} (Fig. 3). The formation of the second bond stabilizes the first bond, which is taken into account by introducing the second unbinding rate K_2^{off}, typically smaller than K_1^{off}. The membrane-transmitted bond correlations, which promote radial growth [19], are thus encoded in the effective rates. Since these correlations decay on short length scales [44], and because the shape and the fluctuations of the moving front remain practically constant for small changes in the radius of the seed (Fig. 1), the association and dissociation rates of the second and every subsequent bond remain the same ($K_n^{\mathrm{on}} = K_1^{\mathrm{on}}$ and $K_n^{\mathrm{off}} = K_2^{\mathrm{off}}$ for $n > 2$).

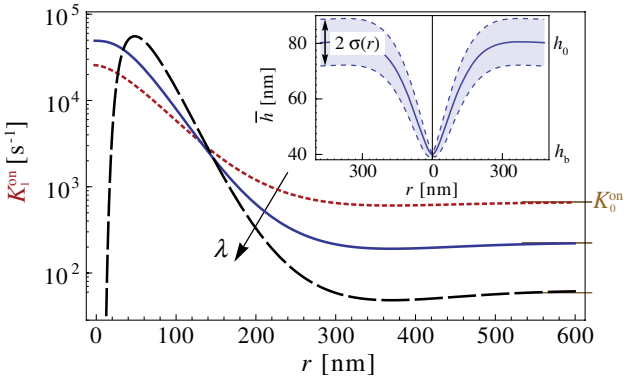

FIG. 3 (color online). The effective binding rate K_1^{on} for a formation of a bond at the distance r from a preexisting bond for $\lambda = \infty$, 0.05, and $0.02 k_B T$ nm^{-2}, shown with dashed black, full blue, and the dotted red lines, respectively. Furthermore, we set $\alpha = 10$ nm and $k_0 = 10^6$ s^{-1}. Inset: Average membrane profile in the envelop of local fluctuation amplitude $\pm\sigma$ around a stiff bond placed at $r = 0$.

Interestingly, the binding rate K_1^{on} changes over several orders of magnitude compared to its asymptotic values in the case of the biologically relevant stiff bonds, $\lambda \to \infty$ (Fig. 3). Thereby, in the direct vicinity of the first bond $K_1^{\mathrm{on}} \ll K_0^{\mathrm{on}}$, despite the small ligand-receptor separation. Under these conditions, strong suppression of fluctuations prevents the contact between the binders. At intermediate distances between the receptors, an optimum between membrane-substrate separation and the intensity of fluctuations is achieved (maximum in K_1^{on}), which may considerably promote nucleation.

With the four effective rates discussed above, the master equation [40] for the probability distribution of nucleation times $\mathcal{P}(\tau)$ on an *a priori* chosen receptor becomes

$$\mathcal{P}(\tau) = -\partial_\tau \sum_{n=0}^{N_c-1} P_n(\tau) \equiv N_s K_1^{\mathrm{on}} P_{N_c-1}(\tau). \tag{6}$$

Here, N_s is the number of neighboring receptors around the seed with $N_c - 1$ bonds. Equation (6) is conditioned by a set of probabilities P_n to find aggregates with $n < N_c$ bonds (see Supplemental Material [36]). Its numerical solution yields the exact characteristic nucleation time $\bar{\tau}$ (Fig. 4). On the other hand, analytical analysis provides an expression for $\bar{\tau}$ in the limit of large K_0^{on}

$$\bar{\tau} \simeq \binom{N_c+2}{3}^{-1} \frac{K_1^{\mathrm{off}}}{K_0^{\mathrm{on}}} \left(\frac{K_2^{\mathrm{off}}}{K_1^{\mathrm{on}}}\right)^{(N_c-2)} \frac{1}{K_1^{\mathrm{on}}}. \tag{7}$$

The first factor on the right-hand side of Eq. (7) accounts for the geometry of the (square) lattice. The three remaining terms are effective reaction constants for forming the first bond, the second and penultimate bonds, and finally the N_cth bond, respectively. This intuitive expression performs very well in the biologically relevant regime of relatively low ligands density (Fig. 4). In this case, $\bar{\tau}$ is found to be

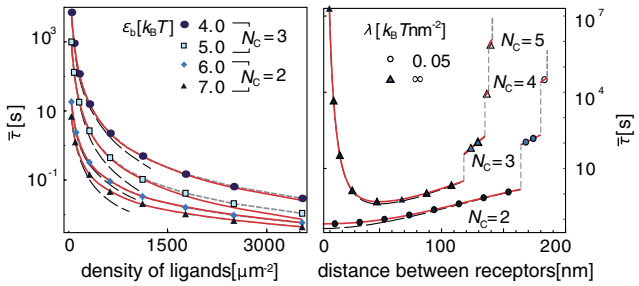

FIG. 4 (color online). Characteristic nucleation time as a function of the number density of ligands for several binding affinities (left), and as a function of the distance between bonds for different stiffness of the receptors (right). The numerical solution of Eq. (6) is shown with the symbols while the approximate solutions given by Eq. (7) and Eq. (SI-30) in the Supplemental Material [36] are displayed with the dashed black and full red lines. This short-dashed lines are guidance for the eye.

particularly sensitive to small variations in receptor density, binding affinity and bond stiffness. For stiff bonds, the signature of the K_1^{on} rate is clearly observable in $\bar{\tau}$, with the appearance of a minimum at intermediate receptor densities. Beyond the regime of large K_0^{on}, we calculated a more general form for $\bar{\tau}$ [Eq. (SI-30) in the Supplemental Material [36]], which predict an exponential dependence of the nucleation time on the number of bonds in the seed, as suggested previously by scaling arguments [45].

Comparison with simulations.—The validation of the presented model emerges from comparison with extensive Langevin simulations, based on the Hamiltonian in Eq. (1). Thereby, the formation of bonds is explicitly coupled to the deformation of the membrane [19,20,35], whose fluctuations are set by the fluctuation-dissipation theorem, with fully resolved hydrodynamics. Bond association and dissociation are stochastic processes governed by the local $k^{\mathrm{on}}(h)$ and $k^{\mathrm{off}}(h)$ rates obeying detailed balance [Eqs. (3) and (4)]. Unbound ligands are allowed to diffuse as self-avoiding Brownian particles, with diffusion constant D.

To reflect the assumptions of the model, we initially performed "biased" simulations in which the nucleation was permitted to start from an *a priori* selected receptor (see Supplemental Material [36]). Comparison with our numerical solution of the master equation (left panel, Fig. 5) shows extraordinary agreement (no fitting parameters). However, in experiments as well as in standard simulations, nucleation may occur simultaneously on any receptor. Under the condition that the nucleation is a rare event, there is no interaction between different nucleation attempts. Consequently, the probability for nucleating a stable seed anywhere in a membrane segment arises as a product of mutually independent probabilities for nucleating on a particular receptor. We thus estimate the probability distribution of nucleation times as $\mathcal{P}_{N_R}(\tau) \simeq -\partial_\tau(\sum_{n=0}^{N_c-1} P_n(\tau))^{N_R}$ where N_R is the number of receptors in the area of interest. This estimate is justified by an

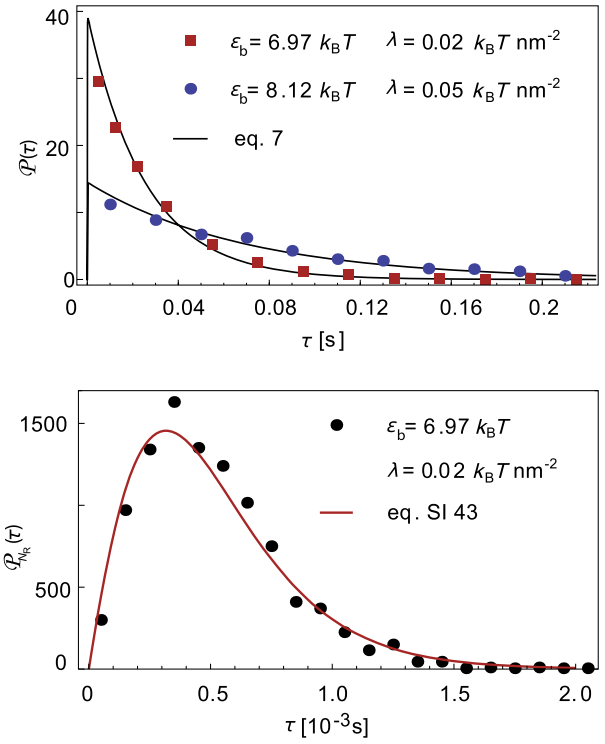

FIG. 5 (color online). Comparison of modeling (lines) and simulations (symbols). Probability distribution of nucleation time $\mathcal{P}(\tau)$ for a single radially growing seed (up). The probability distribution of nucleation time $\mathcal{P}_{N_R}(\tau)$ generated from a segment of a membrane nucleating on $N_R = 1024$ receptors simultaneously (down). For curves with $\epsilon_b = 6.97 k_B T$, we take $k_0 \simeq 10^6$ s^{-1}, $D = 5 \times 10^6$ nm s^{-2}, whereas for $\epsilon_b = 8.12 k_B T$, we use $k_0 \simeq 7 \times 10^5$ s^{-1}, $D = 5 \times 10^7$ nm s^{-2}.

exceedingly favorable comparison with the $\mathcal{P}_{N_R}(\tau)$ generated in a number of "unbiased" simulations with multiple seeds forming simultaneously (right panel in Fig. 5). Such agreement is expected as long as the density of free binders is not affected by multiple nucleations.

Conclusions.—We solved the long standing problem of domain nucleation in membrane adhesion by developing a comprehensive theory that accounts for membrane-mediated correlations. We use unbiased, high accuracy simulations to confirm the numerical solutions of our model and, furthermore, find excellent agreement with our analytic estimates for the critical seed size and the characteristic nucleation time.

In the context of experiments, equilibrium adhesion in passive vesicle systems is generally associated with closely packed domains [25,34,46]. Our model, nevertheless, suggests that in such systems, sparsely distributed bonds in the early stages of the adhesion process may precede the formation of compact domains at longer time scales, which was, in effect, recently reported [46]. In the biologically relevant regime of stiff bonds, we find an optimum density of receptors, deviations from which quickly increase the nucleation time by up to several orders of magnitude.

Living cells may utilize this effect by actively adjusting the separation between the receptors, which indeed seems to be the case [10]. A considerable difference between cellular and vesicle adhesion is that the bond formation rates for the former are regulated by active and not only thermal fluctuations. However, as long as these fluctuations are fast, the concepts developed herein should successfully provide the theoretical foundation for the processes taking place during the nucleation of adhesion domains.

We thank K. Sengupta, S. Fenz, and R. Merkel for insightful discussions, D. Schmidt for critical reading of the manuscript, and Deutsche Forschungsgemeinschaft DFG-SE 1119/2-1 for support.

[1] B. Geiger, J. Spatz, and A. Bershadsky, Nat. Rev. Mol. Cell Biol. **10**, 21 (2009).
[2] M. Barda-Saad, A. Braiman, R. Titerence, S. Bunnell, V. Barr, and L. Samelson, Nat. Rev. Immunol. **6**, 80 (2004).
[3] A. Zemel, F. Rehfeldt, A. Brown, D. Discher, and S. Safran, Nat. Phys. **6**, 468 (2010).
[4] A. Engler, S. Sen, H. Sweeney, and D. Discher, Cell **126**, 677 (2006).
[5] M. Dustin, Immunity **30**, 482 (2009).
[6] D. Discher, P. Janmey, and Y. Wang, Science **310**, 1139 (2005).
[7] T. Lecuit and P. Lenne, Nat. Rev. Mol. Cell Biol. **8**, 633 (2007).
[8] Y. Wu, X. Jin, O. Harrison, L. Shapiro, B. H. Honig, and A. Ben-Shaul, Proc. Natl. Acad. Sci. U.S.A. **107**, 17 592 (2010).
[9] M. Schvartzman, M. Palma, J. Sable, J. Abramson, X. Hu, M. P. Sheetz, and S. J. Wind, Nano Lett. **11**, 1306 (2011).
[10] J. Deeg, I. Louban, D. Aydin, C. Selhuber-Unkel, H. Kessler, and J. P. Spatz, Nano Lett. **11**, 1469 (2011).
[11] J. Solon, I. Levental, K. Sengupta, P. Georges, and P. Janmey, Biophys. J. **93**, 4453 (2007).
[12] P. Kollmannsberger and B. Fabry, Soft Matter **5**, 1771 (2009).
[13] A. Pierres, A.-M. Benoliel, D. Touchard, and P. Bongrand, Biophys. J. **94**, 4114 (2008).
[14] R. Bruinsma and E. Sackmann, C. R. Acad. Sci. Paris Ser. IV **2**, 803 (2001).
[15] A.-S. Smith and E. Sackmann, ChemPhysChem **10**, 66 (2009).
[16] D. Cuvelier and P. Nassoy, Phys. Rev. Lett. **93**, 228101 (2004).
[17] P. Streicher, P. Nassoy, M. Bärmann, A. Dif, V. Marchi-Artzner, F. Brochard-Wyart, J. Spatz, and P. Bassereau, Biochim. Biophys. Acta, Biomembr. **1788**, 2291 (2009).
[18] B. G. Lorz, A.-S. Smith, C. Gege, and E. Sackmann, Langmuir **23**, 12 293 (2007).
[19] E. Reister-Gottfried, K. Sengupta, B. Lorz, E. Sackmann, U. Seifert, and A.-S. Smith, Phys. Rev. Lett. **101**, 208103 (2008).
[20] F. Brown, Annu. Rev. Phys. Chem. **59**, 685 (2008).
[21] T. R. Weikl, M. Asfaw, H. Krobath, B. Rozycki, and R. Lipowsky, Soft Matter **5**, 3213 (2009).
[22] A.-S. Smith and U. Seifert, Soft Matter **3**, 275 (2007).
[23] P.-G. de Gennes, P.-H. Puech, and F. Brochard-Wyart, Langmuir **19**, 7112 (2003).
[24] P.-H. Puech, V. Askovic, P. de Gennes, and F. Brochard-Wyart, Biophys. Rev. Lett. **01**, 85 (2006).
[25] A. Boulbitch, Z. Guttenberg, and E. Sackmann, Biophys. J. **81**, 2743 (2001).
[26] V. B. Shenoy and L. B. Freund, Proc. Natl. Acad. Sci. U.S.A. **102**, 3213 (2005).
[27] H. Gao, W. Shi, and L.-B. Freund, Proc. Natl. Acad. Sci. U.S.A. **102**, 9469 (2005).
[28] C.-Z. Zhang and Z.-G. Wang, Phys. Rev. E **77**, 021906 (2008).
[29] H. Krobath, B. Rozycki, R. Lipowsky, and T. R. Weikl, PLoS ONE **6**, e23284 (2011).
[30] A.-S. Smith, S. F. Fenz, and K. Sengupta, Europhys. Lett. **89**, 28 003 (2010).
[31] S. F. Fenz, T. Bihr, R. Merkel, U. Seifert, K. Sengupta, and A.-S. Smith, Adv. Mater. **23**, 2622 (2011).
[32] A. Raudino and M. Pannuzzo, J. Chem. Phys. **132**, 045103 (2010).
[33] A. Raudino and M. Pannuzzo, J. Phys. Chem. B **114**, 15 495 (2010).
[34] R. Bruinsma, M. Goulian, and P. Pincus, Biophys. J. **67**, 746 (1994).
[35] E. Reister, T. Bihr, U. Seifert, and A.-S. Smith, New J. Phys. **13**, 025003 (2011).
[36] See Supplemental Material at http://link.aps.org/supplemental/10.1103/PhysRevLett.109.258101 for the derivation of (i) the critical number of bonds in the nucleus, (ii) the effective reaction rates, and (iii) the approximate solution of the master equation. Furthermore, the methodology for performing the biased simulations of the single seed is described.
[37] R. Lipowsky, in *Structure and Dynamics of Membranes*, edited by R. Lipowsky and E. Sackmann, Handbook of Biological Physics Vol. 1 (North-Holland, Amsterdam, 1995), Chap. 11, pp. 521–602.
[38] R. Bruinsma, A. Behrisch, and E. Sackmann, Phys. Rev. E **61**, 4253 (2000).
[39] J. O. Rädler, T. J. Feder, H. H. Strey, and E. Sackmann, Phys. Rev. E **51**, 4526 (1995).
[40] C. Gardiner, *Stochastic Methods* (Springer, Berlin, 1985).
[41] M. Dembo, D. C. Torney, K. Saxman, and D. Hammer, Proc. R. Soc. B **234**, 55 (1988).
[42] H. Gao, J. Qian, B. Chen, and J. R. Soc, Interface **8**, 1217 (2011).
[43] T. Erdmann and U. Schwarz, Biophys. J. **91**, L60 (2006).
[44] O. Farago, Phys. Rev. E **78**, 051919 (2008).
[45] T. Speck, E. Reister, and U. Seifert, Phys. Rev. E **82**, 021923 (2010).
[46] A.-S. Smith, K. Sengupta, S. Goennenwein, U. Seifert, and E. Sackmann, Proc. Natl. Acad. Sci. U.S.A. **105**, 6906 (2008).

SUPPLEMENTARY INFORMATION
Nucleation of ligand-receptor domains in membrane adhesion

Timo Bihr[1], Udo Seifert[1], Ana-Sunčana Smith[2]
[1] *II. Institut für Theoretische Physik, Universität Stuttgart, Pfaffenwaldring 57, 70550 Stuttgart, Germany and*
[2] *Institut für Theoretische Physik and the Excellence Cluster: Engineering of Advanced Materials, Universität Erlangen-Nürnberg, Nägelsbachstrasse 49b, 91052 Erlangen, Germany*
(Dated: November 7, 2012)

I. CRITICAL NUMBER OF BONDS

A nucleation seed reaches a stable size when the increase in the free energy due to the membrane deformation equals the decrease in enthalpy associated with the formation of bonds. In order to estimate the total deformation energy that depends on the radius of the seed $E_D(R)$, we first scale the deformation energy of the membrane caused by a formation of a single bond $E_D^1 = 4d^2\sqrt{\kappa\gamma}$ (see Ref. [1] for details) by the characteristic lateral extension of the deformation. The latter is simply the double of the lateral correlation length $\zeta \equiv \sqrt[4]{\kappa/\gamma}$ [1, 2]. Under the assumption that the shape of a moving front does not change significantly, the total deformation energy $E_D(R)$ is simply proportional to the circumference R of the seed

$$E_D(R) = 2\pi R\frac{E_D^1}{2\zeta} + E_D^1. \tag{1}$$

The second term on the left hand side has been added to insure a correct limit when $R \to 0$.

The change in enthalpy associated with the formation of bonds is given by

$$E_A(R) = -\pi R^2\left(\rho_r\bar{\epsilon_b} - \frac{\gamma}{2}d^2\right), \tag{2}$$

where ρ_r is the receptor density. The first term on the left hand side is the enthalpy gain due to the formation of bonds (all receptors within the seed are bound), while the second term is the enthalpy cost for displacing a membrane patch within the seed from the minimum of the nonspecific potential.

By evaluating the radius that maximizes the total energy of the seed ($\partial E_D(R)/\partial R = -\partial E_A(R)/\partial R$), one obtains the critical radius of nucleation

$$R_c = \frac{\pi^{-1}d^2\kappa\left(\frac{\gamma}{\kappa}\right)^{3/4}}{\rho_r\bar{\epsilon_b} - \frac{\gamma}{2}d^2}, \tag{3}$$

from which we extract the critical number of bonds N_C forming the seed (equation (2) in the manuscript)

$$N_c = 1 + \frac{4d^4\rho_r\gamma\sqrt{\gamma\kappa}}{\pi\left(\gamma d^2 - 2\bar{\epsilon_b}\rho_r\right)^2}, \tag{4}$$

where the additional bond comes from the fact that the radius of a seed with a single bond is zero.

II. HEIGHT DISTRIBUTION OF THE MEMBRANE AND EFFECTIVE RATES

A. Membrane height distribution

To calculate the effective rates defined in the equation (5) of the manuscript, one needs to evaluate the height probability distribution $p_n(h(\mathbf{r}))$ of a fluctuating membrane pinned by n bonds placed at $\mathbf{r_i}$ positions, where $i = 1, ..., n$. For simplicity we set $\beta \equiv (k_BT)^{-1} \equiv 1$.

By definition

$$p_n(h(\mathbf{r})) = \int \mathcal{D}[h'(\mathbf{r})]\,\mathfrak{p}_n[h'(\mathbf{r})]\delta(h'(\mathbf{r}) - h(\mathbf{r})). \tag{5}$$

To evaluate the above integral, we use the Boltzmann weight for $\mathfrak{p}_n[h'(\mathbf{r})] = \exp(-\mathcal{H}[h(\mathbf{r})])$, with the Hamiltonian $\mathcal{H}[h(\mathbf{r})]$, eq. (1) in the main text. Additionally, we us the Fourier representation to write the Dirac function as $\delta(x) = \frac{1}{\sqrt{2\pi}} \int \mathrm{d}\xi \, \exp(i\xi x)$, and membrane height profile $h'(\mathbf{r}) = \frac{1}{A} \sum_{\mathbf{q}} h'(\mathbf{q}) \exp(i\mathbf{q}\cdot\mathbf{r})$. All together, this yields

$$\begin{aligned} p_n(h(\mathbf{r})) = \frac{1}{2\pi} \int \mathrm{d}\xi \int \mathcal{D}[h'(\mathbf{q})] \, \exp\Big[- \sum_{i=1}^{n} \frac{\lambda}{2} \left(\frac{1}{A} \sum_{\mathbf{q}} h'(\mathbf{q}) \exp(i\mathbf{q}\cdot\mathbf{r_i}) - l_0 \right)^2 - \epsilon_b \\ - \frac{1}{2A} \sum_{\mathbf{q}} \|h'(\mathbf{q})\|^2 \left(\kappa q^4 + \gamma\right) + i\xi \left(\frac{1}{A} \sum_{\mathbf{q}} h'(\mathbf{q}) \exp(i\mathbf{q}\cdot\mathbf{r}) - h(\mathbf{r}) \right) \Big]. \end{aligned} \tag{6}$$

We now apply successively n Hubbard-Stratonovich transformations, one for each bond term in the sum over i. This produces n Gaussian integrals over auxiliary fields ϕ_i and

$$\begin{aligned} p_n(h(\mathbf{r})) \propto & \frac{1}{2\pi} \int \mathrm{d}\xi \int \mathcal{D}[h'(\mathbf{q})] \prod_{i=1}^{n} \int \mathrm{d}\phi_i \sqrt{\frac{1}{2\pi\lambda}} \exp\Big\{ - \sum_{i=1}^{n} \frac{\phi_i^2}{2\lambda} + \sum_{i=1}^{n} i l_0 \phi_i \\ & - i \sum_{i=1}^{n} \frac{\phi_i}{A} \sum_{\mathbf{q}} h'(\mathbf{q}) \exp\left(i\mathbf{q}\cdot\mathbf{r_i}\right) - \frac{1}{2A} \sum_{\mathbf{q}} \|h'(\mathbf{q})\|^2 \left(\kappa q^4 + \gamma\right) \\ & + i\xi \frac{1}{A} \sum_{\mathbf{q}} h'(\mathbf{q}) \exp\left(i\mathbf{q}\cdot\mathbf{r}\right) - i\xi h(\mathbf{r}) \Big\}. \end{aligned} \tag{7}$$

Since the integration over $h'(\mathbf{q})$ is a Gaussian integral, one obtains

$$\begin{aligned} p_n(h(\mathbf{r})) \propto & \int \mathrm{d}\xi \prod_{i=1}^{n} \int \mathrm{d}\phi_i \sqrt{\frac{1}{2\pi\lambda}} \exp\Big(- \sum_{i=1}^{n} \frac{\phi_i^2}{2\lambda} - i\xi h(\mathbf{r}) + \sum_{i=1}^{n} i l_0 \phi_i \Big) \\ & \exp\Big\{ - \frac{1}{2A} \sum_{\mathbf{q}} \Big[\left(\sum_{i=1}^{n} \exp\left(i\mathbf{q}\cdot\mathbf{r_i}\right) \phi_i - \xi \exp\left(i\mathbf{q}\cdot\mathbf{r}\right) \right) \frac{1}{\kappa q^4 + \gamma} \\ & \left(\sum_{j=1}^{n} \exp\left(-i\mathbf{q}\cdot\mathbf{r_j}\right) \phi_j - \xi \exp\left(-i\mathbf{q}\cdot\mathbf{r}\right) \right) \Big] \Big\}. \end{aligned} \tag{8}$$

In the following step, the terms within the curly brackets of equation (8) are reorganized, and the sums over $\mathbf{q}$ are converted to integrals that evaluated independently lead to Kelvin functions [3]. After some sorting

$$\begin{aligned} p_n(h(\mathbf{r})) \propto & \int \mathrm{d}\xi \prod_{i=1}^{n} \int \mathrm{d}\phi_i \sqrt{\frac{1}{2\pi\lambda}} \\ & \exp\Big[- \frac{1}{2} \sum_{i=1}^{n} \sum_{j=1}^{n} \phi_i \underbrace{\left(\frac{\delta_{ij}}{\lambda} - \frac{\mathrm{kei}\left(q_0 |\mathbf{r_i} - \mathbf{r_j}|\right)}{2\pi\sqrt{\kappa\gamma}} \right)}_{\equiv M_{ij}} \phi_j + \sum_{i=1}^{n} i l_0 \phi_i \Big] \\ & \exp\Big[- \frac{1}{2} \frac{\xi^2}{8\sqrt{\kappa\gamma}} - \xi \left(i h(\mathbf{r}) + \sum_{i=1}^{n} \phi_i \frac{\mathrm{kei}\left(q_0 |\mathbf{r_i} + \mathbf{r}|\right)}{2\pi\sqrt{\kappa\gamma}} \right) \Big], \end{aligned} \tag{9}$$

where

$$q_0 \equiv \zeta^{-1} \equiv \sqrt[4]{\frac{\gamma}{\kappa}} \tag{10}$$

is the inverse of the lateral correlation length. Integrating the Gaussian integrals in ξ gives after some algebra

$$\begin{aligned} p_n(h(\mathbf{r})) \propto & \prod_{i=1}^{n} \int \mathrm{d}\phi_i \sqrt{\frac{1}{2\pi\lambda}} \\ & \exp\left[-\frac{1}{2} \sum_{i=1}^{n}\sum_{j=1}^{n} \phi_i \underbrace{\left(M_{ij} - \frac{2\,\mathrm{kei}\,(q_0|\mathbf{r}-\mathbf{r_i}|)\,\mathrm{kei}\,(q_0|\mathbf{r}-\mathbf{r_j}|)}{\pi^2\sqrt{\kappa\gamma}} \right)}_{\equiv G_{ij}} \phi_j \right] \\ & \exp\left[i \sum_{i=1}^{n} \phi_i \left(l_0 + h(\mathbf{r}) \frac{4\,\mathrm{kei}\,(q_0|\mathbf{r}-\mathbf{r_i}|)}{\pi} \right) - \frac{1}{2} 8\sqrt{\kappa\gamma} h^2(\mathbf{r}) \right]. \end{aligned} \tag{11}$$

Since the remaining integrals are again Gaussian, one finally gets

$$\begin{aligned} p_n(h(\mathbf{r})) \propto \exp\Bigg[& - h(\mathbf{r}) \sum_{i=1}^{n}\sum_{j=1}^{n} l_0 G_{ij}^{-1} \frac{4\,\mathrm{kei}\,(q_0\ |\mathbf{r}-\mathbf{r_j}|)}{\pi} \\ & - \frac{1}{2} \left(8\sqrt{\kappa\gamma} + \sum_{i=1}^{n}\sum_{j=1}^{n} \frac{16\,\mathrm{kei}\,(q_0\ |\mathbf{r}-\mathbf{r_i}|)\, G_{ij}^{-1}\, \mathrm{kei}\,(q_0\ |\mathbf{r}-\mathbf{r_j}|)}{\pi^2} \right) h^2(\mathbf{r}) \Bigg]. \end{aligned} \tag{12}$$

Beause the probability distribution (12) is itself a Gaussian distribution, the average height of the membrane pinned by n bonds $\bar{h}_n(\mathbf{r})$ can be calculated by completing the square in the exponent. Consequently, one obtains

$$\bar{h}_n(\mathbf{r}) = \frac{-\frac{4}{\pi}\sum_{i=1}^{n}\sum_{j=1}^{n} l_0 G_{ij}^{-1}\,\mathrm{kei}\,(q_0\ |\mathbf{r}-\mathbf{r_i}|)}{8\sqrt{\kappa\gamma} + \frac{16}{\pi^2}\sum_{i=1}^{n}\sum_{j=1}^{n} \mathrm{kei}\,(q_0\ |\mathbf{r}-\mathbf{r_i}|) G_{ij}^{-1}\,\mathrm{kei}\,(q_0\ |\mathbf{r}-\mathbf{r_j}|)}. \tag{13}$$

The associated fluctuation amplitude $\sigma_n(\mathbf{r})$ is simply given by

$$\sigma_n(\mathbf{r}) \equiv \overline{h_n^2(\mathbf{r})} - \bar{h}_n(\mathbf{r})^2 = \left(8\sqrt{\kappa\gamma} + \sum_{i=1}^{n}\sum_{j=1}^{n} \frac{16\,\mathrm{kei}\,(q_0\ |\mathbf{r}-\mathbf{r_i}|)\, G_{ij}^{-1}\,\mathrm{kei}\,(q_0\ |\mathbf{r}-\mathbf{r_j}|)}{\pi^2} \right)^{-1}. \tag{14}$$

B. Calculation of effective rates

The height dependent Dembo's rates drive the instantaneous and local process of ligand-receptor binding. The local reaction rate $k^{\mathrm{on}}(h)$ for the creation of a bond (also manuscript equation (4)) is defined as

$$k^{\mathrm{on}}(h) = k_0 \sqrt{\frac{\lambda\alpha^2}{2\pi}} \exp\left[-\frac{\lambda}{2} \left\{ (h - l_0) - \alpha \right\}^2 \right]. \tag{15}$$

The off-rate

$$k^{\mathrm{off}}(h) = k_0 \exp\left[-\epsilon_b\right] \exp\left[\lambda\alpha\,(h - l_0) - \frac{\lambda\alpha^2}{2} \right], \tag{16}$$

follows from the on-rate (15) and a detailed balance condition (also manuscript equation (3))

$$\frac{k^{\mathrm{off}}(h)}{k^{\mathrm{on}}(h)} = \exp\left[\frac{\lambda}{2} (h - l_0)^2 - \bar{\epsilon_b} \right]. \tag{17}$$

which associates the height dependent reaction constant with the free energy gain for the formation of a bond (the exponent on the right hand side).

With the help of equations (13) and (14) the above rates can be averaged yielding effective rates K_n^{off} and K_n^{on} to break the n-th or form the $(n+1)$-th bond

$$\begin{aligned} K_n^{\mathrm{off}} &\equiv \int \mathrm{d}h^b\, p_n(h^b) k^{\mathrm{off}}(h^b), \\ K_n^{\mathrm{on}} &\equiv \rho_l \int \mathrm{d}h^r\, p_n(h^r) k^{\mathrm{on}}(h^r). \end{aligned} \tag{18}$$

Accordingly, the local rates defined by eqs. (16) and (17) are averaged by means of the height probability distribution p_n, characteristic for a particular conformation of n bonds. Thereby, h^b and h^r signify the height of the membrane at the position of a bond at the edge of the seed, and above the free receptor that neighbors the seed, respectively.

Substituting the equations (12), (15) and (16) into (18) yields

$$\begin{aligned} K_n^{\mathrm{on}} &= k_0 \frac{\sqrt{\lambda\alpha^2}\rho_l}{\sqrt{2\pi(1+\lambda(\sigma_n^r)^2)}} \exp\left[-\frac{\lambda\left\{\overline{h}_n^r - (\alpha+l_0)\right\}^2}{2(1+\lambda(\sigma_n^r)^2)}\right], \\ K_n^{\mathrm{off}} &= k_0 \exp\left[\left(\frac{\lambda\alpha}{2}\left\{2\left(\overline{h}_n^b - l_0\right) + \alpha\left(\lambda(\sigma_n^b)^2 - 1\right)\right\} - \epsilon_b\right)\right]. \end{aligned} \tag{19}$$

Here $\overline{h}_n^{b,r}$ is the median and $\sigma_n^{b,r}$ the variance of the relevant height distribution $p_n(h^{b,r})$

The free membrane fluctuates in the minimum of the nonspecific potential. Hence its mean height is h_0 (also arising from equation (13) when setting $n = 0$). On the other hand, equation (14), as expected, reduces to

$$\sigma_0 \equiv \overline{h_0^2} - \overline{h_0}^2 = \frac{1}{8\sqrt{\kappa\gamma}}, \tag{20}$$

which is the vertical correlation length of an unbound membrane [2]. After substituting the mean value h_0 of the membrane height and fluctuation amplitude σ_0 into equation (19), one obtains the effective rate for binding the first bond

$$K_0^{\mathrm{on}} = k_0 \frac{\sqrt{\lambda}\rho_l}{\sqrt{2\pi\left(1+\lambda(8\sqrt{\kappa\gamma})^{-1}\right)}} \exp\left(-\frac{\lambda\left[h_0 - (\alpha+l_0)\right]^2}{2(1+\lambda(8\sqrt{\kappa\gamma})^{-1})}\right). \tag{21}$$

If one bond is formed, the height profile (Figs. 1 and 2 of the manuscript)

$$\bar{h}_1(r) = 4\frac{\lambda\left(h_0 - l_0\right)\mathrm{kei}(q_0 r)}{\pi(8\sqrt{\kappa\gamma}+\lambda)} + h_0, \tag{22}$$

is axially symmetric. Here r is the distance from the bond at $r = 0$. The fluctuation of the profile is also axially symmetric and takes the form

$$\sigma_1(r) \equiv \overline{h_1^2(r)} - \overline{h_1(r)}^2 = \frac{1}{8\sqrt{\kappa\gamma}} \frac{8\sqrt{\kappa\gamma} + \lambda - \frac{16}{\pi^2}\lambda\,\mathrm{kei}^2(q_0 r)}{8\sqrt{\kappa\gamma}+\lambda}. \tag{23}$$

If we consider the membrane height and fluctuations at the site of the bond ($r = 0$), the average position of the membrane $\bar{h}_1^b$ is given by

$$\bar{h}_1^b \equiv \overline{h_1(0)} = \frac{8\sqrt{\kappa\gamma}h_0 + \lambda l_0}{8\sqrt{\kappa\gamma}+\lambda}. \tag{24}$$

The fluctuation amplitude σ_1^b is in this case

$$\sigma_1^b \equiv \overline{h_1^2(0)} - \overline{h_1(0)}^2 = \overline{(h_1^b)^2} - (\bar{h}_1^b)^2 = (8\sqrt{\kappa\gamma}+\lambda)^{-1}. \tag{25}$$

Consequently, the effective rate for unbinding of the first bond is

$$K_1^{\mathrm{off}} = k_0 \exp\left(-\epsilon_b + \frac{\lambda\alpha}{2}\left\{2\left(\frac{8\sqrt{\kappa\gamma}h_0 + \lambda l_0}{8\sqrt{\kappa\gamma}+\lambda} - l_0\right) + \alpha[\lambda\left(8\sqrt{\kappa\gamma}+\lambda\right)^{-1} - 1]\right\}\right). \tag{26}$$

In order to calculate the rate for the formation of the second bond K_1^{on} equations (22) and (23) have to be evaluated for a fixed $r \equiv r_r$ which denotes the distance between two neighboring receptors. In this way one obtains h_1^r and σ_1^r that are the mean height and fluctuation amplitude above the next free receptors. These two quantities are then substituted into equation (8) of the manuscript. The unbinding rate of the second and every following bond K_2^{off} has to be calculated at the position of the second bond when $n = 2$, the solution of which is analytic but too lengthy to be presented.

III. MASTER EQUATION AND NUCLEATION TIME DISTRIBUTION

We address the dynamics of nucleation by making the analogy with the methods for calculating the mean first passage time [4]. Thereby, given that the system was initially in state A (no bonds), one calculates the time τ for reaching state B (N_c bonds around an a priory chosen receptor) for the first time. Depending on the path (the sequence of binding and unbinding events prior to the establishment of the N_c^{th} bond), a distribution $\mathcal{P}(\tau)$ of first passage times (e.g. time to form a nucleus) emerges, the first moment of which is the mean first passage time, or in our case, the characteristic nucleation time $\bar{\tau}$.

This can be formalized by a master equation for the distribution of nucleation times $\mathcal{P}(\tau)$

$$\mathcal{P}(\tau) = -\partial_t \sum_{n=0}^{N_c-1} P_n\left(t\right)|_{t=\tau}, \tag{27}$$

where $P_n(t)$ are the probability distributions to have n bonds around a particular binding site formed at the given instance of time t. Their evolution in time is given by

$$\begin{aligned} P_n(0) &= \delta_{n,0} \\ \partial_t P_0(t) &= -K_0^{\mathrm{on}} P_0(t) + K_1^{\mathrm{off}} P_1(t); \quad \text{for } n = 0 \\ \partial_t P_n(t) &= [(n+n_s)-1]K_{n-1}^{\mathrm{on}} P_{n-1}(t) - \left[(n+n_s)K_n^{\mathrm{on}} + nK_n^{\mathrm{off}}\right] P_n(t) + (n+1)K_{n+1}^{\mathrm{off}} P_{n+1}(t)(1-\delta_{n,N_c-1}); \\ &\qquad \text{for } n = 1 \ldots N_c - 1. \end{aligned} \tag{28}$$

which can also be written in a matrix notation (*vide infra*, equation (29)).

The positive contributions to the time variation of $P_n(t)$ in equation (28) arise from changing the seed size by the association of a bond in a seed with $n-1$ bonds or the dissociation of a bond in a seed with $n+1$ bonds. The negative contributions are associated with the decay of the state with n bonds to the state with either with $n-1$ or $n+1$ bonds.

The prefactors $N_s \equiv n + n_s$ account for the increasing number of neighboring binding sites around a growing seed. We find that using $N_s \equiv n + 3$ is a very good approximation for the number of direct neighbors to the seed for our assumed square lattice as it reproduces the number of neighbors of a single bond and a 3×3 patch exactly. Thus, it approximates the number of neighbors for patches with one to nine bonds accurately. However, for larger seeds the number of neighbors would begin to scale with the square root of bonds and the master equation would have to be changed correspondingly.

For example, for a seed with $N_c = 4$ growing on a substrate on which the receptors are organized in a square lattice, the master equation (28) takes form

$$\partial_t \begin{pmatrix} P_0(t) \\ P_1(t) \\ P_2(t) \\ P_3(t) \end{pmatrix} = \begin{pmatrix} -K_0^{\mathrm{on}} & K_1^{\mathrm{off}} & 0 & 0 \\ K_0^{\mathrm{on}} & -(4K_1^{\mathrm{on}} + K_1^{\mathrm{off}}) & 2K_2^{\mathrm{off}} & 0 \\ 0 & 4K_1^{\mathrm{on}} & -(5K_1^{\mathrm{on}} + 2K_2^{\mathrm{off}}) & 3K_2^{\mathrm{off}} \\ 0 & 0 & 5K_1^{\mathrm{on}} & -(6K_1^{\mathrm{on}} + 3K_2^{\mathrm{off}}) \end{pmatrix} \begin{pmatrix} P_0(t) \\ P_1(t) \\ P_1(t) \\ P_3(t) \end{pmatrix}, \tag{29}$$

where we already implemented the relevant reaction rates (see discussion in the manuscript) and set $n_s \equiv 3$ for the square lattice. As already mentioned, the above shown master equation accounts only for the development of a seed around a particular binding site. However, in a typical experiment, the nucleation can take place on any receptor on the substrate. If all receptors are equivalent and if the nucleation is a rare event, one can assume that different nucleation events are spatially separated so that they do not influence one another. Under these circumstances, one can consider the product of the single probabilities to provides a good estimate for the overall probability distribution $\mathcal{P}_{N_R}(\tau)$ of the nucleation times (occurring anywhere in the system containing N_R receptors). Consequently,

$$\mathcal{P}_{N_R}(\tau) \approx -\partial_t \left(\sum_{n=0}^{N_c-1} P_n(t) \right)^{N_R} |_{t=\tau}, \tag{30}$$

A. Calculation of the characteristic nucleation time $\bar{\tau}$

Since the coupling matrix in the equation (28) is tridiagonal one of dimensions $N_c x N_c$, it can always be diagonalized, which gives a set of eigenvalues ν_i $(i = 1, \ldots, N_c)$. Each eigenvalue is a root of the characteristic polynomial $p_{N_c}(\nu)$

and can be associated with one of characteristic times $\tau_i = |\nu_i|^{-1}$, related to the process described by the equation (28). Thereby, the absolute value is taken because typically $\nu_i \leq 0$, as suggested by the Gershgorin circle theorem [5].

If time separation occurs, one eigenvalue has a magnitude considerably smaller then all others. This particular eigenvalue then determines the characteristic nucleation time $\bar{\tau}$ which emerges as the root of the characteristic polynomial approximated to first order in ν. To determine this eigenvalue for an arbitrary seed size, we construct the general solution by means of mathematical induction. Our starting point is the construction of the base case that we calculate for a seed with $N_c = 3$.

We first determine the eigenvalue in the case that $N_c = 1$ for which the exact characteristic polynomial reads

$$p_1(\nu) = K_0^{\mathrm{on}} - \nu, \tag{31}$$

If $N_c = 2$ the characteristic polynomial is given by

$$\begin{aligned} p_2(\nu) &= \left(-K_0^{\mathrm{on}} - \nu\right)\left(-K_1^{\mathrm{off}} - 4K_1^{\mathrm{on}} - \nu\right) - K_1^{\mathrm{off}} K_0^{\mathrm{on}} \\ &= 4K_0^{\mathrm{on}} K_1^{\mathrm{off}} + \nu\left(K_0^{\mathrm{on}} + K_1^{\mathrm{off}} + 4K_1^{\mathrm{on}}\right) + \nu^2. \end{aligned} \tag{32}$$

Within the first order approximation we neglect the last term. In addition, we assume

$$\begin{aligned} K_{1,2}^{\mathrm{off}} &\gg K_0^{\mathrm{on}} \\ K_{1,2}^{\mathrm{off}} &\gg K_1^{\mathrm{on}}. \end{aligned} \tag{33}$$

Under these conditions the characteristic polynomial reduces to

$$p_2(\nu) \approx 4K_0^{\mathrm{on}} K_1^{\mathrm{off}} + \nu K_1^{\mathrm{off}}. \tag{34}$$

For the case of $N_c = 3$ it becomes tedious to calculate the characteristic polynomial by the general rule. Instead, we use the method of extended continuants (see for example Ref. [4]) that are a sequence within which the n^{th} member $\Lambda(n)$ is the determinant of a tridiagonal $n \times n$-Matrix. Specifically,

$$\begin{aligned} &\Lambda(0) \equiv 1 \\ &\Lambda(1) \equiv a_1 \\ &\Lambda(n) \equiv a_n \Lambda(n-1) - b_{n-1} c_{n-1} \Lambda(n-2), \end{aligned} \tag{35}$$

where a_i are the diagonal entries of a tridiagonal matrix whereas b_i and c_i are the off-diagonal terms. Using this sequence and the results for $N_c = 1$ and 2, we obtain

$$\begin{aligned} p_3(\nu) &\approx \left(-2K_2^{\mathrm{off}} - 5K_1^{\mathrm{on}} - \nu\right)\left(4K_0^{\mathrm{on}} K_1^{\mathrm{off}} + K_1^{\mathrm{off}}\nu\right) - 2K_1^{\mathrm{off}} 4K_1^{\mathrm{on}}\left(-K_0^{\mathrm{on}} - \nu\right) \\ &\approx -20K_0^{\mathrm{on}} K_1^{\mathrm{on}} + 2K_2^{\mathrm{off}} K_1^{\mathrm{off}} \nu. \end{aligned} \tag{36}$$

Thereby, we neglect terms proportional to ν^2 and consequently use the assumptions (33).

After considering the cases for $N_c = 1, 2, 3$ we can do the induction step. A detailed analysis of the coupling matrix and observing the results above suggests the induction hypothesis

$$p_{N_c}(\nu) \approx (-1)^{N_c} \frac{(N_c+2)!}{3!} K_0^{\mathrm{on}} \left(K_1^{\mathrm{on}}\right)^{N_c-1} + \nu\left((-1)^{N_c-1}\left(N_c-1\right)! K_1^{\mathrm{off}}\left(K_2^{\mathrm{off}}\right)^{N_c-2}\right). \tag{37}$$

The induction step is done with the help of the sequence (35)

$$\begin{aligned} p_{N_c+1}(\nu) &= a_{N_c+1} p_{N_c}(\nu) - b_{N_c} c_{N_c} p_{N_c-1}(\nu) \\ &\approx \left(-N_c K_2^{\mathrm{off}} - \left(N_c+3\right) K_1^{\mathrm{on}} - \nu\right) \times \\ &\times \left\{(-1)^{N_c} \frac{(N_c+2)!}{3!} K_0^{\mathrm{on}} \left(K_1^{\mathrm{on}}\right)^{N_c-1} + \nu\left(-1\right)^{N_c-1}\left(N_c-1\right)! K_1^{\mathrm{off}}\left(K_2^{\mathrm{off}}\right)^{N_c-2}\right\} \\ &- N_c K_2^{\mathrm{off}}\left(N_c+2\right) K_1^{\mathrm{on}} \times \\ &\times \left\{(-1)^{N_c-1} \frac{(N_c+1)!+1}{3!} K_0^{\mathrm{on}} \left(K_1^{\mathrm{on}}\right)^{N_c-2} + \nu\left(-1\right)^{N_c}\left(N_c-2\right)! K_1^{\mathrm{off}}\left(K_2^{\mathrm{off}}\right)^{N_c-3}\right\}. \end{aligned} \tag{38}$$

After some algebraic manipulations and rearranging the terms, one obtains

$$\begin{aligned}
p_{N_c+1}(\nu) \approx\ & (-1)^{N_c+1} N_c \frac{(N_c+2)!}{3!} K_0^{\mathrm{on}} \left(K_1^{\mathrm{on}}\right)^{N_c-1} K_2^{\mathrm{off}} \\
& + (-1)^{N_c+1} \frac{(N_c+3)!}{3!} K_0^{\mathrm{on}} \left(K_1^{\mathrm{on}}\right)^{N_c} \\
& + (-1)^{N_c} N_c \frac{(N_c+2)!}{3!} K_0^{\mathrm{on}} \left(K_1^{\mathrm{on}}\right)^{N_c-1} K_2^{\mathrm{off}} \\
& + \nu(-1)^{N_c+1} \frac{(N_c+2)!}{3!} K_0^{\mathrm{on}} \left(K_1^{\mathrm{on}}\right)^{N_c-1} \\
& + \nu(-1)^{N_c} N_c! K_1^{\mathrm{off}} \left(K_2^{\mathrm{off}}\right)^{N_c-1} \\
& + \nu(-1)^{N_c} (N_c+3)(N_c-1)! K_1^{\mathrm{on}} K_1^{\mathrm{off}} \left(K_2^{\mathrm{off}}\right)^{N_c-2} \\
& + \nu(-1)^{N_c+1} N_c (N_c+2)(N_c-2)! K_0^{\mathrm{on}} K_1^{\mathrm{off}} \left(K_2^{\mathrm{off}}\right)^{N_c-2} \\
& + \nu^2(-1)^{N_c} (N_c-1)! K_1^{\mathrm{off}} \left(K_2^{\mathrm{off}}\right)^{N_c-2}
\end{aligned} \tag{39}$$

Obviously, the first and the third term cancel, while the last, second order term is dropped. Furthermore, using conditions given in equation (33) leads to neglecting the sixth and the seventh term which are much smaller than the fourth term. As a result, the induction hypothesis is proven yielding the smallest eigenvalue in a form

$$|\nu_s| \approx \binom{N_c+2}{3} K_0^{\mathrm{on}} \frac{K_2^{\mathrm{off}}}{K_1^{\mathrm{off}}} \left(\frac{K_1^{\mathrm{on}}}{K_2^{\mathrm{off}}}\right)^{(N_c-1)}, \tag{40}$$

the inverse of which gives the characteristic nucleation time $\bar{\tau}$ shown in equation (7) in the manuscript.

Somewhat less restrictive is the case when $K_{N_c-1}^{\mathrm{off}}$ is of the same order of magnitude as K_1^{on}. In this case

$$\begin{aligned}
K_i^{\mathrm{off}} &\gg K_0^{\mathrm{on}} \quad \forall_i \\
K_i^{\mathrm{off}} &\gg K_i^{\mathrm{on}} \quad \forall_{i<N_c-1}
\end{aligned} \tag{41}$$

The result given in equation (40) now becomes the (N_c-1)th extended continuant and the induction hypothesis equation (37) can be corrected by the addition of the following term

$$p_{N_c}^{add}(\nu) = \nu(-1)^{N_c-1}(N_c+2)(N_c-2)! K_1^{\mathrm{on}} K_1^{\mathrm{off}} \left(K_2^{\mathrm{off}}\right)^{N_c-3}. \tag{42}$$

The principal eigenvalue is then given by

$$\begin{aligned}
|\nu_s| &\approx \frac{4K_0^{\mathrm{on}} K_1^{\mathrm{on}}}{K_1^{\mathrm{off}} + 4K_1^{\mathrm{on}}} \quad N_c = 2 \\
|\nu_s| &\approx \frac{\binom{N_c+2}{3} \frac{K_0^{\mathrm{on}}}{K_1^{\mathrm{off}}} \left(\frac{K_1^{\mathrm{on}}}{K_2^{\mathrm{off}}}\right)^{(N_c-1)} K_2^{\mathrm{off}}}{1 + \frac{(N_c+2)K_1^{\mathrm{on}}}{(N_c-1)K_2^{\mathrm{off}}}} \quad N_c > 2,
\end{aligned} \tag{43}$$

the inverse of which provides a generalization of equation (7) from the main text. In this expression, we get a correction in the denominator compared to the less general result (40).

IV. BIASED SIMULATIONS

In order to disable simultaneous formation of multiple seeds, initially one receptor is placed on the grid. Immediately after the first bond is formed, the relevant number of receptors are placed on the row of neighboring sites. Further binding and unbinding events prompt placing and removing the neighboring rows, which yields the time evolution of the seed. The simulation is interrupted when a seed with the N_c number of bonds is formed, and the duration of the simulation recorded. The probability distribution shown in figure 5 of the manuscript is actually a normalized histogram of the nucleation times obtained by 2000 independent simulation runs.

[1] Bruinsma, R., Goulian, M., and Pincus, P. *Biophys. J.* **67**(2), 746 – 750 (1994).

[2] Lipowsky, R. Chapter 11 generic interactions of flexible membranes. In Structure and Dynamics of Membranes, Lipowsky, R. and Sackmann, E., editors, volume 1 of *Handbook of Biological Physics*, 521 – 602. North-Holland (1995).
[3] Speck, T., Reister, E., and Seifert, U. *Phys. Rev. E* **82**(2), 021923 (2010).
[4] Gardiner, C. *Stochastic methods*. Springer, (1985).
[5] Muir, T. *A Treatise on the Theory of Determinants*. Dover Publications, Inc., New York, (1960).

P4

Multiscale approaches to protein-mediated interactions between membranes - Relating microscopic and macroscopic dynamics in radially growing adhesions

Multiscale approaches to protein-mediated interactions between membranes - Relating microscopic and macroscopic dynamics in radially growing adhesions

Timo Bihr[1,2], Udo Seifert[2] and Ana-Sunčana Smith[1,3]

[1]Institut für Theoretische Physik and the Excellence Cluster: Engineering of Advanced Materials, Universität Erlangen-Nürnberg, Nägelsbachstrasse 49b, 91052 Erlangen, Germany
[2]II. Institut für Theoretische Physik, Universität Stuttgart, Pfaffenwaldring 57, 70569 Stuttgart, Germany
[3]Institute Ruđer Bošković, Division of Physical Chemistry, Bijenička cesta 54, 10000 Zagreb, Croatia.

New J. Phys. **17** 083016

DOI: 10.1088/1367-2630/17/8/083016
http://iopscience.iop.org/1367-2630/17/8/083016

Abstract Macromolecular complexation leading to coupling of two or more cellular membranes is a crucial step in a number of biological functions of the cell. While other mechanisms may also play a role, adhesion always involves the fluctuations of deformable membranes, the diffusion of proteins and the molecular binding and unbinding. Because these stochastic processes couple over a multitude of time and length scales, theoretical modeling of membrane adhesion has been a major challenge. Here we present an effective Monte Carlo scheme within which the effects of the membrane are integrated into local rates for molecular recognition. The latter step in the Monte Carlo approach enables us to simulate the nucleation and growth of adhesion domains within a system of the size of a cell for tens of seconds without loss of accuracy, as shown by comparison to 10^6 times more expensive Langevin simulations. To perform this validation, the Langevin approach was augmented to simulate diffusion of proteins explicitly, together with reaction kinetics and membrane dynamics. We use the Monte Carlo scheme to gain deeper insight to the experimentally observed radial growth of micron sized adhesion domains, and connect the effective rate with which the domain is growing to the underlying microscopic events. We thus demonstrate that our technique yields detailed information about protein transport and complexation in membranes, which is a fundamental step toward understanding even more complex membrane interactions in the cellular context.

New Journal of Physics
The open access journal at the forefront of physics

Deutsche Physikalische Gesellschaft DPG
IOP Institute of Physics

Published in partnership with: Deutsche Physikalische Gesellschaft and the Institute of Physics

OPEN ACCESS

RECEIVED
5 March 2015

REVISED
2 July 2015

ACCEPTED FOR PUBLICATION
8 July 2015

PUBLISHED
10 August 2015

PAPER

Multiscale approaches to protein-mediated interactions between membranes—relating microscopic and macroscopic dynamics in radially growing adhesions

Timo Bihr[1,2], **Udo Seifert**[2] **and Ana-Sunčana Smith**[1,3]

[1] Institut für Theoretische Physik and the Excellence Cluster: Engineering of Advanced Materials, Universität Erlangen-Nürnberg, Nägelsbachstrasse 49b, D-91052 Erlangen, Germany
[2] II. Institut für Theoretische Physik, Universität Stuttgart, Pfaffenwaldring 57, D-70569 Stuttgart, Germany
[3] Institute Ruder Bošković, Division of Physical Chemistry, Bijenička cesta 54, 10000 Zagreb, Croatia

E-mail: smith@physik.fau.de

Keywords: theory, modeling and simulations, protein–ligand interactions, membranes

Abstract

Macromolecular complexation leading to coupling of two or more cellular membranes is a crucial step in a number of biological functions of the cell. While other mechanisms may also play a role, adhesion always involves the fluctuations of deformable membranes, the diffusion of proteins and the molecular binding and unbinding. Because these stochastic processes couple over a multitude of time and length scales, theoretical modeling of membrane adhesion has been a major challenge. Here we present an effective Monte Carlo scheme within which the effects of the membrane are integrated into local rates for molecular recognition. The latter step in the Monte Carlo approach enables us to simulate the nucleation and growth of adhesion domains within a system of the size of a cell for tens of seconds without loss of accuracy, as shown by comparison to 10^6 times more expensive Langevin simulations. To perform this validation, the Langevin approach was augmented to simulate diffusion of proteins explicitly, together with reaction kinetics and membrane dynamics. We use the Monte Carlo scheme to gain deeper insight to the experimentally observed radial growth of micron sized adhesion domains, and connect the effective rate with which the domain is growing to the underlying microscopic events. We thus demonstrate that our technique yields detailed information about protein transport and complexation in membranes, which is a fundamental step toward understanding even more complex membrane interactions in the cellular context.

1. Introduction

At the origin of many biological phenomena is cell adhesion promoted by the formation of macromolecular ensembles. Despite intensive research over the last two decades [1–13] and the pressing biological significance [14–18], the growth of these structures in membranes is still poorly understood. Formation of adhesions involves a number of stochastic events occurring on different length and timescales. The minimal system involves protein diffusion and formation of bonds, which occurs on characteristic times of $10^{-5} - 10^{-2}$ s. These two processes couple to fast membrane fluctuations ($10^{-9} - 10^{-6}$ s). Several length scales are also involved—from nanometer separations necessary for molecular recognition to the micron-sized objects that are being grown. Moreover, molecular complexation induces membrane deformations which in turn promotes long-range cooperative effects. If all these elements are considered, difficulties in modeling the dynamics of macromolecular scaffolding come as no surprise.

Early attempts to model the formation of macromolecular structures were related to interactions of protein-decorated membranes with underlying substrates containing the appropriate binding partners in the adhesion process. Thereby, analogies with classical theories of growth (Stefan problem and kinetically limited aggregation) were explored [19–22]. Other approaches focused on the role of the membrane fluctuations

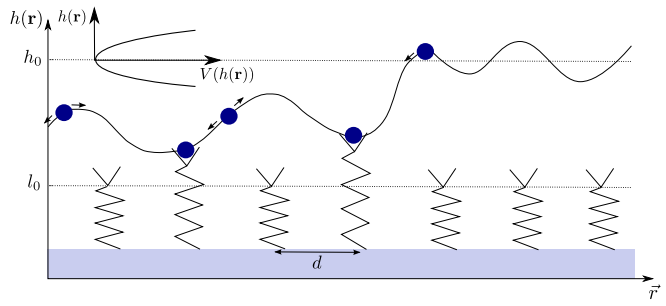

Figure 1. In the model, the fluctuating membrane carries mobile ligands, which bind to immobile receptors placed equidistantly on the surface (characteristic spacing d). The formation of bonds is associated with the deformation of the receptor and the membrane, the latter being subject to a nonspecific harmonic potential with a minimum at h_0.

[23, 24]. Furthermore, a number of scaling laws were suggested after the analysis of the relationship between the various involved stochastic processes[25]. However, only limited experimental confirmation has been obtained to support these arguments [26, 27].

Later efforts concentrated on the construction of accurate simulation schemes that treat the membrane fluctuations explicitly. First, dynamics of domain formation was studied by Monte Carlo approaches where furthermore the diffusion was treated by a random walk and complexation of proteins was explored through Metropolis rates [5, 28, 29]. Concomitantly, Langevin simulations [4, 30–33] were developed. In earlier attempts[4, 30, 31], binding and unbinding was not considered, while later efforts involved rates that are functions of the instantaneous membrane profile [32, 33]. The problem with all these methods is that only micron-sized systems could be studied for about a millisecond. Consequently, long time-scale dynamics associated with the formation of larger macromolecular structures, such as radially growing domains and diffusion-limited aggregation, remained out of reach. To address these biologically relevant issues, significant efforts went toward developing coarse-grained simulation methods. This resulted in mapping the problem onto lattice gas and Ising-like models [34–38], which is, however, accurate only in a limited range of parameters.

Here we build on the experience in coarse-graining the dynamics of nucleation of macromolecular complexes in membranes [39]. We solve the problem of coupling time and length scales by constructing an effective Monte Carlo simulation scheme, for which we demonstrate applicability in a very broad range of parameters. The stepping stone for our approach is the realization that there is a clear separation of time scales between membrane fluctuations and protein binding and diffusion. This allows us to fully circumvent simulating the membrane, by incorporating its influence into effective rates for the (de)complexation of proteins. We validate our scheme against explicit Langevin simulations [33], which themselves were shown to agree very well with experiments in the context of the nucleation [40] and the morphology of adhesion domains [32]. In order to make this comparison easier, we first present the underlying theoretical model, its direct implementation into the augmented Langevin scheme and, then, the upscaling and the construction of the effective Monte Carlo scheme. Furthermore, we demonstrate the potential of the Monte Carlo scheme by simulating radially growing domains containing up to 10^5 ligand–receptor bonds over several seconds, as observed in analogous experiments. This allows us to explore the membrane associated processes with very high precision, and to provide deeper understanding of the overall dynamics.

2. Model

Our model system (see figure 1) consists of a flexible membrane that is positioned above a solid substrate. Receptors on the substrate can form bonds with ligands, embedded in the membrane. Even though the receptors fluctuate in height, they stay normal to the solid substrate. The receptors are placed on a regular square grid and are immobile in the current context. The ligands can diffuse within the membrane until a bond is formed and therefore the membrane is locally pulled towards the substrate. More elaborate versions of our model allow for both binders to be mobile and coupled to different reservoirs, simulating a finite vesicle, or an infinite bilayer. Furthermore, binder species with different properties can be simultaneously introduced.

Table 1. Variables and parameters of our Helfrich–Hamiltonian (see equations (1) and (2)).

Quantity	Meaning	Unit
a	Lattice constant	10 nm
$h(\mathbf{r})$	Membrane profile	a
l_0	Rest length of the bond/receptor	a
α	Width of interaction potential	a
$\mathbf{r_i}$	Position of bond i	a
h_0	Minimum of the interaction potential	a
A	Area of the simulation box	a^2
k_BT	Thermal energy at 300 K	4.14×10^{-21} J
κ	Bending rigidity	k_BT
ϵ_b	Binding enthalpy	k_BT
γ	Curvature of the interaction potential	k_BT/a^4
λ	Stiffness of the bond/receptor	k_BT/a^2
$N_b(t)$	Number of bonds	—

Table 2. Parameters used in the simulations.

Parameter	Values in simulation units	Values in SI units
a	–	10 nm
h_0	8 a	80 nm
α	1 a	10 nm
l_0	4 a	40 nm
d	8 a	80 nm
ρ_l	$1/64\ a^{-2}$	1.5625×10^{-4} nm^{-2}
A	$4096\ a^2$	0.4096 μm^2
ϵ_b	5 to 10 k_BT	2.12×10^{20} to 4.14×10^{20} J
κ	10 k_BT	4.14×10^{20} J
γ	$3.125 \times 10^{-3}\ k_BT/a^4$	1.3×10^{-27} J nm^{-4}
λ	0.75 to 5 k_BT/a^2	3.1×10^{-23} to 2.1×10^{-22} J nm^{-2}
η	$2.4 \times 10^{-7}\ k_BTsa^{-3}$	1 mPa s
k_0	2×10^4 to 5×10^5 s^{-1}	2×10^4 to 5×10^5 s^{-1}
D	5×10^3 to 5×10^5 a^2 s^{-1}	5×10^5 to 5×10^7 nm^2 s^{-1}

2.1. The membrane

The membrane is described as a thin sheet with an energy given by the Helfrich–Hamiltonian [41]

$$\mathcal{H}_M[h(\mathbf{r})] = \int_A \mathrm{d}^2\mathbf{r} \left(\frac{\kappa}{2}(\Delta h(\mathbf{r}))^2 + \frac{\gamma}{2}\Big[h(\mathbf{r}) - h_0\Big]^2 \right). \tag{1}$$

Specifically, the lipid bilayer is parametrized in the Monge gauge, where the height $h(\mathbf{r})$ is given as a function of the position $\mathbf{r}$ of the membrane above the substrate (figure 1). A list of the variables and parameters in equation (1) can be found in tables 1 and 2. Specifically, the first term in equation (1) is the deformation energy of the membrane, that is itself a product of the bending rigidity κ and the local mean curvature of the membrane.

While the specific protein molecules embedded in the cell wall (or membrane) are usually considered to be responsible for cell adhesion, over the past two decades a realization emerged that the cell membrane itself, being a floppy sheet, adds another unavoidable, yet not fully understood, interaction with the opposing surface it binds to. Although this interaction does not depend at all on any specific proteins, it can have a major impact on the protein-mediated adhesion and can be viewed as a mechanism that controls the binding affinity to the cell-adhesion molecules [42]. Such steric interactions [43] typically maintain the two membranes at relatively large separations h_0, which can be modeled by introducing a nonspecific harmonic potential of a strength γ with the minimum at h_0 [33, 44, 45]. The strength of this potential depends directly on the average intensity of membrane fluctuations that are themselves regulated by the tension in a membrane but also by numerous other factors such as the thickness and the composition of the glycocalyx. In the mimetic systems, this contribution is dominated by continuous interactions between the membrane and the substrate, such as gravity, polymer-repulsion, or Van-der-Waals forces [44, 46]. The strength of this potential can be obtained experimentally by the analysis of membrane fluctuations [47, 48].

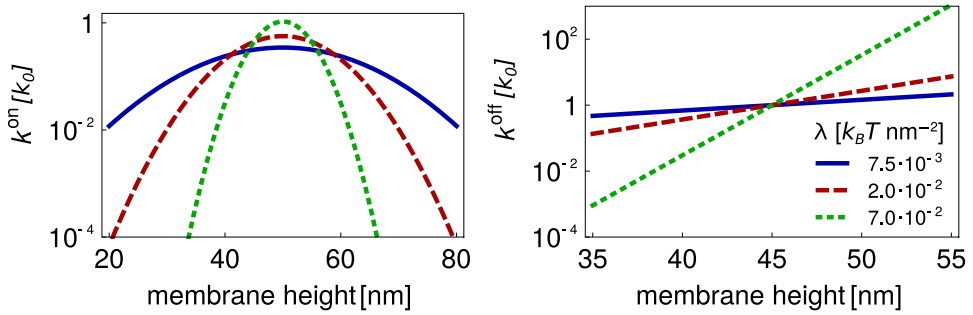

Figure 2. Local reaction binding (left) and unbinding (right) rates equations (4) and (5) shown as function of the membrane height. Other parameters were set as in table 2, except for the binding energy ($\epsilon_b = 0$).

2.2. The bonds

We assume that the receptors are thermalized springs with stiffness λ and rest length l_0. This leads to the following expression for the energy of the N_b bonds in the membrane

$$\mathcal{H}_B[h(\mathbf{r})] = \sum_{i=1}^{N_b} \delta(\mathbf{r} - \mathbf{r}_i)\left[\frac{\lambda}{2}\left(h(\mathbf{r}) - l_0\right)^2 - \epsilon_b\right]. \tag{2}$$

Here, ϵ_b accounts for the bond enthalpy gain for forming a bond and $\delta(\mathbf{r} - \mathbf{r}_i)$ is the Dirac-Delta function for the positions $\mathbf{r}_i$ of the bonds.

For a given instantaneous membrane profile $h(\mathbf{r}, t)$, each bond fulfills a local detailed balance condition for the transitions between the bound and unbound state, determined by the rates $k^{\text{off}}(h(\mathbf{r}, t))$ and $k^{\text{on}}(h(\mathbf{r}, t))$ as

$$\frac{k^{\text{off}}(h(\mathbf{r}, t))}{k^{\text{on}}(h(\mathbf{r}, t))} = \exp\left[\frac{\lambda}{2}\left(h\left(\mathbf{r}, t\right) - l_0\right)^2 - \epsilon_b - \frac{1}{2}\ln\left(\frac{\lambda\alpha^2}{2\pi}\right)\right]. \tag{3}$$

Here, α is the range of the interaction potential of the ligand–receptor bond and for simplicity, we set $\beta = (k_B T)^{-1} \equiv 1$. Equation (3) depends on the stretching energy of the bond (first term in the exponent), the binding affinity (second term) and an entropic contribution (last term) which describes the suppression of fluctuations if a receptor is bound to a ligand. This entropic contribution lowers the effective binding affinity [46], and has to be incorporated if the fluctuations of the receptor are not considered explicitly. The exact form of this term (see appendix B) emerges from the assumption that the structural fluctuations of free receptors occur on a faster time scale than the time scale of the membrane dynamics. This assumption is justified as the dynamics of the receptor is determined by thermal excitations of its secondary structure.

This local detailed balance condition (equation (3)) can be associated with the free energy gain for forming a bond [39], and will govern the stochastic binding and unbinding even if the thermodynamic equilibrium with respect to ligand–receptor binding has not been reached yet.

Inspired by [8, 49, 50], we set the rate $k^{\text{on}}(h(\mathbf{r}, t))$ to form a bond proportional to the probability of the binders being in the binding range α and the intrinsic reaction rate k_0. This naturally depends on the fluctuations, and the barrier for the forward process in the exponent

$$k^{\text{on}}(h(\mathbf{r}, t)) = k_0\sqrt{\frac{\lambda\alpha^2}{2\pi}}\,\exp\left[-\frac{\lambda}{2}\left\{\left(h\left(\mathbf{r}, t\right) - l_0\right) - \alpha\right\}^2\right]. \tag{4}$$

From this local on-rate and the detailed balance condition the local, off-rate can be determined readily

$$k^{\text{off}}(h(\mathbf{r}, t)) = k_0\exp[-\epsilon_b]\exp\left[\lambda\left(h\left(\mathbf{r}, t\right) - l_0\right)\alpha - \frac{\lambda\alpha^2}{2}\right]. \tag{5}$$

We show the reaction rates equations (4) and (5) in figure 2. The association rate adopts the form of a Gaussian with a width inversely proportional to the stiffness of the receptor. The maximal association rate is obtained at $l_0 + \alpha$, which is at the outer edge of the potential well associated with an unperturbed receptor. The off-rate increases exponentially with the distance between the receptor and the ligand. Interestingly, if the ligand is in the middle of the binding region ($l_0 + \alpha/2$), the stiffness of the receptor does not affect the breaking of the bond (the bond is not stressed).

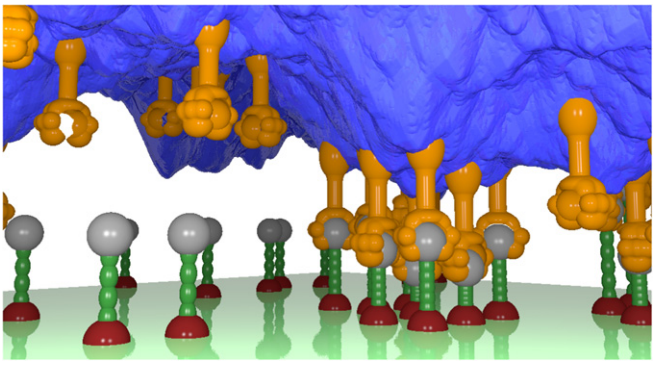

Figure 3. Snapshot of a simulation run. The grey receptor can form bonds with the orange ligands embedded in the fluctuating membrane (blue). The ligands can diffuse freely within in the membrane, whereas the receptors are immobilized and placed on a square grid.

2.3. Diffusion

Due to the membrane fluidity, the molecules within the bilayer diffuse on its surface [51]. Even though there may be an influence of the membrane elasticity on the diffusion of embedded proteins (for example by the curvature that a protein induces in the membrane [32, 52–54]), these effects seem to be small for experimental relevant parameters [53]. Therefore, we simulate the mobility of binders by a random walk, whereby two proteins interact laterally by a hard-core potential. The time step of the random walk is given by

$$\tau_d = \frac{a^2}{4D}, \tag{6}$$

with the diffusion constant D. In the current work, only the ligands embedded in the membrane of the vesicle are allowed to diffuse. However, it is straightforward to extend the simulation scheme to situations in which both binders retain lateral mobility and explore the surface of the membrane. The latter may be finite as in the case of vesicles and cells. These situations are simulated using periodic boundary conditions on the level of the system, with a selected area in the center of the simulation box representing the area of contact between two cells or the cell/vesicle and the substrate. Consequently, the formation of bonds can take place only within this region, and the remainder of the system will be depleted from the binders due to the accumulation in the zone of contact.

Binders can be also embedded in bilayers, which provides a constant chemical potential. For simulations of interactions with vesicles, a contact zone is defined, and the periodic boundary conditions are imposed for the bilayer grid. However, to maintain the constant chemical potential (constant concentration of binders in the bulk), entering and exiting of a binder from the contact zone is associated with placing or removing a binder from a random position outside the contact zone.

3. Langevin simulation scheme

3.1. Equation of motion for the membrane

In this scheme, the membrane shape (see figure 3) is determined explicitly in every time step. Thereby, the system is propagated in time by means of the Langevin equation in Fourier space (see e.g. [4, 32]) derived from the equations (1) and (2)

$$\frac{\partial h(\mathbf{k},\, t)}{\partial t} = -\Lambda(\mathbf{k})\left\{\left[\kappa k^4 + \gamma\right]\left(h\left(\mathbf{k},\, t\right) - \delta_{\mathbf{k},0} A h_0\right) + \sum_{i=1}^{N_b(t)} \lambda\left(h\left(\mathbf{r}_i,\, t\right) - l_0\right)\exp\left(-\mathrm{i}\mathbf{k}\cdot\mathbf{r}_i\right)\right\} + \xi(\mathbf{k}). \tag{7}$$

Here, $\Lambda(\mathbf{k})$ is the Oseen tensor, describing the hydrodynamic interaction between membrane and surrounding fluid, $N_b(t)$ is the number of bonds of the current bond configuration and A is the area of the membrane in the simulation. The stochastic force $\xi(\mathbf{k})$ in the Langevin equation above is set by the temperature of the surrounding fluid. Thereby, the Oseen tensor is connected to the stochastic force by the fluctuation-dissipation theorem

$$\langle \xi(\mathbf{k})\,\xi(\mathbf{k}')\rangle = 2k_B T \Lambda(\mathbf{k})\,\delta(\mathbf{k}+\mathbf{k}'). \tag{8}$$

The definition of the Fourier transformation of the Langevin equation is given by

$$h(\mathbf{k}) = \int_A \mathrm{d}^2\mathbf{r}\ \exp(-\mathrm{i}\mathbf{k}\cdot\mathbf{r})h(\mathbf{r}); \qquad h(\mathbf{r}) = \frac{1}{A}\sum_{\mathbf{k}} \exp(\mathrm{i}\mathbf{k}\cdot\mathbf{r})h(\mathbf{k}). \tag{9}$$

In general, it was shown that the Oseen tensor depends on the geometry of the membrane [55]. However, this dependence is very weak for membranes far away from the substrate and only relevant for the four largest modes of the membrane for the parameters used in the simulations. Such a choice neglects the Helfrich interaction of the membrane with the planar surface [43, 56]. The latter effect should be small for binding of proteins of a size of 20–40 nm when the membrane fluctuates with amplitudes of less than 15 nm, which seems to be the relevant range [9, 57, 58].

Thus, we use the Oseen tensor for a free membrane

$$\Lambda(\mathbf{k}) = \frac{1}{4\eta k}, \tag{10}$$

where η is the viscosity of the surrounding fluid. The Oseen tensor for the $\mathbf{k} = 0$ mode diverges. Following [4], the Oseen tensor for this mode is set to

$$\Lambda(\mathbf{k}) = \frac{3\sqrt{A}}{8\pi\eta}. \tag{11}$$

The Langevin-equation (7) is solved numerically with the help of the Euler–Maruyama scheme (see for example [59]). The time step in this scheme has to be set below the smallest time scale of the membrane

$$\tau\left(k_{\max}\right) = \frac{4\eta k_{\max}}{\kappa k_{\max}^4 + \gamma}, \tag{12}$$

which is the typical relaxation time of the mode with the largest $\mathbf{k}$ in the simulation ($k_{\max} = \sqrt{2}\pi/a \approx 4\ \mathrm{nm}^{-1}$) and is on the order of 10^{-9} s.

3.2. Simulation scheme

The simulation is performed following the algorithm shown on the left in figure 4. The first step initializes the system. This involves the thermal equilibration of a free membrane obtained by executing 10^6 steps in the time loop explained below without the reactions and binder diffusion. After that, the ligands are placed randomly on their lattice, and the receptors are put on a grid of the second lattice.

The second step is the initialization of the time loop, where the step accounts for the shortest characteristic membrane time scale ($\Delta t \equiv \tau(k_{\max})$). Every time step involves (i) the calculation of the force on the membrane induced by the formed bonds in real space; (ii) the transformation of this force to the Fourier space; and (iii) the determination of bending and unspecific forces in Fourier space (first term in equation (7)). The sum of this forces is input to the Euler–Maruyama step, within which the membrane profile is updated in Fourier space and transformed back to real space. This back-transformation is a prerequisite for the execution of the association and dissociation step. Here, the binding probabilities are obtained from the equations (4) and (5), in which the height of the membrane and the time step of the simulation are required. As the time scale of the reactions is much larger than the typical time scale of the membrane, these probabilities are rather small.

Finally, the mobile ligands need to be displaced to one of the neighboring unoccupied sites. In principle, the diffusion of binders is characterized by the time step given by equation (6), in which case the probability to jump in any direction would be 1/4. However, as the time scale of the diffusion is typically several orders of magnitude larger than the step of the time loop (i.e. $\tau_D \gg \tau(k_{\max})$), the probability of a jump is rescaled to

$$p = \frac{\tau\left(k_{\max}\right)}{4\tau_D}. \tag{13}$$

This new probability guarantees the correct diffusive behaviour of the ligands. Here we note that this implementation decouples the simulation of diffusion from the simulation of the membrane. As a result, the ligand shape and the coupling of diffusion to the membrane curvature is not considered, in contrast to earlier works [52, 53, 60]. However, in the context of adhesion, the curvature coupling is a small effect, justifying this approximation.

In the current simulations, the ligands are immobilized after they form a bond with a receptor, which means that only free ligands diffuse. This restriction is motivated by the experimental observation that the bonds change position only if they are subject to a significant lateral force [61]. After the diffusion has been resolved, a new iteration in the time loop is started, or the simulation is terminated.

Computationally, most time in this simulation scheme is consumed by fast Fourier transformations of the membrane profile and the forces, which scale like $N\ \log(N)$, (N is the number of considered lattice points), and

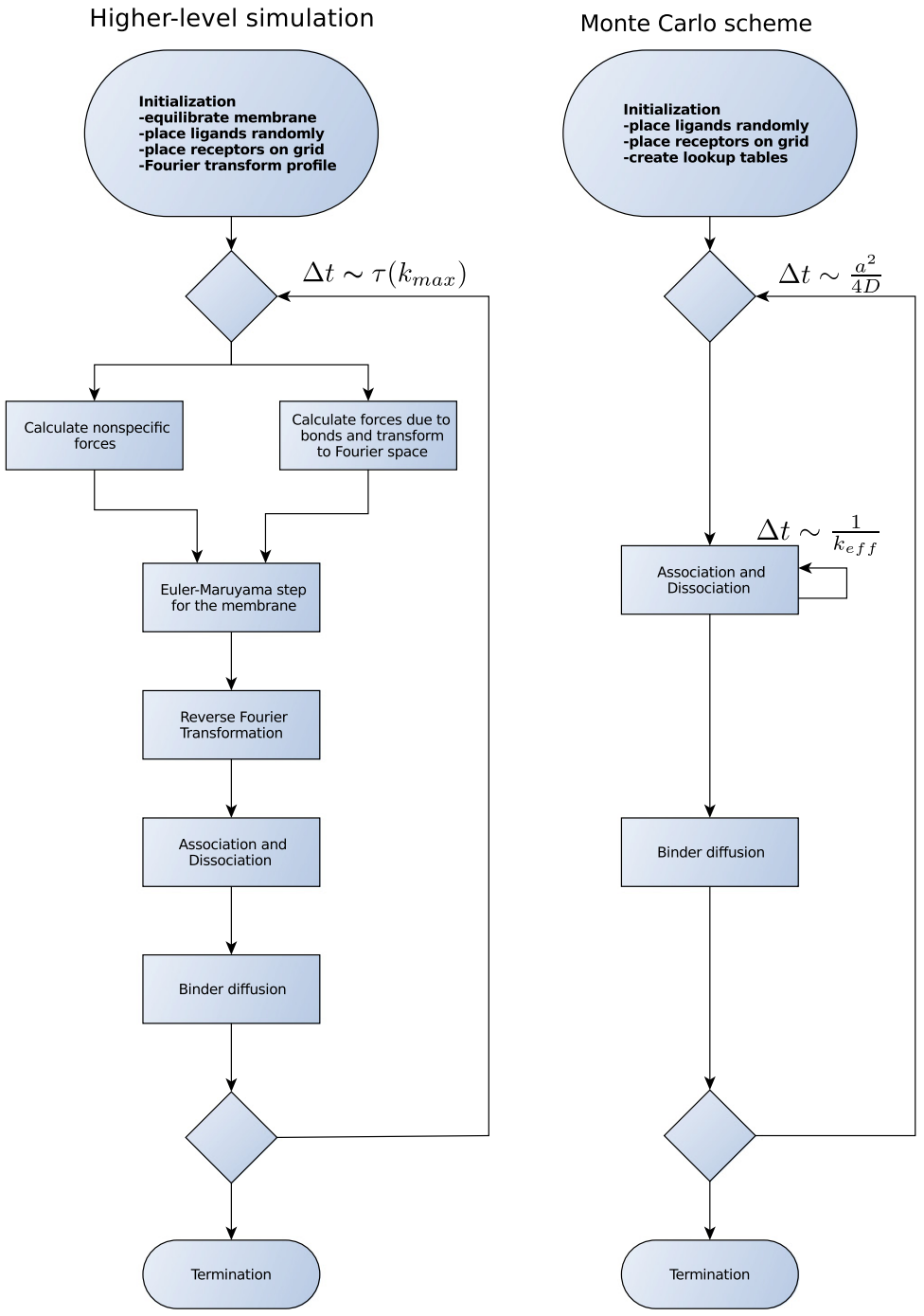

Figure 4. Simulation schemes. Left side: Langevin scheme. The membrane is simulated explicitly. However, computational expensive Fourier transformations have to be performed. Right side: effective Monte Carlo scheme. The binding kinetics is simulated with the effective reaction rates (18) and circumventing the explicit treatment of the membrane.

not linearly like other operations (diffusion and reaction kinetics). Furthermore, the time step has to be chosen very small to accurately describe the time evolution of the membrane, and a large number of replicas must be produced to obtain a statistically sound representation of the system. These are the main reasons which make this simulation scheme computationally very expensive allowing only for length scales of up to 1 μm^2 to be simulated for up to 10^{-1} s.

4. Effective Monte Carlo simulation

4.1. Effective rates

The difficulties that arise with Langevin simulations could be circumvented if the explicit treatment of the membrane could be avoided. We achieve this goal in an effective Monte Carlo scheme which is based on the recently acquired understanding of the effects of the membrane on the formation of bonds [39, 46, 48]. This scheme relies on the fact that the typical time scale of the membrane fluctuations depends on the viscosity η of the surrounding fluid

$$\tau_{\mathrm{mem}} = \frac{4\eta q_0}{\kappa q_0^4 + \gamma} = \frac{2\eta q_0}{\gamma} \simeq 2 \times 10^{-5}\ \mathrm{s}. \tag{14}$$

Here, $q_0 = (\gamma/\kappa)^{1/4}$ is the inverse lateral correlation length for a membrane without tension.

Importantly, even the slowest modes are significantly faster than the reaction kinetics for ligand–receptor binding (the fastest avidin-biotin in membranes was reported to take place at $\sim 10^3\ \mathrm{s}^{-1}$ [40, 42]), while other pairs are found at $\sim 10^2\ \mathrm{s}^{-1}$ [8, 42]. Consequently, the membrane fluctuations can be regarded as equilibrated with fixed mean shape as long as the configuration of bonds interacting with the membrane remains unchanged. During this time, the fluctuating membrane, and with it the ligands, sample the entire probability distribution of distances between ligands and receptors. In the following, we denote the height distribution at the considered binding site $\mathbf{r}$ before the bond has formed by $p(h^r)$, and the height distribution after a bound ligand–receptor pair is formed by $p(h^b)$. Here h^r is the height at a binding site before a bond is established and h^b is the height after a bond is established. The distribution of the latter is nontrivial if the receptor or the bond itself maintains some flexibility.

The first and the second moment of these typically Gaussian distributions (equations (15) and (16)) can be calculated explicitly [46] yielding the mean height h^s and the fluctuation amplitude σ^s of the membrane at the binding site for an arbitrary bond configuration. Here the superscript s denotes the state at the binding site, which can be either a free receptor ($s = r$) or an existing bond ($s = b$). Specifically, we calculate a functional integral over all membrane profiles weighted by their Boltzmann factor (see appendix A for technical details). As result, we obtain the mean height

$$\langle h(\mathbf{r})\rangle \equiv \bar{h}^s(\mathbf{r}) = \frac{-\frac{4}{\pi}\sum_{ij} l_0 G_{ij}(\mathbf{r})^{-1}\mathrm{kei}\left(q_0\ |\mathbf{r}-\mathbf{r}_\mathrm{i}|\right)}{8\sqrt{\kappa\gamma} + \frac{16}{\pi^2}\sum_{ij}\mathrm{kei}\left(q_0\ |\mathbf{r}-\mathbf{r}_\mathrm{i}|\right)G_{ij}(\mathbf{r})^{-1}\mathrm{kei}\left(q_0\ |\mathbf{r}-\mathbf{r}_\mathrm{j}|\right)} \tag{15}$$

and the fluctuation amplitude

$$\begin{aligned}\langle h^2(\mathbf{r})\rangle - \langle h(\mathbf{r})\rangle^2 &\equiv \left(\sigma^s\right)^2(\mathbf{r}) \\ &= \left(8\sqrt{\kappa\gamma} + \sum_{ij}\frac{16\mathrm{kei}\left(q_0\ |\mathbf{r}-\mathbf{r}_\mathrm{i}|\right)G_{ij}(\mathbf{r})^{-1}\mathrm{kei}\left(q_0\ |\mathbf{r}-\mathbf{r}_\mathrm{j}|\right)}{\pi^2}\right)^{-1}.\end{aligned} \tag{16}$$

The sum runs over all pairs of bonds in the membrane at the positions $\mathbf{r}_\mathrm{i}$ and $\mathbf{r}_\mathrm{j}$, while $\mathrm{kei}(x)$ is the Kelvin function [62]. The elements of the coupling matrix $G_{ij}(\mathbf{r})$ are the effects of the existing bonds on the shape and fluctuations at the arbitrary position $\mathbf{r}$, whereby the membrane mediated interaction between the bonds are comprised in the off-diagonal elements (see equation (A.9) for the explicit form of the matrix).

The average shape and the fluctuation amplitude of a membrane containing a small cluster of bonds are shown in the top panels of figure 5. At large distances from the cluster, the membrane is on average flat since it resides and fluctuates in the minimum of the nonspecific potential. Because of a relatively high concentration of bonds within the cluster the membrane is likewise flat on average, but much closer to the substrate. At the same time, its fluctuations are strongly suppressed. However, the shape and fluctuations of the membrane are significantly different in the vicinity of the bonds at the edge and in the center of the cluster.

We use the two height distribution functions to average the Bell–Dembo rates (equation (4) and (5)) at the position of a free or a bound receptor giving rise to effective binding and unbinding rates

$$\begin{aligned}K^{\mathrm{on}} &\equiv \int \mathrm{d}h^r p\left(h^r\right)k^{\mathrm{on}}\left(h^r\right) \\ K^{\mathrm{off}} &\equiv \int \mathrm{d}h^b p\left(h^b\right)k^{\mathrm{off}}\left(h^b\right).\end{aligned} \tag{17}$$

Appropriately inserting equations (4), (5), (15), and (16) into the the above expression, and evaluating the integrals yields

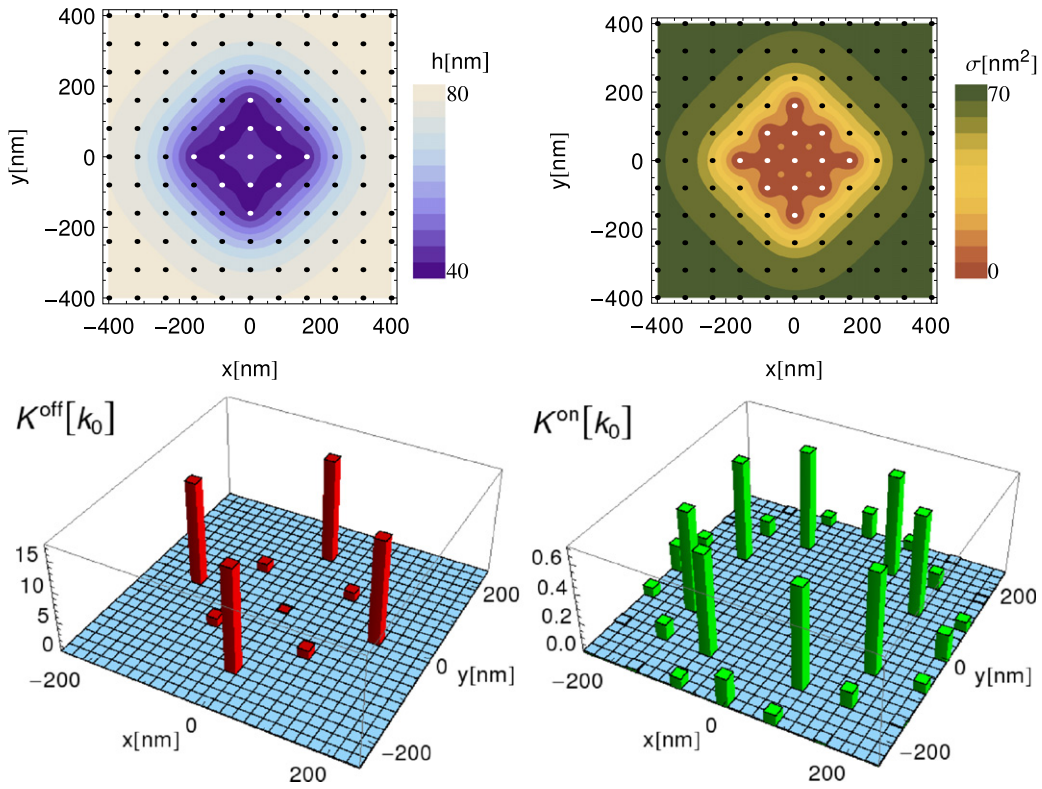

Figure 5. Membrane profile (top, left), fluctuations (top, right), effective off-rates (bottom, left) and effective on-rates (bottom, right) for a given bond configuration (white bonds and black free binding sites). The bond stiffness λ is set to infinity and the binding affinity ϵ_b to zero for simplicity. The remaining parameters can be found in table 2.

$$K^{\mathrm{on}} = k_0 \frac{\sqrt{\lambda\alpha^2}}{\sqrt{2\pi\left(1+\lambda\left(\sigma^r\right)^2\right)}} \exp\left[-\frac{\lambda\left[\bar{h}^r-\left(\alpha+l_0\right)\right]^2}{2\left(1+\lambda\left(\sigma^r\right)^2\right)}\right],$$

$$K^{\mathrm{off}} = k_0 \exp\left[\left(\frac{\lambda\alpha}{2}\left\{2\left(\bar{h}^b-l_0\right)+\alpha\left[\lambda\left(\sigma^b\right)^2-1\right]\right\}-\epsilon_b\right)\right]. \tag{18}$$

In this manner, the effective rates describing the association and the dissociation of a bond depends on the exact position of a bond, and the time dependent configuration of all bonds in the system. Examples of such rates for one bond configuration can be seen in bottom panels of figure 5. Obviously, the rates reflect the average shape and fluctuations within the membrane (top panels), which are the result of the bond configuration around the respective binding site. The dissociation rate of a bond at the rim is up to two orders of magnitude larger than for a bond deep within the domain (see figure 5). This is due to the stabilization effects of the neighboring bonds, which share the deformation load and cooperatively suppress the fluctuations. On the other hand, the association rate is the largest near the bond domain and exponentially decreases on the length scale of the lateral correlation length with increasing distance to the domain.

To summarize, cooperative effects between bonds and binding sites are induced by the deformation of the membrane in the vicinity of the bond and the changes in membrane fluctuations. In the absence of cooperative effects, the rates are constant at every binding site (see figure 3, [39] for additional details), because the deformation is either not reaching the first neighbors (very soft membranes) or the membrane does not deform at all (receptors significantly more flexible than the membrane). However, if the formation of a bond induces changes in the membrane, the effect is relatively short range.

4.2. Simulation scheme

We can now construct a Monte Carlo simulation of the adhesion process in which only the reaction kinetics and the diffusion of binders must be treated explicitly. Thereby, the effective rates for breaking or forming a bond at the given site must be determined for each site in every time step. This in turns requires inverting the coupling matrix containing all bonds, for every site in every step. In order to make the simulation fast, we assume that only the first two sets of neighboring bonds affect the rates on a particular (un)binding site (figure 6). Consequently, only the configuration of bonds in the immediate environment is taken into account in the calculation of the

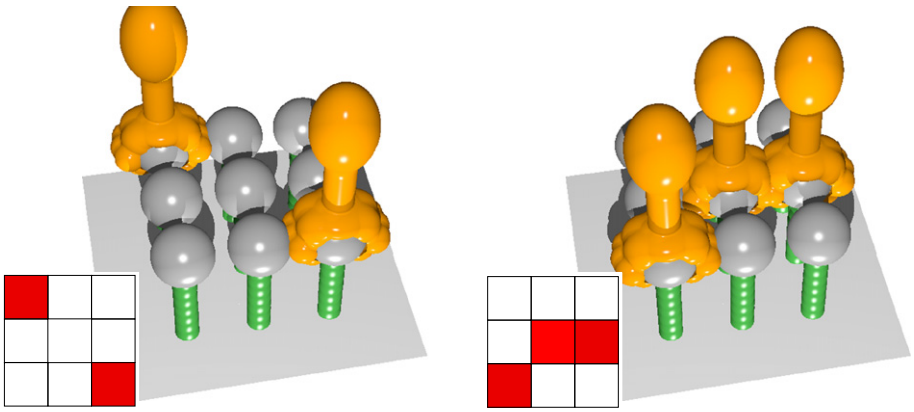

Figure 6. Example for a possible bond configuration two (left) or three (right) bonds (red squares). The association (left) or dissociation (right) rate at the considered binding site (center square) is determined by identifying the bond configurations (red) around the binding site and retrieving the appropriate reaction rate from the lookup table. This is done for all binding sites during one iteration.

effective rates. Since this environment consists only of 9 sites, all possible configurations can be explored *a priori*, and their respective rates used to create a lookup table. This restriction to the next-nearest neighbours is justified because the binding rates decay very fast with increasing distance between the bonds.

A flow chart of the Monte Carlo scheme is shown on the right panel of figure 4. To initialize the system, all ligands and receptors are positioned on their respective grids as in the Langevin simulations (random and ordered distributions are possible). Furthermore, the characteristic time steps are determined. The time step of the simulation is given by the characteristic diffusion–time $\Delta\tau_D$ (equation (6)). The time step for the reaction kinetics is set to be $\Delta t_B = \Delta\tau_D/n$, where n is the smallest integer satisfying the inequality $K^{\mathrm{on/off}}\Delta\tau_D/n < 1$. From here the probabilities for binding and unbinding are calculated as $K^{\mathrm{on/off}}\Delta t_B$, and stored in a lookup table.

The simulation step starts with the reaction loop which consists of n iterations. In each iteration, for every binding site (i) the bond configuration is determined, (ii) the appropriate rate is retrieved from the lookup table, (iii) association or dissociation is attempted, and (iv) the bond configuration is updated. Following the reaction loop, each binder attempts to move to a neighboring site in a same manner as in the Langevin scheme. This completes the simulation step and the system is propagated in time until the program is terminated. While the program allows for the diffusion of both binder types, the following discussion will be restricted to the case when the receptors are immobilized.

The advantage of the Monte Carlo scheme is that it allows for a larger time step and avoids fast Fourier transformations limiting the Langevin code. This allows us to simulate length scales of several tens of micrometers and time scales of several seconds with the resolution of about 100 nm and 10^{-5} s, which is necessary to understand biological processes.

5. Validation of the Monte Carlo scheme

In order to evaluate the applicability of the effective rates, we perform an extensive comparison of the results of the Langevin and Monte Carlo simulations. For this purpose, all parameters, the system size, and the statistics of data acquisition in the two approaches is identical and no fit parameters are used in the following discussion.

We explore a very wide range of parameters: from soft to rather stiff receptors, binding affinities from the unstable to the enthalpy dominated adhesion, fast and slow diffusion of ligands (equivalent to changing the attempt reaction frequency).

5.1. Early stages of domain formation–nucleation dynamics

We first focus on the simulation of rare events such as is the nucleation of adhesion domains. The number of bonds in such a domain can be calculated explicitly within the capillary approximation [39]. Once this number is estimated we perform about 2000 simulations with each method to generate the distribution of nucleation times (figure 7). Specifically, each simulation is set to start from an equilibrated box with zero bonds. When a cluster of bonds of critical size is formed anywhere in the system, the simulation is interrupted, and the time necessary to achieve this domain size is recorded. As shown in figure 7, very good correspondence of the coarse-grained and the higher-level simulation approach is obtained for the entire distribution of nucleation times. This agreement could have been anticipated from the successful comparison of Langevin simulations with the

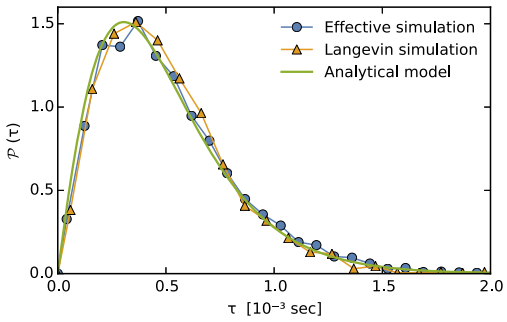

Figure 7. Distribution of nucleation times. The effective scheme, the Langevin scheme and the analytical model produce the same distribution of nucleation times (without fitting parameter). The analytical curve is determined from the equation (6) in Bihr *et al* [39]. The intrinsic binding affinity for protein binding is set to $\epsilon_b = 6.56\ k_BT$, while the diffusion constant is $D = 5\ \mu\text{m}^2\ \text{s}^1$. All simulations were performed in a simulation box of 640 nm × 640 nm with the densities of receptors and ligands of $\rho_r = \rho_l = 1.5625 \times 10^{-4}\ \text{nm}^{-2}$. The intrinsic binding rate was set to $k_0 = 10^5\ \text{s}^{-1}$, and the receptors are modeled as springs of stiffness $\lambda = 2 \times 10^{-2}\ k_BT\ \text{nm}^{-2}$.

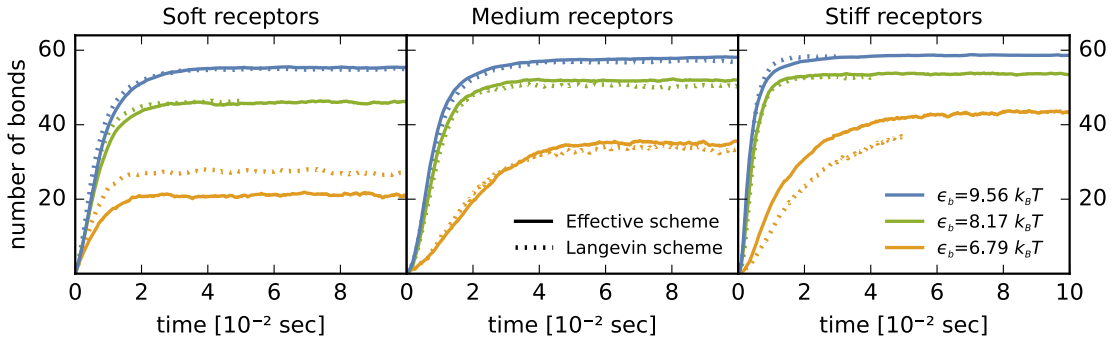

Figure 8. Time evolution of the number of bonds for $\lambda = 7.5 \times 10^{-3}\ k_BT\ \text{nm}^{-2}$ and $k_0 = 1.6 \times 10^5\ \text{s}^{-1}$(left), $\lambda = 2 \times 10^{-2}\ k_BT\ \text{nm}^{-2}$ and $k_0 = 10^5\ \text{s}^{-1}$ (middle) and $\lambda = 5 \times 10^{-2}\ k_BT\ \text{nm}^{-2}$ and $k_0 = 6.1 \times 10^4\ \text{s}^{-1}$ (right) (remaining parameters see table 2). We compare the effective scheme (full lines) with the Langevin scheme (dotted lines).

analytic model for the nucleation dynamics of a single seed, based on a simplified version of the here used effective rates [39]. The current, more accurate approach fully validates the concept of the effective rates and enables studies of the early stages of the adhesion process in the regimes that are either not accessible to analytic modeling or are extremely demanding from the computational point of view. Examples of such regimes, which can be now addressed with ease, are fast nucleation, competitive growth of multiple seeds, or diffusion limited nucleation.

5.2. Full dynamics

Encouraged by our results reproducing the nucleation dynamics, we validate the Monte Carlo scheme by reproducing the results of the higher level scheme for the full dynamic adhesion process, i.e. nucleation, growth and saturation to equilibrium. More specifically, for each set of parameters we perform 200 runs over which we average the dynamic process. This level of accuracy was found previously to produce converged results for the Langevin scheme in thermal equilibrium [32, 33].

We first explore the correspondence of the two schemes when the diffusion of ligands is fast ($D = 5 \times 10^7\ \text{nm}^2\ \text{s}^{-1}$), for soft, moderately stiff, and stiff receptors (figure 8). In each graph, the number of bonds as a function of time is presented for three different binding affinities (the smallest being at the phase transition to the unstable adhesion dominated by unbinding, two intermediate affinities, and one large affinity where the unbinding is negligible). In general, we find that the two approaches show very similar dynamics, irrespective of the choice of parameters.

Somewhat larger deviations (up to 15%) are observed at the phase boundary ($\epsilon_b = 6.79\ k_BT$) between the 'stable' and 'unstable' adhesion. Here, stable adhesion denotes a state with an equilibrium number of bonds that is always larger than zero, whereas in the 'unstable' state the membrane occasionally unbinds and the number of bonds spontaneously drops to zero [33]. In this regime, the simulations are more sensitive to the size of the micro-environment, unlike in the rest of the phase space where considering the first two sets of nearest

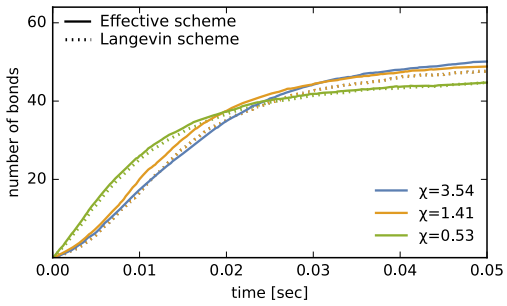

Figure 9. Simulation curves (full lines for effective scheme, dotted lines for Langevin scheme) for different values of $\chi = \lambda/(8\sqrt{\kappa\gamma})$ ($\epsilon_b = 7.26 k_B T$ and $D = 5 \times 10^5$ nm^2 s^{-1}), remaining parameters as in figure 8.

neighbors produces results which are very similar, and more accurate than considering larger neighborhoods with up to 20 sites.

Very similar results are obtained for slow diffusion of ligands (figure 9), where the adhesion dynamics is shown for three receptor rigidities, at an intermediate binding affinity. Equally good, quantitative agreement is obtained for all affinities above the transition energy (data not shown). These results validate convincingly the concept of effective rates, and establish the Monte Carlo approach as a reliable and versatile method for the simulation of protein mediated membrane interactions.

It should be noted that different effective Monte Carlo schemes, based on the integration of membrane fluctuations in the Hamiltonian were successful in comparison with the Langevin simulation [37], with the time scale of reactions being a free fitting parameter. However, the accuracy of that scheme relied on the magnitude of the effective cooperativity parameter χ to be much smaller than one. This dimensionless parameter evaluates the fluctuations of the unbound membrane with respect to the fluctuations of free receptors

$$\chi \equiv \frac{\lambda}{8\sqrt{\kappa\gamma}}. \tag{19}$$

The accuracy of the current scheme does not depend on the effective cooperativity parameter, which for the systems shown in figure 9 range from 0.53, for the softest receptors, to 3.54, for the stiff receptors. Actually, the regime of large effective cooperativity parameters seems to be very important in the context of experiments with cells or vesicles [63].

6. Simulations of radially growing domains

One of the basic mechanisms for the growth of adhesion domains is their radial expansion from a stable nucleus. As observed both in the cellular and cell-mimetic context, with different ligand–receptor pairs, such growth occurs naturally in membranes where the characteristic nucleation time is small compared to the dynamics of the domain expansion, and is common in situations where one of the binding partners is immobilized [61, 64]. Particularly well-studied are radially growing domains in ligand-decorated vesicles binding on a substrate functionalized with receptors [19, 42, 65]. In these systems, radial growth was used for the determination of the effective binding rate of various ligand–receptor pairs. This rate was found to depend significantly on the properties of the membrane due to strong correlations between the bonds [42].

The analysis of the growth dynamics [19, 20, 22] reveals that the growth of the domain is diffusion limited and the area of the domain increases linearly in time if the concentrations of ligands is smaller than the concentration of receptors [21, 42]. Otherwise, the growth is reaction limited, and the area grows quadratically. Treating the growth dynamics as a diffusion-reaction problem, the diffusion constant of ligands, and the effective binding constant was extracted from the data [19]. However, very little is known about the relation of such macroscopic measurements with the underlying microscopic binding and unbinding events, as well as protein motions in the membrane.

Unfortunately, the limited size of systems that can be studied with the Langevin scheme makes this approach unsuited for the analysis of the radial growth process. Nevertheless, using a large number of replicas to reconstruct the representative dynamics, effective affinity, as well as the growth patterns could be identified in the reaction limited case [32]. However, the issue of the system size is particularly acute for diffusion limited processes, when a depletion zone around the growing domain forms, and extends faster than the domain itself [19–21, 42]. This regime, as well as the continuous dynamics in the reaction limited case can only be obtained with the effective Monte Carlo approach developed here. As it will be shown in this section, such a study should

clarify how the cooperative effects transmitted by the membrane affect the microscopic rates and the overall dynamics.

6.1. Simulation details

We perform a series of Monte Carlo simulations, where we use two opposing square grids of a size of $40.96 \times 40.96\ \mu m^2$ in the diffusion limited case and of $10.24 \times 10.24\ \mu m^2$ in the reaction limited case (typical sizes of a giant unilamellar vesicle). The first grid carries 2.5×10^5 receptors (soft or stiff), immobilized on a lattice. To simulate diffusion or reaction limited growth, the second grid is decorated by randomly placing 5×10^4 diffusing ligands or placing immobile ligands above the receptors, respectively. These concentrations, as well as the other parameters are strongly inspired by the analogous experimental realizations of the system [42]. Specifically, the height of the membrane ($h_0 - l_0 = 55$ nm), curvature of the nonspecific potential ($\gamma = 3.125 \times 10^{-3}\ k_B T/a^4$), bending rigidity of the membrane ($\kappa = 10\ k_B T$), binding affinity ($\epsilon_b = 10\ k_B T$), intrinsic reaction attempt frequency ($k_0 = 10^5\ s^{-1}$) and the diffusion constant ($D = 5\ \mu m^2 s^{-1}$) is chosen such that the nucleation of domains and the unbinding of bonds are rare. Furthermore, we investigate the reaction and diffusion limited growth regimes for stiff ($\lambda = 5\ k_B T/a^2$) and soft receptors ($\lambda = 2\ k_B T/a^2$) mimicking bulky cell adhesion receptors and glycoprotein receptors, respectively.

6.2. Reaction limited growth

For ligand densities larger than the receptor density, we expect a quadratic growth of the domain area [19, 42, 65] containing N_b uniformly distributed bonds

$$N_b(t) = \pi \left(K_R^{on}\right)^2 a^4 \rho_l^{\,2} t^2. \tag{20}$$

Here, ρ_l is the initial density of ligands and K_R^{on} is the effective rate at the rim. This expression explicitly takes into account the two-dimensional nature of the growth process.

The results of our Monte Carlo approach (blue full lines in figures 10(c) and (d) confirm that the growth of the domain is, quadratic as expected. This is confirmed by the very good agreement of the data which we fit by equation (20), shown in figure 10 with dashed orange lines. The observed processes show that growth is faster for stiff ($K_R^{on} = 3.7 \times 10^4\ s^{-1}$) than for soft ($K_R^{on} = 2.0 \times 10^4\ s^{-1}$) receptors, presumably because of stronger correlations between bonds. Clear deviations from the quadratic behavior take place when the finite size effects start to play a role and the domain begins to cover the whole simulation box.

In order to relate the rates extracted from the fit to the microscopic rates which were actually used to grow the domains, we construct bubble charts for binding and unbinding rates (figures 10(e)–(h)), which are classified by the number of neighbors. A fixed number of neighbors can be organized in several different configurations around the receptor of interest, which results in the multiple bubbles for each number of neighbors. In the bubble charts, the area of the bubble is associated with the occurrence of a particular rate in the simulation.

Interestingly, the effective rate K_R^{on} corresponds very well to the average rate recorded in the simulation. Actually, for the stiff bonds the average rate at the rim, obtained by averaging all rates forming with up to five neighbors $\bar{K}^{on}$, is $\bar{K}^{on} = 3.7 \times 10^4\ s^{-1}$, and for soft bonds $\bar{K}^{on} = 2.5 \times 10^4\ s^{-1}$. Rates for the formation of bonds with three to five bonds in the neighborhood are most commonly observed (largest bubbles), which is consistent with the formation of new bonds at the edge of the domain. The rates for the formation of bonds with six or more neighbors are considered to be the results of events from rebinding within the domain, in agreement with the large number of dissociation events with seven and eight neighbors (figures 10(g) and (h)).

The analysis of microscopic rates in the bubble plots shows that the binding rates have a tendency to increase up to five neighbors. This happens because the formation of additional bonds, in principle, reduces the distance between the receptor and the ligand at the position of the binding site. The rates for forming the bond with 3–5 neighbors are significantly larger for stiff receptors, which is the source of the difference in the speed of the overall growth process of the domain. The reason for this difference is that for stiff receptors, the membrane approaches closer to the substrate than for soft receptors, which themselves deform while forming a bond, leaving the membrane at a larger height. Rates for forming a bond with 6–8 neighbors decrease with increasing the number of adjacent bonds. This effect is more significant for stiff receptors, because the fluctuations in the membrane are suppressed to a larger extent, and while the distance from the receptor is relatively small, stronger thermal membrane excitation is necessary to bring the ligand into the reaction zone of the receptor. The unbinding rates occur less frequently. The most common unbinding rate is the one with eight adjacent bonds, which is clearly associated with unbinding within the domain. The unbinding rates decrease exponentially as a function of the number of neighbors, for both stiff and soft receptors, showing the stabilization effects that binding in the surrounding has on the respective bonds.

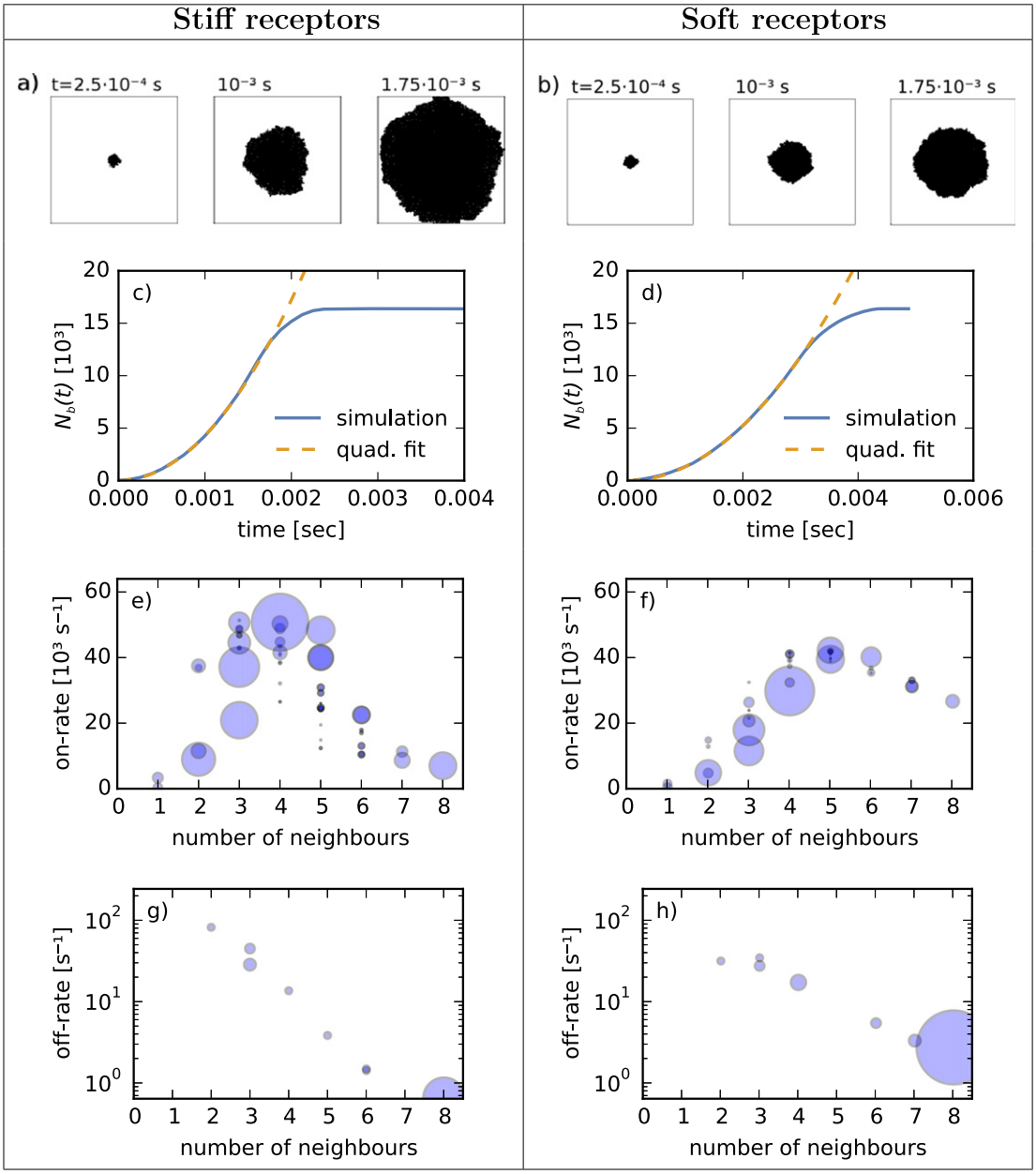

Figure 10. Simulation results of the reaction limited radial growth for stiff receptors (left panels) and soft receptors (right panels). The first row (a), (b) shows snapshots of the growing domain as a function of time whereas the second row (c), (d) shows the number of bonds in the domain as a function of time. In the third (e), (f) and the fourth row (g), (h), we present bubble charts of the binding and unbinding rates depending on the number of neighboring bonds during the growth phase. The area of the bubbles represents the number of reactions with charts.

6.3. Diffusion limited growth

For ligand densities lower than the receptor density, the growth is diffusion limited (figure 11), and depends only implicitly on the effective reaction rates through the density of ligands and bonds at the edge of the domain. In other words, the growth explicitly depends only on the diffusion constant, and the area of the growing domain $A(t)$ is given by [19, 21]

$$A(t) = 4\pi\alpha^2 Dt. \tag{21}$$

In this equation, α is a dimensionless speed factor (in contrast to earlier sections where it was the width of the interaction potential between the binders), which is, in two dimensions, determined from the implicit equation [21]

$$\frac{\rho_l - \rho_e}{\rho_b} = \alpha^2 \exp\left(\alpha^2\right) \mathrm{Ei}\left(\alpha^2\right). \tag{22}$$

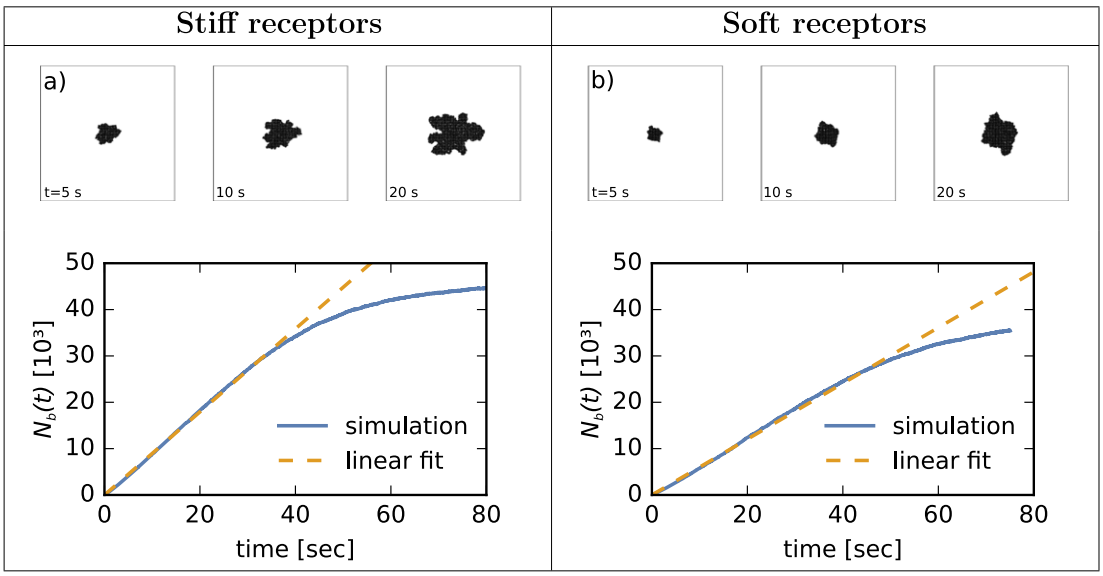

Figure 11. Simulation results of radial growth in the diffusion limited case. Top: snapshots of the growing domains. Bottom: growth curves with linear fit indicating diffusion limited growth. Parameters like in figure 10 except for initial ligand density (only 0.4×10^6 diffusing ligands).

Here, ρ_e is the density of ligands at the edge of the domain and $Ei(x)$ is the so-called exponential integral [62]. This relation is obtained from the binder conservation at the rim of the domain and the respective solution of the diffusion equation (see Shenoy and Freund [21] for details).

We numerically solve equation (22) using the densities of bonds and ligands at the edge of the domain evaluated from the radially averaged density profiles. We obtain $\alpha = 0.34$ for stiff receptors and $\alpha = 0.27$ for soft receptors. The difference in the speed factors emerges from the somewhat larger density of ligands at the rim of a domain with soft receptors in the simulation. This difference is due to the smaller binding rates at the rim of the domain with soft receptors. Using these speed factors, we can calculate the expected diffusion constant from the linear fit (orange dashed lines in figure 11). Specifically, we obtain a diffusion constant of $4.8 \pm 0.6\ \mu m^2\ s^{-1}$ for the large bond stiffness, and $5.2 \pm 0.7\ \mu m^2\ s^{-1}$ for the low bond stiffness (right column of figure 11). The error is due to the error of the bond density ρ_b and the density at the rim ρ_e. The relative error of the values of the diffusion constant compared with the diffusion constant of the simulation ($5.0\ \mu m^2\ s^{-1}$) is 4% which is within the accuracy of the fits. This confirms our initial hypothesis that in this density regime the diffusion limited growth is well accounted by the mean field approach.

6.4. Remarks in the experimental context

The obtained results from the simulations of the growth of ligand–receptor domains show that it is, in principle, possible to relate macroscopic measurements with the underlying microscopic processes. From diffusion limited processes we can extract the diffusion constant with excellent accuracy, which is also accessible from experimental data. However, as noted before [42], issues may arise if the crossover to the saturation of the growth curve due to the finite size of the vesicle or cell occurs relatively quickly and the vesicle runs out of free binders. Furthermore, it is possible to relate the mean reaction rate to the microscopic events.

The above presented analysis allows us to validate the Monte Carlo simulations, and in addition to show how the parameters characteristic for the mean field modelling relate to the microscopic stochastic processes of binding and diffusion. However, the behaviour described in this section is characteristic only in particular limits, whereas different growth laws are valid in different parts of the phase space. For example, if ligand–receptor bonds already form during the formation of the initial contact zone between the vesicle and the substrate, the dynamics has a different scaling behaviour [66]. The methods presented herein are a necessary prerequisite for the systematic study of the growth laws and will enable deeper understanding of the domain development in the regimes which are not accessible to analytic modelling.

7. Conclusions

We presented two different approaches for simulating protein-mediated adhesion between membranes. The first simulation scheme considers the deformation and the fluctuations of the membrane explicitly, by evolving the membrane profile with the help of a Langevin equation. The latter was derived from the Helfrich–Hamiltonian and included the hydrodynamic interaction between membrane and surrounding fluid. The binding and unbinding of ligands and receptors is modeled by Dembo's rates that are in detailed balance with the instantaneous shape of the membrane. Simpler variants of this scheme have been used successfully in earlier studies to describe thermal equilibrium [33] and reaction limited dynamics [32]. However, this scheme fails to describe the dynamics on longer length scales as well as diffusion limited processes. The problem arises from the fact that time step is as short as 10^{-9} s to correctly recover the membrane thermal excitations. Furthermore, the calculation of the membrane profile requires the use of Fast Fourier Transformations which scale the simulation time with $N\ \log(N)$, where N is the number of considered membrane segments. As a result, only membrane patches of about μm^2 carrying about 1000 proteins can be simulated for about 0.1 seconds.

We overcome these constraints by constructing an effective Monte Carlo scheme. In this scheme, we coarse-grain the adhesion dynamics by integrating the effects of the membrane into a set of effective reaction rates for ligand–receptor (un)binding. These rates are derived by averaging Dembo's rates over the membrane height fluctuations, which we do semi-analytically for an arbitrary bond configuration. This allows us to circumvent the explicit treatment of the membrane, and use a much larger time step in the simulation. Consequently, cell-sized objects (10^4 μm^2) carrying 10^6 proteins can be simulated for several tens of seconds with the resolution of 10 nm and 10^{-6} s. In this scheme, the simulation time scales linearly with the number of binders and the simulation time is thus reduced by a factor of about 10^6 for the parameters used in this study compared to the Langevin approach.

The current Langevin and MC approaches do not account for the effects of the tension in the membrane prior to adhesion. However, both simulation schemes can be easily adjusted to consider tension explicitly. For membranes dominated by bending deformations and fluctuations, the in-depth analysis of the correspondence between the Langevin and Monte Carlos simulations shows that the increased efficiency is achieved basically without loss of accuracy. This result was confirmed from the nucleation of adhesion domains and the early stages of growth to the asymptotic growth behavior and the saturation to an appropriate equilibrium state.

This very good performance allows a successful study of completely realistic scaffolding processes. As an example, we performed an analysis for radially growing domains, which is one of the most common scenarios for the development of adhesions. We demonstrate that the measurables that can be extracted from the macroscopic development of the domain can be related to underlying microscopic stochastic processes, namely the protein diffusion and the binding kinetics.

The simulations presented herein set a foundation for an in-depth analysis of protein transport and complexation dynamics in membranes, which is key to the understanding of the formation of functional microdomains and rafts. Furthermore, processes which present slow convergence or require correlations and signaling on the level of the entire cell are within the reach of accurate modeling. Now that the adhesion on the level of the membrane can be studied in great detail, the challenge becomes to couple the membrane to other cell structures and processes, which is a direction for future development.

Acknowledgments

We thank D Schmidt for stimulating discussions and critically reading the manuscript, and M Knoll for his support in the initial stages of this project. ASS and TB acknowledge the funding of the ERC StG 2013–337283 'MembranesAct', and the DFG RTG 1962 'Dynamic Interactions at Biological Membranes—from Single Molecules to Tissue' at FAU Erlangen.

Appendix A. Calculation of the membrane height distribution

The membrane height distribution depends on the bond configuration of the membrane and as well on the position of the binding site as can be seen in the following equation. By definition

$$p(h(\mathbf{r})) = \int \mathcal{D}[h'(\mathbf{r})]\ p[h'(\mathbf{r})]\,\delta(h'(\mathbf{r}) - h(\mathbf{r})), \tag{A.1}$$

where we have on the left side the probability distribution of the height $p(h(\mathbf{r}))$ at the binding site $\mathbf{r}$, whereas on the right side $p[h'(\mathbf{r})]$ is the probability for having a membrane profile $h'(\mathbf{r})$. This probability depends on the bond configuration (i.e. the positions $\mathbf{r_i}$ of the ligand–receptor bonds). For simplicity, we set $\beta \equiv (k_B T)^{-1} \equiv 1$.

To evaluate the above integral, the Boltzmann weight for $p[h'(\mathbf{r})]$ determined by the Helfrich–Hamiltonian equation (1) and (2) is plugged in and the Dirac function is written in the Fourier representation, which gives

$$p(h(\mathbf{r})) \propto \int \mathrm{d}\nu \int \mathcal{D}[h'(\mathbf{q})] \exp\Bigg[-\sum_{i=1}^{N_b} \frac{\lambda}{2}\left(h'(\mathbf{r}_i) - l_0\right)^2 - \frac{1}{2A}\sum_{\mathbf{q}} \| h'(\mathbf{q})\|^2 \left(\kappa q^4 + \gamma\right) + i\nu\left(h'(\mathbf{r}) - h(\mathbf{r})\right)\Bigg]. \tag{A.2}$$

We now apply successively N_b Hubbard–Stratonovich transformations, one for each bond term in the sum over i. This produces N_b Gaussian integrals over auxiliary fields ϕ_i. Furthermore, we write $h'(\mathbf{r})$ in the Fourier representation. As a result, we get

$$\begin{aligned} p(h(\mathbf{r})) \propto \int \mathrm{d}\nu \int \mathcal{D}[h'(\mathbf{q})] \left(\prod_j \int \mathrm{d}\phi_j\right) \\ \times \exp\Bigg\{ -\sum_j \frac{\phi_j^2}{2\lambda} + \sum_j \mathrm{i}l_0\phi_j - \mathrm{i}\sum_j \frac{\phi_j}{A}\sum_{\mathbf{q}} h'(\mathbf{q}) \exp\left(\mathrm{i}\mathbf{q}\cdot\mathbf{r}_j\right) \\ - \frac{1}{2A}\sum_{\mathbf{q}} \| h'(\mathbf{q})\|^2 \left(\kappa q^4 + \gamma\right) + \mathrm{i}\nu\frac{1}{A}\sum_{\mathbf{q}} h'(\mathbf{q}) \exp\left(\mathrm{i}\mathbf{q}\cdot\mathbf{r}\right) - \mathrm{i}\nu h(\mathbf{r})\Bigg\}. \end{aligned} \tag{A.3}$$

Performing the Gaussian integral over $h'(\mathbf{q})$ leads to

$$\begin{aligned} p(h(\mathbf{r})) \propto \int \mathrm{d}\nu \left(\prod_j \int \mathrm{d}\phi_j\right) \exp\left(-\sum_j \frac{\phi_j^2}{2\lambda} - \mathrm{i}\nu h(\mathbf{r}) + \sum_j \mathrm{i}l_0\phi_j\right) \\ \exp\Bigg\{ -\frac{1}{2A}\sum_{\mathbf{q}} \left[\frac{1}{\kappa q^4 + \gamma} \left(\sum_k \exp\left(-\mathrm{i}\mathbf{q}\cdot\mathbf{r}_k\right)\phi_k - \nu \exp(-\mathrm{i}\mathbf{q}\cdot\mathbf{r})\right)^2 \right]\Bigg\}. \end{aligned} \tag{A.4}$$

In the following step, the terms within the curly brackets of equation (A.4) are reorganized. After some sorting, we obtain

$$\begin{aligned} p(h(\mathbf{r})) \propto \int \mathrm{d}\nu \left(\prod_j \int \mathrm{d}\phi_j\right) \exp\left[-\frac{1}{2}\sum_{jk}\phi_j \left(\frac{\delta_{jk}}{\lambda} + \frac{1}{A}\sum_{\mathbf{q}} \frac{\exp\left(\mathrm{i}\mathbf{q}\cdot(\mathbf{r}_j - \mathbf{r}_k)\right)}{\kappa q^4 + \gamma}\right)\phi_k \right. \\ \left. + \sum_j \mathrm{i}l_0\phi_j \right] \exp\left[-\frac{1}{2}\frac{\nu^2}{8\sqrt{\kappa\gamma}} - \nu\left(\mathrm{i}h(\mathbf{r}) - \sum_j \phi_j \frac{1}{A}\sum_{\mathbf{q}} \frac{\exp\left(\mathrm{i}\mathbf{q}\cdot(\mathbf{r}_j - \mathbf{r})\right)}{\kappa q^4 + \gamma}\right)\right]. \end{aligned} \tag{A.5}$$

The sum over the Fourier modes in the first line can be transformed to an integral

$$\begin{aligned} \frac{1}{A}\sum_{\mathbf{q}} \frac{\exp\left(\mathrm{i}\mathbf{q}\cdot(\mathbf{r}_j - \mathbf{r}_k)\right)}{\kappa q^4 + \gamma} = \frac{1}{(2\pi)^2}\int \mathrm{d}\mathbf{q} \frac{\exp\left(\mathrm{i}\mathbf{q}\cdot(\mathbf{r}_j - \mathbf{r}_k)\right)}{\kappa q^4 + \gamma} \\ = \frac{1}{2\pi}\int_0^\infty \mathrm{d}q \frac{q J_0\left(q\,|\mathbf{r}_j - \mathbf{r}_k|\right)}{\kappa q^4 + \gamma} = -\frac{\mathrm{kei}\left(q_0\,|\mathbf{r}_j - \mathbf{r}_k|\right)}{2\pi\sqrt{\kappa\gamma}}, \end{aligned} \tag{A.6}$$

where

$$q_0 \equiv \zeta^{-1} \equiv \sqrt[4]{\frac{\gamma}{\kappa}} \tag{A.7}$$

is the inverse of the lateral correlation length. After the second equal sign, we use the definition of the Bessel function. The resulting integral can be found in [62] (equation (6.537)[4]). The sum at the end of the second line of equation (A.5) can be treated in the same way. This results in

[4] Please note that there is a typo. On the lhs in the nominator, it should be x instead of x^2.

$$p(h(\mathbf{r})) \propto \int \mathrm{d}\nu \left(\prod_j \int \mathrm{d}\phi_j\right) \exp\left[-\frac{1}{2}\sum_{jk}\phi_j \underbrace{\left(\frac{\delta_{jk}}{\lambda} - \frac{\mathrm{kei}\left(q_0\,|\mathbf{r_j}-\mathbf{r_k}|\right)}{2\pi\sqrt{\kappa\gamma}}\right)}_{\equiv M_{jk}}\phi_k + \sum_j \mathrm{i}l_0\phi_j\right] \exp\left[-\frac{1}{2}\frac{\nu^2}{8\sqrt{\kappa\gamma}} - \nu\left(\mathrm{i}h(\mathbf{r}) + \sum_j \phi_j \frac{\mathrm{kei}\left(q_0\,|\mathbf{r_j}-\mathbf{r}|\right)}{2\pi\sqrt{\kappa\gamma}}\right)\right]. \tag{A.8}$$

Performing the Gaussian integrals in ν gives after some algebra

$$p(h(\mathbf{r})) \propto \left(\prod_j \int \mathrm{d}\phi_j\right) \exp\left[-\frac{1}{2}\sum_{jk}\phi_i \underbrace{\left(M_{jk} - \frac{2\mathrm{kei}\left(q_0\,|\mathbf{r}-\mathbf{r_j}|\right)\mathrm{kei}\left(q_0|\mathbf{r}-\mathbf{r_k}\right)}{\pi^2\sqrt{\kappa\gamma}}\right)}_{\equiv G_{jk}(\mathbf{r})}\phi_j\right] \exp\left[\mathrm{i}\sum_j \phi_j\left(l_0 + h(\mathbf{r})\frac{4\mathrm{kei}\left(q_0\,|\mathbf{r}-\mathbf{r_j}|\right)}{\pi}\right) - \frac{1}{2}8\sqrt{\kappa\gamma}h^2(\mathbf{r})\right]. \tag{A.9}$$

Since the remaining integrals are again Gaussian, one finally gets

$$p(h(\mathbf{r})) \propto \exp\left[-h(\mathbf{r})\sum_{ij} l_0 G_{ij}(\mathbf{r})^{-1}\frac{4\mathrm{kei}\left(q_0\,|\mathbf{r}-\mathbf{r_j}|\right)}{\pi} - \frac{1}{2}\left(8\sqrt{\kappa\gamma} + \sum_{ij}\frac{16\mathrm{kei}\left(q_0\,|\mathbf{r}-\mathbf{r_i}|\right)G_{ij}(\mathbf{r})^{-1}\mathrm{kei}\left(q_0\,|\mathbf{r}-\mathbf{r_j}|\right)}{\pi^2}\right)h^2(\mathbf{r})\right]. \tag{A.10}$$

As the probability distribution (A.10) is itself a Gaussian distribution, again, the average height can be calculated by completing the square in the exponent. Consequently, one obtains

$$\langle h(\mathbf{r})\rangle \equiv \bar{h}(\mathbf{r}) = \frac{-\frac{4}{\pi}\sum \mathrm{ij}\; l_0 G_{ij}(\mathbf{r})^{-1}\mathrm{kei}\left(q_0\;\;|\mathbf{r}-\mathbf{r_i}|\right)}{8\sqrt{\kappa\gamma} + \frac{16}{\pi^2}\sum \mathrm{ij}\;\mathrm{kei}\left(q_0\;\;|\mathbf{r}-\mathbf{r_i}|\right)G_{ij}(\mathbf{r})^{-1}\mathrm{kei}\left(q_0\;\;|\mathbf{r}-\mathbf{r_j}|\right)}. \tag{A.11}$$

The fluctuations are simply given by

$$\langle h^2(\mathbf{r})\rangle - \langle h(\mathbf{r})\rangle^2 \equiv \sigma(\mathbf{r}) = \left(8\sqrt{\kappa\gamma} + \sum_{ij}\frac{16\;\mathrm{kei}\left(q_0\;\;|\mathbf{r}-\mathbf{r_i}|\right)G_{ij}(\mathbf{r})^{-1}\mathrm{kei}\left(q_0\;\;|\mathbf{r}-\mathbf{r_j}|\right)}{\pi^2}\right)^{-1}. \tag{A.12}$$

Appendix B. Entropic costs associated with binding of a fluctuating binder

The partition function of a free fluctuating receptor modelled as a harmonic spring is

$$Z_R = \int \mathrm{d}l\;\exp\left(-\frac{\lambda}{2}\left(l-l_0\right)^2\right) = \sqrt{2\pi/\lambda}, \tag{B.1}$$

where l is the coordinate of the spring and l_0 is the rest length. In the bound state, the receptor can explore only the width α of the interaction potential. Hence the entropic term in the free energy difference between an unbound and a bound receptor is

$$\Delta F \approx \frac{1}{2}\ln(2\pi/\lambda) - \ln(\alpha) = \frac{1}{2}\ln\left(\frac{2\pi}{\lambda\alpha^2}\right). \tag{B.2}$$

As such this contribution can be regarded as an entropic penalty for confining the receptor to the binding pocket [46].

References

[1] Sackmann E 1996 *Science* **271** 43–48
[2] Seifert U 1997 *Adv. Phys.* **46** 13–137
[3] Groves J T 2007 *Annu. Rev. Phys. Chem.* **58** 697–717
[4] Brown F L H 2008 *Annu. Rev. Phys. Chem.* **59** 685–712
[5] Weikl T R, Asfaw M, Krobath H, Rozycki B and Lipowsky R 2009 *Soft Matter* **5** 13
[6] Smith A S and Sackmann E 2009 *ChemPhysChem* **10** 66–78
[7] Brown F L H 2011 *Q. Rev. Biophys.* **44** 391–432
[8] Gao H, Qian J and Chen B 2011 *J. R. Soc. Interface* **8** 1217–32
[9] Fenz S F and Sengupta K 2012 *Integr. Biol.* **4** 982–95
[10] Maitre J L, Berthoumieux H, Krens S F G, Salbreux G, Julicher F, Paluch E and Heisenberg C P 2012 *Science* **338** 253–6
[11] James J R and Vale R D 2012 *Nature* **487** 5
[12] Amack J D and Manning M L 2012 *Science* **338** 212–5
[13] Schwarz U S and Safran S A 2013 *Rev. Mod. Phys.* **85** 1327–81
[14] Grakoui A, Bromley S K, Sumen C, Davis M M, Shaw A S, Allen P M and Dustin M L 1999 *Science* **285** 221–7
[15] Dustin M L, Chakraborty A K and Shaw A S 2010 *Cold Spring Harb Perspect. Biol.* **2** a002311
[16] Dustin M L and Groves J T 2012 *Annu. Rev. Biophys.* **41** 543–56
[17] Brasch J, Harrison O J, Honig B and Shapiro L 2012 *Trends Cell Biol.* **22** 299–310
[18] Sackmann E and Smith A S 2014 *Soft Matter* **10** 1644–59
[19] Boulbitch A, Guttenberg Z and Sackmann E 2001 *Biophys. J.* **81** 2743–51
[20] Freund L B and Lin Y 2004 *J. Mech. Phys. Solids* **52** 2455–72
[21] Shenoy V B and Freund L B 2005 *Proc. Natl Acad. Sci. USA* **102** 3213–8
[22] Gao H, Shi W and Freund L B 2005 *Proc. Natl Acad. Sci. USA* **102** 9469–74
[23] Raudino A and Pannuzzo M 2010 *J. Chem. Phys.* **132** 45103
[24] Raudino A and Pannuzzo M 2010 *J. Phys. Chem.* B **114** 15495–505
[25] de Gennes P G, Puech P H and Brochard-Wyart F 2003 *Langmuir* **19** 7112–9
[26] Cuvelier D and Nassoy P 2004 *Phys. Rev. Lett.* **93** 228101
[27] Puech P H, Askovic V, de Gennes P G and Brochard-Wyart F 2006 *Biophys. Rev. Lett.* **1** 85–95
[28] Weikl T R and Lipowsky R 2001 *Phys. Rev.* E **64** 11903
[29] Krobath H, Schütz G J, Lipowsky R and Weikl T R 2007 *Eur. Lett.* **78** 38003
[30] Lin L C L, Groves J T and Brown F L H 2006 *Biophys. J.* **91** 3600–6
[31] Lin L C L, Gov N and Brown F L H 2006 *J. Chem. Phys.* **124** 74903
[32] Reister-Gottfried E, Sengupta K, Lorz B, Sackmann E, Seifert U and Smith A S 2008 *Phys. Rev. Lett.* **101** 208103
[33] Reister E, Bihr T, Seifert U and Smith A S 2011 *New J. Phys.* **13** 25003
[34] Farago O 2008 *Phys. Rev.* E **78** 51919
[35] Farago O 2010 *Phys. Rev.* E **81** 50902
[36] Weil N and Farago O 2010 *Eur. Phys. J. E Soft* **33** 81–87
[37] Speck T, Reister E and Seifert U 2010 *Phys. Rev.* E **82** 21923
[38] Speck T 2011 *Phys. Rev.* E **83** 50901
[39] Bihr T, Seifert U and Smith A S 2012 *Phys. Rev. Lett.* **109** 258101
[40] Fenz S F, Bihr T, Merkel R, Seifert U, Sengupta K and Smith A S 2011 *Adv. Mater.* **23** 2622–6
[41] Helfrich W 1973 *Z. Naturforsch.* **28c** 693–703
[42] Bihr T, Fenz S, Sackmann E, Merkel R, Seifert U, Sengupta K and Smith A S 2014 *Biophys. J.* **107** L33 – L36
[43] Helfrich W 1978 *Z. Naturforsch.* **33** 305
[44] Bruinsma R, Behrisch A and Sackmann E 2000 *Phys. Rev.* E **61** 4253–67
[45] Weikl T R, Andelman D, Komura S and Lipowsky R 2002 *Eur. Phys. J.* E **8** 59–66
[46] Schmidt D, Bihr T, Seifert U and Smith A S 2012 *Europhys. Lett.* **99** 38003
[47] Rädler J O, Feder T J, Strey H H and Sackmann E 1995 *Phys. Rev.* E **51** 4526–36
[48] Schmidt D, Monzel C, Bihr T, Merke R, Seifert U, Sengupta K and Smith A S 2014 *Phys. Rev.* X **4** 021023
[49] Dembo M, Torney D C, Saxman K and Hammer D 1988 *Proc. R. Soc.* B **234** 55–83
[50] Erdmann T and Schwarz U S 2006 *Biophys. J.* **91** 60–62
[51] Saffman P G and Delbrück M 1975 *Proc. Natl Acad. Sci. USA* **72** 3111–3
[52] Naji A, Atzberger P J and Brown F L H 2009 *Phys. Rev. Lett.* **102** 138102
[53] Reister-Gottfried E, Leitenberger S M and Seifert U 2010 *Phys. Rev.* E **81** 31903
[54] Quemeneur F, Sigurdsson J K, Renner M, Atzberger P J, Bassereau P and Lacoste D 2014 *Proc. Natl Acad. Sci. USA* **111** 5083–7
[55] Seifert U 1994 *Phys. Rev.* E **49** 3124–7
[56] Bruinsma R, Goulian M and Pincus P 1994 *Biophys. J.* **67** 746–50
[57] Zidovska A and Sackmann E 2006 *Phys. Rev. Lett.* **96** 048103
[58] Pierres A, Benoliel A M, Touchard D and Bongrand P 2008 *Biophys. J.* **94** 4114–22
[59] Gardiner C W 1985 *Stochastic Methods* (Berlin: Springer)
[60] Leitenberger S M, Reister-Gottfried E and Seifert U 2008 *Langmuir* **24** 1254–61
[61] Smith A S, Sengupta K, Goennenwein S, Seifert U and Sackmann E 2008 *Proc. Natl Acad. Sci. USA* **105** 6906–11
[62] Gradshteyn I S and Rhyzik I M 2007 *Table of Integrals, Series, and Products* 7th edn (New York: Academic)
[63] Smith A S, Fenz S F and Sengupta K 2010 *Europhys. Lett.* **89** 28003
[64] Cavalcanti-Adam E A, Volberg T, Micoulet A, Kessler H, Geiger B and Spatz J P 2007 *Biophys. J.* **92** 2964–74
[65] Cuvelier D, Rossier O, Bassereau P and Nassoy P 2003 *Eur. Biophys. J.* **32** 342–54
[66] Brochard-Wyart F and de Gennes P G 2002 *Proc. Natl Acad. Sci. USA* **99** 7854–9

P5

From growth curves to association rates in specific membrane adhesion

Association rates of membrane-coupled cell adhesion molecules

Timo Bihr[1,2], Susanne Fenz[3,4], Erich Sackmann[5], Rudolf Merkel[3], Udo Seifert[2], Kheya Sengupta[6] and Ana-Sunčana Smith[1,7]

[1]Institut für Theoretische Physik and the Excellence Cluster: EAM, FAU, Erlangen, Germany;
[2]II. Institut für Theoretische Physik, Universität Stuttgart, Germany;
[3]Institute of Complex Systems 7: Biomechanics Forschungszentrum Jülich, Germany;
[4]Department of Cell and Developmental Biology, Theodor-Boveri-Institute, Universität Würzburg, Germany;
[5]Physics Department, Biophysics E22, Technische Universität München, Germany;
[6]Aix-Marseille Université, CNRS, CINaM UMR 7325, Marseille, France;
[7]Institute Ruđer Bošković, Division of Physical Chemistry, Zagreb, Croatia.

Biophysical Journal **107** (2014) L33-L36

DOI: 10.1016/j.bpj.2014.10.033
http://www.cell.com/biophysj/abstract/S0006-3495%2814%2901116-3

Abstract Thus far, understanding how the confined cellular environment affects the lifetime of bonds, as well as the extraction of complexation rates, has been a major challenge in studies of cell adhesion. Based on a theoretical description of the growth curves of adhesion domains, we present a new (to our knowledge) method to measure the association rate kon of ligand-receptor pairs incorporated into lipid membranes. As a proof of principle, we apply this method to several systems. We find that the k_{on} for the interaction of biotin with neutravidin is larger than that for integrin binding to RGD or sialyl Lewis^x to E-selectin. Furthermore, we find k_{on} to be enhanced by membrane fluctuations that increase the probability for encounters between the binders. The opposite effect on k_{on} could be attributed to the presence of repulsive polymers that mimic the glycocalyx, which points to two potential mechanisms for controlling the speed of protein complexation during the cell recognition process.

Biophysical Letter

Association Rates of Membrane-Coupled Cell Adhesion Molecules

Timo Bihr,[1,2] Susanne Fenz,[3,4] Erich Sackmann,[5] Rudolf Merkel,[3] Udo Seifert,[2] Kheya Sengupta,[6] and Ana-Sunčana Smith[1,7,*]

[1]Institut für Theoretische Physik and Cluster of Excellence Engineering of Advanced Materials, Friedrich-Alexander-Universität, Erlangen, Germany; [2]II. Institut für Theoretische Physik, Universität Stuttgart, Stuttgart, Germany; [3]Institute of Complex Systems 7: Biomechanics Forschungszentrum Jülich, Jülich, Germany; [4]Department of Cell and Developmental Biology, Theodor-Boveri-Institute, Universität Würzburg, Würzburg, Germany; [5]Physics Department, Biophysics E22, Technische Universität München, München, Germany; [6]Aix-Marseille Université, CNRS, CINaM UMR 7325, Marseille, France; and [7]Institute Ruđer Bošković, Division of Physical Chemistry, Zagreb, Croatia

ABSTRACT Thus far, understanding how the confined cellular environment affects the lifetime of bonds, as well as the extraction of complexation rates, has been a major challenge in studies of cell adhesion. Based on a theoretical description of the growth curves of adhesion domains, we present a new (to our knowledge) method to measure the association rate k_{on} of ligand-receptor pairs incorporated into lipid membranes. As a proof of principle, we apply this method to several systems. We find that the k_{on} for the interaction of biotin with neutravidin is larger than that for integrin binding to RGD or sialyl Lewis^x to E-selectin. Furthermore, we find k_{on} to be enhanced by membrane fluctuations that increase the probability for encounters between the binders. The opposite effect on k_{on} could be attributed to the presence of repulsive polymers that mimic the glycocalyx, which points to two potential mechanisms for controlling the speed of protein complexation during the cell recognition process.

Received for publication 3 July 2014 and in final form 24 October 2014.

*Correspondence: smith@physik.uni-erlangen.de

Chemical reaction kinetics in the confined environment of fluctuating membranes can be very different from those in an unconstrained situation. For example, it is well established that the enthalpy for ligand-receptor binding differs significantly for events occurring in two and three dimensions (1–3). This is particularly important in the context of cell adhesion, where membrane-bound ligands react with receptors on another surface. Furthermore, although 2D dissociation rates have been extensively modeled (4–7) and measured with reasonable confidence, often in single-molecule experiments (8,9), determining the association rate seems to be more challenging (10–15). For instance, when one of the reactants is bound to a membrane (16) or the tip of a polymer (17), the thermal fluctuations of the membrane (or polymer) will determine how often the binding partners come into the interaction range, thus influencing the association rate k_{on}. Similarly, repellent polymers on one or both of the interacting surfaces will hinder the reactant encounters (14,18), thus reducing k_{on}.

We measure k_{on} for three ligand-receptor pairs in different environments: 1), the strong biotin-neutravidin pair (3D binding energy $E_b^{3D} \approx 35 k_B T$) (16), which is often used as a model but has no known physiological relevance; 2), the Arg-Gly-Asp (RGD)-$\alpha_{IIb}\beta_3$ integrin pair, which is considered strong in the context of cell adhesion ($E_b^{3D} \approx 10 k_B T$) (19); and 3), the weaker sialyl Lewis^x binding to E-selectin ($E_b^{3D} \approx 5 k_B T$) (20).

As cell models, we use giant unilamellar vesicles (GUVs) (21,22) that are functionalized with lipid-anchored ligands (biotin, RGD, or sialyl Lewis^x) of size a at an initial concentration (see Supporting Material for details). Due to the fluidity of the GUV membrane, the ligands can explore their surface with a diffusion constant $D \approx 10\ \mu m^2/s$. The corresponding receptors are fixed on a 2D planar substrate at density ρ_r. E-selectin and integrin are deposited by physisorption, whereas the neutravidin is incorporated into a solid supported bilayer, where it is nevertheless immobile at the considered densities due to crowding (23). We modulate the rate of ligand-receptor encounters by adding polymers (polyethyleneglycol (PEG)) to the GUV membrane or by increasing the membrane fluctuations after the osmotic deflation of vesicles.

In the early stages of the experiment, vesicles sediment onto the substrate and form a strongly fluctuating contact zone, which when visualized by reflection interference contrast microscopy (RICM) (24) appears as a patch of variable intensity surrounded by a few quasi-circular fringes against a gray background (Fig. 1, *top*). Experimental details can be found in the Supporting Material and Fig. S3. At some point, an adhesion domain rich in bonds nucleates

Editor: Markus Deserno.

http://dx.doi.org/10.1016/j.bpj.2014.10.033

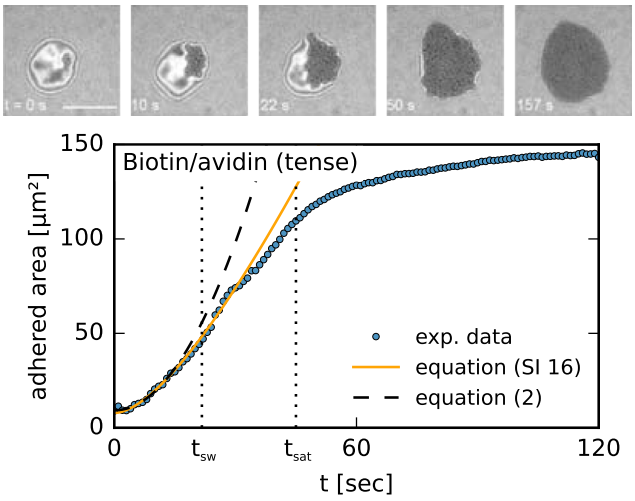

FIGURE 1 Top: RICM snapshots of a growing adhesion domain (*dark area*) mediated by biotin-avidin bonds. The scale bar is 10 μm. Bottom: experimental growth curve including fits to our theoretical results.

(as shown by a dark, homogeneous patch with strongly reduced fluctuations in RICM) and begins to grow radially outward (16,19,20). After a certain time, its area saturates due to the finite size of the vesicle (Fig. 1, *bottom*). In the case of weaker bonds, multiple seeds may form; however, such cases are not considered here because interactions between the domains could make a quantitative analysis unreliable.

Qualitatively, the same behavior was observed in a few systems with different binding pairs (20,25,26), and depending on the relative importance of viscous dissipation, membrane elasticity, and bond density and strength, several mechanisms were theoretically suggested to be responsible for the dynamics (27,28). Furthermore, two qualitatively different regimes were identified depending on the relative density of receptors and ligands. Specifically, for $\rho_l^0/\rho_r>1$, the growth of the adhesion area was quadratic in time, as expected for reaction-limited kinetics (19,29). Alternatively, for $\rho_l^0/\rho_r<1$, the area of a domain displayed a linear time dependence (19), which is consistent with the solution of the Stefan problem (29–31). By inspection of our own and previously published data (19) for which $\rho_l^0/\rho_r<1$, we notice deviations from the linear behavior at short timescales (Fig. 1). We explain this effect by reformulating the Stefan problem (see Fig. S1 and Supporting Material for details) to account for a k_{on}-dependent radiation boundary condition (Eq. S2). The full solution (Eq. S16) of this diffusion problem shows that the growth of a domain is always reaction limited in the initial stages. At later times, the growth becomes diffusion limited because the contact zone becomes depleted of ligands, which then have to be transported from the bulk of the vesicle. The crossover time, from which we can also obtain the reaction rate, is estimated from the full solution to be

$$t_{sw} = \frac{D}{(k_{on}a)^2}, \tag{1}$$

Consequently, if $\rho_l^0/\rho_r<1$ for $t < t_{sw}/4$, the time evolution of the area is quadratic (see Fig. S2 and Supporting Material for the derivation) and given by

$$A(t) = \pi\left(\frac{\rho_l^0}{\rho_r}\right)^2 k_{on}^2 a^2 t^2. \tag{2}$$

Interestingly, Eq. 2 also emerges from the solution for the reaction-limited kinetics and can be applied for $\rho_l^0/\rho_r>1$.

Due to the finite size of the vesicle, however, the growth will saturate as the system approaches a thermodynamic equilibrium (18). Actually, from t_{sat} (Eq. S26), the concentration of free ligands in the entire vesicle will begin to drop. This will affect the dynamics of growth in a way that is not accounted for in modeling (29–31), where one typically assumes the constant binder density (Eq. S2) at the rim. Actually, the smaller the number of ligands in the vesicle compared with the number of receptors (and formed bonds), the shorter is the reaction-limited regime and the quicker is the expansion of the depletion zone over the area of the entire vesicle. Hence, the finiteness will more strongly affect the diffusion-limited regime, which therefore should not be used to directly extract the diffusion constant of the ligand.

The crossover from the quadratic to the linear regime is clearly seen in our fastest neutravidin-biotin system (Fig. 1), as well as for the slower integrin-RGD binding (Fig. S4). The binding rate is obtained from both Eq. 1 and Eq. 2, as shown in Table 1. In principle, the two approaches provide relatively similar k_{on}-values. However, the results obtained with Eq. 2 may underestimate the rate by up to 50%. This is because the fits are extended to t_{sw}, which for fast processes may still be beneficial due to the limited time resolution of sampling. On the other hand, k_{on} obtained from the Eq. 1 agrees excellently with the values obtained from the fits of the full solution of the diffusion problem (Eq. S16). This is despite relatively large uncertainties in determining t_{sw}, and is due to the square-root dependency of the rate on this typical time.

Regardless of the abovementioned uncertainties, it is interesting that the difference in the binding rates between floppy and tense vesicles (neutravidin-biotin system) is significant. As was previously predicted theoretically (32,33),

TABLE 1 Association rate k_{on} in units of s^{-1} from experiments

	ρ_l^0/ρ_b	Eq. 1	Eq. 2
Biotin (floppy)	0.4	$(1.8 \pm 0.2)\cdot 10^3$	$(1.5 \pm 0.03)\cdot 10^3$
Biotin (tense)	0.4	$(1.2 \pm 0.1)\cdot 10^3$	$(0.6 \pm 0.02)\cdot 10^3$
RGD (1% PEG)	5.9		$(7.9 \pm 0.2)\cdot 10^1$
RGD (3% PEG)	5.9		$(6.0 \pm 0.1)\cdot 10^0$
sLe^x	59		$(4.1 \pm 0.1)\cdot 10^{-1}$

See Supporting Material for details and calculation of the error bars.

larger fluctuations of vesicle membrane increase the association rate k_{on} because encounters between ligands and receptors are more frequent.

Even more prominent is the change in the binding rate due to the presence of repelling polymers (PEG) mimicking the cellular glycocalyx. We incorporated these polymers at concentrations of 1 mol% and 3 mol% into vesicles carrying RGDs binding to integrins and found that k_{on} was one order of magnitude lower for vesicles with more PEG (Table 1). This clearly demonstrates that repelling molecules affect not only the thermodynamic equilibrium but also the rates for bond formation. In addition, the reported rate (1% PEG) is in full agreement with the rates extracted from the set of growth curves (19) where the concentration of RGD in the vesicles was varied systematically to induce the change from the diffusion-limited regime to the reaction-limited one (see Fig. S5 and Table S1 in the Supporting Material).

The condition for reaction-limited growth (second column in Table 1) is also very well satisfied for the slowest sialyl Lewis^x binding to E-selectin (20). As expected, the growth curves are well fitted with the parabola (for an example, see Supporting Material) corresponding to Eq. 2. This rate is of the same order of magnitude as the previously reported binding rates of membrane-bound P and L selectins (11) measured by the micropipette technique (10).

Here, we have presented a new (to our knowledge) strategy to measure the association constant k_{on} from adhesion growth curves. We used well-controlled cell models with three different kinds of ligand-receptor pairs to demonstrate proof of principle. We obtained the highest k_{on}-values for the energetically strongest bonds. The results suggest a mechanism that could be relevant for the control of cell adhesion dynamics, namely, the membrane shape fluctuations, which increase the association rate (32,33) when enhanced. On a similar note, we find that repelling polymer cushions, which were previously used to modulate unspecific GUV adhesion (20,34) as well as to influence bond formation in the context of surface-surface interactions (14,20), directly influence the association rate. This result is also interesting in the context of cells, as it suggests that bonds between binding pairs with long extracellular domains (e.g., as selectin-PSLG links) could form rapidly. In contrast, the links with integrins (hidden in the glycocalyx) should be very slow. These hypotheses are further supported by the fact that cells regulate both the membrane fluctuations and the thickness of the glycocalyx (22).

Interestingly, although they differ by at least an order of magnitude, the association rates for the integrin-RGD binding and the recognition of sialyl Lewis^x motifs by E-selectin are relatively low. This suggests that at physiological concentrations, the reaction-limited regimes could extend for a very long time before entering the diffusive regime. For example, for the sialyl Lewis^x binding to E-selectin, this time is on the order of 10^5 s, which is beyond the timescale of a cell or a vesicle. This suggests that a diffusion-limited behavior could not be relevant for cell adhesion with these two binding pairs unless extreme crowding effects would affect the recruitment of proteins to adhesion patches, which does not seem to be the case.

SUPPORTING MATERIAL

Supplemental Material, five figures, and one table are available at http://www.biophysj.org/biophysj/supplemental/S0006-3495(14)01116-3.

ACKNOWLEDGMENTS

We thank B. Lorz and Z. Guttenberg for providing some of the experimental data, and D. Schmidt for useful discussions.

A.S.S. and T.B. received funding from the European Research Council (Starting Grant 2013-337283) and Research Training Group 1962 at Friedrich-Alexander-Universität Erlangen.

REFERENCES and FOOTNOTES

1. Nguyen-Duong, M., K. W. Koch, and R. Merkel. 2003. Surface anchoring reduces the lifetime of single specific bonds. *Europhys. Lett.* 61:845–851.
2. Wu, Y., J. Vendome, …, B. Honig. 2011. Transforming binding affinities from three dimensions to two with application to cadherin clustering. *Nature.* 475:510–513.
3. Schmidt, D., T. Bihr, …, A.-S. Smith. 2012. Coexistence of dilute and densely packed domains of ligand-receptor bonds in membrane adhesion. *Europhys. Lett.* 99:38003.
4. Evans, E., and K. Ritchie. 1997. Dynamic strength of molecular adhesion bonds. *Biophys. J.* 72:1541–1555.
5. Seifert, U. 2000. Rupture of multiple parallel molecular bonds under dynamic loading. *Phys. Rev. Lett.* 84:2750–2753.
6. Erdmann, T., S. Pierrat, …, U. S. Schwarz. 2008. Dynamic force spectroscopy on multiple bonds: experiments and model. *Europhys. Lett.* 81:48001.
7. Krobath, H., B. Rozycki, …, T. R. Weikl. 2009. Binding cooperativity of membrane adhesion receptors. *Soft Matter.* 5:3354–3361.
8. Alón, R., D. A. Hammer, and T. A. Springer. 1995. Lifetime of the P-selectin-carbohydrate bond and its response to tensile force in hydrodynamic flow. *Nature.* 374:539–542.
9. Lorenz, B., L. Álvarez de Cienfuegos, …, A. Janshoff. 2012. Model system for cell adhesion mediated by weak carbohydrate-carbohydrate interactions. *J. Am. Chem. Soc.* 134:3326–3329.
10. Chesla, S. E., P. Selvaraj, and C. Zhu. 1998. Measuring two-dimensional receptor-ligand binding kinetics by micropipette. *Biophys. J.* 75:1553–1572.
11. Chen, W., E. A. Evans, …, C. Zhu. 2008. Monitoring receptor-ligand interactions between surfaces by thermal fluctuations. *Biophys. J.* 94:694–701.
12. Huang, J., V. I. Zarnitsyna, …, C. Zhu. 2010. The kinetics of two-dimensional TCR and pMHC interactions determine T-cell responsiveness. *Nature.* 464:932–936.
13. Huppa, J. B., M. Axmann, …, M. M. Davis. 2010. TCR-peptide-MHC interactions in situ show accelerated kinetics and increased affinity. *Nature.* 463:963–967.
14. Robert, P., A. Nicolas, …, L. Limozin. 2011. Minimal encounter time and separation determine ligand-receptor binding in cell adhesion. *Biophys. J.* 100:2642–2651.

15. Zarnitsyna, V., and C. Zhu. 2012. T cell triggering: insights from 2D kinetics analysis of molecular interactions. *Phys. Biol.* 9:045005.

16. Fenz, S. F., T. Bihr, …, A.-S. Smith. 2011. Switching from ultraweak to strong adhesion. *Adv. Mater.* 23:2622–2626.

17. Jeppesen, C., J. Y. Wong, …, C. M. Marques. 2001. Impact of polymer tether length on multiple ligand-receptor bond formation. *Science.* 293:465–468.

18. Smith, A., and U. Seifert. 2007. Vesicles as a model for controlled (de-) adhesion of cells: a thermodynamic approach. *Soft Matter.* 3:275–289.

19. Boulbitch, A., Z. Guttenberg, and E. Sackmann. 2001. Kinetics of membrane adhesion mediated by ligand-receptor interaction studied with a biomimetic system. *Biophys. J.* 81:2743–2751.

20. Lorz, B. G., A.-S. Smith, …, E. Sackmann. 2007. Adhesion of giant vesicles mediated by weak binding of sialyl-LewisX to E-selectin in the presence of repelling poly(ethylene glycol) molecules. *Langmuir.* 23:12293–12300.

21. Fenz, S. F., and K. Sengupta. 2012. Giant vesicles as cell models. *Integr. Biol. (Camb.).* 4:982–995.

22. Sackmann, E., and A.-S. Smith. 2014. Physics of cell adhesion: some lessons from cell-mimetic systems. *Soft Matter.* 10:1644–1659.

23. Fenz, S. F., A.-S. Smith, …, K. Sengupta. 2011. Inter-membrane adhesion mediated by mobile linkers: effect of receptor shortage. *Soft Matter.* 7:952–962.

24. Limozin, L., and K. Sengupta. 2009. Quantitative reflection interference contrast microscopy (RICM) in soft matter and cell adhesion. *ChemPhysChem.* 10:2752–2768.

25. Cuvelier, D., and P. Nassoy. 2004. Hidden dynamics of vesicle adhesion induced by specific stickers. *Phys. Rev. Lett.* 93:228101.

26. Cuvelier, D., M. Théry, …, L. Mahadevan. 2007. The universal dynamics of cell spreading. *Curr. Biol.* 17:694–699.

27. Brochard-Wyart, F., and P. G. de Gennes. 2002. Adhesion induced by mobile binders: dynamics. *Proc. Natl. Acad. Sci. USA.* 99:7854–7859.

28. Reister-Gottfried, E., K. Sengupta, …, A.-S. Smith. 2008. Dynamics of specific vesicle-substrate adhesion: from local events to global dynamics. *Phys. Rev. Lett.* 101:208103.

29. Shenoy, V. B., and L. B. Freund. 2005. Growth and shape stability of a biological membrane adhesion complex in the diffusion-mediated regime. *Proc. Natl. Acad. Sci. USA.* 102:3213–3218.

30. Freund, L., and Y. Lin. 2004. The role of binder mobility in spontaneous adhesive contact and implications for cell adhesion. *J. Mech. Phys. Solids.* 52:2455–2472.

31. Gao, H., W. Shi, and L.-B. Freund. 2005. Mechanics of receptor-mediated endocytosis. *Proc. Natl. Acad. Sci. USA.* 102:9469–9474.

32. Bihr, T., U. Seifert, and A.-S. Smith. 2012. Nucleation of ligand-receptor domains in membrane adhesion. *Phys. Rev. Lett.* 109:258101.

33. Hu, J., R. Lipowsky, and T. R. Weikl. 2013. Binding constants of membrane-anchored receptors and ligands depend strongly on the nanoscale roughness of membranes. *Proc. Natl. Acad. Sci. USA.* 110:15283–15288.

34. Sengupta, K., and L. Limozin. 2010. Adhesion of soft membranes controlled by tension and interfacial polymers. *Phys. Rev. Lett.* 104:088101.

Supplementary Information

Association rates of membrane-coupled cell adhesion molecules

Timo Bihr[1,2], Susanne Fenz[3,4], Erich Sackmann[5], Rudolf Merkel[3],
Udo Seifert[2], Kheya Sengupta[6] and Ana-Sunčana Smith[1,7]

[1]Institut für Theoretische Physik and the Excellence Cluster: EAM, FAU, Erlangen, Germany; [2]II. Institut für Theoretische Physik, Universität Stuttgart, Germany; [3]Institute of Complex Systems 7: Biomechanics Forschungszentrum Jülich, Germany; [4]Department of Cell and Developmental Biology, Theodor-Boveri-Institute, Universität Würzburg, Germany; [5]Physics Department, Biophysics E22, Technische Universität München, Germany; [6] Aix-Marseille Université, CNRS, CINaM UMR 7325, Marseille, France; [7]Institute Ruđer Bošković, Division of Physical Chemistry, Zagreb, Croatia.

Theoretical Methods

Defining the Extended Stefan Problem

We consider a giant unilamellar vesicle that placed above a substrate, forms a contact zone where mobile ligands (initial density in the vesicle membrane ρ_l^0) can bind to immobile receptors (size a and density ρ_r on the substrate). Each bond deforms the membrane locally and pulls the membrane closer to the substrate (figure SI 1), which promotes the formation of a radially growing domain (bond density ρ_b). The deformation of the membrane at the rim brings free ligands in that region closer to the substrate, which then enhances the probability of binding at the edge of the domain. As the nucleation dynamics is in the current systems much slower than the spreading dynamics of a domain, only one (at most two) domains develop within the contact zone. In the model below, we assume that all receptors within a domain are bound, i. e. $\rho_b = \rho_r$.

The growth of such a domain can be regarded as a variant of the Stefan diffusion problem. We start by describing the flux of ligands, which are exploring the vesicle membrane with diffusion constant D, by the usual diffusion equation

$$\frac{\partial \rho_l(x,t)}{\partial t} = D\frac{\partial^2 \rho_l(x,t)}{\partial x^2}. \qquad \text{(SI 1)}$$

Here, $\rho_l(x,t)$ is the time dependent density profile of the ligands around the domain.

We, furthermore, set the number of binding events to be proportional to the density at the rim and to the association rate k_{on}, and equal to the diffusive flux at the rim. This implies

$$k_{\text{on}} a \rho_l\left(R(t),t\right) = D\left.\frac{\partial \rho_l(x,t)}{\partial x}\right|_{x=R(t)}, \qquad \text{(SI 2)}$$

where $R(t)$ is the radius of the domain. This expression should be valid as long as the edge of the expanding domain does not "move into" the concentration gradient. This is generally fulfilled because the motion of the rim and the relaxation of the concentration gradient is set by the diffusion of binders to the rim.

The above choice of the boundary condition is different to the usual approach where the density of ligands at the rim of the domain is fixed, as shown previously (refs. (29-31) of the main text). In the limit of infinite reaction rates, the solutions of our boundary conditions converge to the solution of the diffusion equation with the fixed boundary conditions. Furthermore, in the long time limit, the results obtained with the two approaches are asymptotically identical. However, using eq. (SI 2) allows us to explain the experimentally observed, short time quadratic regime of growth that precedes the diffusion limited growth.

The stated equation needs to be coupled to the growth of the domain, which is proportional to the flux of the ligands at the rim into the domain and the average distance between the bonds in the domain $1/\rho_r$ (see also refs. (29-31) of the main text). Therefore

$$\frac{\partial R(t)}{\partial t} = \frac{D}{\rho_r}\left.\frac{\partial \rho_l(x,t)}{\partial x}\right|_{x=R(t)} \text{ with } R(0) = R_0 \equiv 0. \qquad \text{(SI 3)}$$

Here, we set the initial radius of the domain to zero.

The above presented variation of the Stefan problem can be solved if the density of ligands is set at $t = 0$ and at infinite distance from the domain to

$$\rho_l(x, t=0) = \rho_l^0, \qquad \text{(SI 4)}$$

and

$$\lim_{x\to\infty} \rho_l(x,t) = \rho_l^0, \qquad \text{(SI 5)}$$

respectively.

Solving the Extended Stefan Problem

In order to solve the system of equation given by eqs. (SI 1)-(SI 5), we convert it to the co-moving frame and introduce the substitution

$$y = x - R(t). \qquad \text{(SI 6)}$$

In this frame, we obtain the diffusion equation

$$\frac{\partial \rho_l(y,t)}{\partial t} = D\frac{\partial^2 \rho_l(y,t)}{\partial y^2} + \frac{\partial R(t)}{\partial t}\frac{\partial \rho_l(y,t)}{\partial y}, \qquad \text{(SI 7)}$$

the adapted boundary condition

$$\rho_l\left(0\right) = \frac{D}{k_{\text{on}} a}\left.\frac{\partial \rho_l(y,t)}{\partial y}\right|_{y=0}, \qquad \text{(SI 8)}$$

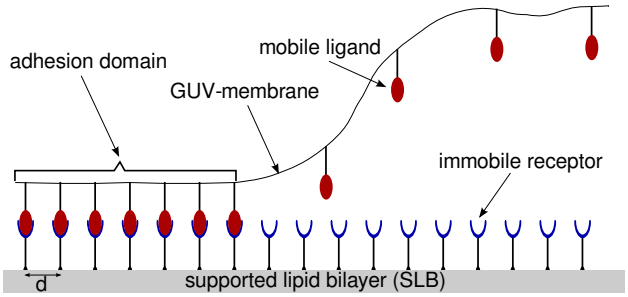

FIGURE SI 1 Sketch of the rim of the adhesion domain. The red ligands diffuse to the rim where they form bonds with the immobilize receptors increasing the size of the domain. The distance d between receptors is assumed to be uniform ($1/d = \rho_r$).

the moving boundary

$$\frac{\partial R(t)}{\partial t} = \frac{D}{\rho_r} \left. \frac{\partial \rho_l(y,t)}{\partial y} \right|_{y=0}, \tag{SI 9}$$

the initial condition

$$\rho_l(y, t=0) = \rho_l^0, \tag{SI 10}$$

and the boundary condition at infinity

$$\lim_{y\to\infty} \rho_l(y,t) = \rho_l^0. \tag{SI 11}$$

In the limit of close packing of receptors ρ_b, the second term in eq. (SI 7) disappears as the growth of the radius following eq. (SI 9) vanishes. In this case, the system reduces to an absorbing trap without moving boundaries and the boundary problem can be solved analytically (see for example Carslaw and Jaeger, Conduction of Heat in Solids), following a perturbation ansatz in ρ_l^0/ρ_r

$$\begin{aligned} \frac{\rho_l(y,t)}{\rho_l^0} &= \sum_{n=0}^{\infty} \varrho_l^n(y,t) \left(\frac{\rho_l^0}{\rho_r}\right)^n \\ \frac{\partial R(t)}{\partial t} &= \sum_{n=0}^{\infty} \frac{\partial R^n(t)}{\partial t} (1-\delta_{n,0}) \left(\frac{\rho_l^0}{\rho_r}\right)^n, \end{aligned} \tag{SI 12}$$

which provides us with a differential equation for every order of (ρ_l^0/ρ_r). The 0^{th} order term of the patch growth vanishes because, on this level of perturbation theory, the absorbing boundary is not moving. Here the differential equation for the concentration profile is

$$\frac{\partial \varrho_l^0(y,t)}{\partial t} = D \frac{\partial^2 \varrho_l^0(y,t)}{\partial y^2}, \tag{SI 13}$$

which is, as expected, the usual diffusion equation.

Even though the concentration of ligands is only correct to the 0^{th} order, the patch growth is obtained to the 1^{th} order

$$\frac{\partial R^1(t)}{\partial t} = D \left. \frac{\partial \varrho_l^0(y,t)}{\partial y} \right|_{y=0}. \tag{SI 14}$$

As suggested in Carslaw and Jaeger, Conduction of Heat in Solids (page 70ff) for this type of reduced boundary value problems, the solution for the ligand concentration profile reads

$$\begin{aligned} \frac{\varrho_l^0(y,t)}{\rho_l^0} &= \operatorname{erf}\left(\frac{y}{2\sqrt{Dt}}\right) + \\ &+ \exp\left(\frac{k_{\text{on}}^2 a^2 t + k_{\text{on}} a y}{D}\right) \operatorname{erfc}\left(\frac{y + 2k_{\text{on}} a t}{2\sqrt{Dt}}\right). \end{aligned} \tag{SI 15}$$

With this result, and with the help of eq. (SI 9), the time development of the radius of the adhesion domain can be calculated

$$R(t) \simeq \frac{\rho_l^0}{\rho_r} \left(\frac{D \exp\left(\frac{k_{\text{on}}^2 a^2 t}{D}\right) \operatorname{erfc}\left(\frac{k_{\text{on}} a t}{\sqrt{Dt}}\right)}{k_{\text{on}} a} + \frac{2\sqrt{Dt}}{\sqrt{\pi}} \right). \tag{SI 16}$$

This result is correct to the first order of ρ_l^0/ρ_r. The analysis of this solution indicates that the first term on the right hand side dominates the short time scales while the second term, proportional to $\sqrt{Dt}$ becomes relevant at the long time scales. The crossover between time t_{sw} (eq. (1) in the main text) between the two regimes is determined by comparing the terms depending on the reaction rate k_{on} (last term in eq. (SI 15) and the first term in brackets of eq. (SI 16))

$$t_{\text{sw}} = \frac{D}{(k_{\text{on}} a)^2}. \tag{SI 17}$$

The appearance of the two regimes is even more obvious after performing a Taylor expansion of eq. (SI 16) in $\sqrt{t}$ to the fourth order (i. e. to the second order in t), around $t = 0$

$$\begin{aligned} \frac{R(t)}{\rho_l^0} = \frac{R_0}{\rho_l^0} + \frac{k_{\text{on}} a t}{\rho_r} - \frac{4\left(\frac{k_{\text{on}}^2 a^2}{\rho_r}\right) t^{3/2}}{3\left(\sqrt{\pi D}\right)} \\ + \frac{\left(\frac{k_{\text{on}}^3 a^3}{\rho_r}\right) t^2}{2D} + O\left(t^{5/2}\right), \end{aligned} \tag{SI 18}$$

The obtained result contains no first order term ($\sqrt{t}$) which cancels out. Furthermore, it is easy to show the proportionality between the width of the concentration profile (eq. (SI 15)) and $\sqrt{Dt}$, as found in the arguments of the error function and the complementary error function. In other words, there is no stationary solution with a constant concentration profile. Instead, the solution of the extended Stefan problem has a constantly growing depletion zone. However, in the early stages of the domain growth, the depletion zone is not free of ligands, and its depth develops on a time scale of $D/(k_{\text{on}} a)^2$ (top panel in Fig. SI 2). Actually, only in the limit of an infinite effective binding rate, the ligand concentration around the adhesion domain would be zero from $t = 0$.

To summarize, we define two regimes for the growth behavior of the adhesion domain with the crossover at t_{sw} (lower

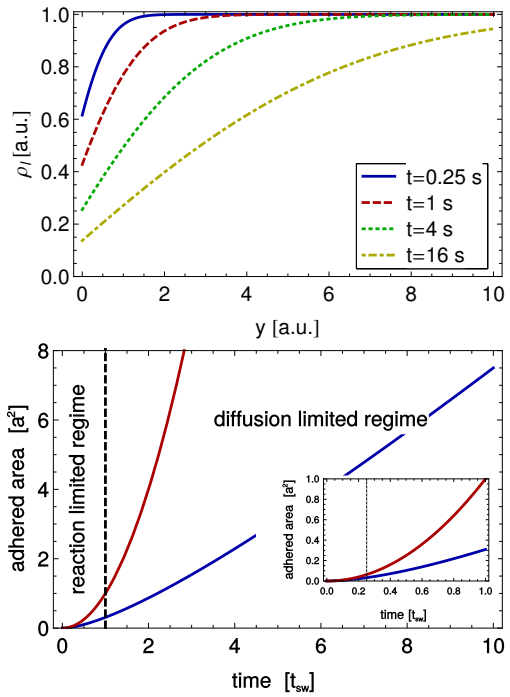

FIGURE SI 2 Top: Concentration profile as a function of the distance from the edge of the domain (set at $y = 0$) (SI 15). All parameters (D, k and a) were set to unity. Due to the finite reaction rate and uniform density of ligands prior to the formation of the domain, it takes some time before the concentration of ligands drops to zero at the edge of the adhesion domain. From this point, the concentration profile grows with $2\sqrt{Dt}$. Bottom: Theoretical growth curve for the adhered area (blue curve) and the initial quadratic curve (red curve). The length of the reaction limited regime depends on the initial ligand and receptor concentration as well as on the effective binding rate.

panel in Fig. SI 2). In the short time regime, the diffusion of ligands does not affect the growth because the surrounding of the adhesion domain is not yet depleted of binders and the growth is limited by the reaction kinetics. This is confirmed by eq. (SI 18), where the lowest order $\sqrt{t}$ disappears and the growth of the radius is linear (area is quadratic) for short times, i. e. reaction limited. From the first order term of eq. (SI 17), we derive the time development of the adhered area (eq. (2) from the main text),

$$A(t) = \pi \left(\frac{\rho_l^0}{\rho_r}\right)^2 {k_{\text{on}}}^2 a^2 t^2. \qquad \text{(SI 19)}$$

The asymptotic long time regime is only determined by the diffusion of ligands to the adhesion domain (i. e. it is diffusion limited). This also means that the first term of eq. (SI 16), which depends on the effective reaction rate k_{on}, can be neglected compared to the last, rate-independent term. This leads to a growth of the radius that is proportional to $\sqrt{Dt}$ (the domain area proportional in time) in the long time limit.

It should be noted that eq. (SI 19) also emerges from the consideration of the reaction limited dynamics, and consequently can be used also when $\rho_l^0/\rho_r > 1$, which is beyond the above presented perturbative scheme.

The reaction limited regime and the saturation time

We assume that the concentration of ligands is constant outside the adhered area and the number of reactions is proportional to the concentration at the rim of the adhered area and the reaction rate. Under those assumptions, the growth process can be described by

$$\frac{\partial N_b(t)}{\partial t} = k_{\text{on}} C_{\text{patch}}(t) a \left(\frac{N_{\text{t}} - N_b(t)}{A_{\text{V}}}\right), \qquad \text{(SI 20)}$$

where $N_b(t)$ is the number of bonds within the adhered area, N_t is the number of ligands at the beginning of the growth phase on the vesicle surface (i. e. $N_t = 4\pi r_V^2 \rho_l^0$), $C_{\text{patch}}(t)$ the circumference of the domain and A_{V} the surface of the vesicle. We transform equation (SI 20) by the relation

$$N_b(t) = \rho_b \frac{C_{\text{patch}}(t)^2}{2\pi} \qquad \text{(SI 21)}$$

to

$$\frac{\partial N_b(t)}{\partial t} = 2k_{\text{on}} \sqrt{\frac{\pi N_b(t)}{\rho_b}} a \left(\frac{N_{\text{t}} - N_b(t)}{A_{\text{V}}}\right), \qquad \text{(SI 22)}$$

which, now, only depends on the number of domain particles $N_b(t)$. This differential equation can be solved easily

$$N_b(t) = N_t \tanh^2\left(\frac{k_{\text{on}} a \sqrt{\pi N_t} t}{A_{\text{V}} \sqrt{\rho_b}}\right). \qquad \text{(SI 23)}$$

The solution has a quadratic onset of the growth curve which then saturates due to the finite size vesicle, even if the diffusion constant was infinite. Actually, the Taylor expansion to the second order in t yields an expression identical to the one shown in eq. (2) of the main text (i.e. eq. (SI 19)) (if the surface area A_{V} and the number of ligands N_t is replaced by $\rho_l^0 = A_{\text{V}}/N_t$).

From the full solution given by eq. (SI 23), we can read the typical saturation time

$$t_{\text{sat}} = \frac{A_{\text{V}}\sqrt{\rho_b}}{k_{\text{on}} a \sqrt{\pi N_t}} = \frac{2r_V}{k_{\text{on}} a} \sqrt{\frac{\rho_b}{\rho_l^0}}. \qquad \text{(SI 24)}$$

This time tells when the concentration of free binders drops considerably on the vesicle surface if the diffusion is very fast and, thus, gives the lower bound of the time at which the growth will be affected by the finiteness of the system.

Experimental Methods

Sample preparation

GUVs (Giant unilamellar vesicle), carrying appropriate ligands, were prepared by electroswelling. Their interaction with

a specially prepared substrate exhibiting the corresponding receptor was monitored by micro-interferometric (RICM) imaging. The preparation process for each ligand-receptor pair is presented below:

For **the biotin-neutravidin pair**, GUVs consisting of SOPC (1-stearoyl-2-oleoyl-sn-glycero-3-phospho-choline) supplemented with 2 mol% DOPE-PEG 2000 (1,2-dioleoyl-sn-glycero-3-phospho-ethanolamine-N-(methoxy(polyethyl-eneglycol)-2000)) and varying amounts of DOPE-cap-biotin (1,2-dio leoyl-sn-glycero-3-phosphoethanolamine-N-(cap biotinyl)) were prepared in 230 mOsm/L sucrose solution via electroswelling. For micro-interferometry imaging, they were transferred to the observation chamber filled with 300 mOsm/L PBS. The bottom glass slide of the observation chamber had been coated with a supported lipid bilayer (bottom layer: pure SOPC, top layer: SOPC / 2 mol% DOPE-PEG 2000 / 5 mol% DOPE-cap-biotin) following the Langmuir Blodgett -Langmuir Schäfer technique and functionalized with neutravidin. It should be noted that although the neutravidin receptors were coupled to a fluid lipid bilayer, the receptors were effectively immobile due to crowding effects (Fenz et al., Langmuir, **25**:1074-1085 (2009)). The biotins covered an area of around 0.5 nm^2. Further details can be found in ref. (23) of the main text.

For **sialyl-Lewis^x binding to E-selectin**, the vesicles were prepared from an equimolar mixture of DMPC (1,2-dimyristoyl-sn-glycero-3-phosphocholine), cholesterol and 15 mol% of sialyl-Lewis^x-glyco-sphingolipids (C. Gege, S. Oscarson, and R.R. Schmidt, Tetrahedron Lett. **42**:377-380 (2001)). The vesicles were prepared by electro-swelling in a 170mOsm/L sucrose solution and placed in a 210 mOsm/L salt buffer (100 mM NaCl, 1 mM CaCl2, 1 mM NaN_3, 10 mM HEPES at pH of 7.2). The substrate was a clean glass cover slide (Merck, Germany) which was hydrophobized by immersion in a 1% toluene solution of aminosilanes (3-amino-propyltriethoxysilane) (both Fluka, Swiss) for 4 minutes at 60°C which was followed by rinsing with pure toluene and drying under N_2. Finally a recombinant form of the extracellular domain of human E-selectin (Calbiochem, San Diego, CA, USA) was physsorbed on the substrate by incubating the protein solution (maximum 5 µg/ml in the salt buffer) for two hours at room temperature, while the whole chamber was gently mixed on a shaking platform. After rinsing with buffer, the substrate was incubated at room temperature for one more hour with a buffer solution containing 3% of Blotting Grade Blocker Non-Fat Dry Milk (BioRad, Hercules, CA, USA) in order to prevent any direct contact of glass with the vesicle. Final careful rinsing of the slide with buffer completed the preparation. Here, the slex had a lateral size of around 10 nm^2. Further details on the preparation can be found in our earlier work (ref. (20) of the main text).

For **the RGD-integrin case**, giant vesicles were prepared from a 1:1 mixture of DMPC and cholesterol, to which 1 and 3 mol% of PDOPE-PEG 2000 were added. We also added 0.08–2 mol% of lipid-coupled cyclic hexapeptide containing an RGD sequence. Integrin $\alpha_{IIb}\beta_3$ receptors were prepared from blood platelets (Hu et al. Biochemistry **39**:12284–12294 (2000)) solubilized by Triton X100, and fixed on a clean glass substrate by physisorption during incubation. For this purpose, integrins were dissolved in Tris-buffer (20 mM Tris pH 7.25, 150 mM NaCl, 1 mM $MgCl_2$, 1 mM $CaCl_2$, 1 mM NaN_3, 0.01% Triton X100) to a concentration of 68 nM and the substrates were incubated in this solution for 1 h. In a second step, the substrates were incubated in a solution of 3 weight% bovine serum albumin in HEPES buffer (10 mM HEPES pH 7.25, 100 mM NaCl, 1 mM $CaCl_2$, 1 mM NaN_3). After each incubation, the substrates were thoroughly washed with HEPES buffer. The RGDs covered a size equivalent to the area covered by a lipid, hence, 0.5 nm^2 Further details of the preparation can be found in (ref. (19) of the main text).

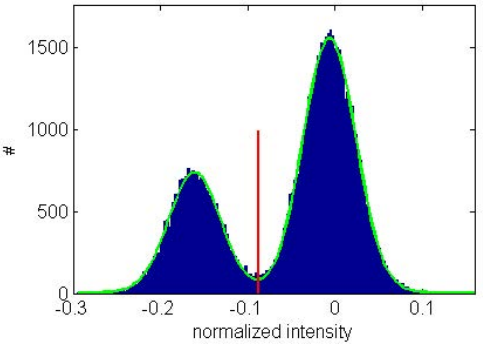

FIGURE SI 3 Histogram of intensities in a typical RICM image. The red line indicates the chosen threshold

Measuring setup and data analysis

In all cases, the observation chamber was covered with a glass slide to prevent changes in the buffer osmolarity due to evaporation. GUVs were located with the phase contrast mode of the microscope and observed during sedimentation. When the vesicles were close to the substrate the the contact zone was observed by reflection interference contrast microscopy (RICM) and the adhesion process was recorded at an image rate of 10 Hz (for more information on RICM see a recent review (ref. (24) of the main text). Thereby, the adhered area was determined by thresholding the intensity.

The threshold was extracted from the last image of the movie showing the adhered vesicle in its steady state. The histogram of all intensity values in the image exhibited two well separated peaks corresponding to the adhered and unadhered zones. Two Gaussians were fitted to the histogram. We defined the intersection between the two Gaussian distributions as the threshold value. Due to the well separated peaks (see Fig. SI 3), small variations from the threshold value did not result in substantial variations of the extracted area and did not affect the observed dynamics. After the completion

of the adhesion process, the vesicles were also recorded in phase contrast in order to measure their diameters.

Evaluation of the reduced volume of vesicles

Overall, our vesicles have a reduced value between 0.90 and 0.98 which was typically determined on the level of each swelling preparation, by measuring the radius of the vesicle in its equatorial plane in phase contrast. Combining this information with the measure of the radius of the contact zone, we were able to reconstruct the spherical cap describing the shape of the vesicle, and from there, to determine the reduced volume of the vesicle V_{red} following the expression

$$V_{red} = \frac{V_t}{V_i} \tag{SI 25}$$

where V_t denotes the volume of the truncated sphere and V_i the volume of the ideal sphere with the same surface area A. V_t, A, and V_i were calculated from the known radii of the vesicle measured in phase contrast r_V and of the contact zone measured in RICM r_{CZ}.

$$\begin{aligned} A &= 4r_V^2\pi - \pi\left(r_V - \sqrt{r_V^2 - r_{CZ}^2}\right)^2 \\ V_t &= \frac{4}{3}r_V^3\pi - \left[\frac{1}{3}\pi\sqrt{r_V^2 - r_{CZ}^2}\left(3r_V - \sqrt{r_V^2 - r_{CZ}^2}\right)\right] \\ V_i &= \frac{4}{3}\left(\sqrt{\frac{A}{4\pi}}\right)^3\pi \end{aligned} \tag{SI 26}$$

In the case of biotin-avidin bonds, where we investigated the role of membrane height fluctuations (see main text), we determined the reduced volume for each vesicle independently. Specifically, for floppy vesicles the reduced volume was 0.95 and for tense vesicles 0.97.

Extraction of reaction rates

Only data for which $t < t_{\text{sat}}$ was used in the analysis. If $\rho_l^0/\rho_r > 1$, eq. (2) (e.g. eq. (SI 19)) was systematically applied to all data using the least square method as implemented in *Mathematica 9.0*. Thereby, we used all data points from the beginning to the saturation (see also plots in figure SI 4).

In the case of $\rho_l^0/\rho_r < 1$, the reaction rate is first extracted from the crossover time eq. (SI 17) which is determined from the growth curves as time at which the long term linear regime fails to account for the data (i.e. the linear function going through the data points in the linear regime is around 15% smaller than the experimental values). Due to this procedure, the error in determining t_{sw} may be relatively large (up to 20% determined from small variations of the range of the linear fit). However, due to the square root dependence of the reaction rate on the cross-over time, the impact of this error on the accuracy of the rate is limited. Furthermore, the

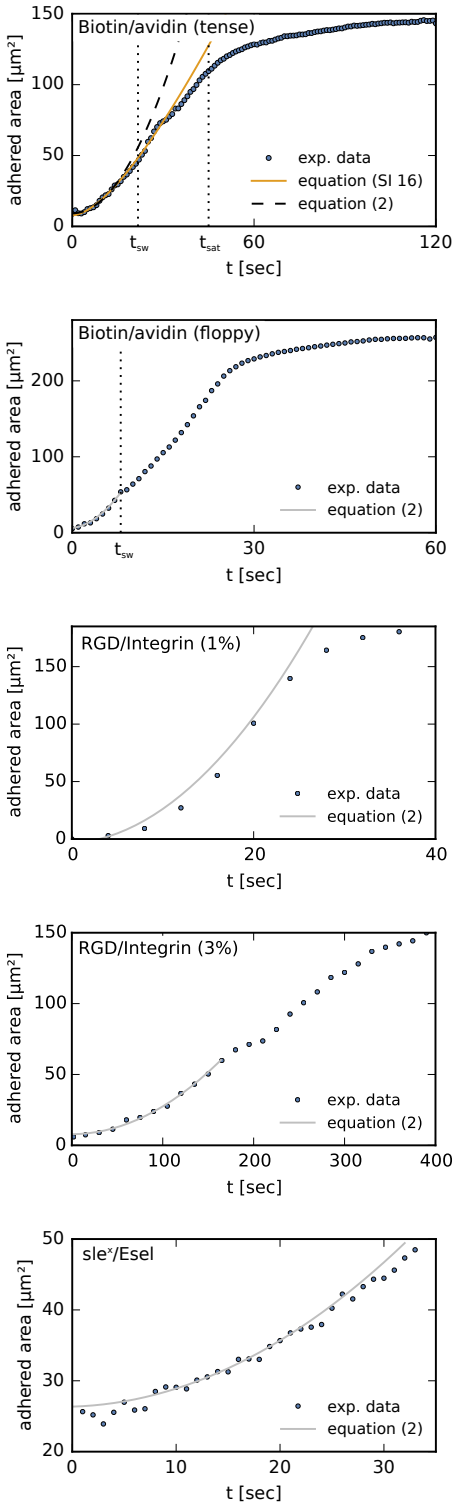

FIGURE SI 4 Characteristic growth curves of the adhered area for different binding pairs. In the top panel t_{sat} was estimated with eq. (SI 24) using $r_V = 10\mu m$ and $k_{\text{on}} = 10^3\, s^{-1}$

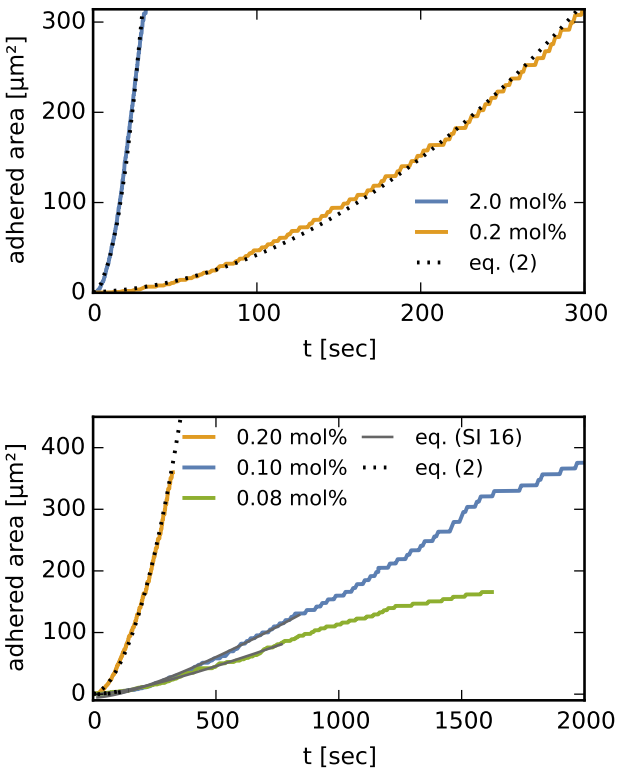

FIGURE SI 5 Top: Reaction limited curves and corresponding fits. This regime is relevant for large densities. Bottom: Diffusion limited curves and corresponding fits. Asymptotically, the curves are diffusion limited (i. e. linear in time) except for the largest density, where the rim of the contact zone is reached before the switch between reaction limited and diffusion limited behavior. Initially, the growth is reaction limited (i. e. the area grows quadratically in time). Here, the unit mol% is the percentage of lipids in the membrane carrying an RGD-molecule. Data taken from Boulbitch et al. (19) of the main text.

early stages of growth are fitted by the least square method to a parabola (eq. (2) of the main text). In principle, the convergence of eq. (2) to the true solution suggests that eq. (2) should be used only at very short time scales. However, due to the limited time resolution and a limited number of data points, the fitting interval was extended to t_{sw}. As a result the determined rates are systematically smaller than those obtained from t_{sw}, despite the good accuracy of the fit. We also applied the full solution of the Stefan problem to the data (eq. (SI 16)), which provides a rate that very well agrees with the rate obtained from t_{sw}. However, the complexity of the fitting function may render the fit unstable.

The reported errors were either determined from the fitting procedure (quadratic fits) or by linear error propagation (transition time).

Table SI 1 Values for the association rate obtained by different methods (in units of $[s^{-1}]$).

data set	eq. (1)	eq. (2)
0.08 mol%	61±6	64±1
0.10 mol%	66±7	46±1
0.20 mol%	-	78±2
2.00 mol%	-	79±1

Analysis of data published by Boulbitch et al. in Biophys. J. 81:2743

In order to show the applicability of the extended Stefan problem eq. (SI 1) to (SI 5), we apply our fitting procedure to data taken from Boulbitch et al. (19) of the main text. The growth curves can be seen in figure SI 5.

To show that the cross-over between two regimes is not a unique property of biotin-avidin binding discussed in the main text, we reanalyse growth curves published earlier. In this study, the authors systematically varied the density of ligands from the reaction to the diffusion limited regime for RGD-integrin binding (their preparation is identical to ours for 1% PEG content).

The extracted data clearly show the cross over behavior for the preparations with $\rho_l^0/\rho_r < 1$ and only a quadratic behavior for $\rho_l^0/\rho_r > 1$. Furthermore, we extract this reaction rates following the procedure outlined above and summarize the results in Table SI 1. Since only the density of ligands is changed between various preparations, the rate obtained from all curves should be the same (and equivalent to the rate reported in the main text).

Although direct fitting of eq. (SI 16) suggested a rate of $105 \pm 5s^{-1}$, the obtained results show a remarkable consistency. The systematic, however small variations in the results can be explained by saturation effects which may have affected the diffusion limited curves. This confirms our hypothesis, that the growth at low ligand densities can be described by our extended Stefan problem, whereas at high ligand densities the growth is reaction limited.

P6

Facile colloidal coating of polystyrene nanospheres with tunable gold dendritic patches

Facile colloidal coating of polystyrene nanospheres with tunable gold dendritic patches

Huixin Bao[1,4], Timo Bihr [2,3,4], Ana-Sunčana Smith[3,4] and Robin N. Klupp Taylor[1,4]

[1]Institute of Particle Technology, FAU Erlangen-Nürnberg, Cauerstr. 4, 91058 Erlangen, Germany
[2]Institute of Theoretical Physics, FAU Erlangen-Nürnberg, Nägelsbachstr. 49b, 91052 Erlangen, Germany
[3]II. Institute of Theoretical Physics, University of Stuttgart, Pfaffenwaldring 57/III, 70550 Stuttgart, Germany
[4]Cluster of Excellence "Engineering of Advanced Materials", FAU Erlangen-Nürnberg, Nägelsbachstr. 49b, 91052 Erlangen, Germany.

Nanoscale **6** (2014) 3954-3966

DOI: 10.1039/C3NR04016J 10.1039/C3NR04016J
http://pubs.rsc.org/EN/content/articlehtml/2013/nr/c3nr04016j

Abstract Patchy particles comprise regions of differing material or chemical functionality on otherwise isotropic cores. To meet the great potential of these anisotropic structures in a wide range of application fields, completely new approaches are sought for the scalable and tunable production of patchy particles, particularly those with nanoscale dimensions. In this paper the synthesis of patchy particles via a simple colloidal route is investigated. Using surfactant-free cationic polystyrene nanospheres as core particles, gold patches are produced through the in situ reduction of chloroauric acid with ascorbic acid. The fact that such nanostructured metal patches can be heterogeneously nucleated on polymer nanospheres is related to the electrostatic interaction between core and metal precursor. Furthermore, the lateral expansion of the gold patches over the polystyrene surface is facilitated by an excess of ascorbic acid. The morphology of the patches is highly dendritic and process-induced variations in the structure are related to gold surface mobility using Monte Carlo simulations based on the diffusion limited aggregation principle. Considering the pH dependent behaviour of ascorbic acid it is possible to predict the moiety which most likely adsorbs to the polymer surface and promotes gold surface diffusion. This enables the judicious adjustment of the pH to also obtain non-dendritic patches. On account of the plasmonic behaviour of gold, the patchy particles have morphology-dependent optical properties. The systematic development of the synthetic approach described here is expected to lay a foundation for the development of functional materials based on the self- or directed-assembly of nanoscale building blocks with anisotropic interactions and properties.

Nanoscale

PAPER

View Article Online
View Journal | View Issue

Cite this: *Nanoscale*, 2014, **6**, 3954

Facile colloidal coating of polystyrene nanospheres with tunable gold dendritic patches†

Huixin Bao,[ad] Timo Bihr,[bcd] Ana-Sunčana Smith[bd] and Robin N. Klupp Taylor*[ad]

Patchy particles comprise regions of differing material or chemical functionality on otherwise isotropic cores. To meet the great potential of these anisotropic structures in a wide range of application fields, completely new approaches are sought for the scalable and tunable production of patchy particles, particularly those with nanoscale dimensions. In this paper the synthesis of patchy particles *via* a simple colloidal route is investigated. Using surfactant-free cationic polystyrene nanospheres as core particles, gold patches are produced through the *in situ* reduction of chloroauric acid with ascorbic acid. The fact that such nanostructured metal patches can be heterogeneously nucleated on polymer nanospheres is related to the electrostatic interaction between core and metal precursor. Furthermore, the lateral expansion of the gold patches over the polystyrene surface is facilitated by an excess of ascorbic acid. The morphology of the patches is highly dendritic and process-induced variations in the structure are related to gold surface mobility using Monte Carlo simulations based on the diffusion limited aggregation principle. Considering the pH dependent behaviour of ascorbic acid it is possible to predict the moiety which most likely adsorbs to the polymer surface and promotes gold surface diffusion. This enables the judicious adjustment of the pH to also obtain non-dendritic patches. On account of the plasmonic behaviour of gold, the patchy particles have morphology-dependent optical properties. The systematic development of the synthetic approach described here is expected to lay a foundation for the development of functional materials based on the self- or directed-assembly of nanoscale building blocks with anisotropic interactions and properties.

Received 1st August 2013
Accepted 4th November 2013

DOI: 10.1039/c3nr04016j

www.rsc.org/nanoscale

Introduction

The interest in so-called patchy particles has risen significantly in the last few years due to strong theoretical motivation in addition to their promising practical advantages. The growing status of the field is underlined by the numerous reviews published recently and covering patchy or Janus particles, the latter being a patchy particle with a single 50% coverage patch.[1–6] The surface heterogeneity of patchy particles permits their use as building blocks for complex structures by self-assembly,[7] and they have numerous possibilities as interfacial stabilizers,[8] chemically or magnetically driven swimmers for drug delivery,[9] and as sensor components.[10] Furthermore, patchy particles comprising metallic patches[11] such as gold or silver on dielectric cores such as metal oxide,[12–14] or polymer,[15,16] have drawn much attention due to their promising optical properties.[17,18] The synthesis of metallic patchy particles can be classified into two categories depending how the surface asymmetry is introduced: with and without interfacial templating. The immobilization of particles on a flat substrate followed by the sputtering of metal[19] and the Pickering emulsion method[20] are typical examples of patchy particle fabrication with interfacial templating. The advantage of these techniques is that the obtained particles have uniform morphology. However, serious drawbacks of the approach are lack of tunability (the formation of an arbitrary number of patches in defined locations) and prohibitive scalability.

Patchy particle fabrication without interfacial templating has so far received rather less attention. We recently reported a facile and versatile colloidal route for the synthesis of silver or silver–gold patches on non-functionalized silica particles in aqueous solution.[21,22] Our approach is based on the heterogeneous nucleation of silver directly onto the bare silica surface followed by surface diffusion dominated growth. Although protocols for metal coating of silica particles are already well-known, these mainly rely on a preceding core functionalization step and usually lead to complete shell coatings or metal

[a]*Institute of Particle Technology, FAU Erlangen-Nürnberg, Cauerstr. 4, 91058 Erlangen, Germany. E-mail: robin.klupp.taylor@fau.de*
[b]*Institute of Theoretical Physics, FAU Erlangen-Nürnberg, Nägelsbachstr. 49b, 91052 Erlangen, Germany*
[c]*II. Institute of Theoretical Physics, University of Stuttgart, Pfaffenwaldring 57/III, 70550 Stuttgart, Germany*
[d]*Cluster of Excellence "Engineering of Advanced Materials", FAU Erlangen-Nürnberg, Nägelsbachstr. 49b, 91052 Erlangen, Germany*

† Electronic supplementary information (ESI) available: Further details of the experimental conditions used in the work; SEM images showing the effect of reducing agent, ascorbic acid concentration, core particle concentration, chloroauric acid concentration, temperature and core particle type; zeta potential measurements of core particles. See DOI: 10.1039/c3nr04016j

nanoparticles homogeneously distributed over the surface. Our novel approach relies on non-functionalized cores and makes use of low metal ion concentrations combined with carefully controlled reduction reactions. It was demonstrated that the patch morphology can be tuned from dense cup-like structures to dendritic patches simply by changing the reaction temperature or reactant addition rate. The strong affinity of the metal for the (amorphous) oxide surface observed in that work was unprecedented and led us to investigate whether such a simple synthetic process could be expanded to other materials systems. However, we found that when the silver precursor was replaced with chloroauric acid, no choice of reducing agent could result in the heterogeneous nucleation and growth of gold patches. This negative result is backed up by related literature, which also indicates that while functionalization of silica with amine groups enables some heterogeneous nucleation of gold to occur, there is no surface growth and instead the formation of surface-bound spheroidal nanoparticles.[23] We propose the hypothesis that the relative sign of the electrostatic charge of the core particle and metallic precursor ions or complexes is a critical factor in the heterogeneous nucleation of metal patches as it permits the necessary surface supersaturation for nucleation to be attained. In other words, metals with positively charged precursor ions *e.g.* Ag^+ would nucleate on anionic cores whereas those with negatively charged ions *e.g.* $[Au(OH)_xCl_{4-x}]^-$ would prefer cationic cores. Furthermore, we suggest that surface conformal growth relies on the presence of "sticky" interactions (*e.g.* hydrogen bonds) between at least one reactant and the core particle. This would increase the chance that components of the growing patch arrive predominantly at the patch edge (*via* surface diffusion) rather on the patch face, leading to patch thickening *i.e.* outwards into the bulk solution.

To investigate these hypotheses, we selected polystyrene nanospheres as core particles due to the fact that they can be synthesized with both strongly anionic and cationic character, avoiding the need for post-functionalization as in the case of silica particles. Having demonstrated that our previously reported one-pot approach for silver patch growth on silica could be successfully repeated for anionic polystyrene nanospheres (data not shown), we considered whether gold patches could likewise be formed on cationic polystyrene cores. This will be the main theme of the present work.

Besides aiming to demonstrate further generalization of the heterogeneous nucleation and growth approach for patchy particle synthesis, the work described herein adds to a growing interest on functional gold nanostructures fabricated on polystyrene core particles. Most of the related literature has focused on forming a homogeneous distribution of gold nanoparticles or even a complete gold nanoshell on PS spheres. In the former case, a popular approach has been to adsorb gold nanoparticles onto the core particle surface either by electrostatic interaction or by covalent bonding.[24,25] For instance, 2-aminoethanethiol hydrochloride was used to modify polystyrene particles so that it enabled the covalent binding of gold nanoparticles by thiol groups.[26] In addition, inverting the surface charge *via* the Layer-by-Layer technique and subsequently absorbing oppositely charged nanoparticles is another commonly utilized approach to fabricate this kind of composite material.[27] The swelling and deswelling of PS microspheres in aqueous dispersion in response to tetrahydrofuran has also been demonstrated as a means to deposit preformed gold nanoparticles onto the core surface.[28] In that work it was also showed in one micrograph that patchy coatings with a dendritic morphology could be obtained although the potential significance of this was apparently not recognized and the phenomenon not investigated further.

To produce a complete gold nanoshell from a nanoparticle "seeded" core, further deposition of metal *via* electroless plating leads to an increase in the size of the seed nanoparticles until a complete shell is formed.[26] Another approach is "seedless" direct metallization, namely, the *in situ* reduction of a metallic precursor in the presence of the core particles leading to the deposition of metal on the surface.[29,30] Along these lines, the reduction of gold with aniline-swelled anionic PS microspheres led to the formation of large gold nanoparticles arrayed on the surface of the cores.[31,32] Furthermore, Li *et al.* recently carried out the reduction of gold in the presence of cationic PS using a range of reducing agents, including ascorbic acid, as used in the present work.[33] They claim that the obtained gold-spheroid decorated spheres formed *via* heterocoagulation of homogeneously nucleated gold nanoparticles and the core particles.

Jang *et al.* reported the direct metallization of silica spheres functionalized with an amine-rich multilayer using ascorbic acid as reductant and polyvinylpyrolidone (PVP) as surface active additive.[12] Although the authors of that work were clearly aiming to produce complete gold nanoshells, an intermediate step in the growth was shown in one micrograph to be a partial coating of the core with a single large patch having a dendritic morphology. The authors attribute this morphology, which is rather analogous to the dendritic structures observed in our earlier work on silver patchy particles, to diffusion limited aggregation (DLA) of gold nuclei at the core's surface. Although following a similar approach to that described in the current work, the mechanism stated by Jang *et al.* raises questions regarding the exact contribution of the ascorbic acid and PVP to the dendritic patch growth.

In the current article we show that in fact cationic PS nanospheres can be coated with multiple gold patches using only ascorbic acid to reduce the auric ion. In particular, our work constitutes the first explicit study of a one pot approach to produce gold patchy particles in homogeneous colloidal solution *i.e.* without interfacial or emulsion templating. We also demonstrate, as with our earlier work on silver patch coatings of silica, that simple process variables can lead to morphological control over the patches formed. By means of systematic experimentation and supported by Monte Carlo simulation of diffusion limited aggregation we show that the dendritic morphology of the patch is particularly sensitive to the ascorbic acid concentration, the pH and the reaction temperature. Our work shows an important step in the establishment of a scalable chemical approach for the formation of anisotropic gold coatings directly onto nanospheres and reveals possibilities for tuning the patch morphology by controlling the surface interaction. The patchy particles show morphology dependant optical properties. Our approach, in comparison with almost all other studies into metal coating of non-metallic core particles may be highly suited for

future work to produce large quantities of surface anisotropic building blocks for self-assembled functional materials.

Methods

Synthesis of polystyrene nanospheres

Cationic polystyrene (PS) nanospheres were synthesized under a surfactant-free condition as previously described.[34] Briefly, the synthesis was carried out in a three-necked round bottom flask fitted with a condenser. A portion of 150 mL Millipore water was firstly bubbled with nitrogen for 1 hour at 40 °C. The initiator, 2,2′-azobis(2-methylpropionamidine) dihydrochloride (97%, V-50, Sigma-Aldrich GmbH, Germany), 0.15 g dissolved in 1 mL water, was added, followed by the addition of a mixture of 68 mL styrene monomer (99%, Merck KGaA, Germany) and 0.28 mL hexadecane (Sigma-Aldrich). The polymerization was carried out at 80 °C under nitrogen bleed for 24 hours. The particles were subsequently washed by centrifugation and re-dispersion in water. The concentration of the final PS nanospheres suspension was 160 mg mL^{-1}. For the synthesis of gold patchy particles, a 10-fold diluted suspension was used. The mean and standard deviation particle diameters as determined by scanning electron microscopy (50 particles measured) were 256 nm and 48 nm respectively. The mean zeta-potential as determined by electrophoretic light scattering at neutral pH was +32.7 mV. Due to the cationic character arising from the anchored amidinium groups provided by the initiator, the suspension remained stable over a long period and no further stabilizing agents were added.

Synthesis of gold nanostructures on PS nanospheres

Tables S1 and S2 in the ESI† provides an overview of the synthetic conditions for the samples described in this work. Gold nanostructure-decorated PS nanospheres were fabricated by reducing aqueous chloroauric acid (gold chloride trihydrate, 99.9%, Sigma-Aldrich) with aqueous L-ascorbic acid (99%, Carl Roth GmbH, Germany) in the presence of the core particles. This reaction was initially performed in the order (1) PS dilution, (2) chloroauric acid addition, (3) ascorbic acid addition while later the order of addition of chloroauric and ascorbic acids was reversed *i.e.* the gold precursor was added to a stirred mixture of PS nanospheres and ascorbic acid. In all cases the three components had a total concentration in the reaction mixture of typically 16 μg mL^{-1} (PS), 0.15 mM (chloroauric acid) and 0.01–100 mM (ascorbic acid). A color-change corresponding to the formation of gold nanostructures was observed immediately following addition of the final reactant. Without further treatment, the optical extinction spectrum of the product suspension was obtained. Prior to microscopical characterization, the particles were separated from the mother solution by centrifugation (14 000 rpm for 5 minutes) and were re-dispersed in water.

Synthesis of gold nanostructures on PS nanospheres with different functional groups and amine functionalized silica spheres

To demonstrate the effect of using alternative cationic spheres in the gold patch coating reaction, amino ($-NH_2$) functionalized PS and silica spheres were used. A suspension of polystyrene particles terminated with amino groups was purchased from Micromod Particle Technology GmbH (Germany) and was used without further treatment. Silica spheres (Monospher M500, Merck KGaA, Germany) functionalized with amine groups were used to replace the polystyrene. The functionalization of silica with 3-aminopropyltriethoxysilane (99%, Sigma-Aldrich) was carried out as detailed in the ESI.† Table S3 in the ESI† provides the details of the synthetic conditions for gold coating of the amino functionalized PS and silica spheres.

Characterization

The optical extinction spectra of the product dispersion were measured by using a Lambda 35 spectrophotometer (Perkin-Elmer GmbH, Germany). The washed product dispersion was dropped onto silicon substrates, allowed to evaporate and was examined using an ULTRA 55 field emission SEM (Carl Zeiss AG, Germany) operating at 10 kV. Transmission electron microscopy (TEM) in high resolution and diffraction contrast modes was carried out using a CM 300 Ultra Twin microscope (Philips/FEI Company, The Netherlands). TEM samples were prepared by dropping the washed product dispersion on a copper grid supported carbon film. The size distribution and zeta potential of the PS nanospheres were measured using a Zetasizer instrument (Nano ZS, Malvern Instruments GmbH, Germany). The particles produced in this work were analyzed by X-ray diffraction (XRD) using a D8 Advance instrument (Bruker AXS GmbH, Germany) with CuKα radiation ($\lambda = 0.15405$ nm). The diffraction experiments were conducted at 2θ values ranging from 10° to 80° with a step size of 0.141°, a step time of 2 s, an applied potential of 30 kV and 40 mA current. The sample for measurement was prepared by drop casting the particles suspension onto the holders which comprise low background sample cups with a vicinal (911) Si crystal of 25 mm diameter (Bruker AXS GmbH).

DLA simulations

We perform Monte Carlo simulations of diffusion limited aggregation[35] with a finite sticking probability *s*.[36] Thereby it is well accepted that lowering the sticking probability increases the density of a growing dendrite,[37] which is related to the survival time of a free tracer when in contact with the dendrite. To account for the finite nature of surface diffusion processes occurring on the PS nanospheres, the simulations were executed on a quadratic square grid of the size 1024 × 1024 sites and using periodic boundary conditions. Thereby curvature effects are not taken into account as they are considered to be small.[38] Furthermore, since the absorption of gold onto the nanospheres is assumed to be fast compared to the growth of the cluster, all tracers (gold atoms) were placed randomly at time $t = 0$ on the grid (the PS colloid) to meet an initial density of choice. Each simulation step propagates the system for δt, when each free tracer performs a self-avoiding random walk with a diffusion constant $D = a^2/4\delta t$, with a being the lattice constant. The domain is nucleated at the beginning of the simulation by a single immobilized tracer particle, placed in the

middle of the lattice. A free particle positioned on a neighbouring site of the domain may attach to the domain with a DLA sticking probability $s(0 \leq s \leq 1)$, which is for the current purposes defined as

$$s = 1 - e^{-k_{on}\delta t}. \quad (1)$$

Here k_{on} should be interpreted as the binding probability of two gold atoms in the domain. Binding to a growing domain depletes the reservoir of diffusing tracers, which ultimately limits the growth to a finite size agglomerate. For small k_{on}

$$s \approx \frac{k_{on}a^2}{4D}.$$

Typically, as the sticking coefficient vanishes, the fractal dimension becomes close to the spatial dimension – close to 2 in the current case.

For presentation purposes, the clusters obtained in simulations are shown with the same resolution as the experimental electron microscopy images.

Results and discussion

Synthesis of gold patches on PS particles

The starting point for the present work was motivated by our previous finding that when anionic silica nanospheres were dispersed in a dilute solution of silver nitrate and a suitable reducing agent added, the heterogeneous nucleation and growth of surface-conformal silver patches occurred.[21] We test our hypothesis, that the electrostatic interaction between core particle and metal precursor was the main factor determining the success of heterogeneous nucleation, by exploring whether gold patches can be formed on cationic spheres from the negatively charged chloroauric ion. We therefore dispersed an aliquot (20 μL) of 16 mg mL^{-1} cationic PS nanospheres in 5 mL of 0.15 mM $HAuCl_4$ aqueous solution. To this dispersion, small aliquots (<50 μL) of ascorbic acid with concentrations of either 0.5 M or 0.1 M were added rapidly during vigorous stirring. Upon the addition of ascorbic acid, the colour of the suspension immediately changed to greenish-blue for larger ascorbic acid amounts and dark purple for smaller. SEM images of four samples prepared in this way are shown in Fig. 1. It can be seen

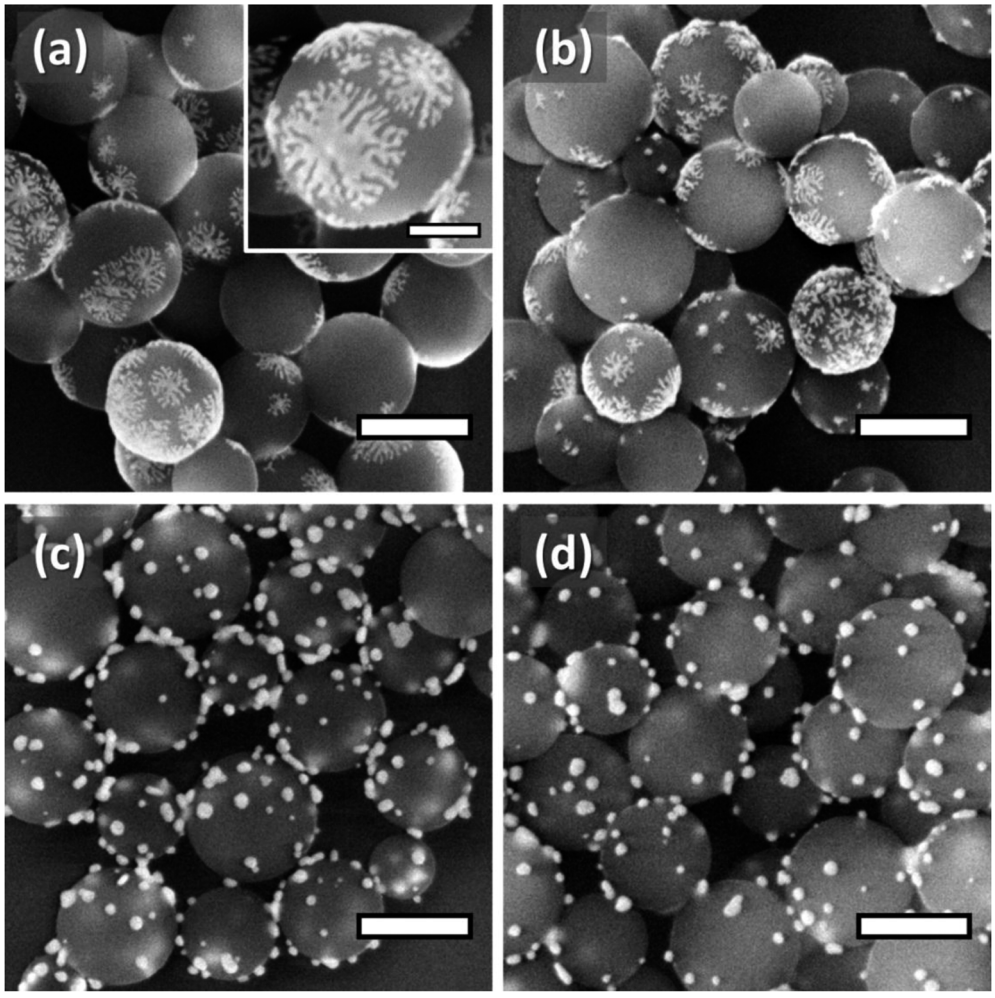

Fig. 1 SEM images of gold nanostructure-decorated cores formed by adding different amounts of ascorbic acid into a mixture of chloroauric acid and cationic PS nanospheres. The ascorbic acid amounts added were (a) 2.5×10^{-5} mol, (b) 2.5×10^{-6} mol, (c) 1.25×10^{-6} mol, (d) 6.25×10^{-7} mol. Scalebars correspond to 250 nm (main micrographs) and 100 nm (inset).

that for larger additions of ascorbic acid (Fig. 1a and b) the polystyrene nanospheres are coated by multiple gold patches with a dendritic morphology. While all core particles possess a patch it is clear that the number of patches per core is somewhat distributed. In particular, for the lower amount of ascorbic acid (Fig. 1b), both small dendritic patches and spheroidal particles, possibly with small surface protrusions are seen. For even smaller ascorbic acid amounts (Fig. 1c and d) no dendritic patches are observed, but rather, the nanospheres are decorated by spheroidal and slightly elongated gold islands. As is already well known, the reduction of the auric ion by ascorbic acid is stoichiometric at a molar ratio of ascorbic acid to gold ($AA : Au^{3+}$) of 1.5.[39] Given that the sample corresponding to Fig. 1c was formed at an $AA : Au^{3+}$ ratio of 1.67 it is clear that the dendritic patch morphology results from an excess of ascorbic acid.

This initial result indicates both similarities and differences with our earlier work on silver patch formation. In both cases heterogeneous nucleation occurs, though our experience shows that a high yield (fraction of cores possessing a patch) is less easily achieved in the case of silver–silica.[21] In the present case, the widespread heterogeneous nucleation may result from the fact that *both* the gold precursor, $[Au(OH)_xCl_{4-x}]^-$ and the ascorbic acid could be expected to adsorb to the core particles, further raising the probability of nucleation. Another similarity between the two systems is the surface conformal growth of a metal on a curved non-metallic surface. In the case of silver–silica fairly continuous patches of metal were produced although these could become somewhat dendritic at higher reaction temperatures.[21] In contrast, the dendritic gold patches formed in the present case are rather finer suggesting that surface diffusion of gold on the PS nanospheres is slower. Furthermore, we did not observe a dendrite-to-nanospheroid transition in the earlier case of silver patchy particle formation. This suggests that there is a minimum concentration of ascorbic acid necessary to induce adsorption of gold that weakly binds to the surface of the core particle and undergoes surface diffusion.

Our present result is also in contrast to the findings of several other groups who reduced gold precursors in the presence of core particles with an opposite valence. Li *et al.* used cationic PS particles synthesized with azoisobutyronitrile initiator and stabilized with polyvinylpyrrolidone (PVP).[33] Using various reducing agents and chloroauric acid, the authors obtained only gold-spheroid decorated particles, a result attributed to a heterocoagulation process but which could also have been explained by heterogeneous nucleation. It should be noted that in our case the gold concentration used was 3.33 times lower and we cover a wider range of $AA : Au^{3+}$ ratios (between 3 times lower and 10 times higher). This, together with the fact that our system is PVP free underlines the profound effect of ascorbic acid on the patch growth. Further earlier work reported that cationic polyelectrolyte grafted polystyrene particles can interact with gold ions ($AuCl_4^-$) electrostatically and result in a homogeneous distribution of gold nanoparticles over the surface when using sodium borohydride as reducing agent.[40,41] Finally, the work of Lee *et al.* showed the direct deposition of gold on anionic polystyrene particles by using a cationic gold precursor to create the stronger interaction between the surface. Once again, however, a homogenous distribution of gold nanoparticles on the surface was obtained.[42] It is therefore clear that while some structures reported in the literature are quite similar to what we observed for lower concentration of ascorbic acid (Fig. 1c and d) gold morphologies corresponding to the clear patchy structures on multiple particles (Fig. 1a and b) have never been reported before.

The relevance of ascorbic acid for producing surface conformal patches was also made clear by our own attempts to use alternative reducing agents. Fig. S1† shows that when ascorbic acid is replaced with formaldehyde, sodium borohydride, sodium citrate or hydroxylamine, heterogeneous nucleation occurs but no evidence of surface conformal growth can be seen. In the case of formaldehyde, large flower-like structures protrude from the PS cores. For all other reducing agents various sized spheroidal gold nanoparticles were formed on the surface as was previously reported.[32] Extremely small surface-bound nanoparticles were formed with the strongest reducing agent (sodium borohydride). For trisodium citrate, along with gold nanospheroids, rod- and prism-like structures are observed. These do not appear to be affected by the reducing agent concentration, however. Thus, while it is clear that the heterogeneous nucleation of gold on cationic PS nanospheres can be achieved using other reducing agents, none of them are able to provide the necessary interfacial conditions to enable surface conformal growth.

Effect of ascorbic acid concentration on patchy particle morphology and optical properties

To explore in more depth the influence of the ascorbic acid we reversed the order of addition of the reactants. In other words, in a series of nine syntheses we mixed a constant amount of PS nanospheres (20 μL) with 5 mL of ascorbic acid solution having a concentration in the range 0.05 mM to 100 mM. Following this, 30 μL of a 25 mM chloroauric acid solution was injected. This reaction series corresponded to a variation of the $AA : Au^{3+}$ ratio from 0.3 to 667. We intended that the order reversal should eliminate any dynamic effects relating to the ascorbic acid adsorption at the same time as the gold reduction is proceeding. Fig. 2 show SEM images of typical products from the series (larger area micrographs are included in the ESI, Fig. S2†). As in the case where the ascorbic acid was added after the chloroauric acid (Fig. 1) we observe a clear transition in morphology. At very large ascorbic acid concentrations (10–100 mM, corresponding to $AA : Au^{3+}$ ratios of 67–667) well-defined dendritic patches with continuous branches are seen along with a small number of loosely bound spheroidal nanoparticles apparently resulting from homogeneous nucleation. At somewhat lower concentrations (2.5–5 mM, corresponding to $AA : Au^{3+}$ ratios of 17–33) dendritic patches are also seen, albeit with apparently coarser dendrites and displaying a high degree of pearling at the tips of the dendrites. The latter is most likely caused by thinning of the dendrite due to the finiteness of the

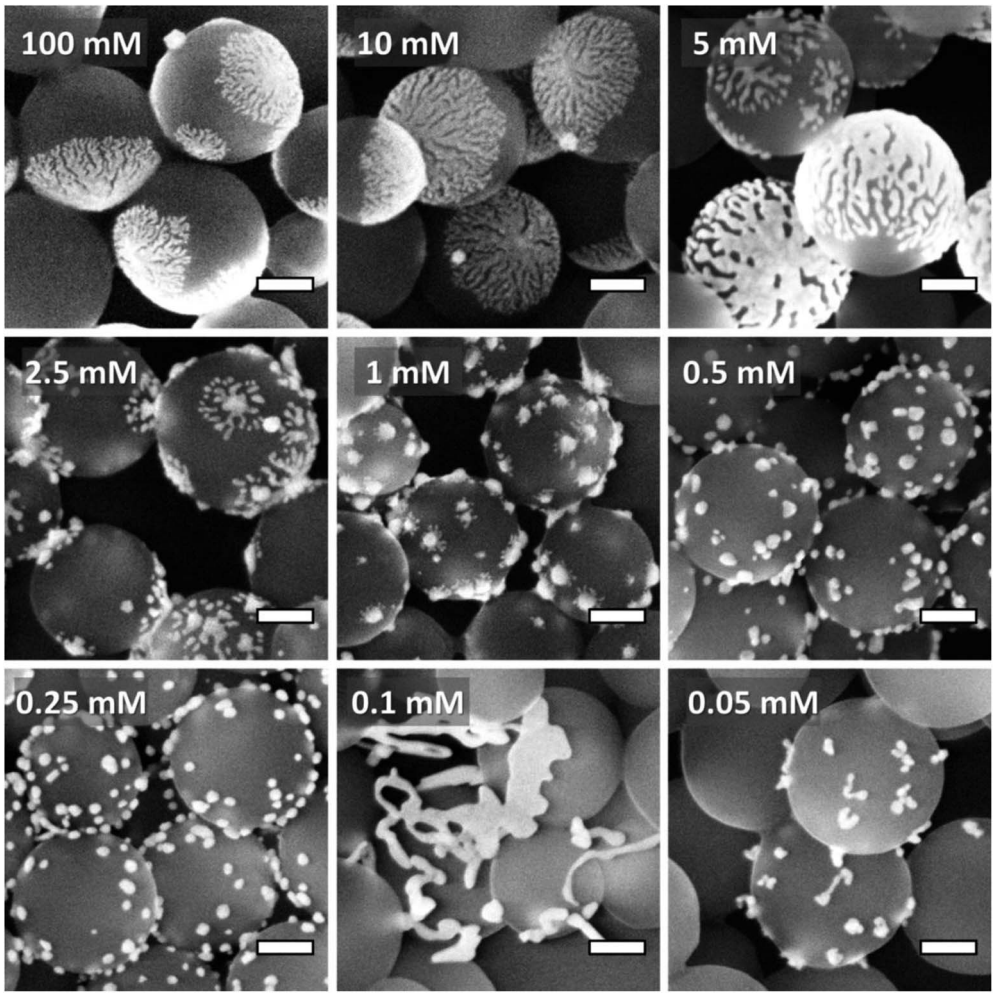

Fig. 2 SEM images of gold nanostructure decorated cores formed by mixing the same amount of cationic PS nanospheres with different concentrations of ascorbic acid (see image label) followed by addition of the same amount of chloroauric acid. Scalebars correspond to 100 nm.

reservoir of diffusing gold atoms and a consequent unbinding of atoms from the dendrite. At 1 mM ascorbic acid (AA : Au^{3+} ratios of 6.7) a very interesting intermediate structure has been isolated. Here, numerous spheroidal nanoparticles are formed on the PS nanospheres, with evidence of the onset of surface growth in the form of small "tentacles" of gold protruding radially from them. For even lower concentrations of ascorbic acid (0.25–0.5 mM, corresponding to AA : Au^{3+} ratios of 1.7–3.3) surface growth is no longer observed, with gold appearing as surface-bound nanospheroids only. For this concentration range we found that the number of gold particles per core nanosphere could be adjusted simply by varying the amount of PS nanospheres added (Fig. S3†). When this amount was very small, the coalescence of some of the surface-bound nanocrystals into elongated islands was promoted (Fig. S3d†). Finally, for the lowest (sub-stoichiometric) ascorbic acid concentrations investigated (0.05–0.1 mM, corresponding to AA : Au^{3+} ratios of 0.33–0.67) highly irregular and often elongated gold nanostructures along with many uncoated PS nanospheres are seen.

To further understand the morphological variation of the gold patches we carried out TEM and XRD analysis on samples produced at ascorbic acid concentrations of 100 mM and 0.5 mM (Fig. 3, S4 and S5†). Besides confirmation of the highly dendritic structure, Fig. 3a shows that the patches with this structure are extremely thin (estimated thickness of 6 nm), further underlining the dominance of diffusion at the PS-solvent interface (rather from the bulk) in their growth. Fig. 3b shows that the surface bound particles which appeared mainly spheroidal in the SEM images of Fig. 1 and 2 are actually rather conical due to the apparently good wetting of the gold for the PS surface. This also demonstrates that, for an ascorbic acid concentration of 0.5 mM at least, these structures are unlikely to have formed in the bulk and attached to the PS nanospheres by heterocoagulation but have in fact heterogeneously nucleated and grown slightly in all accessible dimensions (laterally as well as towards the bulk solvent). Bright- and dark-field images of the same dendritic patchy particle are shown in Fig. 3c and d respectively. The fairly random pattern of contrast especially seen in the dark field image suggests that the patches are polycrystalline, indicating a diffusion-dominated formation mechanism wherein gold clusters adding to the patch are not able to reorientate to preserve a single crystalline habit. This polycrystallinity is also confirmed by the high resolution TEM

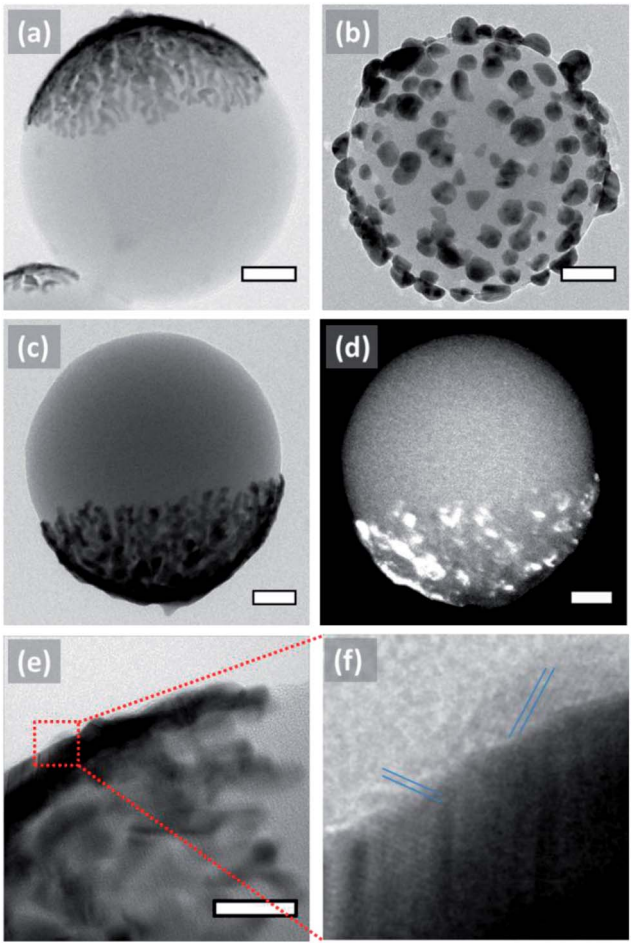

Fig. 3 TEM images of gold nanostructure decorated cores formed by adding equal amounts of chloroauric acid to a mixture of cationic PS nanospheres and ascorbic acid with concentrations of (a, c–f) 100 mM and (b) 0.5 mM. (a–c) Bright field images, (d) dark field image, (e and f) HRTEM images. Scalebars correspond to 50 nm for (a–d) and 20 nm for (e).

images (Fig. 3e and f) and by electron diffraction (Fig. S4†). Finally, XRD patterns of samples corresponding to Fig. 3a and b clearly reveal the fcc structure of gold through peaks at 38.2, 44.4, 64.6 and 77.5° which can be assigned to the (111), (200), (220), and (311) planes respectively (Fig. S5†).[43]

It is interesting to compare some differences in the results between Fig. 1–3 *i.e.* the result of varying the order of addition of ascorbic and chloroauric acid. When the AA : Au^{3+} ratio was 3.3, small dendritic patches were obtained when ascorbic acid was added last (Fig. 1b) but only spheroids were formed when chloroauric acid was added last (Fig. 2 and 3, 0.5 mM). This difference is most likely due to mixing effects in the case of the earlier experiment – in regions where the local ascorbic acid concentration was high, dendritic patches were able to form. Conversely, when ascorbic acid was added first, an adsorption equilibrium over the whole sample could develop prior to addition of gold. As a result, the structures shown in Fig. 2 and 3 are more narrowly dispersed than in Fig. 1 and the spheroid-to-dendrite transition appears to occur at a higher ascorbic acid concentration.

We considered whether the patch coverage could be tailored using our approach. One method could be to change the amount of PS core particles while keeping the ascorbic acid and chloroauric acid additions constant. Another could be to increase the amount of gold, keeping the ascorbic acid and PS cores constant. Fig. S6† demonstrates that both approaches successfully produce gold coatings on the PS nanospheres with a coverage approaching 100%. The fact that coatings approaching complete gold nanoshells could be obtained is consistent with the results of the study on amine multilayer functionalized silica particles by Jang *et al.*[12] Our work demonstrates that gold nanoshells could be produced with an even simpler processes, avoiding the need for a functionalization step and making use of just ascorbic acid (*i.e.* no PVP) to produce the nanoshell.

The strong variation seen in the gold morphology resulting from the concentration of ascorbic acid used is expected to influence the optical properties. Indeed, samples containing dendritic patches had a greenish appearance while those with surface-bound spheroidal patches were purple-coloured. Fig. 4 shows the extinction spectra of gold–PS patchy particles synthesized in the same way as the samples shown in Fig. 2. Due to the strong scattering of polystyrene ($n = 1.59$), features arising from the metal patches are only marginally visible. For the highest concentration of ascorbic acid a clear peak is seen at about 950 nm. This presumably corresponds to the averaged dipole resonance of the large dendritic patches. Compared to our earlier work on (continuous) silver patches this peak is nevertheless rather weak. We believe that this is a result of the significant amount of intrastructural plasmonic coupling leading to broadening of the patch plasmon resonance. Electrodynamic simulations are currently underway to confirm this

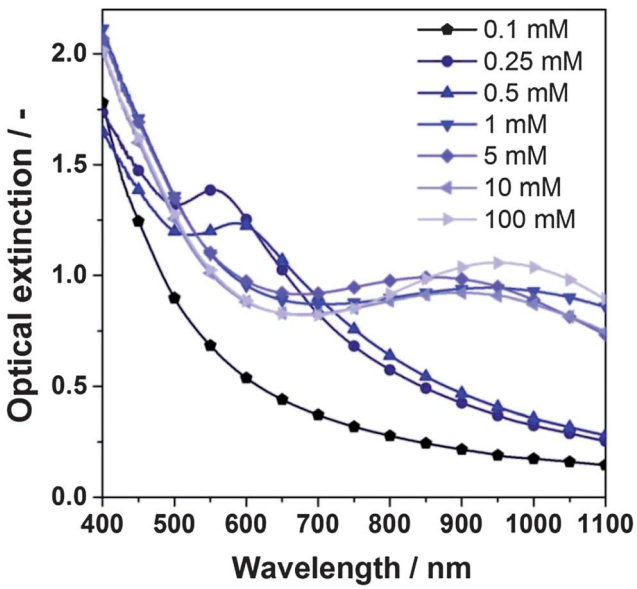

Fig. 4 Optical extinction spectra of gold nanostructure-decorated cores formed by mixing the same amount of cationic PS nanospheres with different concentrations of ascorbic acid followed by addition of the same amount of chloroauric acid.

effect. These will also show the extent of electromagnetic enhancement close to the dendrites. If this is high, such patchy particles could show great promise as substrates for surface enhanced Raman spectroscopy (SERS), similar to observations with other types of dendritic or rough gold nanoparticles.[44,45]

Returning to Fig. 4, as the ascorbic acid concentration decreases (5–10 mM) the patch resonance is seen to blue-shift and broaden, most likely the result of the narrowing and fragmentation of the patch. At 1 mM ascorbic acid an unexpected red-shift occurs. This is possibly due to the highly anisotropic morphology (spheroidal nanoparticles with thin lateral protrusions) at this concentration (see Fig. 2). For further reductions in ascorbic acid, a large blue-shift to 600 nm (0.5 mM ascorbic acid) is seen. As was observed in Fig. 3c, the gold in this sample is mostly in the form of small conical islands, which could account for the fact that the resonance is red-shifted compared to that expected for a perfect sphere of the same volume. Indeed, when the amount of ascorbic acid is further reduced (0.25 mM), a further blue-shift to about 550 nm is seen, suggesting the particles become more spherical. Finally, for the lowest ascorbic acid concentration, the incomplete reduction of gold and observed anisotropic nanostructures results in an undetectable optical response and the extinction spectrum is dominated by the polystyrene nanospheres.

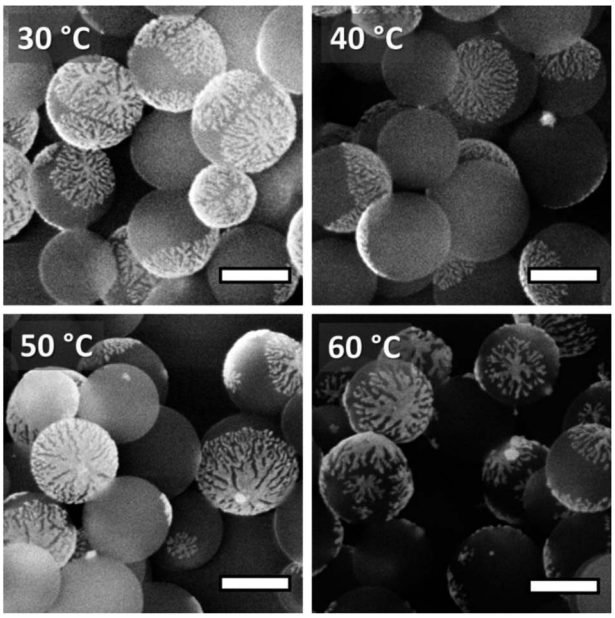

Fig. 5 SEM images of gold nanostructure-decorated cores formed by mixing the same amount of cationic PS nanospheres in 100 mM ascorbic acid followed by addition of the same amount of chloroauric acid. This reaction was carried out at the different temperatures shown. Scalebars correspond to 200 nm.

Influence of reaction temperature on patchy particle morphology

Our earlier work regarding silver patch nucleation and growth on silica spheres was strongly influenced by the reaction temperature.[21] In particular, this parameter was shown to affect both the extent of heterogeneous nucleation and the surface-diffusion mediated growth. In the current work we obtain a high heterogeneous nucleation rate at room temperature resulting in most particles possessing at least one patch. We investigated how the reaction temperature influences the resulting morphology. Fig. 5 shows the results for 100 mM ascorbic acid concentration (AA : Au^{3+} ratio of 667). In contrast to our earlier work on silver–silica only slight morphological changes can be detected. In particular, coarsening of the dendritic structure can be seen as the temperature increases. This may be a result of the increase of surface diffusion constant of gold, as will also be shown later in our simulations. A more profound effect was observed for lower ascorbic acid concentrations (Fig S7†). Here, a distinct spreading of the spheroidal gold nanoparticles over the PS nanospheres surface was observed at the higher temperature. This seems to indicate a slight improvement in surface diffusion but the particle growth is still integration limited.

Discussion of the patch formation mechanism

The experiments described above show that the one-pot formation of gold patchy particles *via* the heterogeneous nucleation and growth approach is possible when chloroauric acid is reduced by ascorbic acid in the presence of cationic PS nanospheres. Our original hypothesis was that patch nucleation requires an electrostatic attraction between core particles and metal precursor. This would facilitate direct heterogeneous nucleation or promote homogeneous nucleation of gold clusters and rapid adsorption to the surface. Here we have used polystyrene core particles which, by virtue of the azo-initiator employed, possess cationic amidinium surface groups which endow the PS nanospheres with a positive zeta potential over a wide pH range (see Fig. S8†). This is expected to provide a strong attraction to the negatively charged chloroauric complex ion and promote heterogeneous nucleation. Given that when the same reaction was carried out in the presence of anionic PS nanospheres, no gold nanostructures attached to the cores were seen (Fig. S9†) it would appear that our hypothesis is correct.

In order to rule out that the chemistry of the polystyrene core particles themselves might have an effect on the patch formation, we carried out the same gold coating procedure on PS and silica core particles which were cationic by virtue of amine groups on their surface (Fig. S10†). In both cases patchy metal coatings with dendritic morphology were formed. While some spheroidal particles were formed on and off the core particle surfaces, it is believed that optimization of the process parameters for these core particles could eliminate this feature. The fact that gold patches can be formed on amine-functionalized PS or silica constitutes further proof of our hypothesis that core particle chemistry is rather irrelevant and that a prerequisite for patch nucleation is that the precursor has an opposite charge to the core particle. This is also consistent with earlier findings that polymer microspheres with different charged functional groups could influence the formation of gold nanospheres of different sizes on the surface.[46] Differences in the morphologies of the patches in Fig. S10† compared to those formed using amidimium–PS, as used in the rest of this work, can be seen. In

particular, the dendritic morphology appears to have more separated, "star-like" branches with a wider distribution of lengths than when amidimium–PS was used. These differences presumably arise from the different conditions for adsorption of ascorbic acid and diffusion of gold atoms or clusters on the amine-functionalized surface. Furthermore, in the case silica core nanospheres (Fig. S10b†) partial separation of the patches from the cores was sometimes observed, indicating that the amine ligand may provide less adhesion for a grown patch. Due to the rapid patch growth reaction (<1 minute), the study of differences in patch growth mode for different core functionalization demands more sophisticated *in situ* analytical techniques. To this end, in our present work we are exploring options such as non-linear optical spectroscopy and *in situ* TEM.

Having discussed the conditions for patch nucleation, consideration will now be made of parameters which influence the characteristic surface conformal patch growth seen in the present work. In order to obtain patches and not just small spheroidal particles decorating the core nanospheres it is clear that some additional requirements have to be fulfilled. While for the silver–silica system studied previously patch growth was readily achieved over a wide range of conditions, for the gold–PS system considered here surface conformal growth seems to depend critically on the concentration of ascorbic acid. In particular, high excesses of ascorbic acid (at least 40 times the stoichiometric amount) are needed for well-defined patches to be formed. We suggest that enrichment of the PS-nanosphere surface with ascorbic acid promotes the Langmuir-like adsorption of gold, which, once on the surface, maintains lateral mobility. In other words, we suggest the function of ascorbic acid on the surface is to alter the adhesiveness of the surface to gold atoms or clusters. The resulting patches, as we have seen, are highly dendritic in nature and this underlines the relevance of surface diffusion here. Furthermore, for a constant amount of gold precursor added the number of patches per core particle appears to be considerably smaller than the number of surface-bound spheroidal nanoparticles formed at lower ascorbic acid concentrations. This gives the clue that when conditions are perfect for dendritic growth, there is also a reduction in the probability of heterogeneous nucleation. A reason for this might be that at high ascorbic acid concentrations the surface becomes more adhesive for the $AuCl_4^-$ ion or a reaction intermediate such as $AuCl_2^-$.[47] Moreover, this interaction appears weak enough to allow the surface mobility of gold. In other words the gold moiety can reside longer at the surface in a non-aggregated state than in the case when the surface is less adhesive, namely at lower concentration of ascorbic acid. Therefore, if the barrier for nucleation is overcome more gold will be present on an adhesive surface to provide material for patch growth. Consequently a nucleus will tend to grow laterally over the surface and competition for gold by this growing patch will result in dendritic growth, as demonstrated by the polycrystallinity of patches observed in our TEM study (Fig. 6). If the surface is non-adhesive to gold then firstly nucleation will more likely be determined by gold arriving directly from the bulk solution *via* the coulombic interaction referred to above. Secondly, very little lateral growth will be possible due to the lack of surface sites adhesive to gold. Consequently spheroidal surface islands will be formed. In between these two extremes it is expected that there will be a critical concentration of ascorbic acid where the adhesiveness is at an intermediate level so that both appreciable surface diffusion and exchange of gold with the bulk solution can co-exist. Such a situation would be expected to lead to a thinning of the dendrite structure and "pearling", the formation of satellite islands at the edge of the patch. This phenomenon is indeed observed (see Fig. 2, 2.5–5 mM). The appearance of pearls could also indicate some cooperativity between gold atoms that stabilise parts of the structure, an effect that needs to be explored in greater detail.

As suggested above, we hypothesize that an increase in adhesiveness of the PS nanospheres due to the increased concentration of ascorbic acid affects the mobility of gold on the surface of PS. This can be interpreted as a decreasing diffusion constant for gold with increasing the concentration of ascorbic acid and is evidenced by the trend towards finer dendrites (Fig. 2, 5–100 mM). In principle, the density of the dendrite and the thickness of its arms are regulated by the density of gold on the PS particle. However, the dominant effect on the morphology of the dendrite is associated with the DLA parameter s. The latter combines two system parameters – the diffusion constant D of gold on the PS surface, and the binding rate of gold atoms to the gold dendrite, regulated by k_{on} (see eqn (1)). Since there is no indication that the ascorbic acid significantly affects the gold–gold interactions, the main influence on the dendrite morphology must be associated with the change in D. Fig. 6 shows Monte Carlo simulations of gold monolayer domains formed from a constant finite amount of gold and with varying D. We firstly found a value of D which leads to a domain morphology similar to that seen in the experiments for the highest concentration of ascorbic acid of 100 mM (*i.e.* the most gold-adhesive surface). We then found that an increase of D of 1.5 and 6 times was necessary to reproduce the main features of the dendrite morphology at 10 mM and 5 mM respectively (Fig. 6). This shows that reducing the ascorbic acid concentration indeed corresponds to a reduced adhesiveness of the PS surface to gold.

Apart from regulating the morphology of the growth by the ascorbic acid concentration, similar effects are obtained by varying the reaction temperature (Fig. 5). In principle, temperature could affect several aspects of the process. Firstly, the change in entropy of gold in the bulk solution could impact the process of adsorption. Hence the concentration of gold on the surface of the PS particle could be decreased with the increasing temperature. However, since the coverage of the PS colloid does not appear to significantly change with temperature, we assume this effect to be small. It would also be reasonable to assume that increasing temperature could increase the binding rate of gold to the gold dendrite. However, this would imply an increase in the DLA sticking parameter s, leading to thinner dendritic morphologies which are not seen in the experiments. However, increased temperature should also increase the lateral diffusion of gold on the PS particle leading

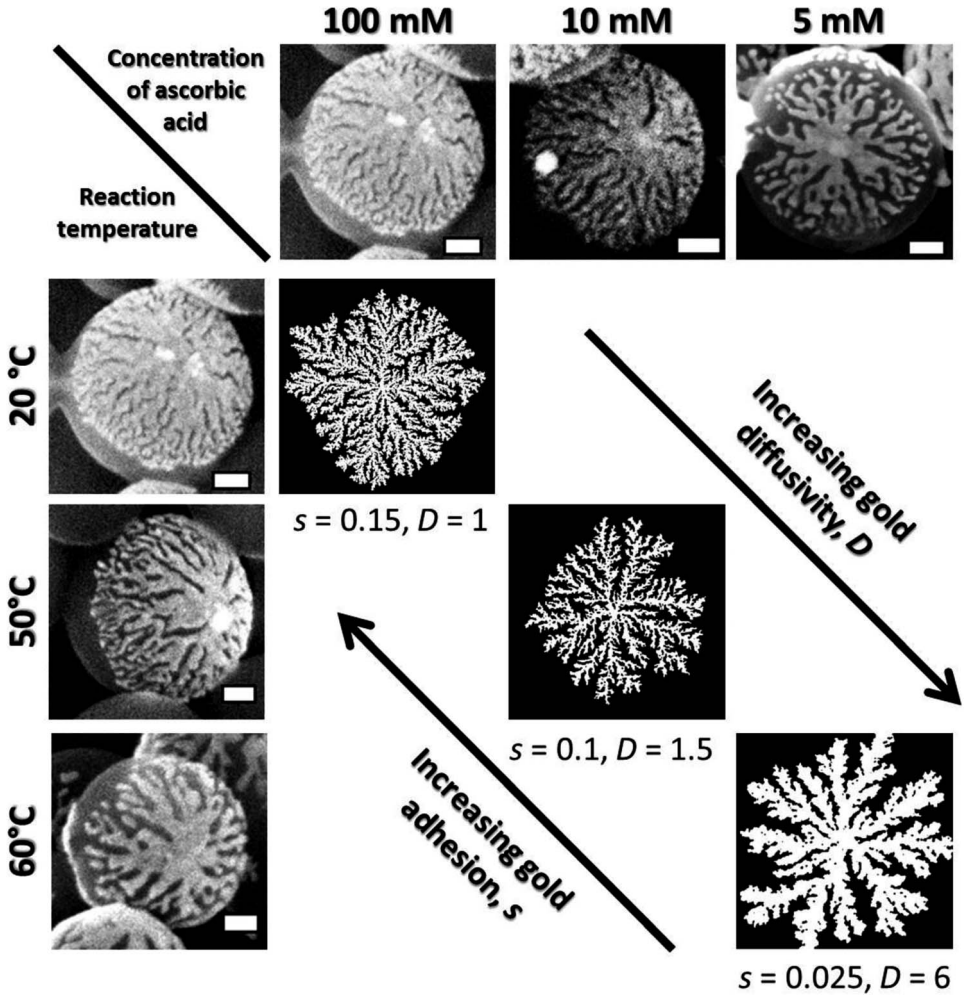

Fig. 6 Comparison of Monte Carlo simulations of gold monolayer domains formed *via* diffusion limited aggregation (DLA) with actual gold patches produced by the reduction of chloroauric acid by ascorbic acid in the presence of cationic PS nanospheres. The variation of the dendritic morphology, invoked experimentally by the ascorbic acid concentration and reaction temperature is shown to correspond to parameters of the DLA simulations (see text). The density of gold atoms on the simulation grid was 0.3. Scalebars correspond to 50 nm.

to the observed slight increase in the thickness of the arms (Fig. 5 and 6). Consequently, we conclude that while a number of parameters could be influenced by the temperature, the dominant effect is most likely the change of lateral mobility of gold atoms.

Having shown using simulations that our hypothesis regarding dendritic patch formation is correct, the question remains, what is it about high concentrations of ascorbic acid that make the core particle surface adhesive? Firstly it should be noted that like many "model" nanostructure-producing reactions, the reduction of the chloroauric ion with ascorbic acid is known to be quite complex with a number of possible parallel reactions taking place and intermediates existing.[47] In particular, the nature of gold reduction depends strongly on the degree of dissociation of the ascorbic acid molecule. As indicated in Table S1,† the pH of the reactions carried out in this work varied between 2.36 (100 mM ascorbic acid), 3.49 (for 1 mM ascorbic acid) and 8.4 (for 0.05 mM ascorbic acid). With dissociation constants $pK_{a,1} = 4.17$ and $pK_{a,2} = 11.58$, it is therefore expected that mainly the non-dissociated (H_2Asc) and singly deprotonated ($HAsc^-$) forms participate in the gold reduction reaction. As has been previously noted, the reducing strength of ascorbic acid increases with pH *i.e.* with the prevalence of the $HAsc^-$ form.[47] However, in the present work, dendritic gold patch growth occurred preferentially at high ascorbic acid concentrations *i.e.* at low pH values, where H_2Asc is prevalent (see Fig. S11†). Consequently we propose that the main species responsible for the adhesiveness of the PS nanospheres surface for gold is H_2Asc. To test this we carried out the gold coating reaction at three different ascorbic acid concentrations (100 mM, 1 mM and 0.5 mM) and for each case carrying out three reactions where we attempted to maintain the pH at around 2.4, 5.1 and 10.3, where H_2Asc, $HAsc^-$, $HAsc^-$ and Asc^{2-} are the dominate species, respectively. Additions of hydrochloric acid and sodium hydroxide were used to make the pH adjustments. The results shown in Fig. 7 indicate that pH indeed has a strong influence on the gold coating morphology. As before, for high ascorbic acid concentration (100 mM), which anyway leads to a low pH, dendritic patches are formed. For the same ascorbic acid concentration, raising the pH to 5.3 leads to

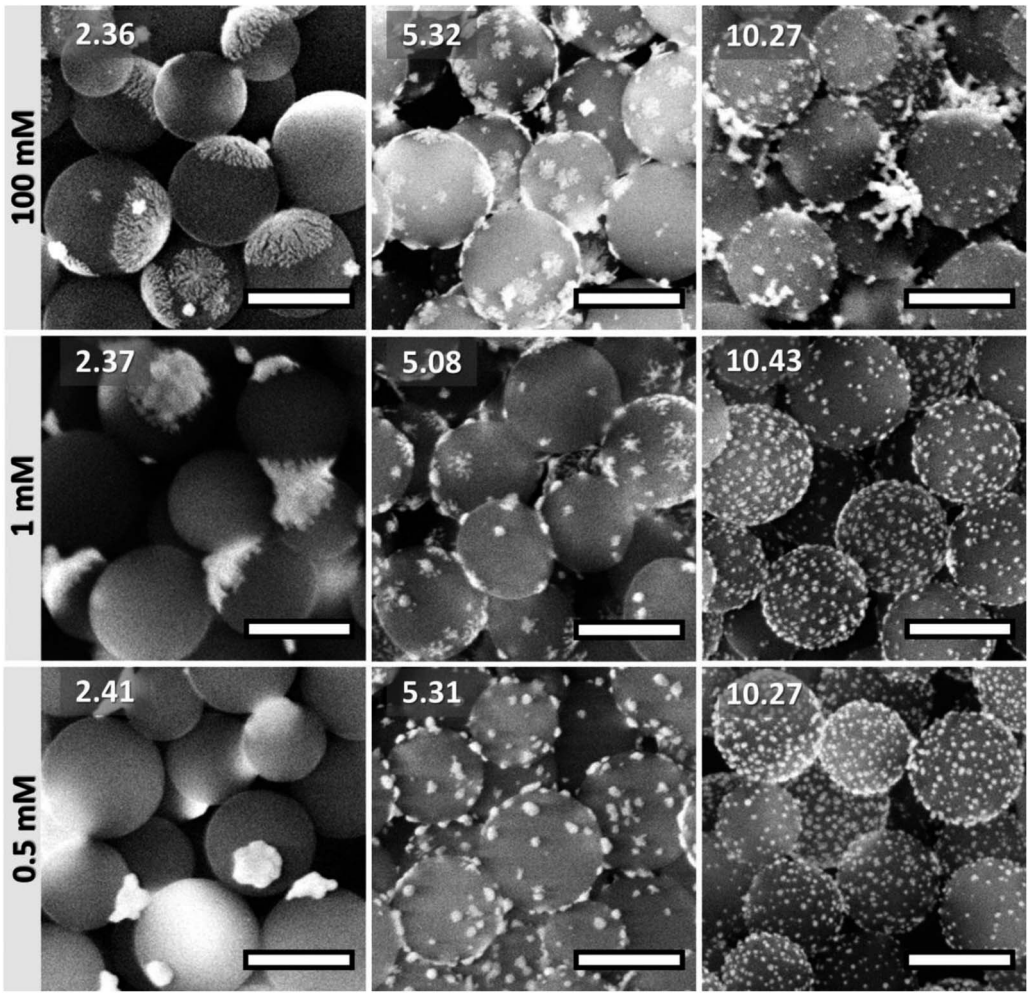

Fig. 7 SEM images of gold nanostructure decorated cores formed by mixing the same amount of cationic PS nanospheres with different concentrations of ascorbic acid (horizontal rows), adjusting the pH to the value shown on the image label, followed by addition of the same amount of chloroauric acid. Scalebars correspond to 250 nm.

smaller patches with a rather coarse dendritic character in addition to many small nanoparticles which may have resulted from homogeneous nucleation. Finally, at a pH of 10.27, many small surface-bound nanoparticles are seen along with aggregates of apparently free nanoparticles. At 1 mM ascorbic acid concentration, deliberate reduction in the naturally occurring pH leads to the formation of quite thick patches with coarse dendritic edges. Although the yield of these patches is rather low, the surface-conformal growth is unmistakable and the structure is somewhat reminiscent of that obtained with the silver–silica system.[21] When the pH is rather increased, small spheroidal particles with dendritic surface protrusions, similar to the structure without pH adjustment (Fig. 2, 1 mM) are seen. For the highest pH, as with 100 mM ascorbic acid, a large number of small nanoparticles are produced. The trends for coated particles produced at 0.5 mM ascorbic acid concentration are similar to those for 1 mM. At reduced pH evidence for some surface conformal growth is present, although the patch yield is again low and patch thickening has also occurred. At higher pH, mostly spheroidal nanoparticles are again formed.

The study of the pH influence on the gold–PS nanostructure morphological evolution confirms our earlier suggestion that the non-dissociated form of ascorbic acid (H_2Asc) promotes the surface-conformal growth of gold. The specific adsorption of H_2Asc could be expected *via* strong N–H···O–C hydrogen bonds between the amidinium groups on the PS and the vinylogous carboxylate group of ascorbic acid.[48] The surface-adsorbed H_2Asc would then participate in $[AuCl_4]^-$ reduction. How it specifically mediates surface diffusion of gold or its intermediates has yet to be determined and will be the subject of future work. However, it is clear that when the concentration of ascorbic acid decreases a change in the adhesiveness of the surface for gold reduces. Moreover, the pH increases and the commensurate increase in the amount of $HAsc^-$ leads to an increase in the rate of reduction. This would explain the preference for a larger number of spheroidal gold nanoparticles to be nucleated on the PS nanospheres at lower ascorbic acid concentrations (see Fig. 2 1 mM ascorbic acid and lower), and is possibly also due to the fact that $[AuCl_4]^-$ will undergo partial hydrolysis to $[Au(OH)_xCl_{4-x}]^-$.[47]

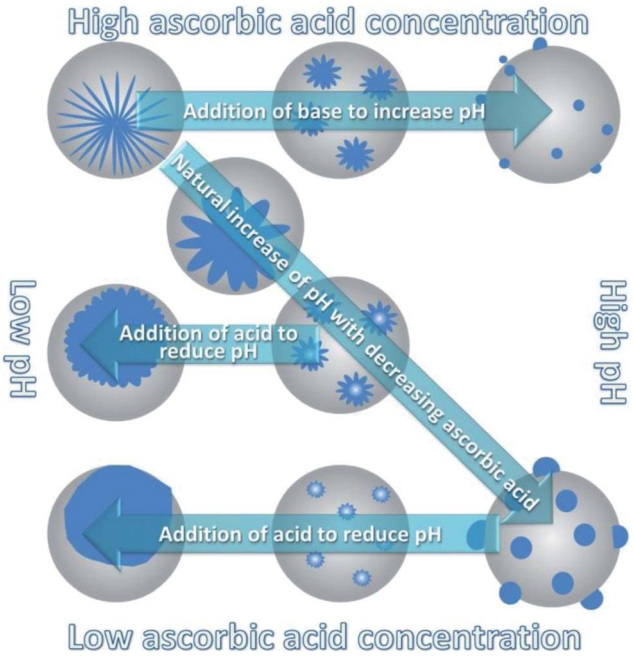

Scheme 1 Schematic representation of the influence of reaction parameters on the morphological variation of gold nanostructures on cationic PS nanospheres.

Since the moiety which we propose makes the PS more adhesive for gold (H_2Asc) is highly pH sensitive and the ascorbic acid concentration itself determines the pH, surface conformal growth could also be activated at lower concentrations of ascorbic acid by adjustment of the pH. Scheme 1 summarizes the key reaction parameters which influence the morphological evolution of gold coatings on cationic PS nanospheres as determined by this study.

Conclusions

A simple and environmentally-friendly method of preparing gold patches on cationic polystyrene nanospheres in aqueous solution has been described. The strategy was based on the novel heterogeneous nucleation and growth approach whereby chloroauric acid was reduced by ascorbic acid in the presence of the core particles. The heterogeneous nucleation of patches was shown to depend mainly on the electrostatic interaction between core and metal precursor. Moreover, the lateral surface growth of gold patches was highly dependent on the ascorbic acid concentration, with an excess of at least 40 times the stoichiometric amount required to produce large thin gold patches on the nanospheres. The patches had a highly dendritic morphology and the dependence of this on reactant concentration, pH and temperature were studied. Furthermore, Monte Carlo simulations assisted with the development of a model for the surface conformal growth. In the latter it is believed that the non-dissociated form of ascorbic acid is responsible for adsorbing to the core particles and providing an adhesive surface for gold. It was shown that non-dendritic patches could be formed if a lower concentration of ascorbic acid was used and the pH deliberately reduced. These conditions resulted in a less adhesive surface for gold but avoided the fast reduction which leads to the nucleation and growth of small spheroidal nanoparticles bound to the polystyrene surface. The patchy particles produced in this work were shown to possess morphology-dependent optical properties, a result of the plasmonic resonances of the highly anisotropic gold coatings. These properties, along with the surface anisotropy are expected to make the patchy particles produced according to the novel method interesting candidates for up-coming studies of self- and directed-organization, self-propelling nanoswimmers, particulate surfactants and plasmonic sensors.

Acknowledgements

The authors gratefully acknowledge the support of the German Research Foundation (DFG), which, within in the framework of its 'Excellence Initiative', supports the Cluster of Excellence 'Engineering of Advanced Materials' at FAU Erlangen-Nürnberg. We kindly acknowledge Prof. Udo Seifert for helpful discussions.

Notes and references

1 G. Loget and A. Kuhn, *J. Mater. Chem.*, 2012, **22**, 15457.
2 J. Du and R. K. O'Reilly, *Chem. Soc. Rev.*, 2011, **40**, 2402.
3 E. Bianchi, R. Blaak and C. N. Likos, *Phys. Chem. Chem. Phys.*, 2011, **13**, 6397.
4 A. B. Pawar and I. Kretzschmar, *Macromol. Rapid Commun.*, 2010, **31**, 150.
5 S. Jiang, Q. Chen, M. Tripathy, E. Luijten, K. S. Schweizer and S. Granick, *Adv. Mater.*, 2010, **22**, 1060.
6 A. Walther and A. H. E. Müller, *Chem. Rev.*, 2013, **113**, 5194.
7 J. Yan, M. Bloom, S. C. Bae, E. Luijten and S. Granick, *Nature*, 2012, **491**, 530.
8 A. Walther, M. Hoffmann and A. H. E. Müller, *Angew. Chem., Int. Ed.*, 2008, **47**, 711.
9 D. Kagan, R. Laocharoensuk, M. Zimmerman, C. Clawson, S. Balasubramanian, D. Kang, D. Bishop, S. Sattayasamitsathit, L. Zhang and J. Wang, *Small*, 2010, **6**, 2741.
10 H. Takei and N. Shimizu, *Langmuir*, 1997, **13**, 1865.
11 D. Rodriguez-Fernandez and L. M. Liz-Marzan, *Part. Part. Syst. Charact.*, 2013, **30**, 46.
12 S. G. Jang, S. H. Kim, S. Y. Lee, W. C. Jeong and S. M. Yang, *J. Colloid Interface Sci.*, 2010, **350**, 387.
13 C. Bae, J. Moon, H. Shin, J. Kim and M. M. Sung, *J. Am. Chem. Soc.*, 2007, **129**, 14232.
14 X. Fu, J. Liu, H. Yang, J. Sun, X. Li, X. Zhang and Y. Jia, *Mater. Chem. Phys.*, 2011, **130**, 334.
15 Y. Xia, Y. Yang, J. Zheng, W. Huang and Z. Li, *RSC Adv.*, 2012, **2**, 5284.
16 V. N. Paunov and O. J. Cayre, *Adv. Mater.*, 2004, **16**, 788.
17 C. Xu, B. Wang and S. Sun, *J. Am. Chem. Soc.*, 2009, **131**, 4216.
18 S. Pradhan, D. Ghosh and S. Chen, *ACS Appl. Mater. Interface*, 2009, **1**, 2060.

19 C. Casagrande and M. Veyssie, *C. R. Acad. Sci., Ser. II: Mec., Phys., Chim., Sci. Terre Univers*, 1988, **306**, 1423.
20 L. Hong, S. Jiang and S. Granick, *Langmuir*, 2006, **22**, 9495.
21 H. Bao, R. N. Klupp Taylor and W. Peukert, *Adv. Mater.*, 2011, **23**, 2644.
22 H. Bao, B. Butz, Z. Zhou, E. Spiecker, M. Hartmann and R. N. Klupp Taylor, *Langmuir*, 2012, **28**, 8971.
23 R. L. Oliveira, D. Zanchet, P. K. Kiyohara and L. M. Rossi, *Chem.–Eur. J.*, 2011, **17**, 4626.
24 A. Sokoutchaev, J. T. James, S. C. Koene, S. Pathak, G. K. S. Prakash and M. E. Thompson, *Chem. Mater.*, 1999, **11**, 2389.
25 J. H. Lee, M. A. Mahmoud, V. Sitterle, J. Sitterle and J. C. Meredith, *J. Am. Chem. Soc.*, 2009, **131**, 5048.
26 W. L. Shi, Y. Sahoo, M. T. Swihart and P. N. Prasad, *Langmuir*, 2005, **21**, 1610.
27 Z. J. Liang, A. S. Susha and F. Caruso, *Adv. Mater.*, 2002, **14**, 1160.
28 J. Lee, M. A. Mahmoud, V. B. Sitterle, J. J. Sitterle and J. C. Meredith, *Chem. Mater.*, 2009, **21**, 5654.
29 J. Zhang, J. Liu, S. Wang, P. Zhan, Z. Wang and N. Ming, *Adv. Funct. Mater.*, 2004, **14**, 1089.
30 A. Dong, Y. Wang, Y. Tang, N. Ren, W. Yang and Z. Gao, *Chem. Commun.*, 2002, 350.
31 J. Gong, X. Zu, W. Mu and Y. Deng, *Colloid Polym. Sci.*, 2013, **291**, 239.
32 Y. Li, Z. Huang, Y. Wu, C. Yang, Y. Gao and Z. Wang, *Colloids Surf., A*, 2012, **407**, 71.
33 Y. Li, Y. Pan, L. Zhu, Z. Wang, D. Su and G. Xu, *Macrmol. Rapid Commun.*, 2011, **32**, 1741.
34 K. Y. van Berkel, G. T. Russell and R. G. Gilbert, *Macromolecules*, 2003, **36**, 3921.
35 A.-L. Barabási, *Fractal concepts in surface growth*, Cambridge University Press, 1995; P. Meakin, *Physica D*, 1995, **86**, 104; T. A. Witten Jr and L. M. Sander, *Phys. Rev. Lett.*, 1981, **47**, 1400.
36 P. Meakin, *Phys. Rev. A*, 1983, **27**, 1495.
37 R. F. Voss and M. Tomkiewicz, *J. Electrochem. Soc.*, 1985, **132**, 371.
38 J. Choi, D. Crowdy and M. Z. Bazant, *Europhys. Lett.*, 2010, **91**, 46005.
39 A. M. Bode, L. Cunningham and R. C. Rose, *Clin. Chem.*, 1990, **36**, 1807.
40 G. Sharma and M. Ballauff, *Macromol. Rapid Commun.*, 2004, **25**, 547.
41 M. Schrinner, S. Proch, Y. Mei, R. Kempe, N. Miyajima and M. Ballauff, *Adv. Mater.*, 2008, **20**, 1928.
42 J. Lee, D. O. Kim, G. Song, Y. Lee, S. Jung and J. Nam, *Macromol. Rapid Commun.*, 2007, **28**, 634.
43 Y. Sun and Y. Xia, *Science*, 2002, **298**, 2176.
44 X. Tang, P. Jiang, G. Ge, M. Tsuji, S. Xie and Y. Guo, *Langmuir*, 2008, **24**, 1763.
45 P. Aldeanueva-Potel, E. Carbó-Argibay, N. Pazos-Pérez, S. Barbosa, I. Pastoriza-Santos, R. A. Alvarez-Puebla and L. M. Liz-Marzán, *ChemPhysChem*, 2012, **13**, 2561.
46 W. Liu, X. Yang and L. Xie, *J. Colloid Interface Sci.*, 2007, **313**, 494.
47 M. Luty-Blocho, K. Paclawski, M. Wojnicki and K. Fitzer, *Inorg. Chim. Acta*, 2013, **395**, 189.
48 I. Kuzmenko, M. Kindermann, K. Kjaer, P. B. Howes, J. Als-Nielsen, R. Granek, G. v. Kiedrowski, L. Leiserowitz and M. Lahav, *J. Am. Chem. Soc.*, 2001, **123**, 3771.

Part IV

Outlook

7 Outlook

In this thesis, the dynamics of intermembrane adhesion was studied. Thereby, especially, the new simulation scheme using effective reaction rates enables future work (see publication P4). This includes the systematic simulation of systems on biological relevant length and time scales using no assumptions or approximations like the use of very small system sizes with periodic boundary conditions. Hence, results from very small simulation boxes do not have to be mapped to biological relevant length scales. Additionally, the Langevin scheme has still potential to simulate systems on intermediate length scales because it has not been parallelized, yet. However, the computational performance will still be worse than the performance of the effective Monte Carlo scheme discussed in Publication P4 because the scaling behavior of the Langevin scheme is not linear but scales with $N \log(N)$ (with N being the number of lattice nodes of the membrane).

So far, we simulated with our effective Monte Carlo scheme only very simple geometries. However, it is easily possible to introduce geometries that represent biological or experimental situations more appropriately. The most obvious geometry is a radial contact area which is connected to a surrounding finite reservoir. This setup represents a vesicle binding to an underlying scaffold. With similar setups, other experimental situations can be simulated like cell-cell adhesion. Most notably, such setups can be of the size of a true cell or vesicle, showing the usefulness of the effective reaction rates. We use such a setup in the appendix A to simulate the unregulated formation of ring-like adhesion domains in a biomimetic model system. The rings that occur in these experiments are similar to rings in in-vivo system, for example in the immune synapse [13]. We find that, in the simulation, the ring formation critically depends on the ratio of the binder densities in the opposing allowing conclusions about the mechanisms in living cells.

In future work, we could consider additional terms in the Helfrich-Hamiltonian

(equation (4.11). For example, surface tension could be integrated easily into both simulation schemes discussed in this thesis. This is interesting from an experimental point of view because the surface tension can be changed experimentally (see for example [14]). Another possible extension are curvature mediated interactions [174]. Here proteins embedded in the membrane interact by their curvature that they imprint on the membrane. Besides that, different types of binder pairs with different lengths and, possibly, different stiffnesses can be introduced into the Helfrich-Hamiltonian. From the physical point of view, this would be interesting because binder pairs with different binder lengths repel each other and so there should be an interesting phase behavior of the adhered state. From the biological point of view, this is relevant there are two different types of binding pairs in the immunological synapse (for a review see [13]). There, the binding pairs show a complex dynamic behavior (see also section I.5). Additionally, parts of the results that were derived in this thesis can be either directly applied for this purpose or require only slightly different treatment. For example, in equation (4.19), one only has to fill the vectors with the respective height differences. Furthermore, it is possible to map this model to the lattice gas models using similar approximations and techniques like Speck et al. [72]. While the equilibrium can be approximately described by the Ising model, the dynamics can be simulated by slightly changed versions of the simulation schemes presented in this thesis or by Monte Carlo methods like Metropolis algorithm.

The effective reaction rates that we derived in publication P4 are only valid in the limit of slow intrinsic reaction rates, i. e. if the transport of the first binding protein to the other protein does not limit the reaction kinetics. According to this reasoning, our effective reaction rates are reaction limited. While the above assumption is well satisfied for the system that we considered, this assumption is not necessarily true for other experimental setups with atomic force microscopes where the limiting process is the diffusion of the binder into the reaction zone of the other binder. In more technical terms, this would be a first passage problem of a diffusing particle in a harmonic potential. Such first passage problems are analytically accessible and hence in this limit the definition of effective reaction rates, this time diffusion limited, are also possible. Furthermore, in experiments both regimes should be easily distinguishable because in the case of reaction limited effective reaction rates the dynamics are independent of the viscosity of the solvent whereas in the other case the viscosity plays a role.

In publication P5, we determined the association rate of a ligand-receptor bond in its respective, quasi two dimensional environment., i. e. the membrane. There, we neglected the dissociation constant. This was justified because of the large binding affinities of the considered binding pairs (at least in a 3D environment). However, the dissociation constant can be included into the boundary conditions that we use. This slight change leads to a simple shift in the density

in the solution of the Stefan problem. Then, with the knowledge of the bond density and the asymptotic mobile binder density at the rim, it would be possible to extract the dissociation constant from the growth curve. As the dissociation constant is directly linked to the binding affinity, we would be able to determine the binding affinity in the respective 2D-environment and verify models describing the influence of confinement in a quasi two dimensional environment on the binding affinity [126, 129].

Surface diffusion limited growth of metal domains has only been studied in certain parameter regimes (see publication P6). Additionally, the amount of metal precursors in the bulk solution is finite and there are several processes on different time scales influencing the growth dynamics, e. g. the nucleation, the absorption on the colloidal surface or the metallic surface and the growth kinetics on the surface. Those processes can be either diffusion limited, reaction limited or determined by Michaelis-Menten dynamics. Combining at least some of those processes in a model can provide valuable insight relevant for finding optimal parameters for the synthesis of patchy particles in experiments. More specifically, such a model can provide, among other information, the patch coverage or the layer thickness of a patch depending on experimental parameters like the size of the colloid, the density of colloids in the solution or the bulk density of the metal precursor. Furthermore, extinction curves of light in combination with simulations of the interaction between light and the metal patches can provide information about the growth dynamics in the experiment. The above discussed extensions of our previous work should enable to identify the experimental relevant parameter regimes and lead to progress in this research field in the near future.

Part V

Bibliography

Bibliography

[1] Canham, P. *The minimum energy of bending as a possible explanation of the biconcave shape of the human red blood cell*. *J. Theor. Biol.* **26**, 61 – 81 (1970).

[2] Helfrich, W. *Elastic properties of lipid bilayers: Theory and possible experiments*. *Z. Naturforsch.* **28 c**, 693–703 (1973).

[3] *The nobel prize in chemistry 2014*. URL `http://www.nobelprize.org/nobel_prizes/chemistry/laureates/2014/`.

[4] Rädler, J. O., Feder, T. J., Strey, H. H. & Sackmann, E. *Fluctuation analysis of tension-controlled undulation forces between giant vesicles and solid substrates*. *Phys. Rev. E* **51**, 4526–4536 (1995).

[5] Dembo, M., Torney, D. C., Saxman, K. & Hammer, D. *The reaction-limited kinetics of membrane-to-surface adhesion and detachment*. *Proc. R. Soc. London, Ser. B* **234**, pp. 55–83 (1988).

[6] Bell, G. *Models for the specific adhesion of cells to cells*. *Science* **200**, 618–627 (1978).

[7] Stefan, J. *Über die Theorie der Eisbildung*. *Monatshefte für Mathematik und Physik* **1**, 1–6 (1890).

[8] Boulbitch, A., Guttenberg, Z. & Sackmann, E. *Kinetics of membrane adhesion mediated by ligand-receptor interaction studied with a biomimetic system*. *Biophys. J.* **81**, 2743 – 2751 (2001).

[9] Freund, L. & Lin, Y. *The role of binder mobility in spontaneous adhesive contact and implications for cell adhesion*. *J. Mech. Phys. Solids* **52**, 2455 – 2472 (2004).

[10] Shenoy, V. B. & Freund, L. B. *Growth and shape stability of a biological membrane adhesion complex in the diffusion-mediated regime*. *Proc. Nat. Acad. Sci. U.S.A.* **102**, 3213–3218 (2005).

[11] Gao, H., Shi, W. & Freund, L.-B. *Mechanics of receptor-mediated endocytosis*. *Proc. Nat. Acad. Sci. U.S.A.* **102**, 9469–9474 (2005).

[12] Sackmann, E. & Smith, A.-S. *Physics of cell adhesion: some lessons from cell-mimetic systems*. *Soft Matter* **10**, 1644–1659 (2014).

[13] Dustin, M. L. & Groves, J. T. *Receptor signaling clusters in the immune synapse*. *Annu. Rev. Biophys.* **41**, 543–556 (2012).

[14] Fenz, S. F. & Sengupta, K. *Giant vesicles as cell models*. *Integr. Biol.* **4**, 982–995 (2012).

[15] Sackmann, E. *Supported membranes: Scientific and practical applications*. *Science* **271**, 43–48 (1996).

[16] Limozin, L. & Sengupta, K. *Quantitative reflection interference contrast microscopy (RICM) in soft matter and cell adhesion*. *ChemPhysChem* **10**, 2752–2768 (2009).

[17] Reister-Gottfried, E., Sengupta, K., Lorz, B., Sackmann, E., Seifert, U. & Smith, A.-S. *Dynamics of specific vesicle-substrate adhesion: From local events to global dynamics*. *Phys. Rev. Lett.* **101**, 208103 (2008).

[18] Smith, A.-S., Fenz, S. F. & Sengupta, K. *Inferring spatial organization of bonds within adhesion clusters by exploiting fluctuations of soft interfaces*. *Europhys. Lett.* **89**, 28003 (2010).

[19] Fenz, S. F., Smith, A.-S., Merkel, R. & Sengupta, K. *Inter-membrane adhesion mediated by mobile linkers: Effect of receptor shortage*. *Soft Matter* **7**, 952–962 (2011).

[20] Bihr, T., Fenz, S., Sackmann, E., Merkel, R., Seifert, U., Sengupta, K. & Smith, A.-S. *Association rates of membrane-coupled cell adhesion molecules*. *Biophys. J.* **107**, L33 – L36 (2014).

[21] Safran, S. A. Statistical thermodynamics of surfaces, interfaces, and membranes (Addison-Wesley Reading, MA, 1994).

[22] Bao, H., Peukert, W. & Taylor, R. K. *One-pot colloidal synthesis of plasmonic patchy particles*. *Adv. Mater.* **23**, 2644–2649 (2011).

[23] Bao, H., Butz, B., Zhou, Z., Spiecker, E., Hartmann, M. & Klupp Taylor, R. N. *Silver-assisted colloidal synthesis of stable, plasmon resonant gold patches on silica nanospheres*. *Langmuir* **28**, 8971–8978 (2012).

[24] Bao, H., Bihr, T., Smith, A.-S. & Klupp Taylor, R. N. *Facile colloidal coating of polystyrene nanospheres with tunable gold dendritic patches*. *Nanoscale* **6**, 3954–3966 (2014).

[25] Israelachvili, J. N., Marčelja, S. & Horn, R. G. *Physical principles of membrane organization*. *Q. Rev. Biophys.* **13**, 121–200 (1980).

[26] Lipowsky, R. & Sackmann, E. Structure and Dynamics of Membranes: I. From Cells to Vesicles/II. Generic and Specific Interactions (Elsevier, 1995).

[27] Phillips, R., Kondev, J., Theriot, J. & Garcia, H. Physical Biology of the Cell (Garland Science, 2012), 2 edn.

[28] Saffman, P. G. & Delbrück, M. *Brownian motion in biological membranes*. *Proc. Nat. Acad. Sci. U.S.A.* **72**, 3111–3113 (1975).

[29] Seifert, U. *Configurations of fluid membranes and vesicles*. *Adv. Phys.* **46**, 13–137 (1997).

[30] Lyman, E. & Patel, S. *Molecular dynamics of lipid bilayers*. *Liposomes, Lipid Bilayers and Model Membranes: From Basic Research to Application* 69 (2014).

[31] Deserno, M. *Fluid lipid membranes: From differential geometry to curvature stresses*. *Chem. Phys. Lipids* – (2014).

[32] Brown, F. *Elastic modeling of biomembranes and lipid bilayers*. *Annu. Rev. Phys. Chem.* **59**, 685–712 (2008).

[33] Müller, M. *Studying amphiphilic self-assembly with soft coarse-grained models*. *J. Stat. Phys.* **145**, 967–1016 (2011).

[34] Kox, A., Michels, J. & Wiegel, F. *Simulation of a lipid monolayer using molecular dynamics*. *Nature* **287**, 317–319 (1980).

[35] van der Ploeg, P. & Berendsen, H. J. C. *Molecular dynamics simulation of a bilayer membrane*. *J. Chem. Phys.* **76**, 3271–3276 (1982).

[36] Marrink, S. J., de Vries, A. H. & Mark, A. E. *Coarse grained model for semiquantitative lipid simulations*. *J. Phys. Chem. B* **108**, 750–760 (2004).

[37] Marrink, S. J., Risselada, H. J., Yefimov, S., Tieleman, D. P. & de Vries, A. H. *The martini force field: Coarse grained model for biomolecular simulations*. *J. Phys. Chem. B* **111**, 7812–7824 (2007).

[38] Limbach, H., Arnold, A., Mann, B. & Holm, C. *Espresso - an extensible simulation package for research on soft matter systems*. *Comput. Phys. Commun.* **174**, 704–727 (2006).

[39] Reynwar, B., Illya, G., Harmandaris, V., Müller, M., Kremer, K. & Deserno, M. *Aggregation and vesiculation of membrane proteins by curvature-mediated interactions*. *Nature* **447**, 461–464 (2007).

[40] Goulian, M., Bruinsma, R. & Pincus, P. *Long-range forces in heterogeneous fluid membranes*. *Europhys. Lett.* **22**, 145 (1993).

[41] Weikl, T. R., Kozlov, M. M. & Helfrich, W. *Interaction of conical membrane inclusions: Effect of lateral tension*. *Phys. Rev. E* **57**, 6988–6995 (1998).

[42] Bartolo, D. & Fournier, J.-B. *Elastic interaction between "hard" or "soft" pointwise inclusions on biological membranes*. *Eur. Phys. J. E Soft* **11**, 141–146 (2003).

[43] Carmo, M. P. D. Differential Geometry of Curves and Surfaces (Pearson, 1976), 1 edn.

[44] Noguchi, H. *Membrane simulation models from nanometer to micrometer scale*. *J. Phys. Soc. Jpn.* **78**, 1007 (2009).

[45] Seifert, U., Berndl, K. & Lipowsky, R. *Shape transformations of vesicles: Phase diagram for spontaneous- curvature and bilayer-coupling models*. *Phys. Rev. A* **44**, 1182–1202 (1991).

[46] Jarić, M., Seifert, U., Wintz, W. & Wortis, M. *Vesicular instabilities: The prolate-to-oblate transition and other shape instabilities of fluid bilayer membranes*. *Phys. Rev. E* **52**, 6623–6634 (1995).

[47] Ziherl, P. & Svetina, S. *Nonaxisymmetric phospholipid vesicles: Rackets, boomerangs, and starfish*. *Europhys. Lett.* **70**, 690 (2005).

[48] Bahrami, A. H., Lipowsky, R. & Weikl, T. R. *Tubulation and aggregation of spherical nanoparticles adsorbed on vesicles*. *Phys. Rev. Lett.* **109**, 188102 (2012).

[49] Huang, C., Zhang, Y., Yuan, H., Gao, H. & Zhang, S. *Role of nanoparticle geometry in endocytosis: Laying down to stand up*. *Nano Lett.* **13**, 4546–4550 (2013).

[50] Dasgupta, S., Auth, T. & Gompper, G. *Wrapping of ellipsoidal nanoparticles by fluid membranes*. *Soft Matter* **9**, 5473–5482 (2013).

[51] Bahrami, A. H., Raatz, M., Agudo-Canalejo, J., Michel, R., Curtis, E. M., Hall, C. K., Gradzielski, M., Lipowsky, R. & Weikl, T. R. *Wrapping of nanoparticles by membranes*. *Adv. Colloid Interface Sci.* **208**, 214 – 224 (2014).

[52] Raatz, M., Lipowsky, R. & Weikl, T. R. *Cooperative wrapping of nanoparticles by membrane tubes*. *Soft Matter* **10**, 3570–3577 (2014).

[53] Weikl, T. R., Asfaw, M., Krobath, H., Różycki, B. & Lipowsky, R. *Adhesion of membranes via receptor-ligand complexes: Domain formation, binding cooperativity, and active processes*. *Soft Matter* **5**, 3213–3224 (2009).

[54] Brown, F. L. H. *Continuum simulations of biomembrane dynamics and the importance of hydrodynamic effects*. *Q. Rev. Biophys.* **44**, 391–432 (2011).

[55] Weikl, T. R. & Lipowsky, R. *Adhesion-induced phase behavior of multicomponent membranes*. *Phys. Rev. E* **64**, 011903 (2001).

[56] Krobath, H., Różycki, B., Lipowsky, R. & Weikl, T. R. *Line tension and stability of domains in cell-adhesion zones mediated by long and short receptor-ligand complexes*. *PLoS One* **6**, e23284 (2011).

[57] Weikl, T. R., Groves, J. T. & Lipowsky, R. *Pattern formation during adhesion of multicomponent membranes*. *Europhys. Lett.* **59**, 916 (2002).

[58] Reister, E., Bihr, T., Seifert, U. & Smith, A.-S. *Two intertwined facets of adherent membranes: Membrane roughness and correlations between ligand-receptors bonds*. *New J. Phys.* **13**, 025003 (2011).

[59] Fenz, S. F., Bihr, T., Merkel, R., Seifert, U., Sengupta, K. & Smith, A.-S. *Switching from ultraweak to strong adhesion*. *Adv. Mater.* **23**, 2622–2626 (2011).

[60] Lin, L. C.-L. & Brown, F. L. H. *Brownian dynamics in fourier space: Membrane simulations over long length and time scales*. *Phys. Rev. Lett.* **93**, 256001 (2004).

[61] Lin, L. C.-L. & Brown, F. L. H. *Dynamic simulations of membranes with cytoskeletal interactions*. *Phys. Rev. E* **72**, 011910 (2005).

[62] Reister-Gottfried, E., Leitenberger, S. M. & Seifert, U. *Hybrid simulations of lateral diffusion in fluctuating membranes*. *Phys. Rev. E* **75**, 011908 (2007).

[63] Leitenberger, S. M., Reister-Gottfried, E. & Seifert, U. *Curvature coupling dependence of membrane protein diffusion coefficients*. *Langmuir* **24**, 1254–1261 (2008).

[64] Reister-Gottfried, E., Leitenberger, S. M. & Seifert, U. *Diffusing proteins on a fluctuating membrane: Analytical theory and simulations*. *Phys. Rev. E* **81**, 031903 (2010).

[65] Lin, L. C.-L., Groves, J. T. & Brown, F. L. *Analysis of shape, fluctuations, and dynamics in intermembrane junctions*. *Biophys. J.* **91**, 3600 – 3606 (2006).

[66] Browicz, T. *Weitere Beobachtungen über Bewegungsphänomene an roten Blutkörperchen in pathologischen Zuständen*. *Zbl. Med. Wissen* **28**, 625–627 (1890).

[67] Lipowsky, R. *Chapter 11 generic interactions of flexible membranes*. *In Lipowsky, R. & Sackmann, E. (eds.)* Structure and Dynamics of Membranes, vol. 1 of *Handbook of Biological Physics*, 521 – 602 (North-Holland, 1995).

[68] Schmidt, D., Monzel, C., Bihr, T., Merkel, R., Seifert, U., Sengupta, K. & Smith, A.-S. *Signature of a nonharmonic potential as revealed from a consistent shape and fluctuation analysis of an adherent membrane*. *Phys. Rev. X* **4**, 021023 (2014).

[69] Mecke, K. R., Charitat, T. & Graner, F. *Fluctuating lipid bilayer in an arbitrary potential: theory and experimental determination of bending rigidity*. *Langmuir* **19**, 2080–2087 (2003).

[70] Gradshteyn, I. & Rhyzik, I. Table of Integrals, Series, and Products (Academic Press, 2007), 7th edn.

[71] Schmidt, D., Bihr, T., Seifert, U. & Smith, A.-S. *Coexistence of dilute and densely packed domains of ligand-receptor bonds in membrane adhesion*. *Europhys. Lett.* **99**, 38003 (2012).

[72] Speck, T., Reister, E. & Seifert, U. *Specific adhesion of membranes: Mapping to an effective bond lattice gas*. *Phys. Rev. E* **82**, 021923 (2010).

[73] Bruinsma, R., Goulian, M. & Pincus, P. *Self-assembly of membrane junctions*. *Biophys. J.* **67**, 746 – 750 (1994).

[74] Bihr, T., Seifert, U. & Smith, A.-S. *Nucleation of ligand-receptor domains in membrane adhesion*. *Phys. Rev. Lett.* **109**, 258101 (2012).

[75] Speck, T. *Effective free energy for pinned membranes*. *Phys. Rev. E* **83**, 050901 (2011).

[76] Speck, T. & Vink, R. L. C. *Random pinning limits the size of membrane adhesion domains*. *Phys. Rev. E* **86**, 031923 (2012).

[77] Bruinsma, R., Behrisch, A. & Sackmann, E. *Adhesive switching of membranes: Experiment and theory*. *Phys. Rev. E* **61**, 4253–4267 (2000).

[78] Doi, M. The theory of polymer dynamics. 73 (Oxford university press, 1988).

[79] Van Kampen, N. G. Stochastic processes in physics and chemistry, vol. 1 (Elsevier, 1992).

[80] Uhlenbeck, G. E. & Ornstein, L. S. *On the theory of the Brownian motion*. *Phys. Rev.* **36**, 823–841 (1930).

[81] Gardiner, C. Stochastic methods (Springer, 1985).

[82] Seifert, U. *Dynamics of a bound membrane*. *Phys. Rev. E* **49**, 3124–3127 (1994).

[83] Liu, A. P. & Fletcher, D. A. *Biology under construction: in vitro reconstitution of cellular function*. *Nat. Rev. Mol. Cell Biol.* **10**, 644–650 (2009).

[84] Tanaka, M. & Sackmann, E. *Polymer-supported membranes as models of the cell surface*. *Nature* **437**, 656–663 (2005).

[85] Smith, A.-S. *Physics challenged by cells*. *Nat. Phys.* **6**, 726–729 (2010).

[86] Grakoui, A., Bromley, S. K., Sumen, C., Davis, M. M., Shaw, A. S., Allen, P. M. & Dustin, M. L. *The immunological synapse: A molecular machine controlling T cell activation*. *Science* **285**, 221–227 (1999).

[87] Arnold, M., Cavalcanti-Adam, E. A., Glass, R., Blümmel, J., Eck, W., Kantlehner, M., Kessler, H. & Spatz, J. P. *Activation of integrin function by nanopatterned adhesive interfaces*. *ChemPhysChem* **5**, 383–388 (2004).

[88] Cavalcanti-Adam, E. A., Micoulet, A., Blümmel, J., Auernheimer, J., Kessler, H. & Spatz, J. P. *Lateral spacing of integrin ligands influences cell spreading and focal adhesion assembly*. *Eur. J. Cell Biol.* **85**, 219 – 224 (2006).

[89] Cavalcanti-Adam, E. A., Volberg, T., Micoulet, A., Kessler, H., Geiger, B. & Spatz, J. P. *Cell spreading and focal adhesion dynamics are regulated by spacing of integrin ligands*. *Biophys. J.* **92**, 2964 – 2974 (2007).

[90] Huang, J., Gräter, S. V., Corbellini, F., Rinck, S., Bock, E., Kemkemer, R., Kessler, H., Ding, J. & Spatz, J. P. *Impact of order and disorder in rgd nanopatterns on cell adhesion*. *Nano Lett.* **9**, 1111–1116 (2009).

[91] Deeg, J., Axmann, M., Matic, J., Liapis, A., Depoil, D., Afrose, J., Curado, S., Dustin, M. L. & Spatz, J. P. *T cell activation is determined by the number of presented antigens*. *Nano Lett.* **13**, 5619–5626 (2013).

[92] Monzel, C., Fenz, S. F., Merkel, R. & Sengupta, K. *Probing biomembrane dynamics by dual-wavelength reflection interference contrast microscopy*. *ChemPhysChem* **10**, 2828–2838 (2009).

[93] Monzel, C., Fenz, S. F., Giesen, M., Merkel, R. & Sengupta, K. *Mapping fluctuations in biomembranes adhered to micropatterns*. *Soft Matter* **8**, 6128–6138 (2012).

[94] Smith, A.-S., Sengupta, K., Goennenwein, S., Seifert, U. & Sackmann, E. *Force-induced growth of adhesion domains is controlled by receptor mobility*. *Proc. Nat. Acad. Sci. U.S.A.* **105**, 6906–6911 (2008).

[95] Phair, R. D. & Misteli, T. *Kinetic modelling approaches to in vivo imaging*. *Nat. Rev. Mol. Cell Biol.* **2**, 898–907 (2001).

[96] Lippincott-Schwartz, J. & Patterson, G. H. *Development and use of fluorescent protein markers in living cells*. *Science* **300**, 87–91 (2003).

[97] Betz, T., Lenz, M., Joanny, J.-F. & Sykes, C. *ATP-dependent mechanics of red blood cells*. *Proc. Nat. Acad. Sci. U.S.A.* **106**, 15320–15325 (2009).

[98] Sackmann, E. & Merkel, R. Lehrbuch der Biophysik (Wiley-VCH, 2010).

[99] Schilling, J., Sengupta, K., Goennenwein, S., Bausch, A. R. & Sackmann, E. *Absolute interfacial distance measurements by dual-wavelength reflection interference contrast microscopy*. *Phys. Rev. E* **69**, 021901 (2004).

[100] Smith, A.-S. & Sackmann, E. *Progress in mimetic studies of cell adhesion and the mechanosensing*. *ChemPhysChem* **10**, 66–78 (2009).

[101] Evans, E. *Probing the relation between force-lifetime-and chemistry in single molecular bonds*. *Annu. Rev. Biophys. Biomol. Struct.* **30**, 105–128 (2001).

[102] Evans, E. A. & Calderwood, D. A. *Forces and bond dynamics in cell adhesion*. *Science* **316**, 1148–1153 (2007).

[103] Evans, E. & Ritchie, K. *Dynamic strength of molecular adhesion bonds*. *Biophys. J.* **72**, 1541 – 1555 (1997).

[104] Evans, E., Leung, A., Hammer, D. & Simon, S. *Chemically distinct transition states govern rapid dissociation of single L-selectin bonds under force*. *Proc. Nat. Acad. Sci. U.S.A.* **98**, 3784–3789 (2001).

[105] Kramers, H. *Brownian motion in a field of force and the diffusion model of chemical reactions*. *Physica* **7**, 284 – 304 (1940).

[106] Lee, G. U., Kidwell, D. A. & Colton, R. J. *Sensing discrete streptavidin-biotin interactions with atomic force microscopy*. *Langmuir* **10**, 354–357 (1994).

[107] Florin, E., Moy, V. & Gaub, H. *Adhesion forces between individual ligand-receptor pairs*. *Science* **264**, 415–417 (1994).

[108] Merkel, R., Nassoy, P., Leung, A., Ritchie, K. & Evans, E. *Energy landscapes of receptor–ligand bonds explored with dynamic force spectroscopy*. *Nature* **397**, 50–53 (1999).

[109] Izrailev, S., Stepaniants, S., Balsera, M., Oono, Y. & Schulten, K. *Molecular dynamics study of unbinding of the avidin-biotin complex*. *Biophys. J.* **72**, 1568 – 1581 (1997).

[110] Baumgartner, W., Hinterdorfer, P., Ness, W., Raab, A., Vestweber, D., Schindler, H. & Drenckhahn, D. *Cadherin interaction probed by atomic force microscopy*. *Proc. Nat. Acad. Sci. U.S.A.* **97**, 4005–4010 (2000).

[111] Seifert, U. *Rupture of multiple parallel molecular bonds under dynamic loading*. *Phys. Rev. Lett.* **84**, 2750–2753 (2000).

[112] Seifert, U. *Dynamic strength of adhesion molecules: Role of rebinding and self-consistent rates*. *Europhys. Lett.* **58**, 792–798 (2002).

[113] Erdmann, T. & Schwarz, U. S. *Stability of adhesion clusters under constant force*. *Phys. Rev. Lett.* **92**, 108102 (2004).

[114] Erdmann, T. & Schwarz, U. S. *Stochastic dynamics of adhesion clusters under shared constant force and with rebinding*. *J. Chem. Phys.* **121**, 8997–9017 (2004).

[115] Erdmann, T. & Schwarz, U. *Bistability of cell-matrix adhesions resulting from nonlinear receptor-ligand dynamics*. *Biophys. J.* **91**, L60–L62 (2006).

[116] Erdmann, T. & Schwarz, U. S. *Impact of receptor-ligand distance on adhesion cluster stability*. *Eur. Phys. J. E Soft* **22**, 123–137 (2007).

[117] Qian, J., Wang, J. & Gao, H. *Lifetime and strength of adhesive molecular bond clusters between elastic media. Langmuir* **24**, 1262–1270 (2008).

[118] Qian, J., Wang, J., Lin, Y. & Gao, H. *Lifetime and strength of periodic bond clusters between elastic media under inclined loading*. *Biophys. J.* **97**, 2438 – 2445 (2009).

[119] Gao, H., Qian, J. & Chen, B. *Probing mechanical principles of focal contacts in cell–matrix adhesion with a coupled stochastic–elastic modelling framework*. *J. R. Soc. Interface* **8**, 1217–1232 (2011).

[120] Schwarz, U. S. & Safran, S. A. *Physics of adherent cells*. *Rev. Mod. Phys.* **85**, 1327–1381 (2013).

[121] Lorenz, B., Keller, R., Sunnick, E., Geil, B. & Janshoff, A. *Colloidal probe microscopy of membrane–membrane interactions: From ligand–receptor recognition to fusion events*. *Biophys. Chem.* **150**, 54 – 63 (2010).

[122] Lorenz, B., Álvarez de Cienfuegos, L., Oelkers, M., Kriemen, E., Brand, C., Stephan, M., Sunnick, E., Yüksel, D., Kalsani, V., Kumar, K., Werz, D. B. & Janshoff, A. *Model system for cell adhesion mediated by weak carbohydrate–carbohydrate interactions*. *JACS* **134**, 3326–3329 (2012).

[123] Erdmann, T., Pierrat, S., Nassoy, P. & Schwarz, U. S. *Dynamic force spectroscopy on multiple bonds: Experiments and model*. *Europhys. Lett.* **81**, 48001 (2008).

[124] Thomas, W. E., Vogel, V. & Sokurenko, E. *Biophysics of catch bonds*. *Annu. Rev. Biophys.* **37**, 399–416 (2008).

[125] Manibog, K., Li, H., Rakshit, S. & Sivasankar, S. *Resolving the molecular mechanism of cadherin catch bond formation*. *Nat. Commun.* **5**, 3941 (2014).

[126] Wu, Y., Vendome, J., Shapiro, L., Ben-Shaul, A. & Honig, B. *Transforming binding affinities from three dimensions to two with application to cadherin clustering*. *Nature* **475**, 510–513 (2011).

[127] Bell, G., Dembo, M. & Bongrand, P. *Cell adhesion. Competition between nonspecific repulsion and specific bonding*. *Biophys. J.* **45**, 1051 – 1064 (1984).

[128] Wu, Y., Honig, B. & Ben-Shaul, A. *Theory and simulations of adhesion receptor dimerization on membrane surfaces*. *Biophys. J.* **104**, 1221 – 1229 (2013).

[129] Hu, J., Lipowsky, R. & Weikl, T. R. *Binding constants of membrane-anchored receptors and ligands depend strongly on the nanoscale roughness of membranes*. *Proc. Nat. Acad. Sci. U.S.A.* **110**, 15283–15288 (2013).

[130] Torney, D., Dembo, M. & Bell, G. *Thermodynamics of cell adhesion. II. Freely mobile repellers*. *Biophys. J.* **49**, 501 – 507 (1986).

[131] Dembo, M. & Bell, G. I. *The thermodynamics of cell adhesion*. *Curr. Topics Memb. Trans* **29**, 71–89 (1987).

[132] Helfrich, W. *Steric interaction of fluid membranes in multilayer systems*. *Z. Naturforsch.* **33**, 305 (1978).

[133] Lipowsky, R. *Adhesion of membranes via anchored stickers*. *Phys. Rev. Lett.* **77**, 1652–1655 (1996).

[134] Smith, A.-S. & Seifert, U. *Effective adhesion strength of specifically bound vesicles*. *Phys. Rev. E* **71**, 061902 (2005).

[135] Smith, A.-S. & Seifert, U. *Vesicles as a model for controlled (de-)adhesion of cells: a thermodynamic approach*. *Soft Matter* **3**, 275–289 (2007).

[136] Seifert, U. & Lipowsky, R. *Adhesion of vesicles*. *Phys. Rev. A* **42**, 4768–4771 (1990).

[137] Smith, A.-S., Sackmann, E. & Seifert, U. *Effects of a pulling force on the shape of a bound vesicle*. *EPL* **64**, 281 (2003).

[138] Smith, A.-S., Sackmann, E. & Seifert, U. *Pulling tethers from adhered vesicles*. *Phys. Rev. Lett.* **92**, 208101 (2004).

[139] Smith, A.-S., Lorz, B. G., Seifert, U. & Sackmann, E. *Antagonist-induced deadhesion of specifically adhered vesicles*. *Biophys. J.* **90**, 1064 – 1080 (2006).

[140] Lorz, B. G., Smith, A.-S., Gege, C. & Sackmann, E. *Adhesion of giant vesicles mediated by weak binding of sialyl-lewisx to e-selectin in the presence of repelling poly(ethylene glycol) molecules*. *Langmuir* **23**, 12293–12300 (2007).

[141] Becker, R. & Döring, W. *Kinetische Behandlung der Keimbildung in übersättigten Dämpfen*. *Ann. Phys.* **416**, 719–752 (1935).

[142] Zhang, C.-Z. & Wang, Z.-G. *Nucleation of membrane adhesions*. *Phys. Rev. E* **77**, 021906 (2008).

[143] Raudino, A. & Pannuzzo, M. *Nucleation theory with delayed interactions: An application to the early stages of the receptor-mediated adhesion/fusion kinetics of lipid vesicles*. *J. Chem. Phys.* **132**, 045103 (2010).

[144] Raudino, A. & Pannuzzo, M. *Adhesion kinetics between a membrane and a flat substrate. An ideal upper bound to the spreading rate of an adhesive patch*. *J. Phys. Chem. B* **114**, 15495–15505 (2010).

[145] Farago, O. *Membrane fluctuations near a plane rigid surface*. *Phys. Rev. E* **78**, 051919 (2008).

[146] Farago, O. *Fluctuation-induced attraction between adhesion sites of supported membranes*. *Phys. Rev. E* **81**, 050902 (2010).

[147] Weil, N. & Farago, O. *Entropy-driven aggregation of adhesion sites of supported membranes*. *Eur. Phys. J. E Soft* **33**, 81–87 (2010).

[148] Bihr, T., Seifert, U. & Smith, A.-S. *Multiscale approaches to protein-mediated interactions between membranes - relating microscopic and macroscopic dynamics in radially growing adhesions*. *New J. Phys.* **17**, 083016 (2015).

[149] Wiederhorn, S. M., Chae, Y.-H., Jr., C. G. S., Cahn, J., Deng, Y. & Day, D. *Cell adhesion to borate glasses by colloidal probe microscopy*. *Acta Biomater.* **7**, 2256 – 2263 (2011).

[150] Carslaw, H. S. & Jaeger, J. C. Conduction of Heat in Solids (Oxford University Press, USA, 1986), 2 edn.

[151] Frank, F. C. *Radially symmetric phase growth controlled by diffusion*. *Proc. R. Soc. London, Ser. A* **201**, 586–599 (1950).

[152] Krapivsky, P. L., Redner, S. & Ben-Naim, E. A kinetic view of statistical physics (Cambridge University Press, 2010).

[153] Mullins, W. W. & Sekerka, R. F. *Morphological stability of a particle growing by diffusion or heat flow*. *J. Appl. Phys.* **34**, 323–329 (1963).

[154] Witten, T. A. & Sander, L. M. *Diffusion-limited aggregation, a kinetic critical phenomenon*. *Phys. Rev. Lett.* **47**, 1400–1403 (1981).

[155] Witten, T. A. & Sander, L. M. *Diffusion-limited aggregation*. *Phys. Rev. B* **27**, 5686–5697 (1983).

[156] Castro, M., Cuerno, R., Nicoli, M., Vázquez, L. & Buijnsters, J. G. *Universality of cauliflower-like fronts: From nanoscale thin films to macroscopic plants*. *New J. Phys.* **14**, 103039 (2012).

[157] Nicoli, M., Castro, M. & Cuerno, R. *Unified moving-boundary model with fluctuations for unstable diffusive growth*. *Phys. Rev. E* **78**, 021601 (2008).

[158] Petroff, A. P., Beukes, N. J., Rothman, D. H. & Bosak, T. *Biofilm growth and fossil form*. *Phys. Rev. X* **3**, 041012 (2013).

[159] Farrell, F. D. C., Hallatschek, O., Marenduzzo, D. & Waclaw, B. *Mechanically driven growth of quasi-two-dimensional microbial colonies*. *Phys. Rev. Lett.* **111**, 168101 (2013).

[160] Mullins, W. W. & Sekerka, R. F. *Stability of a planar interface during solidification of a dilute binary alloy*. *J. Appl. Phys.* **35**, 444–451 (1964).

[161] Meakin, P. *Diffusion-controlled cluster formation in 2-6-dimensional space*. *Phys. Rev. A* **27**, 1495–1507 (1983).

[162] Meakin, P. & Deutch, J. M. *Monte Carlo simulation of diffusion controlled colloid growth rates in two and three dimensions*. *J. Chem. Phys.* **80**, 2115–2122 (1984).

[163] Voss, R. F. *Multiparticle fractal aggregation*. *J. Stat. Phys.* **36**, 861–872 (1984).

[164] Voss, R. F. *Multiparticle diffusive fractal aggregation*. *Phys. Rev. B* **30**, 334–337 (1984).

[165] Vicsek, T. *Pattern formation in diffusion-limited aggregation*. *Phys. Rev. Lett.* **53**, 2281–2284 (1984).

[166] Voss, R. F. & Tomkiewicz, M. *Computer simulation of dendritic electrodeposition*. *J. Electrochem. Soc.* **132**, 371–375 (1985).

[167] Nagatani, T. *Laplacian growth phenomena with the third boundary condition: Crossover from dense structure to diffusion-limited aggregation fractal*. *Phys. Rev. A* **40**, 7286–7291 (1989).

[168] Fujikawa, H. & Matsushita, M. *Fractal growth of bacillus subtilis on agar plates*. *J. Phys. Soc. Jpn.* **58**, 3875–3878 (1989).

[169] *100+ experiments in chemistry*. URL `http://www.chemicum.com/electrochemistry/`.

[170] *Simulation and nature in design*. URL `http://n-e-r-v-o-u-s.com/education/simulation/week3.php`.

[171] Bico, J., . URL `http://www.pmmh.espci.fr/~jbico/Research.html`.

[172] Niemeyer, L., Pietronero, L. & Wiesmann, H. J. *Fractal dimension of dielectric breakdown*. *Phys. Rev. Lett.* **52**, 1033–1036 (1984).

[173] Saffman, P. G. & Taylor, G. *The penetration of a fluid into a porous medium or hele-shaw cell containing a more viscous liquid*. *Proc. R. Soc. A* **245**, 312–329 (1958).

[174] Yolcu, C. & Deserno, M. *Membrane-mediated interactions between rigid inclusions: An effective field theory*. *Phys. Rev. E* **86**, 031906 (2012).

Part VI

Miscellaneous

Curriculum vitae

Timo Bihr

Böblinger Str. 10B
70178 Stuttgart
☎ *0711/685-64920*
✉ *timo.w.bihr@physik.uni-erlangen.de*

Personal details

Date of birth 28 February 1981
Place of birth Ellwangen/Jagst, Germany
Nationality German

Education

since October 2010 **Phd studies in theoretical physics**, *Universität Stuttgart and Universität Erlangen-Nürnberg*.
Member of Graduate School "Advanced Materials and Processes"
Topic: *Dynamics of intermembrane adhesion*
Supervisors: Professor Udo Seifert, Universität Stuttgart
Professor Ana-Sunčana Smith, Universität Erlangen-Nürnberg

October 2005–September 2010 **Diploma in physics**, *Universität Stuttgart*, Stuttgart.
Physics with focus on statistical mechanics
Diploma thesis
Title: *Specific adhesion of fluctuating membranes*
Supervisor: Professor Udo Seifert, Universität Stuttgart

September 2002–June 2005 **Abitur–equivalent to Highschool degree**, *Abendgymnasium Ostwürttemberg*, Aalen.

Work Experience

Apprenticeship

September 1997–January 2000 **General business administration**, *Carl Zeiss AG*, Oberkochen.

Vocational

January 2000 – April 2001 and February 2002 – September 2005 **Financial administration**, *Carl Zeiss AG*, Oberkochen, Accounts payable, Accounts receivable.

Mai 2001–January 2002 **Compulsory military service**, 1. *Feldjägerbataillon 760 (Military police)*, Munich, Human resources.

Language skills

German Mothertongue
English Fluent
French Basic

Publications in peer-reviewed journals

[1] Reister, E., Bihr, T., Seifert, U. & Smith, A.-S. *Two intertwined facets of adherent membranes: Membrane roughness and correlations between ligand-receptors bonds*. *New J. Phys.* **13**, 025003 (2011).

[2] Fenz, S. F., Bihr, T., Merkel, R., Seifert, U., Sengupta, K. & Smith, A.-S. *Switching from ultraweak to strong adhesion*. *Adv. Mater.* **23**, 2622–2626 (2011).

[3] Bihr, T., Seifert, U. & Smith, A.-S. *Nucleation of ligand-receptor domains in membrane adhesion*. *Phys. Rev. Lett.* **109**, 258101 (2012).

[4] Schmidt, D., Bihr, T., Seifert, U. & Smith, A.-S. *Coexistence of dilute and densely packed domains of ligand-receptor bonds in membrane adhesion*. *Europhys. Lett.* **99**, 38003 (2012).

[5] Bao, H., Bihr, T., Smith, A.-S. & Klupp Taylor, R. N. *Facile colloidal coating of polystyrene nanospheres with tunable gold dendritic patches*. *Nanoscale* **6**, 3954–3966 (2014).

[6] Schmidt, D., Monzel, C., Bihr, T., Merkel, R., Seifert, U., Sengupta, K. & Smith, A.-S. *Signature of a nonharmonic potential as revealed from a consistent shape and fluctuation analysis of an adherent membrane*. *Phys. Rev. X* **4**, 021023 (2014).

[7] Bihr, T., Fenz, S., Sackmann, E., Merkel, R., Seifert, U., Sengupta, K. & Smith, A.-S. *Association rates of membrane-coupled cell adhesion molecules*. *Biophys. J.* **107**, L33 – L36 (2014).

[8] Bihr, T., Seifert, U. & Smith, A.-S. *Multiscale approaches to protein-mediated interactions between membranes - relating microscopic and macroscopic dynamics in radially growing adhesions*. *New J. Phys.* **17**, 083016 (2015).

Conferences

[1] Bihr, T., Reister, E. & Seifert, U. *The role of diffusion on specific adhesion*. DPG Frühjahrstagung, Regensburg (2010).

[2] Bihr, T., Reister, E., Smith, A.-S. & Seifert, U. *The role of membrane fluctuations in specific adhesion*. 467. WE-Heraeus -Seminar: Biophysics om membrane transformations (2010).

[3] Bihr, T., Smith, A.-S. & Seifert, U. *Dynamics of specific adhesion*. DPG Frühjahrstagung, Dresden (2011).

[4] Bihr, T., Smith, A.-S. & Seifert, U. *Nucleation of ligand-receptor-domains in intermembrane adhesion*. DPG Frühjahrstagung, Berlin (2012).

[5] Bihr, T., Schmidt, D., Seifert, U. & Smith, A.-S. *Dynamics of specific adhesion*. PhysCell, Hyères, France (2012).

[6] Bihr, T., Seifert, U. & Smith, A.-S. *Nucleation of ligand-receptor-domains in intermembrane adhesion*. Annual meeting of the German Biophysical Society, Göttingen (2012).

[7] Bihr, T., Smith, A.-S. & Seifert, U. *Reaction-diffusion binding of a membrane to an underlying scaffold*. DPG Frühjahrstagung, Regensburg (2013).

[8] Bihr, T., Smith, A.-S. & Seifert, U. *Dynamics of binding to an underlying scaffold*. Dynamics of crowded systems, Potsdam (2013).

[9] Bihr, T., Schmidt, D., Seifert, U. & Smith, A.-S. *Reaction-diffusion binding of a membrane to an underlying scaffold*. International Soft Matter, Rome (2013).

[10] Bihr, T., Bao, H., Klupp Taylor, R. N., Seifert, U. & Smith, A.-S. *Formation of patchy particles by diffusion limited growth*. DPG Frühjahrstagung, Dresden (2014).

[11] Bihr, T., Bao, H., Klupp Taylor, R. N., Seifert, U. & Smith, A.-S. *Formation of patchy particles by diffusion limited growth*. Venice meeting on Fluctuations in small complex systems II (2014).

[12] Bihr, T., Fenz, S. F., Schmidt, D., Merkel, R., Sengupta, K., Seifert, U. & Smith, A.-S. *Nucleation and growth of cadherin adhesions: The role of membrane elasticity and shape fluctuations*. Symposium Physics and Medicine, Erlangen (2015).

Articles in co-authorship

According to §10, Absatz (3) der Promotionsordnung der Universität Erlangen-Nürnberg and §6, Absatz (5) der Promotionsordnung für die Naturwissenschaftlichen Fakultät der Friedrich-Alexander-Universität Erlangen-Nürnberg it is necessary for scientific contributions in Co-authorship to declare unambiguously which part of such a contribution originate from the candidate. This has to be confirmed by the other co-authors. On the following pages, the respective documents for the publications P1 und P6 can be found. In the other publications in this thesis, the author of this thesis is the first author.

Two intertwined facets of adherent membranes: membrane roughness and correlations between ligand–receptors bonds

Declaration The peer-reviewed article in Chapter P1 of this thesis with the title "Two intertwined facets of adherent membranes: membrane roughness and correlations between ligand–receptors bonds" (hereafter article) was written with the collaboration of the author of this thesis (hereafter author). The author ran the simulations that were discussed in the article and analyzed them. Furthermore, the author created the graphs and was involved in preparing the text of the article.

I hereby declare the correctness of the above statements.

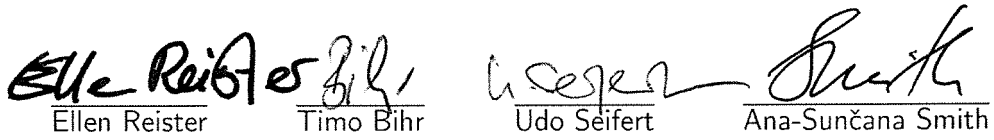

Ellen Reister Timo Bihr Udo Seifert Ana-Sunčana Smith

Facile colloidal coating of polystyrene nanospheres with tunable gold dendritic patches

Declaration The peer-reviewed article in Chapter P6 of this thesis with the title "Facile colloidal coating of polystyrene nanospheres with tunable gold dendritic patches" (hereafter article) was written with the collaboration of the author of this thesis (hereafter author). The author wrote and ran the simulation used in this article. The author analyzed the simulation data, was involved in the interpretation of the simulation results, also, with respect to the experimental data. Furthermore, the author was involved in writing the respective parts of the text of the article.

I hereby declare the correctness of the above statements.

Huixin Bao Timo Bihr Ana-Sunčana Smith Robin N. Klupp Taylor

Statuary declaration

Statuary declaration

Friedrich Alexander Universität Erlangen-Nürnberg
Statuary declaration

Candidate: Timo Wolfgang Bihr
Faculty: Faculty of Sciences
Title: Adhesion of fluctuating membranes

Statuary declaration:
I declare that I have authored this thesis independently, that I have not used other than the declared sources or resources, and that I have explicitly marked all material which has been quoted either literally or by content from the used sources. This work has not been presented to any other examination board in the same or a similar form.

Erlangen, 16.12.2014

Timo Bihr

Timo Bihr

Danksagungen

An dieser Stelle möchte ich mich bei allen bedanken, die zum Gelingen der Doktorarbeit beigetragen haben. Besonders bedanken möchte ich mich bei

- Herr Prof. Dr. Udo Seifert und Prof. Dr. Ana Smith für die Ermöglichung dieser Arbeit, die wissenschaftliche Betreuung, die Ermöglichung der Teilnahme an vielen Tagungen und das gute Arbeitsklima.
- Herr Prof. Eric Lutz für die freundliche Übernahme des Mitberichts.
- Robin Klupp-Taylor und seinem Team für die erfolgreiche Zusammenarbeit bei seinem "Patchy Particles"-Projekt.
- Susanne Fenz, Kheya Sengupta und allen anderen Mitautoren unserer Papers (und "Noch-Drafts") für die ertragreiche Zusammenarbeit auf dem Gebiet der Membranadhäsion.
- Daniel Schmidt für die vielen wissenschaftlichen Diskussionen über die Membranphysik und das Korrekturlesen meiner unendlichen Anzahl von Drafts.
- Zlatko Brkljača, Mislav Cvitković, Sara Kaliman, Zoran Miličević, Jayant Pande, David Smith, Robert Stepić und Damir Vurnek, die mit ihrer Gastfreundschaft das AB-Hotel in Erlangen fast erträglich gemacht haben.
- David Smith für das andauernde Weiterreichen des Telefonhörers an Ana.
- Anja Steinhauser, Waltraud Meinecke, Dragana Vurnek und Ira Röllinghoff für die Hilfe bei allem Organisatorischen.

- Michael Bauer, Boris Lander und Robert Wulfert für die hervorragende Zusammenarbeit bei der Systemadministration. Wann trinken wir eigentlich endlich den Kasten Bier von Frau Steinhauser?
- Anja Steinhauser für den Kasten Bier.
- Michael Bauer, David Hartich, Daniel Schmidt und Robert Wulfert für das Korrekturlesen dieser Arbeit.
- Bei allen Kollegen und ehemaligen Kollegen für das gute Betriebsklima.

A

Receptor jamming induces ring-like adhesions in model membranes

Receptor jamming induces ring-like adhesions in model membranes

Daniel Schmidt[1,2], Timo Bihr[1,2], Susanne Fenz[3,4], Rudolf Merkel[3], Udo Seifert[1], Kheya Sengupta[5] and Ana-Sunčana Smith[6]

[1] Institut für Theoretische Physik and Cluster of Excellence: Engineering of Advanced Materials, Friedrich Alexander Universität Erlangen-Nürnberg, 91052 Erlangen, Germany
[2] II. Institut für Theoretische Physik, Universität Stuttgart, 70569 Stuttgart, Germany
[3] Institute of Complex Systems 7: Biomechanics, Forschungszentrum Jülich GmbH, 52425 Jülich, Germany
[4] Lehrstuhl für Zell- und Entwicklungsbiologie (Zoologie I), Biozentrum der Universität Würzburg, 97074 Würzburg, Germany
[5] Aix-Marseille Université, CNRS, CINaM UMR 7325, 13288 Marseille, France
[6] Insitut Ruđer Bošković, 10000 Zagreb, Croatia

Biochim. Biophys. Acta **In Press, Corrected Proof**

DOI: 10.1016/j.bbamcr.2015.05.025
http://www.sciencedirect.com/science/article/pii/S0167488915001792

Abstract The dynamics of formation of macromolecular structures in adherent membranes is key to a number of cellular processes. However, the interplay between protein reaction kinetics, diffusion and the morphology of the growing domains, governed by membrane mediated interactions, is still poorly understood. Here we show, experimentally and in simulations, that a rich phase diagram emerges from the competition between binding, cooperativity, molecular crowding and membrane spreading. In the cellular context, the spontaneously-occurring organization of adhesion domains in ring-like morphologies is particularly interesting. These are stabilized by the jamming of bulky proteins, and the membrane-transmitted correlations between bonds. Depending on the density of the receptors, this phase may be circumvented, and instead, the adhesions may grow homogeneously in the contact zone between two membranes. If the development of adhesion occurs simultaneously with membrane spreading, much higher accumulation of binders can be achieved depending on the velocity of spreading. The mechanisms identified here, in the context of our mimetic model, may shed light on the structuring of adhesions in the contact zones between two living cells.

Biochimica et Biophysica Acta xxx (2015) xxx–xxx

Contents lists available at ScienceDirect

Biochimica et Biophysica Acta

journal homepage: www.elsevier.com/locate/bbamcr

Crowding of receptors induces ring-like adhesions in model membranes☆

Daniel Schmidt [a,b], Timo Bihr [a,b], Susanne Fenz [c,d], Rudolf Merkel [c], Udo Seifert [b], Kheya Sengupta [e], Ana-Sunčana Smith [a,f,*]

[a] Institut für Theoretische Physik and Cluster of Excellence: Engineering of Advanced Materials, Friedrich Alexander Universität Erlangen–Nürnberg, 91052 Erlangen, Germany
[b] II. Institut für Theoretische Physik, Universität Stuttgart, 70569 Stuttgart, Germany
[c] Institute of Complex Systems 7: Biomechanics, Forschungszentrum Jülich GmbH, 52425 Jülich, Germany
[d] Lehrstuhl für Zell- und Entwicklungsbiologie (Zoologie I), Biozentrum der Universität Würzburg, 97074 Würzburg, Germany
[e] Aix-Marseille Université, CNRS, CINaM UMR 7325, 13288 Marseille, France
[f] Insitut Ruđer Bošković, 10000 Zagreb, Croatia

ARTICLE INFO

Article history:
Received 9 March 2015
Received in revised form 21 May 2015
Accepted 22 May 2015
Available online xxxx

Keywords:
Cell adhesion
Immunological synapse
Adhesion dynamics
Membrane transmitted correlations
Ligand-receptor bonds
Crowding effects
Membrane fluctuations
Diffusion–reaction systems

ABSTRACT

The dynamics of formation of macromolecular structures in adherent membranes is a key to a number of cellular processes. However, the interplay between protein reaction kinetics, diffusion and the morphology of the growing domains, governed by membrane mediated interactions, is still poorly understood. Here we show, experimentally and in simulations, that a rich phase diagram emerges from the competition between binding, cooperativity, molecular crowding and membrane spreading. In the cellular context, the spontaneously-occurring organization of adhesion domains in ring-like morphologies is particularly interesting. These are stabilized by the crowding of bulky proteins, and the membrane-transmitted correlations between bonds. Depending on the density of the receptors, this phase may be circumvented, and instead, the adhesions may grow homogeneously in the contact zone between two membranes. If the development of adhesion occurs simultaneously with membrane spreading, much higher accumulation of binders can be achieved depending on the velocity of spreading. The mechanisms identified here, in the context of our mimetic model, may shed light on the structuring of adhesions in the contact zones between two living cells. This article is part of a Special Issue entitled: Mechanobiology.

1. Introduction

Reorganization of cell surface molecules at the adhesive interface is recognized as an essential feature of cell adhesion and has been extensively studied in the context of integrins, cadherins, and many other cell adhesion molecules [1–6]. A particularly intriguing example is the drastic molecular rearrangement at the interface between a T lymphocyte and an antigen presenting cell, leading to the formation of concentric rings, each enriched in certain specific cell surface molecules [1]. Interestingly, T cells interacting with supported lipid bilayers (SLBs) carrying mobile ligands reproduce this phenomenon [2], and studies on such hybrid systems have revealed the detailed structure and dynamics of formation of these so called SMACs (Supra Molecular Adhesion Structures) [4,3] and elucidated the connection to receptor mobility [5]. From a theoretical perspective, several groups have proposed different effects as the possible driving mechanism for ring-like SMAC formation. These include differences in binding affinity and stiffness [7,8], biased diffusion of antigen complexes towards the interior of the synapse [9] and membrane driven interaction between binding pairs of different lengths [10–15]. The current consensus in the immunology community, based on seemingly decisive experiments with size modified binders [16,17], is that if two types of binders are not of different length the segregation is disrupted. In this context, theoretical considerations suggest that even with two binders, ring-like SMACs are unstable [12].

However, recent experiments showed that the T cell receptor is actually driven by actin, obviating the need to invoke the difference in length between the receptors to explain segregation [4].

Very recently, a ring like structure was also found during the formation of tight junctions in spreading epithelial cells [6]. While the late stage of spreading, which takes place after the ring is formed, is clearly driven by actin, the mechanism for the initial structuring of cadherin adhesions into a ring like structure is not yet understood [6].

Adhesion experiments with model membranes, where the cell in hybrid systems described above is replaced by a giant unilamellar vesicle (GUV, for a sketch of the model see Fig. 1), have furthered our understanding of membrane adhesion, and have vastly aided theoretical

☆ This article is part of a Special Issue entitled: Mechanobiology.

* Corresponding author at: Institut für Theoretische Physik and Cluster of Excellence: Engineering of Advanced Materials, Friedrich Alexander Universität Erlangen–Nürnberg, 91052 Erlangen, Germany and Insitut Ruđer Bošković, 10000 Zagreb, Croatia.
E-mail address: smith@physik.uni-erlangen.de (A.-S. Smith).

http://dx.doi.org/10.1016/j.bbamcr.2015.05.025
0167-4889/

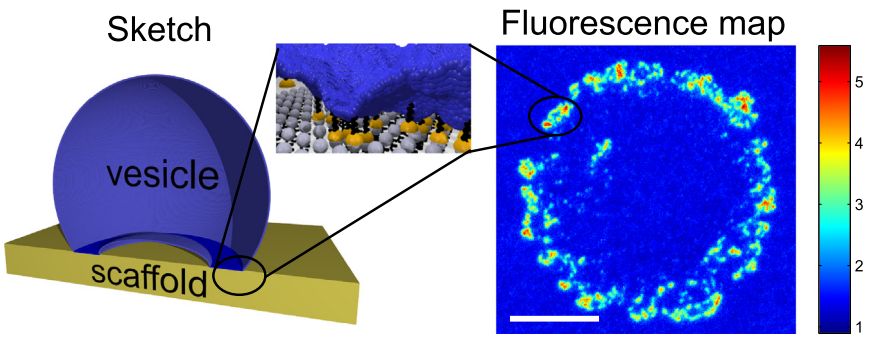

Fig. 1. Left: Cartoon of the system involving a vesicle (blue) which adheres to a scaffold (yellow). The specific adhesion domain (dark-blue and zoom-in on right side) forms a ring. For better visibility, a cut through the vesicle is shown. The inset visualizes a typical microscopic membrane profile. Vertical and lateral dimensions are not to scale. Right: Fluorescence map of a vesicle showing the accumulated receptors in a color code (units in 10^3 μm^{-2}). The scale bar is 10 μm.

modeling [18–20]. In many cases, especially if the GUV is floppy, a ring like domain was seen [21]. However, in most of these cases, the ring, observed in reflection interference contrast microscopy (RICM) images as a dark domain, is transient [21]. One notable exception was reported recently where biotin carrying GUVs adhering to neutravidin carrying SLBs gave rise to SMAC like rings of fluorescent labeled receptors [22]. These rings, formed under conditions of receptor shortage, were reported to be long lived and seemingly stable.

From a theoretical point of view, a thermodynamically stable ring-like domain should be associated with a global minimum of the free energy of adhesion. The latter can be calculated for a fixed number of bonds confined to a particular configuration (see Fig. 2). In this case, the free energy of an adhesion domain emerges as a sum over all bonds for the gain in binding enthalpy and the cost for deforming both the flexible membrane and the adhesion proteins. Additional entropic costs emerge from confining the diffusive binders upon the formation of the bond [23–25] and for suppressing membrane fluctuations. Such a free energy possesses a global minimum for a topologically circular domain where the bond density is not maximal, but is determined by balance of energetic terms that favor maximal bond density and the entropic terms that push the bonds apart. However, we find that in addition to the global minimum, a local minimum exists for a ring-like topology. Since the free energy difference between the global and the meta-stable ring configuration is of several k_BT per bond (see Fig. 2), it is not clear, even for model membranes, what leads to the formation of adhesions in a ring configuration. In the cellular context, coupling to the actin was found to play a major role at longer time scales, but the mechanism for the selective binding at the edge of the contact zone has not been clearly identified yet.

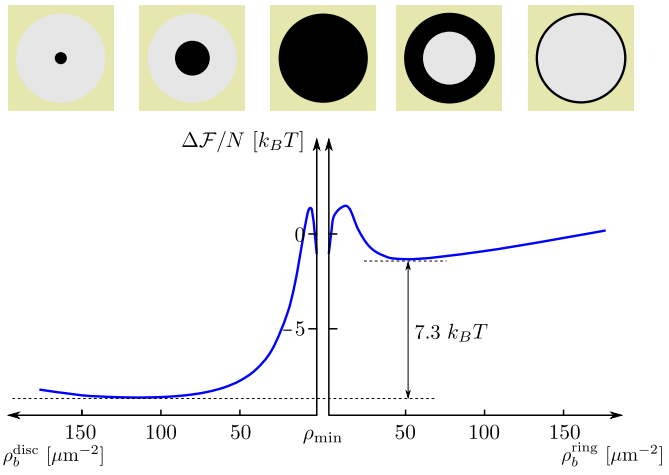

Fig. 2. Free energy per bond $\Delta\mathcal{F}/N$ for a bond domain with a circular (left) and ring like (right) shape. The sketches in the top row illustrate the domain area (black) in the contact zone (gray) accordingly to the axis in the graph. For the circular domain the bond density decreases from left to right while for the ring-like domain it increases. The number of bonds is fixed to $N_b = 200$ for all bond densities with $\rho_{\min} \approx 1.4$ μm^{-2}. All other parameters are chosen according to Table 1.

The aim of our current work is to deepen the understanding of the physical mechanisms that determine the number of adhesion domains, their growth patterns and final morphology. The goal is to identify physical mechanisms that drive the formation of ring-like adhesions, which were experimentally observed in model systems but also in the cellular context. In the latter case, this work may shed light on the role of active processes (not considered here explicitly), which can be used to control the dynamics and the emergent structure of adhesions, including the ring-shaped domains. We achieve this goal by performing an extensive theoretical analysis of the experimentally observed phenomena. We show that ring like structures appear spontaneously in vesicular systems due to the interplay of slow protein diffusion and fast binding kinetics, which results in the formation of bonds at the periphery of the vesicle-substrate contact zone. Furthermore, we find that the necessary conditions for the formation of stabilized rings are (i) the mobility of both binding partners, (ii) membrane transmitted correlations, (iii) bulkiness of binders which allows for crowding and (iv) a significant slowing down of bulky receptors upon binding.

Following this introduction, we first present details of the experimental and simulation procedures. We proceed with constructing the phase diagrams of adhesion for mobile and immobile receptors on the supported bilayer. We analyze and analytically model the identified regimes of growth, and study the stability of ring-like structures. We compare our theoretical framework to the experimental result, and find excellent agreement between the two approaches.

2. Experimental methods

Giant unilamellar vesicles (GUVs) containing a specified amount (0.1 to 5%) of DOPE-cap-biotin (1,2-dioleoyl-sn-glycero-3-phosphoethanolamine-N-(cap biotinyl)) and 2% DOPE-PEG2000 (1,2-dioleoyl-sn-glycero-3-phosphoethanolamine-N-(methoxy (polyethyleneglycol)-2000)), dispersed in a matrix of SOPC (1-stearoyl-2-oleoyl-sn-glycero-3-phosphocholine) (all from Avanti Polar Lipids, Alabaster), are prepared by electro-swelling [26]. Supported lipid bilayers (SLBs) of equivalent composition are prepared by the Langmuir–Blodgett/Langmuir–Schäfer technique and are functionalized with neutravidin covalently linked to the fluorescent label Oregon Green or tetra-methylrhodamine (neutravidin-fl, both Invitrogen, Eugene, OR) and suitable passivated with bovine serum albumin (BSA, 98% purity, Sigma, Saint Louis, MO) (both reconstituted in PBS buffer and ultracentrifugated to eliminate protein aggregates) [26]. The experimental design ensures that both ligands (biotins) and receptors (neutravidins) are mobile [26]. The amount of biotinylated lipids in the GUV and SLB determines the density of ligands and receptors,

Please cite this article as: D. Schmidt, et al., Crowding of receptors induces ring-like adhesions in model membranes, Biochim. Biophys. Acta (2015), http://dx.doi.org/10.1016/j.bbamcr.2015.05.025

respectively. In a typical experiment, 10 μl of the vesicle solution is added to the SLB in a total volume of 1 ml PBS buffer.

Vesicles adhering in steady state are identified by imaging with reflection interference contrast microscopy (RICM) [27,28]. The corresponding receptor distribution of neutravidin-fl is recorded with epifluorescence microscopy using a 63× Antiflex Plan-Neofluar 1.25 oil objective.

The enrichment factor of the receptors, which reflects how much receptors are accumulated in the contact zone, relative to the bulk density, is calculated as described earlier [22]. The diameters of GUVs are determined from phase contrast microscopy in the final state and typically range from 20 to 30 μm.

3. Simulation method

To simulate the process of domain formation we use our recently developed Monte Carlo approach [29]. In this scheme, the vesicle membranes and the SLB membranes are represented by rectangular superimposed grids (lateral size of 40.96 μm), functionalized with ligands and receptors, respectively. To account for different sizes of ligands and receptors, the two lattices have different lattice constants (the lattice constant of the ligand grid is 8 times smaller (4096 × 4096 lattice nodes) than that of the receptor grid).

A circular region is selected on each membrane to represent a contact zone. Both the vesicle membrane and the SLB are treated as reservoirs with a constant number of binders. In both cases periodic boundary conditions for binder diffusion are imposed at the edge of the system. Diffusion is simulated by a simple random walk (diffusion constant D) of particles that mutually interact in the plane of the membrane by hard core repulsion.

To simulate creation and disruption of bonds, we use effective binding and unbinding rates [30], which are sensitive to the local configuration of bonds [31], and integrate the local shape and fluctuations of the vesicle membrane [29]. Binding attempts take place when a free ligand and a free receptor find each other at the same lateral position. Motivated by experimental findings [32,26] which suggest a drastic decline of the mobility of a ligand-receptor complex compared to the diffusion of the unbound species, the formation of a bond is associated with the immobilization of the involved ligand and receptor. If a bond breaks, the ligand and the receptor regain their initial mobility.

The simulation starts by randomly placing ligands on their lattice (lattice constant a) such that the desired ligand density ρ_l^0 is obtained. Furthermore, if the receptors are deemed immobile, they are regularly spaced on their lattice at separations of $\bar{r} = 1/\sqrt{\rho_r^0}$. Alternatively, when simulating mobile receptors, a randomly distributed starting configuration is generated, with the appropriate density ρ_r^0. The simulation is executed until the number of bonds saturates for a significant amount of time.

To be able to compare with experiments, in the simulation we choose the membrane bending rigidity to be $\kappa = 20\ k_BT$ [33], the strength of the interaction potential $\gamma = 6.5$ J/cm^2 [34]. The difference between the equilibrium position of the unbound vesicle membrane and the height for specific adhesion to the substrate is set to $\Delta h = 45$ nm and the vesicle radius is $R = 11.6$ μm with a volume fraction of 97.5% (standard average conditions in the experiments). The binding enthalpy of the biotin–neutravidin bond is taken to be $\epsilon_b \approx 10\ k_BT$ in accordance with previous estimates [22] for the enthalpy of membrane bound biotin–neutravidin bonds, which is considerably weakened because of the coupling of the ligands and receptors to the membrane. All parameters are summed up in Table 1.

Table 1
Parameters used in the simulations.

	Meaning	Value
a	Lattice constant	10 nm
k_BT	Thermal energy at 300 K	$4.14 \cdot 10^{-21}$ J
κ	bending rigidity [33]	20 k_BT
γ	Curvature of the interac. pot.†	6.5 J/cm^4
Δh	Distance between equilibrium Positions of membr. and bond†	45 nm
λ	Stiffness of the bond/receptor*	0.21 mJ/m^2
ϵ_b	Binding enthalpy [22]	9.55 k_BT
D	Diffusion constant [26]	5.0 μm^2/s
R_c	Radius of contact zone†	6.81 μm
d	Lateral size of simulation box (size of the vesicle)†	40.96 μm

† Measured.
* Typical value from literature.

4. Morphological phase diagram

The analysis of simulation and experimental data shows that there are, in principle, four regimes of adhesion processes, mainly determined by the initial ligand and receptor density (Fig. 3). The first is the regime of unstable adhesion at low ligand and receptor densities. Increasing the density of at least one of the binders enables adhesion. Several morphologically different processes ensue. If the density of ligands is larger than the receptor density, numerous randomly distributed nucleation seeds form within the contact zone. The domains grow independently of each other until they come in direct contact and merge, developing further as a large, single domain. We denote this as the regime of multiple nucleation (first row in Fig. 3C). At higher densities of immobile receptors we find a transient ring regime (second row in Fig. 3C). It occurs because ligands diffuse from the bulk of the vesicle into the contact zone, where they bind to the surplus of receptors close to the edge of the contact zone, forming a ring. However, due to the small size of ligands, they are able to diffuse through a bond domain restoring the ligand density in the interior of the ring and continue thickening the ring. Furthermore, upon unbinding from the inner edge of the ring, the ligands move deeper into the contact zone, making the ring morphology only transient. At low densities of mobile receptors, the ring morphology is stabilized by the inability of bulky receptors to penetrate the contact zone (stable ring shown in the third row in Fig. 3C). The large packing density of receptors stabilizes the morphology on time scales that are significantly longer than those accessible in an experiment (stable ring regime).

4.1. Unstable adhesion

For very small ligand and receptor densities, only single bonds opening and closing over the whole contact zone could be observed without ever forming a stable nucleus. We also find that for the current choice of the binding affinity, temperature and membrane bending stiffness, enthalpic arguments [30] predict the critical size of the seed to be two or more bonds. Actually, for immobile receptors, the critical size of the nucleus diverges if the density of bonds (receptors) or ligands becomes too low (dashed line in Fig. 3). For mobile ligands, the density of bonds is self-regulated and typically sufficiently large, such that the adhesion should never be impeded. Indeed, the unstable regime occurs at significantly lower densities than for immobile receptors. However, eventually the domains no longer appear even if receptors are mobile, which suggests that the nucleation process is diffusion limited at very low binder densities. Namely, while the ligands and receptors form occasionally one bond, the time necessary for another pair of binders to diffuse and form the second bond is longer than the life time of the first bond. This, in effect, impedes nucleation.

4.2. Multiple nucleation

This growth regime is reaction limited (initial receptor density ρ_r^0 smaller than initial ligand density ρ_l^0) and it occurs because the nucleation rate is large (the full lines indicate the cross-over from diffusion to reaction limited regimes in Fig. 3A and B). However, the multiple

Please cite this article as: D. Schmidt, et al., Crowding of receptors induces ring-like adhesions in model membranes, Biochim. Biophys. Acta (2015), http://dx.doi.org/10.1016/j.bbamcr.2015.05.025

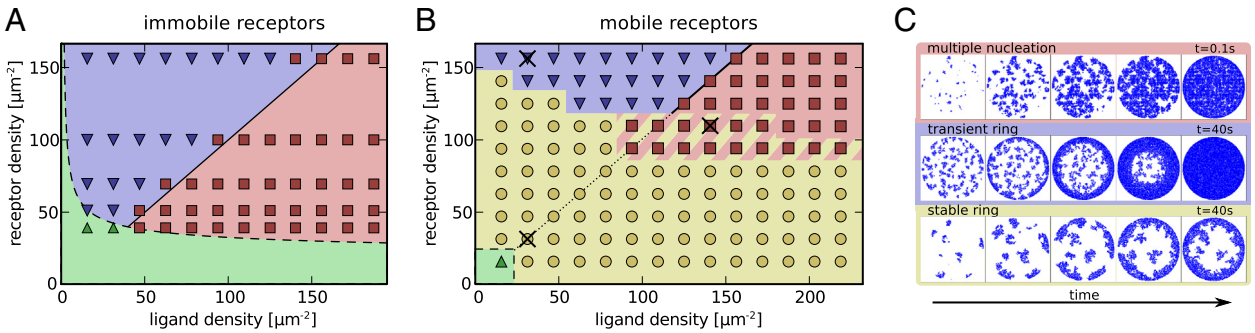

Fig. 3. Phase diagrams for immobile (A) and mobile receptors (B), showing the four regimes of growth: (i) unstable adhesion (green) (ii) regime of multiple nucleation (red) characterized by the formation of small domains all over the contact zone, (iii) transient rings (blue), (iv) stable rings (yellow). (C) Time evolution of adhesions in the contact zone for the three adhesive regimes. The particular parameters are marked in (B) with crosses. Growth dynamics of adhesion obtained in simulations is provided in supplementary material in a form of a movie for each phase.

nucleation regimes are not always accessible in the phase space. For example, a smaller binding affinity leads to a coarsening of the adhesion process, i. e. larger individual adhesion domains and fewer nucleation seeds, and ultimately to radial growth [35]. While having immobile receptors, we find this regime to overlap with the reaction limited part of the phase space, for mobile receptors multiple nucleation occurs at high binder densities where diffusion into the contact zone plays no role and the receptors are almost immobile due to crowding. On the other hand, the surplus of ligands keeps the nucleation rate constant.

This situation is well accounted by the Johnson–Mehl—Avrami–Kolmogorov-theory (JMAK) [36,37] describing the growth dynamics of domains that nucleate at constant nucleation rate Γ and grow with a radial velocity v, independent of time. Under these conditions the number of bonds as a function of time is given by [37]

$$N_b(t) = N_{\mathrm{eq}}\left(1-\exp\left[-\frac{\pi}{3}\Gamma v^2 t^3\right]\right) \tag{1}$$

where N_{eq} denotes the number of bonds in equilibrium and the growth curve has a cubic time dependence in the exponent.

A comparison of this theory with exemplary simulation data with mobile (Fig. 4, yellow diamonds) and immobile receptors (red squares and blue circles) shows reasonable agreement. Small deviations in the growth law arise because the domains do not grow independently due to the relatively small area they are confined to. Furthermore, the vesicle reservoir of ligands becomes depleted over time, affecting both the nucleation rate and the growth velocity. Ultimately, the simulation growth curve saturates and the equilibrium state is achieved.

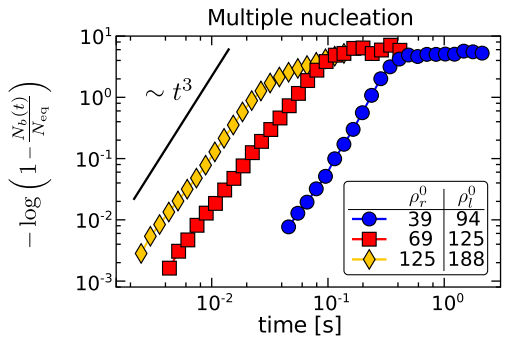

Fig. 4. Avrami plot for three exemplary curves of domain growth in the multiple nucleation regime. The solid black line is a cubic function for comparison with analytical prediction, Eq. (1). Yellow diamonds originate from mobile receptors whereas red squares and blue circles belong to immobile receptors. The densities in the legend are in units of μm^{-2}.

4.3. Transient ring

The formation of a transient ring morphology (blue shaded regions in Fig. 3 A and B) is driven by the diffusion of ligands into the contact zone, where an enthalpy gain is induced upon binding. The formation of transient rings occurs if the initial density of receptors is larger than the initial density of ligands, and if the diffusion of receptors plays no role (immobile receptors or high density of mobile receptors). Because of the relatively large binding affinity, and the surplus of receptors, the ligands bind relatively fast after penetrating the contact zone. This promotes nucleation and a faster growth of domains at the periphery of the contact zone. Eventually, these domains merge and form a ring (identified as an enhancement in the radially averaged bond density close to the edge of the contact zone, relative to the density at the center). However, because of their small size, ligands can move between bonds in the ring. If not bound in the ring, the ligands may penetrate through the ring and bind to free receptors in the interior of the contact zone. This leads to thickening of the ring until it is completely transformed to a disk and the entire contact zone is filled with bonds (second row in Fig. 3C).

As the limiting time scale of the ring closure is determined by diffusion dynamics, the reaction kinetics, earlier important in the regime of multiple nucleation, do not need to be considered. Hence, the dynamics ensuing the establishment of the ring can be modeled by the radially symmetric diffusion equation for the ligand density $\rho_l(r, t)$ [38–41]

$$\frac{\partial \rho_l(r,t)}{\partial t} = D\left(\frac{\partial^2 \rho_l(r,t)}{\partial r^2} + \frac{1}{r}\frac{\partial \rho_l(r,t)}{\partial r}\right). \tag{2}$$

Here D is the diffusion constant of ligands, the radial distance r is measured from the center of the contact zone, and the bond density within the ring will be denoted by ρ_b. This equation is accompanied with a moving boundary condition for the inner radius $R(t)$ of the ring

$$\frac{\partial R(t)}{\partial t} = -\frac{D}{\rho_b}\frac{\partial \rho_l(r,t)}{\partial r}\bigg|_{r=R(t)}, \tag{3}$$

and the density of ligands at the inner interface

$$\rho_l(R(t),t) = \rho_l^e. \tag{4}$$

Initial conditions intuitively set the density of ligands and the thickness of the ring at $t = 0$ to be

$$\rho_l(r,0) = \rho_l^0, \quad \text{and} \quad R(0) = R_c. \tag{5}$$

Since no full analytic solution is available for this moving boundary problem, Eqs. (2) to (5) are solved numerically for $\rho_l^e = 0$ and ρ_b is extracted from simulations. The solution is compared with the results of

Please cite this article as: D. Schmidt, et al., Crowding of receptors induces ring-like adhesions in model membranes, Biochim. Biophys. Acta (2015), http://dx.doi.org/10.1016/j.bbamcr.2015.05.025

the simulation in Fig. 5A. Without any fit parameters, we find excellent agreement between the two approaches confirming that the closure of the ring is mainly driven by the diffusion of ligands from the bulk of the vesicle into the contact zone.

Interestingly, the dynamics of the ring closure is stable with respect to the shape of the inner interface. This is unusual behavior for diffusion limited growth processes where typically dendritic or even fractal patterns evolve in time [42,43]. However, this can be understood from the ligand density profile around a ring domain with shape perturbations at the inner interface (Fig. 5B). Because the flux of ligands from the outside is larger at trailing parts of the interface than at the leading parts, the shape instability is suppressed and the inner shape of the ring is stabilized.

4.4. Stable rings

Formation of the stable ring morphology (yellow shaded regions in Fig. 3B) is driven by the diffusion of receptors into the contact zone. It occurs at densities where the receptor mobility is not significantly impeded by crowding effects (low receptor densities), but is sufficiently large for stable nucleation to take place. For this reason, the stable ring regime strongly relies on the membrane-transmitted cooperative effects between bonds.

The importance of cooperativity is clearly demonstrated in Fig. 6A, where we show snapshots from a simulation without (left) and with (right) the membrane implicitly resolved. In the first case the formation of bonds does not affect the shape and the fluctuations of the membrane (no cooperativity), hence, the ligand-receptor reaction rates are constant. In the second case, the reaction rate is coupled to the membrane as discussed in the method section. Due to this cooperativity, the bonds organize into domains, and the number of bonds is an order of magnitude larger compared to the case without the membrane transmitted interactions between bonds. In the latter case, the bonds are randomly distributed over the contact zone. In fact, without correlations, nucleation is suppressed, and stable adhesion may not take place. If this occurs, the formation of the ring is significantly delayed. Yet, in the latter case, the closing of the ring occurs on significantly shorter time scales than for stable rings, suggesting a transient ring regime.

The stability of the ring is hence promoted by the cooperative effects which promote binding in the vicinity of already existing bonds. However, because of their size, bulky bound receptors become obstacles for diffusing receptors, which slow down their transport toward the center of the contact zone, and further promote their binding at the edge. This induces crowding of receptors and seals the interior of the contact zone from the outer reservoir of binders. Another consequence of cooperativity is the significantly diminished unbinding rate. Hence, even receptors at the inner edge unbind extremely rarely, which suppresses further thickening of the ring on experimentally accessible time scales.

In very long simulations (Fig. 6B), however, we observe the increase of the ring thickness of about 50% after extending the simulation to an order of magnitude longer than time necessary for the formation of the ring. This suggest, that ultimately, even "stable" ring-like domains are, in essence, transient even though not on accessible time scales. However, as the ring growth depends solely on the unbinding and rebinding of bonds at the inner edge of the ring domain, increasing the effective binding affinity drastically decreases the growth of the ring.

Last but not least, the stability of the phase diagram depends on the system size. For example, decreasing the number of available ligands by keeping the same concentration but decreasing the size of the vesicles, at some point induces a shortage of ligands. Hence, the small domains may not merge to cover the entire contact zone or to close the rings. On the other hand, quadrupling the area of the vesicle (ligand reservoir of 8192×8192 lattice points for a vesicle of a radius $R = 23.1$ μm) induced no changes in the phase diagram.

Additional effects arise from the finite size of the contact zone. It does not affect the regimes of transient ring formation and multiple nucleation. However, for smaller radii of the contact zone, the phase space for the formation of stable rings shrinks because the ring thickness depends only on the concentrations of binders and not on their absolute number. The thickness of the ring is related to the length of the mean free path of a receptor coming from the bulk into the contact zone before forming a bond. If the contact zone is smaller than this mean free path, the receptor can explore the surface entirely, and the contact zone will be filled up with bonds. Conversely, increasing the size of the contact zone increases the phase space associated with stable rings.

5. Comparison with the experiments

5.1. Steady state morphology and size of adhesions

To study the interplay between protein diffusion, binding kinetics, and membrane transmitted correlations in an experimental system, we construct the experimental phase diagram for adhesion of a biotin decorated vesicle that binds to SLB with mobile neutravidins. We systematically change the concentration of neutravidin and of biotin and image the distribution of neutravidin in the steady state in 44 vesicles (Fig. 7A).

In previous work [28], we showed that within biotin–neutravidin adhesions the membrane is nearly flat, very close to the SLB, and fluctuations are completely suppressed (< 1 nm). This suggests that the affinity for biotin–neutravidin binding is very high, and that each neutravidin in the contact zone is bound to its ligand [25]. This is confirmed by simulations where we find that the number of bonds is at least 95% of the number of available receptors, even though the binding affinity used in simulations is smaller than the binding affinity of a biotin–neutravidin

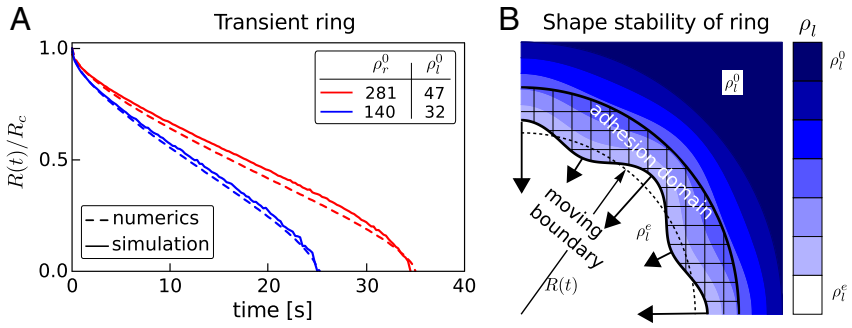

Fig. 5. A) Dynamics of the ring closure from simulations (solid lines) and the numerical model (dashed lines). B) Ligand density profile around a perturbed inner edge of the ring-like domain (shaded with squares). Arrows represent the magnitude and the directions of the flux of ligands towards the interior. The unperturbed interior edge is shown with a dotted line.

Please cite this article as: D. Schmidt, et al., Crowding of receptors induces ring-like adhesions in model membranes, Biochim. Biophys. Acta (2015), http://dx.doi.org/10.1016/j.bbamcr.2015.05.025

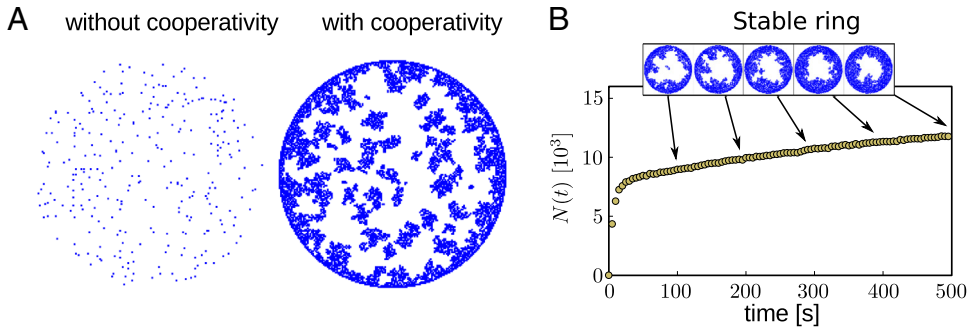

Fig. 6. A) Snapshots of the contact zone in steady state. A snapshot of the contact zone for a system without cooperativity (left), is compared to the contact zone from the full simulation including membrane induced cooperative effects between bonds (right). Both simulations are performed with identical parameters as stated in the simulation method section, except for the effective binding affinity which was increased to 15 k_BT. The binder densities are set to $\rho_l^0 = \rho_r^0 = 31\ \mu m^{-2}$. B) A very long simulation in the stable ring regime with an effective binding affinity of 10 k_BT shows slow thickening of the ring. Increasing the binding affinity slows down the thickening of the ring (data not shown).

pair within adhesions. The same result can be visualized by comparison of the bond and receptor distributions (Fig. 7B and C).

Compared to biotin ligands, neutravidin receptors are very large, and are expected to crowd when penetrating the contact zone, and hence, induce stable rings. Indeed, as in simulations, at high concentrations of receptors the contact zone is uniformly filled with bonds, but decreasing the receptor concentration results in the appearance of ring-like adhesions.

If the concentration of receptors is low, increasing the ligand density for a fixed receptor density, decreases the average area of adhesions (Fig. 7B, bottom rows) and, moreover, the ring thickness d decreases, too (Fig. 8A). For example, for vesicles shown in Fig. 7A, increasing the ligand density by factor of 10 from $\rho_l^0 = 1.4 \cdot 10^3\ \mu m^{-2}$, induces a decrease of the adhesion area from 51% to 35% of the contact zone, and the ring thickness from 3.6 to 2.4 μm (Fig. 8A inset). On the other hand, increasing the receptor density from $\rho_b^0 = 1.4 \cdot 10^3$ to $3.5 \cdot 10^3\ \mu m^{-2}$ for a constant ligand density of $\rho_l^0 = 14 \cdot 10^3\ \mu m^{-2}$, results in the increase of the adhesion area from 35% to 76%. This trend is confirmed in simulations which show that not only the thickness of the ring is smaller, but also the actual number of bonds becomes smaller at larger concentrations of ligands. More specifically, the thickness of the ring drops by a factor about 3 over the entire range of ligand surface coverage.

The reason for the density dependency lies in the dynamics of ring formation. For high ligand densities, the ring closes faster than for low ligand densities. Consequently, the number of receptors diffusing into the contact zone, before crowding, is smaller for the high ligand densities than for low ligand densities allowing only for a thin ring and therefore a smaller number of bonds.

5.2. Enrichment factor

In simulations, we find that the final number of bonds is almost equal to the initial receptor density ρ_r^0 (see Fig. 8B), and only at low receptor concentrations, it is affected by the initial ligand density ρ_l^0 (see Fig. 8B inset). Such a trend emerges because the receptor density shows only little enrichment of the initial receptor density in the contact zone. This is due to the fact that at large receptor densities, bonds form over the entire contact zone which prevents further accumulation of binders. The significantly smaller ligands, in contrast, diffuse through a bond domain restoring the ligand density in the contact zone at every stage of domain formation, until the growth process is stopped by the lack of receptors.

This result agrees well with experimental observations of the enrichment factor at low temperatures (small diffusion constants). However, at high temperatures (fast diffusion) very high enrichment factors (see Fig. 9), maximizing the packing of neutravidin in the contact zone (blue doted line) are observed, even at low initial receptor densities. It was previously argued [26], that such high enrichments occur because the accumulation of receptors takes place during the spreading of the vesicle, and not after the contact zone is formed.

To confirm this hypothesis, we perform a set of simulations where the vesicle falls onto the substrate with a constant velocity v_s, i.e. the contact area changes linearly in time. Moreover, in these simulations the nucleation time is fast.

In such a scenario, the bonds start to form in a very small contact zone, and the binders accumulate in the contact zone while it is spreading. As a result, the enrichment factor becomes a function of the velocity v_s (in units of μm/s). To compare different initial ligand and receptor

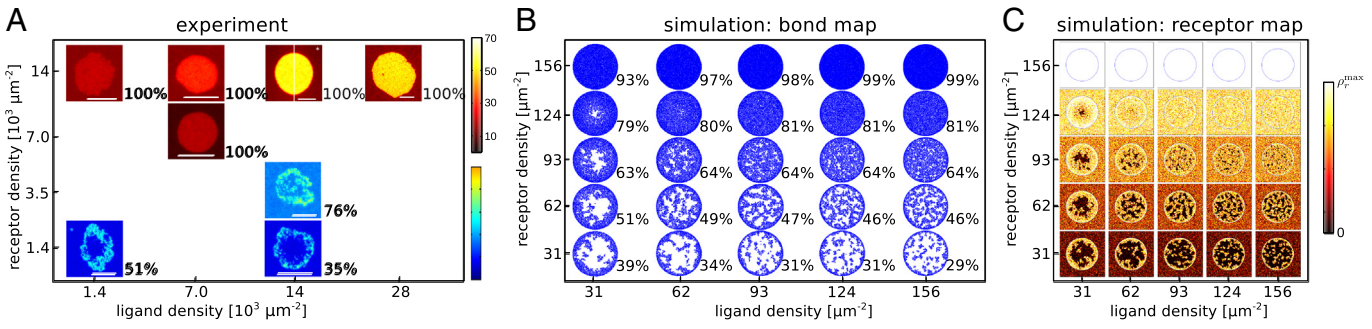

Fig. 7. Comparison of the measured (A) and simulated phase diagrams (B, C). Epifluorescent images of neutravidins in the steady state as a function of ligand and receptor coverage is shown in A. The increase in bulk concentration of receptors is seen by the change of color outside of the contact zone. The number indicates the fraction of the contact zone occupied by adhesions. The scale bar shows 10 μm and the color code in units of 10^3 μm. (B) Contact zones in the steady state obtained from simulations as a function of ligand and receptor bulk density. Bonds are marked with blue, and the respective receptors distributions are shown in (C).

Please cite this article as: D. Schmidt, et al., Crowding of receptors induces ring-like adhesions in model membranes, Biochim. Biophys. Acta (2015), http://dx.doi.org/10.1016/j.bbamcr.2015.05.025

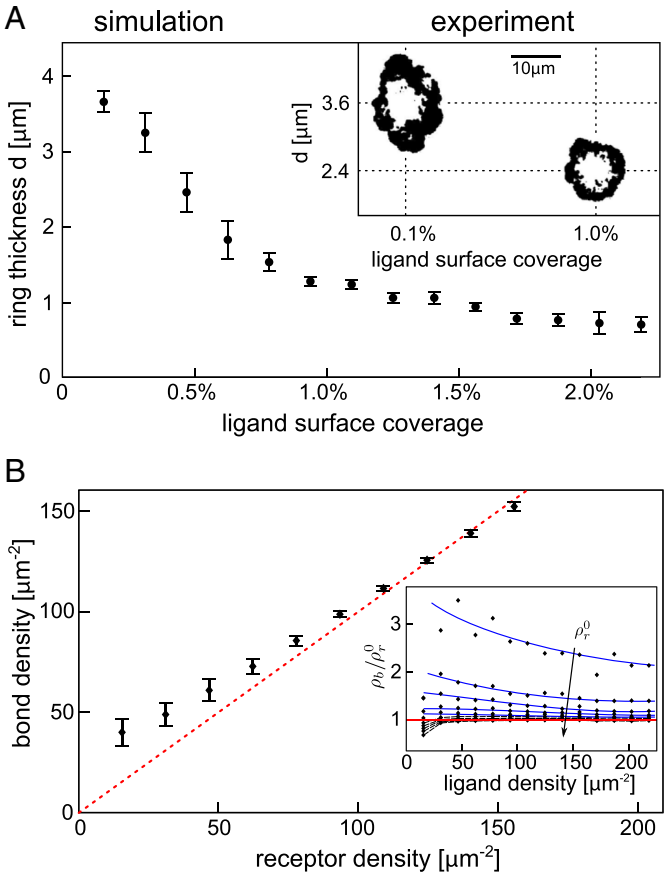

Fig. 8. (A) Ring thickness as a function of the ligand density for the simulation and the experiment (inset). Error bars mark the standard deviation for various receptor densities. Inset: Snapshots of the bond domain from the experiment (black area) for two different ligand densities. (B) Accumulated bond density ρ_b in the contact zone as a function of the initial receptor density ρ_r^0. The inset shows the normalized bond density ρ_b/ρ_r^0 as a function of the initial ligand density ρ_l^0.

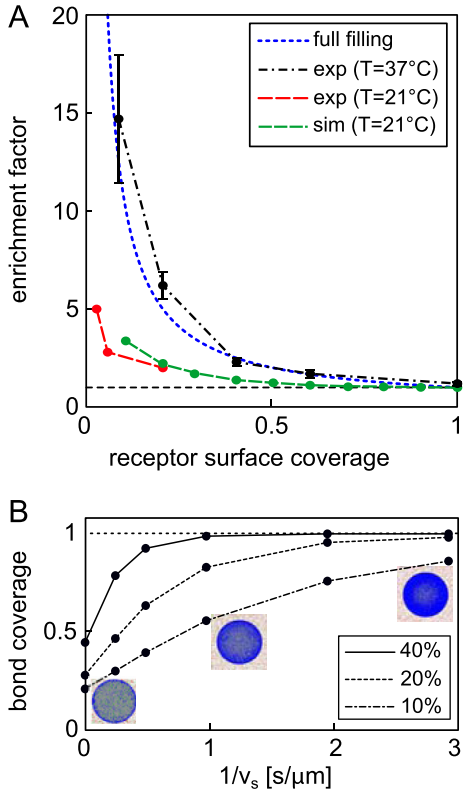

Fig. 9. (A) Enrichment factor observed experimentally at different temperatures and in simulations. The experiments presented in this work are performed at $T = 21$ °C. The enrichment factors at high temperature ($T = 37$ °C) was taken from Fenz et al. [26] (B) Simulated steady state bond coverages for vesicles spreading as the bonds are being formed. The vesicles sediment to the substrate with constant velocity v_s ($\rho_l^0 = \rho_r^0$, indicated in the legend).

densities, we show in Fig. 9 (bottom) the bond coverage in steady state. We find that as the inverse of v_s increases the thickness of the ring of crowded receptors also increases up to full packing above a critical value.

The actual value of the critical velocity depends sensitively on the concentration of both, receptors and ligands. At low ligand and high receptors densities, the reservoir of ligands may be fully depleted before the spreading is completed which results in densely packed domains in the center of the contact zone and the edge free of bonds.

6. Discussion and conclusions

In this work, we studied the interplay between the capacity of binders to diffuse through growing structures in the membrane and the morphology of these structures. We find that the initial density of bulky binders plays a major role as a control parameter for the final organization of adhesions. Furthermore, a rich phase space of growth patterns was identified, showing very similar features in simulations and experiments.

Particularly interesting are spontaneously forming ring-like structures, which arise due to the recruitment of binders into the contact zone of two membranes. If the ring is created as a consequence of accumulation of small binders (ligands), the ring structure is transient. On the other hand, if it is caused by crowding of bulky binders (receptors), the ring becomes significantly more stable, due to the inability of the large proteins to diffuse through the already established structure. Such a ring naturally creates a coral in the membrane, isolating the interior of the ring from the outside. In the cellular context, our results suggest that the formation of the ring may be passive, but the transport through the ring should involve active mechanisms. The latter seems to be the case for the T cell receptors that are transported, by coupling to the actin retrograde flow [4].

The formation of rings may be preceded by a formation of numerous small domains within the entire contact zone. This result is in agreement with recent observations of the formation of cadherin rings in the contact zone between two epithelial cells [6], where in the initial stage, multiple nucleation is promoted by homogeneous fluctuations of the composite cell membrane. However, a ring forms within a minute, at the edge of the contact zone by nucleations of small adhesions, which grow both by accumulation of cadherin from the bulk, as well as from cadherins within the emergent coral. The closure of the ring seems to provide a signal to the actin–myosin apparatus to actively exert contractile forces on the cadherin junctions, expanding the ring and increasing the contact zone. This scenario of ring-closure agrees very well with the simulations presented in this study (Fig. 7), suggesting that the initial stage of the cell–cell recognition process may rely on cadherin binding, regulated by their density and the physical properties of the cell envelope. Furthermore, our results suggest that active actin driven cell spreading couples to the development of adhesion in a highly regulated fashion, an idea which could be explored beyond the current manuscript.

Another interesting observation is the increase of the enrichment factor with the speed of the spreading of the contact zone. While this effect was demonstrated on a relatively large scale, the mechanism applies also for small contact areas. This would allow cells to regulate the density of binders in the forming of adhesions by controlling the speed of protruding lamellipodia and filopodia from the cell surface.

Please cite this article as: D. Schmidt, et al., Crowding of receptors induces ring-like adhesions in model membranes, Biochim. Biophys. Acta (2015), http://dx.doi.org/10.1016/j.bbamcr.2015.05.025

In conclusion, we established a Monte Carlo scheme with which we are able to understand the details of experimental observations, from the stability of bonds to the organization into macromolecular structures. Intriguingly, the micro-domain bond structures described here closely resemble those reported since more than a decade ago for integrin/TCR mediated adhesion in immune cells [1–3,5], as well as more recent reports on cadherin mediated adhesion in epithelial carcinoma cells [6]. The insights gained from the dual simulation and experimental model system can potentially identify regulating mechanisms, that can then be tested in a cellular system. Receptor crowding, arising from steric hindrance or lateral interactions, as well as ring closure, which itself is determined by molecular concentrations, interactions, and transport, have been identified here as potential important players in cell adhesion.

Acknowledgments

We thank Michael Dustin and Virgile Viasnoff for insightful discussions. A.S.S., D.S., and T.B. received funding from the European Research Council (starting grant 2013-337283), Research Training Group 1962 at Friedrich-Alexander-Universität Erlangen–Nürnberg and were supported by the Excellence Cluster: Engineering of Advanced Materials at Friedrich-Alexander-Universität Erlangen–Nürnberg. K.S. received funding from the European Research Council (307104FP/2007–2013/ERC).

Appendix A. Supplementary data

Supplementary data to this article can be found online at http://dx.doi.org/10.1016/j.bbamcr.2015.05.025.

References

[1] C. Monks, B. Freiberg, H. Kupfer, N. Sciaky, A. Kupfer, Nature 395 (1998) 82–86.
[2] A. Grakoui, S.K. Bromley, C. Sumen, M.M. Davis, A.S. Shaw, P.M. Allen, M.L. Dustin, Science 285 (1999) 221–227.
[3] Y. Kaizuka, A.D. Douglass, R. Varma, M.L. Dustin, R.D. Vale, Proc. Natl. Acad. Sci. U. S. A. 104 (2007) 20296–20301.
[4] M.L. Dustin, J.T. Groves, Annu. Rev. Biophys. 41 (2012) 543–556.
[5] P. Dillard, R. Varma, K. Sengupta, L. Limozin, Biophys. J. 107 (2014) 2629–2638.
[6] W. Engl, B. Arasi, L.L. Yap, J.P. Thiery, V. Viasnoff, Nat. Cell Biol. 16 (2014) 584–591.
[7] P.K. Tsourkas, N. Baumgarth, S.I. Simon, S. Raychaudhuri, Biophys. J. 92 (2007) 4196–4208.
[8] P.K. Tsourkas, M.L. Longo, S. Raychaudhuri, Biophys. J. 95 (2008) 1118–1125.
[9] P.K. Tsourkas, S. Raychaudhuri, Cell. Mol. Bioeng. 3 (2010) 256–268.
[10] S.Y. Qi, J.T. Groves, A.K. Chakraborty, Proc. Natl. Acad. Sci. U. S. A. 98 (2001) 6548–6553.
[11] N.J. Burroughs, C. Wülfing, Biophys. J. 83 (2002) 1784–1796.
[12] T.R. Weikl, J.T. Groves, R. Lipowsky, EPL (Europhysics Letters) 59 (2002) 916.
[13] T.R. Weikl, R. Lipowsky, Biophys. J. 87 (2004) 3665–3678.
[14] D. Coombs, M. Dembo, C. Wofsy, B. Goldstein, Biophys. J. 86 (2004) 1408–1423.
[15] H. Krobath, B. Rozycki, R. Lipowsky, T.R. Weikl, PLoS One 6 (2011) e23284.
[16] J. Brzostek, J.-G. Chai, F. Gebhardt, D.H. Busch, R. Zhao, P.A. van der Merwe, K.G. Gould, Eur. J. Immunol. 40 (2010) 2050–2059.
[17] O. Milstein, S.-Y. Tseng, T. Starr, J. Llodra, A. Nans, M. Liu, M.K. Wild, P.A. van der Merwe, D.L. Stokes, Y. Reisner, M.L. Dustin, J. Biol. Chem. 283 (2008) 34414–34422.
[18] A.-S. Smith, E. Sackmann, ChemPhysChem 10 (2009) 66–78.
[19] S.F. Fenz, K. Sengupta, Integr. Biol. 4 (2012) 982–995.
[20] E. Sackmann, A.-S. Smith, Soft Matter 10 (2014) 1644–1659.
[21] P. Streicher, P. Nassoy, M. Barmann, A. Dif, V. Marchi-Artznerm, F. Brochard-Wyart, J. Spatz, P. Bassereau, Biochim. Biophys. Acta Biomembr. 1788 (2009) 2291–2300.
[22] S.F. Fenz, A.-S. Smith, R. Merkel, K. Sengupta, Soft Matter 7 (2011) 952–962.
[23] G.I. Bell, M. Dembo, P. Bongrand, Biophys. J. 45 (1984) 1051.
[24] A.-S. Smith, U. Seifert, Soft Matter 3 (2007) 275–289.
[25] D. Schmidt, T. Bihr, U. Seifert, A.-S. Smith, EPL (Europhysics Letters) 99 (2012) 38003.
[26] S.F. Fenz, R. Merkel, K. Sengupta, Langmuir 25 (2009) 1074–1085.
[27] L. Limozin, K. Sengupta, ChemPhysChem 10 (2009) 2752–2768.
[28] A.-S. Smith, S.F. Fenz, K. Sengupta, EPL (Europhysics Letters) 89 (2010) 28003.
[29] T. Bihr, U. Seifert, A.-S. Smith, arXiv arXiv:1503.017182015.
[30] T. Bihr, U. Seifert, A.-S. Smith, Phys. Rev. Lett. 109 (2012) 258101.
[31] J. Hu, R. Lipowsky, T.R. Weikl, Proc. Natl. Acad. Sci. U. S. A. 110 (2013) 15283–15288.
[32] A.-S. Smith, K. Sengupta, S. Goennenwein, U. Seifert, E. Sackmann, Proc. Natl. Acad. Sci. U. S. A. 105 (2008) 6906–6911.
[33] E. Evans, W. Rawicz, Phys. Rev. Lett. 64 (1990) 2094–2097.
[34] S.F. Fenz, T. Bihr, R. Merkel, U. Seifert, K. Sengupta, A.-S. Smith, Adv. Mater. 23 (2011) 2622–2626.
[35] T. Bihr, S. F. Fenz, D. Schmidt, R. Merkel, K. Sengupta, U. Seifert and A.-S. Smith, in preparation.
[36] M. Avrami, J. Chem. Phys. 8 (1940) 212–224.
[37] P.L. Krapivsky, S. Redner, E. Ben-Naim, A Kinetic View of Statistical Physics, Cambridge University Press, 2010.
[38] A. Boulbitch, Z. Guttenberg, E. Sackmann, Biophys. J. 81 (2001) 2743–2751.
[39] V.B. Shenoy, L.B. Freund, Proc. Natl. Acad. Sci. U. S. A. 102 (2005) 3213–3218.
[40] H. Gao, W. Shi, L.B. Freund, Proc. Natl. Acad. Sci. U. S. A. 102 (2005) 9469–9474.
[41] T. Bihr, S. Fenz, E. Sackmann, R. Merkel, U. Seifert, K. Sengupta, A.-S. Smith, Biophys. J. 107 (2014) L33–L36.
[42] W.W. Mullins, R.F. Sekerka, J. Appl. Phys. 34 (1963) 323–329.
[43] T.A. Witten, L.M. Sander, Phys. Rev. Lett. 47 (1981) 1400–1403.

Please cite this article as: D. Schmidt, et al., Crowding of receptors induces ring-like adhesions in model membranes, Biochim. Biophys. Acta (2015), http://dx.doi.org/10.1016/j.bbamcr.2015.05.025